

**NEAR-CONCENTRIC OPTICAL RESONATOR  
FOR COHERENT ATOM-PHOTON  
INTERACTION**

by

**ADRIAN NUGRAHA UTAMA**

*(B.Sc.(Hons), National University of Singapore)*

**A THESIS SUBMITTED FOR THE DEGREE OF  
DOCTOR OF PHILOSOPHY**

in

**CENTRE FOR QUANTUM TECHNOLOGIES  
NATIONAL UNIVERSITY OF SINGAPORE**

**2021**

Supervisor:

Professor Christian Kurtsiefer

Examiners:

Asst/Prof Yvonne Y. GAO, National University of Singapore

Prof Pepijn W.H. PINKSE, University of Twente

A/Prof Axel KUHN, University of Oxford

## Declaration

I hereby declare that this thesis is my original work and it has been written by me in its entirety. I have duly acknowledged all the sources of information which have been used in the thesis.

This thesis has also not been submitted for any degree in any university previously.



Adhion Nugraha Utama

---

20 October 2021

*To all seekers of knowledge and fame,  
may you have the serenity to accept what can't be changed,  
may you have the courage to implement what can be changed,  
and may you have the wisdom to know the difference.*

## Acknowledgments

There is no way to apprehend my utmost everlasting gratitude to my supervisor and teacher, Christian Kurtsiefer. I would not have finished this PhD journey without his countless insights, inspirations, and support throughout my ups and downs. I am deeply inspired by his unpretentious and sanguine approach towards Physics and knowledge. The beacon for my arduous thesis-writing journey is one of his quotes to one of his juniors, which I found in a booklet in the lab, “*Eine Doktorarbeit macht mann nicht fertig, man gibt sie einfach irgendwann ab*”.

I would like to thank my mentor and lab partner, Chi Huan, for showing me what it means and takes to pursue a physics research. I deeply value his commitment to provide a safe space for us to explore the project, as an equal lab partner, and for me to stand up for my own ideas and pursuits.

I cherish the accompaniment and support from my other lab partners, Neville, Chang Hoong, Florentin, and Wen Xin. I hope that I didn't do a terribly bad job at being a co-adventurer in the project. I also appreciate the every so often help and cooperation that I received for the cavity project, in particular from Boon Long, Mathias, Jianwei, Lijiong, Matthias, Brenda, Ting You and Xi Jie. I do not want to forget the support from the workshop staffs, which had to endure our funny request at times – Uncle Bob, Teo, Imran, Chorng Wang, Cliff, and others.

Furthermore, I enjoy the presence and discussion from the remaining group members – Peng Kian, Hou Shun, YiCheng, Wilson, Nick and Alessandro. I have a special shout out to Janet for being such a mood-lifter, and Victor for being such a patient mentor, during my pre-PhD stint in the lab. I also would like to commemorate the camaraderie of Jianwei and Mathias, where we together think of funny ideas, which sometimes result in funny projects. I thoroughly enjoyed the physics and meta-physics discussions with primarily the atom group members – Chang Hoong, Boon Long, Neville, and Florentin, which at times, perhaps reluctantly.

Undergraduate students, lab interns and visitors brought colours and energy into the lab. I would like to acknowledge Justin, Nasri, Jun Yan, Alvin, Antony, Jun Tat, Tan Le, Ilija the memelord, Philip, Andreas, Mervin, Kelly, Wai Marn, Kim Hung, Jyn Harng, and Jannis, who was a visitor from the University of Hannover. I am very grateful for the assistance and support from the CQT staffs, and enjoy the

interactions and exchanges with the CQT students, which are too many to name. Last but not least, I would like to thank my mom, dad, sister, family, friends, teachers, mentors, and my partner-in-life, Jesslyn, for their everlasting encouragement for me to pursue and finish the project.

Finally, I would like to thank the examiners for painstakingly reading my thesis, and giving some of the most insightful feedback during the thesis defence.

# Contents

<b>Acknowledgments</b>	<b>ii</b>
<b>Summary</b>	<b>vi</b>
<b>List of Figures</b>	<b>viii</b>
<b>List of Tables</b>	<b>xi</b>
<b>Preamble</b>	<b>1</b>
<b>1 Introduction</b>	<b>3</b>
1.1 Aim of this Work . . . . .	6
1.2 Thesis Outline . . . . .	8
1.3 Other Explorations and Applications . . . . .	10
1.4 A Brief Theory of Cavity Quantum Electrodynamics . . . . .	14
<b>2 Design of a Near-Concentric Optical Cavity</b>	<b>24</b>
2.1 Cavity Mirrors . . . . .	24
2.2 Mechanical Stages . . . . .	30
<b>3 Experimental Setup and Techniques</b>	<b>39</b>
3.1 Laser Systems and Spectroscopy Techniques . . . . .	39
3.2 Vacuum System . . . . .	44
3.3 Stabilisation of Near-Concentric Cavity . . . . .	47
3.4 Measurement of Cavity Parameters . . . . .	52
<b>4 Observation of Atom-Cavity Interaction</b>	<b>57</b>
4.1 Trapping Single Atoms . . . . .	57

4.2	Probing Atom-Cavity Response . . . . .	64
<b>5</b>	<b>Coupling to Near-Concentric Transverse Modes</b>	<b>73</b>
5.1	Mode Preparation with a Spatial Light Modulator . . . . .	74
5.2	Mode Matching to Cavity Transverse Modes . . . . .	79
<b>6</b>	<b>Noise Reduction Techniques</b>	<b>84</b>
6.1	Active Noise Cancellation . . . . .	86
6.2	Friction Damping . . . . .	102
<b>7</b>	<b>Discursion around the Critical Point</b>	<b>111</b>
7.1	Last Stable Resonance . . . . .	111
7.2	Diffraction Loss and Aperture Size . . . . .	114
<b>8</b>	<b>Outlook and Future Studies</b>	<b>120</b>
8.1	Current and Future Capabilities . . . . .	120
8.2	Cavity Setup and Mirror Redesign . . . . .	121
8.3	Near-Concentric Cavity Pathways . . . . .	125
<b>9</b>	<b>Conclusion</b>	<b>128</b>
	<b>Bibliography</b>	<b>131</b>
	<b>List of Publications</b>	<b>163</b>
<b>A</b>	<b>Theory of Near-Concentric Cavity Paraxial Modes</b>	<b>164</b>
<b>B</b>	<b>Geometrical Alignment Theory of Near-Concentric Cavity</b>	<b>169</b>
<b>C</b>	<b>Imperfections of the Cavity Mirror</b>	<b>173</b>
<b>D</b>	<b>Miscellaneous Techniques in Noise Reduction</b>	<b>177</b>

# Summary

Near-Concentric Optical Resonator For Coherent Atom-Photon Interaction

by

Adrian Nugraha Utama

Doctor of Philosophy in Centre for Quantum Technologies

National University of Singapore

Optical resonators are indispensable in engineering coherent interaction between atoms and photons, as fundamental building blocks in hybrid quantum information processing. With their interaction governed by cavity quantum electrodynamics, atom-cavity systems require photons to be contained in a small mode volume, and this is conventionally implemented with small high-finesse optical resonators. However, although largely unexplored, small mode volumes can also be achieved with relatively large optical resonators operated in a near-concentric regime, with a strongly focused cavity mode. Near-concentric optical cavities require a relatively low finesse to operate, and provide a large physical space between the mirrors, which can be useful for atomic ensembles, ions or Rydberg atoms. Furthermore, the frequencies of the cavity transverse modes are near-degenerate, and on the order of the hyperfine or Zeeman level splitting of the atoms, which can be utilised for atom-light interactions employing multiple photonic modes.

This thesis explores different facets of a 11-mm length near-concentric cavity operated extremely close (less than  $5\ \mu\text{m}$ ) to the critical point. First, we observe a coupling of a single  $^{87}\text{Rb}$  atom to the fundamental mode of the near-concentric cavity, with the coupling strength  $g = 2\pi \times 5.0(2)$  MHz exceeding the atomic dipole decay rate by a factor of  $1.7(1)$  – on par with small cavity systems exhibiting strong atom-photon coupling. Due to a low cavity finesse of  $138(2)$ , the atom-cavity cooperativity is  $0.084(4)$ , which can be easily improved easily by using mirrors with higher reflectivities. Second, we selectively excite one or a superposition of the higher-order transverse modes of the near-concentric cavity, with mode-matching efficiencies close to the theoretical prediction. Third, we implement passive and active noise reduction strategies to stabilise the cavity length, and bring the cavity

mechanical noise down to an acceptable level. We also examine a different mounting technique which provides a higher stability for future designs. Last, we explore how the near-concentric cavity becomes unstable around the critical point, and assess the limit to the near-concentric cavity performance.

These studies provide valuable insights into the workings of a near-concentric cavity system. A better understanding of such system, in terms of its mechanical stability and performance limits, enables a coherent interaction between atoms and photons, even with a moderate-finesse near-concentric cavity. Furthermore, it would be fascinating to apply near-concentric cavities in various systems, which exploit the tight-focusing geometry, near-degenerate transverse modes, or highly divergent critical behaviour, as resources for quantum technologies.

# List of Figures

1.1	Energy level diagrams of bare and coupled atom-cavity systems . . . .	16
1.2	A schematic of a Fabry-Perot cavity with its corresponding transmission spectrum . . . . .	17
1.3	Stability diagram for Fabry-Perot cavities . . . . .	20
1.4	Mode volume of symmetrical cavities as a function of their length . . .	21
1.5	Standing-wave modes and resonances of a near-concentric cavity . . . .	22
2.1	A schematic of the anaclastic lens-mirror . . . . .	26
2.2	An illustration of a near-concentric cavity system; the cavity waist radius and coupling strength as a function of the critical distance. . . . .	27
2.3	The threshold distance as a function of the mirror radius; the coupling strength and the ratio of atom-light cross sections at half-wavelength critical distance. . . . .	29
2.4	Pictures of the actuators and translation stages used in the thesis . . .	31
2.5	Schematic of the cavity mechanical design version 1 . . . . .	33
2.6	Schematic of the cavity mechanical design version 2 . . . . .	34
2.7	The alignment setup of the near-concentric cavity . . . . .	37
3.1	A picture of the external cavity diode laser setup . . . . .	40
3.2	Energy level structure of $^{87}\text{Rb}$ $D_1$ and $D_2$ line transitions . . . . .	42
3.3	Atomic FM spectroscopy setup for ECDL stabilisation . . . . .	43
3.4	Pictures of the cavity setup inside the vacuum chamber . . . . .	44
3.5	Schematic of the transfer cavity setup . . . . .	49
3.6	Cavity transmission at different transverse positions of a cavity mirror	50
3.7	Transverse alignment stabilisation via the cavity transmission. . . . .	51
3.8	Cavity transverse mode spacing at different critical distances . . . . .	56

4.1	Schematic of the magneto-optical trap setup . . . . .	58
4.2	Schematic of the far-off resonant trap setup . . . . .	61
4.3	A typical trace of the atomic fluorescence signal . . . . .	62
4.4	Triggered fluorescence of single atom and indeterminate traces . . . . .	63
4.5	Trapped atom lifetime with MOT cooling beams switched off . . . . .	64
4.6	Schematic of the setup to probe the atom-cavity response . . . . .	66
4.7	Experimental sequence of the cavity probe experiment . . . . .	66
4.8	A sample trace of the alternating fluorescence and transmission signal .	67
4.9	Cavity reflection and transmission spectra with a trapped single atom .	71
5.1	Experimental setup for coupling to higher-order transverse modes . . .	77
5.2	Mode-matching spectra for LG modes with $l = 0$ . . . . .	80
5.3	Mode-matching spectra for LG modes with $l \neq 0$ . . . . .	80
5.4	Mode-matching to a superposition of LG modes . . . . .	81
6.1	A typical mechanical noise spectral density in cavity version 2a . . . .	88
6.2	The gain-phase response of the cavity translation stage . . . . .	89
6.3	A block diagram for cavity translation stage actuation and control . . .	90
6.4	The area in <i>PMFC</i> complex plane suitable for noise reduction . . . . .	92
6.5	A typical gain-phase response of a PI and PID control . . . . .	93
6.6	A typical gain-phase response of a lead compensator and notch filter .	95
6.7	Gain-phase responses of the toy models . . . . .	98
6.8	Noise reduction of the toy models by tuning $K_P$ . . . . .	99
6.9	Noise spectral density of the toy models after noise cancellation . . . .	100
6.10	Noise spectral density of cavity version 2a after noise cancellation . . .	102
6.11	Placements of friction dampers on the cavity structure for mechanical noise reduction . . . . .	104
6.12	Frequency-dependent gain ratio between the cavity and the platform vibration amplitudes for different friction damper configurations . . . .	106
6.13	Probing the stick to slip transition of the friction dampers . . . . .	107
6.14	Damping effect of different friction damper masses on the translation stage DC gain and the total vibration noise . . . . .	108
6.15	A typical mechanical noise spectral density in cavity version 2b . . . .	109

7.1	Cavity transmission spectra at the last stable resonance . . . . .	112
7.2	Cavity transverse modes linewidths and transmission amplitudes at different critical distances . . . . .	114
7.3	Camera-captured spatial profiles of the cavity transmission modes . . .	115
7.4	Mode diameter on the cavity mirror containing 99% of total power . .	116
7.5	Numerical calculation of the cavity linewidth using the Prony's method	118
8.1	Prototype of the cavity mechanical redesign . . . . .	123
8.2	A typical mechanical noise spectral density in cavity version 3 . . . . .	124
B.1	Determining the cavity axis geometrically . . . . .	170
B.2	Rotation of cavity axis due to transverse misalignment . . . . .	171
B.3	Equivalence of angular and transverse misalignment . . . . .	172
C.1	The effect of uniform optical coating on the mirror reflectivity . . . . .	174
C.2	The mirror reflectivity and phase as a function of the ray angle . . . . .	175

# List of Tables

2.1	Summary of the cavity mechanical design development . . . . .	32
5.1	Expected values of the mode matching efficiencies between the SLM output and the radial transverse modes . . . . .	77
5.2	Comparison of mode matching efficiencies between simulation and exper- iment for single LG modes . . . . .	81
8.1	Explorations pathways in near-concentric cavities . . . . .	127

# Preamble

In 1899, Charles Fabry and Alfred Pérot developed an interference apparatus made from two silver-coated glass surfaces facing each other [1]. This apparatus, which they called the “interference spectroscope”, produces sharp interference fringes due to multiple reflections back and forth the silver mirrors. This allows them to improve the resolving power of spectroscopy and metrology experiments. Since then, this Fabry-Perot interferometer idea has been extended to many different forms, and is used in many science experiments and technological applications.

The reflectivity of visible light on a silver-coated mirror is around 90%, which gives a pretty decent interference effect. The catalyst for the idea advancement is the construction of mirrors consisting of multiple thin dielectric layers, which allows mirror reflectivity very close to unity with very low loss. Around the 1930s, multilayer thin films were used to develop antireflection coatings [2, 3], which later aided in the war efforts, through the use of antireflection coating on binoculars to improve visibility at dawn and dusk [4]. Dielectric-coated mirrors and antireflectors work through a specific variation of the refraction index and thickness of each layers, based on the interference effect as well [5]. The idea of multilayer interference also spurred into engineering of frequency-selective optical components, such as narrow-band transmission filters or reflectors of specific wavelength [6, 7].

High reflectivity dielectric mirrors were also very useful for the development of lasers in the 1960s, which requires amplification of light [8, 9]. This can be achieved with an optical resonator such as a Fabry-Perot interferometer, as the light energy amplifies between the two highly reflective mirrors due to multiple reflections [10, 11]. Another important theoretical work is the calculation of the steady-state field distribution of the Fabry-Perot interferometer [12], which is later shown to have very low diffraction loss with curved mirrors [11]. This stable configuration for the resonator modes is akin to a light beam passing through a periodic sequence of lenses,

while maintaining the beam size due to repeated refocusing [13, 14]. Furthermore, optical coating deposition techniques have improved considerably in the 1980s [15], allowing for extremely high dielectric mirror reflectivity with ultralow losses at about 1 ppm [16]. This corresponds to around one million back-and-forth light reflection off the mirrors, effectively trapping the light inside the interferometer.

The development of a low-loss optical cavity greatly benefits the field of quantum optics. Since the 1990s, such optical cavities have been used to observe and engineer atom-light interaction at the level of a single quanta [17, 18]. It has also advanced the field of spectroscopy and metrology [19–21], furthering the initial explorations of Fabry and Perot, which turns into various optical cavity-based sensors [22–25]. Furthermore, optical cavities have also been used to test fundamental limits of relativity [26] and detect gravitational waves [27, 28].

In this thesis, I am going to describe a small contribution in the field of quantum optics – using a Fabry-Perot interferometer as an optical resonator or optical cavity, to develop some alternatives and better ways to interface with atoms. I will briefly review the development of this field in the next few sections. Then, I will offer my experiment-informed perspective on the field, by operating the cavity in a less common regime – the near-concentric regime – and presenting our results and technical challenges in detail.

It may be interesting to point out that our near-concentric optical resonator functions principally based on interference, and so do our laser systems. The coatings on the interferometer mirrors also utilise interference effects, and so do the alignment mirrors and optical filters. Some of the measurement and preparation techniques rely on interference features as well. Even what we are trying to accomplish here is to interfere atoms with light. In the end, it all goes back to interference. However, that is just one way to view it. Another view is that, by putting interferences upon interferences, we start to see something interesting and new, and that would be the spirit of my thesis.

# Chapter 1

## Introduction

The founders of quantum physics did not foresee that one day we would find ways to interact with single quantum objects, let alone manipulate them and develop new technologies. As Erwin Schrodinger wrote in 1952, “.. *we never experiment with just one electron or atom or (small) molecule. In thought-experiments we sometimes assume that we do; this invariably entails ridiculous consequences* [29].” Little did he knew that he was a few mere decades from it.

The key enabling technology to perform experiments with single particles, while harnessing their quantum properties, is undoubtedly the laser, which is built within an optical resonator. However, what is more fascinating, and also the way the thesis uses an optical resonator, is the following – the optical cavity is used to store photons as quantum objects, which interact with one or a few atoms placed inside it, in a coherent manner displaying quantum features. This lies in the field of cavity quantum electrodynamics (CQED).

**Cavity Quantum Electrodynamics** CQED is a study of the interaction between atoms (or other particles) with photons confined inside a cavity, with dominant quantum effects. The field of CQED started with a microwave cavity interacting with Rydberg atoms [30, 31], as atoms in the Rydberg state have very high electric-dipole moments with microwave level transitions [32]. The microwave cavity can be constructed with a very high quality factor in the superconducting regime, which leads to the demonstration of a maser operated only by a single atom [33].

One defining feature of CQED is the Rabi oscillation, which is a coherent oscillation between two quantised energy levels in the presence of a driving field. In the CQED

experiments, particularly due to the strong atom-photon coupling in the cavity, the Rabi oscillation can be observed with only one or a few photons present. In 1996, Serge Haroche and his team managed to observe Rabi oscillation in their CQED system, signifying a strong coupling of the atom to the cavity microwave photons [34]. Since then, these systems flourish in demonstrating myriads of textbook examples of quantum experiments [35–38], with applications in quantum information processing [39–41].

Later on, or perhaps concurrently, the field of CQED developed at least two additional main branches. First is the upgrade from the microwave to the optical regime. This allows the photon and atom to exchange roles – in the microwave cavity experiments, the information carriers (“flying” qubit) are the atoms, while in the optical cavity experiments, the flying qubit are the photons. Optical photons have high frequency and information-carrying capacity, can be transmitted over large distances or over fibres with almost negligible loss and dispersion, and can be easily manipulated and detected with standard optical elements, making it a good choice for quantum information carriers [42]. The optical CQED system is the main focus of the thesis, and will be explored further in subsequent sections.

The second branch attempts to mimic the atomic system with solid state devices. The most successful realisation is in superconducting circuits where the cavity is formed by two gaps on a microwave transmission line similar to the Fabry-Perot configuration, while the atom-like nonlinearity is achieved through a Josephson junction element placed close to the cavity [43]. The macroscopic artificial atom can be engineered to have a very high dipole moment in a one-dimensional space, with the Rabi oscillation frequency limited only by the fine structure constant. Quantum information processing capability in this circuit QED system has improved significantly over the last decades [44], leading to possibly the first 53-qubit quantum computer demonstrating supremacy over classical computers [45]. The dynamics of CQED systems can also be observed with trapped ions [46, 47] which are cooled down to very low temperatures [48, 49], reaching zero motional state [50]. In this system, the cavity photons are equivalent to the ion motional states in a harmonic potential, whereas the interaction between the ion motional and electronic states can be generated with an appropriately tuned laser – the laser drives the ion’s electric dipole vibrating along the laser axis, resulting in a motion-modulated phase

in the dipole interaction. A similar Rabi oscillation has thus been observed by David Wineland and his team in the trapped ion system [51]. The seminal quantum computation proposal by Ignacio Cirac and Peter Zoller [52] paved the way for a fundamental quantum logic gate with trapped ions [53], which recently developed into a high fidelity programmable quantum computers with 11 qubits [54]. As the ions are typically arranged in a chain and vibrate collectively, gate operations between any two ionic qubits can be implemented with two laser beams addressing the different ions, yielding a full-connectivity computing architecture [55]. This contrasts with the circuit QED architectures, where a physical connection is necessary for any two-qubit operations, requiring more operations with possibly higher errors [56].

**Single atom trapped in an optical cavity** CQED in the optical regime started with the observation of optical bistability with modified photon statistics [57] and normal-mode splitting [17] in an optical cavity system with only a few atoms at one time, by H. Jeff Kimble and his team. The optical cavity is constructed by two curved mirrors facing each other, in a Fabry-Perot configuration. These mirrors are spaced pretty close apart and have very high reflectivities, typically on the order of 0.1 mm and 99.99% respectively.

Observation of two distinct normal-mode frequencies indicates that the cavity photon modes couple strongly with the atomic energy states, just as two pendulums coupled with a spring exhibit two normal modes corresponding to the in-phase and out-of-phase movements between the pendulums. In the time domain, this corresponds to an oscillatory exchange of energy between the two pendulums, or in our case, between the atomic states and the photons. This Rabi oscillation of the atomic states in an optical cavity, observed shortly afterwards [58], can thus be viewed as a Fourier transformation of the normal-mode splitting.

The early experiments in optical CQED used a flux of atoms flowing perpendicularly to the cavity axis. This was not very ideal, as the atom only spend a short amount of time inside the cavity mode, with a coupling that depends on the atomic position and time [59]. Hence, the atom-cavity interaction process has to be treated statistically, and has some implications to the normal-mode line shapes [60]. Nevertheless, even with such limitation, it was possible to engineer nonclassical correlations of light intensity [61, 62] and controlled-phase quantum gate [63].

Even though the interaction time of the atoms inside the cavity mode can be increased by slowing down the atoms [64], the best way to obtain a sustained coupling is to trap the atoms. Trapping of single atom can be achieved with a far-off resonance dipole-force trap (FORT) [65], or with single photons via the strong nonlinearity of the atom-cavity system [66, 67]. The trap lifetime can be improved to a few seconds by using a state-insensitive FORT [68] or three dimensional cooling schemes [69]. With these techniques, one obtains a clean system of a trapped single atom interacting coherently with the photons of an optical cavity, which displays a normal-mode splitting with a single photon (vacuum Rabi splitting) [70, 71].

## 1.1 Aim of this Work

A single atom trapped in an optical cavity presents a very clean system to study and explore CQED in the optical regime. Apart from using a small Fabry-Perot cavity in the near-planar regime, it is also possible to operate an atom-photon interface with a cavity in the near-concentric regime, which may provide several advantages: (1) atom-cavity coupling strength comparable to small cavities due to small mode waist, (2) large physical volume between the mirrors, (3) lower requirement for the mirror reflectivity and cavity finesse, and (4) near-degeneracy of the cavity transverse modes. However, these advantages come with some demanding requisites in terms of the mode matching, alignment, noise isolation, and so on – hence, largely unexplored or used until quite recently.

The idea of using a physically large cavity with small mode waists was first proposed and demonstrated in 1994 by Thomas Mossberg and his team [72]. The atom-cavity coupling was observed through the enhancement and inhibition of the atomic decay rates – the Purcell effect [73, 74], and was deduced to be similar to the coupling strength of a small cavity.

Along with the development of strong atom-light interaction using a lens with tight focusing in our group [75, 76], we started exploring an optical cavity configuration with a tight-focusing geometry as well [77]. This configuration is called “near-concentric”, as the cavity mode has a rapidly diverging shape from the focal point at the cavity centre (see Figure 1.3). We build the cavity with two “anaclastic” lens-mirrors facing each other – here, anaclastic indicates that the optical element is

refractory, with the lens and mirror combined as one element (see Section 2.1). This allows the rapidly diverging cavity mode to collimate on the lens output [78], and makes the alignment and mode matching procedures much more straightforward.

Since I joined the project, we manage to trap single atoms inside the near-concentric cavity, and observe atom-cavity coupling exceeding the atomic decay rate [79]. The anaclastic design also allows the cavity to be aligned extremely close to the edge of stability – at the last stable resonance before the critical point [80]. Furthermore, we explore the possibility to use and couple to higher-order, near-degenerate transverse modes of the near-concentric cavity [81]. A main technical challenge in operating the near-concentric cavity is the mechanical noise. We discover that the noise can be reduced just by putting a thin metal strips across the mirror mounts [82]. Combining this with an active noise cancellation strategy, the noise is reduced to a much lower level. This thesis aims to present these findings, with a more detailed outline given in Section 1.2.

**Approaching the near-concentricity** A common wisdom to achieve strong atom-light interaction is to use a cavity where the photon is bounded in a small mode volume. While it may seem that a small mode volume requires a small cavity, it may not be necessarily true. A near-concentric cavity, even with a mirror separation of  $\sim 100$  times the small cavity, has a comparable mode volume and atom-photon interaction strength (see Section 1.4). This relatively-unknown *minutia* is mainly due to the strong focusing geometry of the near-concentric cavity, where the transverse extent of the photon is much smaller compared with the small cavity.

Such a large mirror separation greatly benefits quantum systems such as ions, atomic ensembles, and Rydberg atoms. In trapped ion systems, the trapping potential is significantly affected by the induced charges of the dielectric mediums [83], which necessitates a large separation of the ions and the mirror surfaces. Thus, near-concentric cavity systems are actively developed [84] and used for several trapped-ion experiments by Blatt and Northup’s group in Innsbruck [85–89]. In addition, near-concentric cavities are utilised by Schleier-Smith’s group in Stanford to explore spin dynamics in atomic ensembles [90, 91].

Besides the aforementioned experiments, other quantum experiments with near-concentric cavities are few and far between, despite some of the advantages. This may

well be that building and operating a near-concentric cavity require quite a share of technical efforts, as corroborated in the subsequent chapters of the thesis. In fact, a necessary condition to reach the strong-coupling regime with a near-concentric cavity is to use a highly curved mirrors and align the cavity very close to concentricity (see Section 2.1.2). It is worth noting that, in contrast with the other near-concentric cavity experiments, which require only high cooperativity but not strong coupling (see Section 1.4.2), our cavity is designed for both and thus is operated extremely close ( $\sim 1 \mu\text{m}$  away) to concentricity.

Therefore, to approach the near-concentricity required in our cavity system, we introduce several design and operation novelties not commonly found in other systems. Among those are the combined lens and cavity mirror (anaclastic) design, and the three-dimensional alignment of the cavity mirrors, which we believe are indispensable to operate our near-concentric cavity. Construction of cavity mirrors with incorporated mode-matching elements has only been recently explored in fibre cavity systems with photonic crystal [92] and graded-index [93] fibres. On the other hand, transverse alignment of the cavity mirrors is typically only necessary for applications with quantum objects embedded on the mirror substrate [94, 95].

It may be early to determine where such a near-concentric cavity system would bring us. While an early version of the setup requires a large actuator with relatively cumbersome mounting, the newest version uses small and inexpensive actuators (see Section 2.2.2). Combined with the less stringent requirement of the mirror reflectivity, near-concentric cavity systems may see a widespread adoption due to their relative ease of construction and operation. Furthermore, it would also be advantageous to exploit the near-degeneracy of the cavity transverse modes to engineer multi-mode atom-photon interactions (see Chapter 5). At the very least, near-concentric cavity is an interesting alternative platform to explore strong atom-photon interaction with strong focusing modes.

## 1.2 Thesis Outline

The rest of the thesis is organised as follows. We continue the discussion of this chapter with a brief literature review and theory of optical CQED systems.

In **Chapter 2**, we describe the design of our near-concentric optical cavity,

particularly the design of the lens-mirrors, translation stages, and mechanical mounts. Then, in **Chapter 3**, we discuss in depth the experimental setup and techniques to operate the near-concentric cavity – from the laser systems, spectroscopy techniques, vacuum systems, alignment and stabilisation of the cavity, to the measurement of relevant cavity parameters. These two chapters are the culmination of almost a decade worth of scientific explorations, starting from the original proposals [77, 78], and extending the work reported in the PhD theses of Kadir Durak [96] and Nguyen Chi Huan [97] to the newest understanding of our cavity system.

In **Chapter 4**, we describe the observation of atom-light interaction in our cavity system. First, we trap single atoms inside the cavity mode and measure the cavity response. We observe an onset of normal-mode splitting, signifying some degree of interaction, which we characterise with a cooperativity factor. Parts of this work have been published in [79] and reported in Chi Huan’s PhD thesis.

In **Chapter 5**, we explore the possibility of using the higher-order transverse modes of a near-concentric cavity for atom-light interaction. In particular, radial Laguerre-Gaussian (LG) modes can be a good set of cavity modes for atom-light interactions, as they have similar coupling strength with the fundamental Gaussian mode. We use a spatial light modulator to perform the mode conversion and obtain a pretty good mode matching to the LG modes of the cavity. Parts of this work have been published in [81].

Operating a centimetre-sized near-concentric cavity presents a substantial challenge in terms of the mechanical noise due to the need for three-directional alignment. In **Chapter 6**, we describe two different approaches that we use to significantly reduce the noise. First, we employ a digital filter to modify the control loop of the translation stage actuation, and actively suppress the noise. Second, we use thin metal strips as friction dampers and place them across the cavity mounts. We show that this simple modification creates a more rigid mechanical structure in the small movement range, and also allows for large movements. Parts of the second approach is currently under manuscript preparation [82] and has been reported in the bachelor thesis of Chen Jia Pern Neville [98].

Our near-concentric cavity is operated very close to the edge of stability regime. In **Chapter 7**, we explore the behaviour of our cavity near this critical point in several aspects. First, we try to align the cavity close to its operational limit – the

last stable resonance – and observe the effect on the fundamental and higher-order transverse modes. Second, we characterise how the aperture size affects mode formation before and beyond the critical point. A small part of this work has been reported in [79] and in [80].

In **Chapter 8**, we evaluate the current capability of the cavity system, and how it can improve in the future. Then, reflecting on the myriad technical problems in building and operating the cavity system, we propose a redesign of the cavity mirror and the mechanical structure. Finally, we conclude with a few possible research pathways with the near-concentric cavity systems.

On top of the chapters, we also provide several appendices to explicate some of the more technical matters.

### 1.3 Other Explorations and Applications

To highlight the role that optical cavities plays in advancing quantum technologies, we give a brief and non-exhaustive review on the explorations and applications of the field of optical CQED in this section. Starting with a single trapped atom strongly coupled to an optical cavity, it is possible to construct atom-photon quantum interfaces and various types of single photon sources. Furthermore, optical cavities also open up explorations of atom-light interaction in atomic ensembles, pseudo-atomic systems, and cavity optomechanical systems.

**Quantum interfaces** An early demonstration of an atom-photon interface with an optical cavity created an entanglement between the cavity output photon polarisations and the atomic  $m_F$  (Zeeman) sublevels, via a superposition of the two possible decay paths [99]. Due to the strong atom-photon coupling, this scheme is ideally non-probabilistic, unlike earlier experiments in ions [100] or neutral atoms [101] with lens-collected photons. The atomic state can be mapped onto a second cavity output photon, and readout via its polarisation. This interface has later been improved with a trapped single atom [102], enabling a high-fidelity quantum memory [103] and a basic quantum network between two different atom-cavity systems [104].

Such a quantum network is an elementary building block of the so-called “quantum internet” [105] – a vision where remote nodes of quantum systems are linked

via quantum channels which could transport quantum states or even distribute “quantum softwares”. Within this quantum network, quantum gate operations can also be implemented between an atom and a photon [106], between two successive photons [107], or between two distant quantum nodes [108].

Besides neutral atoms, trapped ions in an optical cavity offer another convenient quantum network interface, as it allows interfacing between distant trapped ion quantum computers. A quantum state transfer between an ion and a photon has been achieved previously, albeit with a relatively low efficiency and fidelity [85], due to a relatively weak ion-cavity coupling. This has since been improved in fiber Fabry-Perot cavity systems [109, 110], which lead to the recent demonstrations of a strongly coupled ion-cavity system [111] and ion-photon entanglement [112].

**Single photon sources** Optical CQED systems can also be used to produce single photons – most of the quantum network interfaces are intrinsically single photon sources as well. An early on-demand generation of single photons uses a trapped neutral atom in an optical cavity [113]. The photons produced are confirmed to be single in nature, through a coincidence measurement with a Hanbury Brown and Twiss setup [114]. This is followed shortly afterwards with the generation of polarised single photons, by utilising the Zeeman sublevels of the atom [115]. There are also efforts to generate deterministic single photons with trapped ions [116, 117] or solid state systems [118, 119] via cavity-mediated interaction, with different single-photon emission schemes [120].

An interesting feature of such single-photon sources is the ability to engineer the temporal shape of the photon. In a strongly coupled system, it is possible to create unusual photon shapes using a driving laser with time-varying Rabi frequency [121], or reshaping the temporal shape of the photon across different timescales [122]. In addition, shaping the phase of a single photon reveals interesting interference peculiarities [123]. Apart from a coupled atom-cavity system, it is also possible to use single photons created with some other processes – say, the heralded single photons from the spontaneous parametric down conversion [124] or the four-wave mixing process in cold atomic ensemble [125], and use an optical cavity to modify the outgoing photon, by spectral filtering [126, 127], temporal shape reversion [128], or bandwidth compression [129].

**Atomic ensembles** Placing more than one or a few atoms inside an optical cavity reveals fascinating dynamics of an atomic ensemble. In the dispersive regime, where the atomic transition is detuned from the cavity resonance, moving atoms experience time-dependent dipole force from the cavity field, while the cavity field responds due to the time-varying atomic susceptibility. This back-and-forth interaction allows a coherent momentum exchange between the atoms and the radiation field [130]. With a proper choice of cavity detunings and laser frequencies, this effect has led to the observation of cavity cooling [131], self-organisation of atoms to form density gratings [132], collective atomic motion exhibiting squeezing oscillations [133], optical nonlinearity with low photon numbers [134], and so on.

A Bose-Einstein condensate (BEC) is a special atomic ensemble, as all the atoms occupy a single matter-wave mode and thus couple uniformly to a cavity mode. Since the initial demonstrations to place BEC inside an optical cavity [135, 136], which resulted in an extremely high coupling between the BEC and the cavity in the near-resonant regime, more exotic phenomena have been observed, such as cavity optomechanics using the collective density wave of the BEC [137], realisation of the Dicke-model quantum phase transition [138], formation of supersolid from the translation symmetry breaking [139]. A cavity operated in a multimode regime, e.g. confocal or concentric, supports a set of optical modes with different spatial profiles and Gouy phase shifts, enabling range-tunable [140] and sign-changing [141] interaction of the BEC with the cavity.

In addition to the collective motional states, the spin states also serve as an appropriate toolbox in atomic ensemble CQED with long coherence time. Cavity assisted spin squeezing manipulates the spin distribution of atomic ensemble in order to allow for smaller measurement uncertainties [142, 143]. The quantum phase transition in the Dicke model has also been realized in the spin systems using two raman channels [144, 145]. With the cavity detuned from the level transitions, cavity-mediated unitary processes dominate, which can be used to observe and engineer spin flip-flop dynamics [90, 146].

**Pseudo-atomic systems** There are many solid-state systems that behave like an artificial atom, and can be coaxed to interact coherently with optical cavities. The demonstration of normal-mode splitting in a quantum well semiconductor

optical microcavity system [147] came shortly after the demonstration in atom-cavity system. This system, exhibiting interesting nonlinear optical effects [148], can be grown epitaxially in-between and along with a microcavity. While charge carriers in a quantum well move in a two dimensional plane, quantum dots restrict the charge carriers to effectively zero dimension, acting as an artificial atom exhibiting discrete energy levels [149]. Normal-mode splitting of quantum dot cavity systems has been observed in various microcavity structures with low mode volumes [150], such as micropillars [151], photonic crystal [152], and microdisk cavities [153], with a corresponding observation of antibunched photon correlation confirming the quantum nature of such systems [154]. With the ease of fabrication via semiconductor nanotechnology and high degree of tunability, quantum dot microcavity systems have seen many applications in quantum interfaces [155].

Besides quantum dots, nitrogen-vacancy (NV) centres in diamonds are also good atom-like objects for quantum information processing [156], due to their long spin coherence time [157]. Thus, they have been used as quantum memories [158] with error correction [159]. As the emission spectrum is relatively broad with only a small fraction of coherent emission, an NV centre coupled to an optical microcavity enhances the coherence of the system and photon generation process [95, 160, 161].

**Cavity optomechanical systems** A cavity optomechanical system describes a mechanical resonator coupled to an optical resonator via radiation pressure force. Initial demonstrations of such systems use Fabry-Perot cavities, where one of the mirror is built to vibrate mechanically with very small mass. The system demonstrates that the radiation pressure induces optical bistability and suppression of mirror mechanical motion [162], which later develops into cavity-assisted cooling of mechanical mirrors [163, 164], reaching sub-Kelvin temperatures [165]. Besides vibrating micromirrors, cavity optomechanical systems have been developed with many other devices, such as whispering-gallery mode resonators [166–169], photonic crystal cavities [170–172], pairs of coupled microstructures [173–175], nano-objects inside Fabry-Perot cavities which are either suspended [176, 177] or levitated [178–180], and not surprisingly, atomic systems [137, 181, 182]. A particularly interesting application of an optomechanical system is to convert between optical and microwave photons, which has been achieved with motion-induced capacitance modulation [183]

or piezo optomechanical transducers [184, 185]. This would allow a superconducting quantum computer to interface with quantum modules located in the distance or operated in the optical regime.

In cavity optomechanical systems, both the optical and mechanical modes are harmonic oscillators, and thereby linear, while the optomechanical coupling is inherently a nonlinear process, as it relates the radiation pressure, which is proportional to the photon intensity, to the motional mode [186]. Nevertheless, most systems can be described with linearised optomechanical interaction. To observe nonlinear effects, a photon has to stay in the cavity long enough to displace the mechanical oscillator by more than the mechanical ground state uncertainty [187] – a condition so stringent that it has so far only been observed in atomic ensemble systems [137, 181]. Alternatively, there have been efforts to engineer optomechanical coupling that depends quadratically on the mechanical motion, such as placing thin membranes between two Fabry-Perot mirrors [176, 188]. The most common route to observe nonlinear quantum effects is through post-selection mechanism. With the coupled optomechanical system cooled to its quantum ground state [189, 190], a parametric down conversion process generates a pair of photon and phonon – the detection of a photon heralds the presence of a single phonon [191]. This heralded scheme has been used to perform optomechanical Bell test [192] and remote quantum entanglement between two separated systems [193].

## 1.4 A Brief Theory of Cavity Quantum Electrodynamics

In this section, we give a brief summary on the basic CQED theory in the optical regime. We start with a simple non-dissipative model of atom-cavity interaction, and introduce dissipation to describe a real optical CQED system. Then, we outline different geometrical regimes of a stable optical cavity, and show how near-concentric regime can also be a suitable system to explore atom-cavity interaction.

### 1.4.1 Jaynes-Cummings Model

The Jaynes-Cumming model consists of a single two-level system (atom) interacting with a single near-resonant quantised electromagnetic mode (cavity), assuming

no dissipation [194, 195]. The Jaynes-Cummings Hamiltonian can be written as

$$H_{jc} = H_a + H_c + H_{int} \quad (1.1)$$

$$= \hbar\omega_a\pi^\dagger\pi + \hbar\omega_c a^\dagger a + \hbar g(\pi^\dagger a + \pi a^\dagger), \quad (1.2)$$

where  $\omega_a$  and  $\omega_c$  are the angular frequencies of the atom and cavity, which define their respective energy level spacing,  $\pi^\dagger = |e\rangle\langle g|$  and  $\pi = |g\rangle\langle e|$  are the transition operators between ground and excited states for the two-level system,  $a^\dagger$  and  $a$  are the creation and annihilation operator of photons for the cavity mode, and  $g$  is the atom-cavity coupling strength. The interaction Hamiltonian  $H_{int}$  describes the dipole coupling between the atomic dipole operator  $\mathbf{d} = d_a(\pi^\dagger + \pi)\mathbf{e}_d$  and the quantized electric field operator  $\mathbf{E} = E_0(a^\dagger + a)\mathbf{e}_\lambda$ :

$$H_{int} = -\mathbf{d} \cdot \mathbf{E} = -d_a E_0(\pi^\dagger + \pi)(a^\dagger + a) \quad (1.3)$$

$$= \hbar g(\pi^\dagger a^\dagger + \pi^\dagger a + \pi a^\dagger + \pi a) \quad (1.4)$$

$$\approx \hbar g(\pi^\dagger a + \pi a^\dagger), \quad (1.5)$$

where  $d_a$  is the atomic dipole moment,  $E_0$  is the quantised electric field amplitude, and we assume the same polarisation directions for the dipole and electric field ( $\mathbf{e}_d = \mathbf{e}_\lambda$ ) simplicity. In the last line, we use the rotating-wave approximation and ignore the  $\pi^\dagger a^\dagger$  and  $\pi a$  terms as they evolve on a much faster timescales  $\propto e^{i(\omega_a + \omega_c)t}$  in the interaction picture with time-dependent operators. In another view, as the atom and cavity frequencies are near-resonant ( $\omega_a \approx \omega_c$ ), the off-resonant terms  $\pi^\dagger a^\dagger$  and  $\pi a$  would imply either atom excitation with creation of a photon, or atom de-excitation with destruction of a photon, both of which violate conservation energy in longer timescales. Ignoring the global phase of the Hamiltonian, the atom-cavity coupling strength  $g$  is given by

$$g = \frac{d_a E_0}{\hbar} = d_a \sqrt{\frac{\omega_c}{2\hbar\epsilon_0 V}}, \quad (1.6)$$

where the quantised electric field amplitude  $E_0$  is expressed in terms of the electromagnetic mode volume  $V$  (see Appendix A for more detailed treatment).

The Jaynes-Cummings Hamiltonian can be solved analytically, and the respective energy eigenstates are given by

$$E_{\pm,n} = n\hbar\omega_c + \hbar\frac{\Delta_{ac}}{2} \pm \hbar\sqrt{g^2 n + \frac{\Delta_{ac}^2}{4}}, \quad (1.7)$$

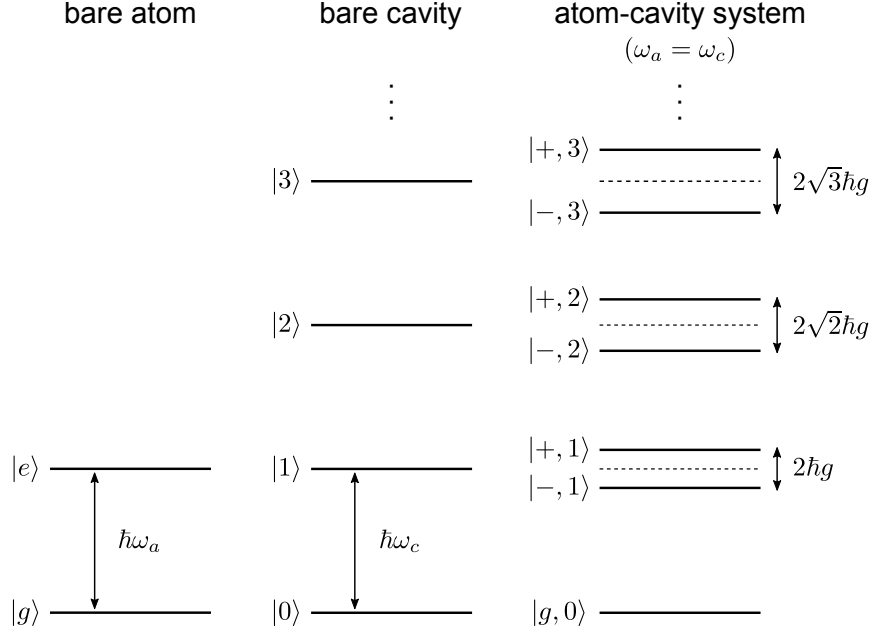


Figure 1.1: Energy level diagrams of bare and coupled atom-cavity systems. The eigenstates of the coupled system with  $n$ -quanta excitation are  $|+, n\rangle$  and  $|-, n\rangle$ , with  $2\hbar g\sqrt{n}$  spacing between them on resonance ( $\omega_a = \omega_c$ ).

with  $n$  as a positive integer which characterises the total excitation quanta of the coupled system,  $\Delta_{ac} = \omega_a - \omega_c$  as the atom-cavity detuning frequency, and the  $\pm$  symbol denotes the two normal modes, with their eigenstates given by

$$|+, n\rangle = \sin \theta |g, n\rangle + \cos \theta |e, n-1\rangle \quad (1.8)$$

$$|-, n\rangle = \cos \theta |g, n\rangle - \sin \theta |e, n-1\rangle, \quad (1.9)$$

with the mixing angle  $\theta$  given by

$$\theta = \arctan \frac{2g\sqrt{n}}{\Delta_{ac} + \sqrt{4g^2n + \Delta_{ac}^2}}. \quad (1.10)$$

Note that there is no normal-mode splitting for the ground state ( $n = 0$ ), and the eigenstate is  $|g, 0\rangle$  with  $E_0 = 0$ . On atom-cavity resonance ( $\Delta_{ac} = 0$ ), the excitation is equally balanced ( $\theta = \pi/4$ ), and the normal-modes splitting is  $2\hbar g\sqrt{n}$  with their eigenstates  $|\pm, n\rangle = (|g, n\rangle \pm |e, n-1\rangle)/\sqrt{2}$  (see Figure 1.1). The vacuum Rabi splitting is defined for an initial case of no excitation (in vacuum or  $n = 0$ ), where a quanta of excitation splits the system into two normal modes with  $2\hbar g$  spacing.

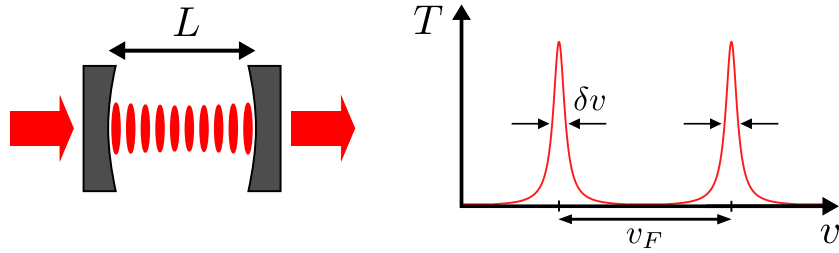


Figure 1.2: A schematic of a Fabry-Perot cavity (left) with its corresponding transmission spectrum (right). Modes of a Fabry-Perot cavity form standing waves and transmit at particular resonances – the frequency spacing between these resonances is the free spectral range  $v_F = c/2L$ . For high cavity finesse ( $\mathcal{F} \gg 1$ ), the transmission profile is Lorentzian, and its width  $\delta v$  determines the cavity finesse  $\mathcal{F} = v_F/\delta v$ .

### 1.4.2 Interaction, Dissipation, and Cooperativity

We describe atom-cavity interaction in a physical system with dissipation. There are two different points of view that yield similar conclusions. First, the many round-trips of the photon inside the cavity enhances the scattering rate of the atom. Second, the atom-light coupling has to overcome dissipation losses to ensure coherent interaction.

In the first picture, inside a cavity with length  $L$  and mirror reflectivities  $\mathcal{R}_1$  and  $\mathcal{R}_2$ , the photon bounces back and forth with effectively  $n_{rt} = \mathcal{F}/\pi$  round trips. The cavity finesse  $\mathcal{F}$  is given by

$$\mathcal{F} = \frac{v_F}{\delta v} = \frac{\pi(\mathcal{R}_1\mathcal{R}_2)^{1/4}}{1 - \sqrt{\mathcal{R}_1\mathcal{R}_2}}, \quad (1.11)$$

with  $v_F = c/2L$  as the cavity free spectral range, and  $\delta v$  is the FWHM of the cavity transmission spectrum (see Figure 1.2). In a free-space system with focused Gaussian beam [196], the focal spot is  $\sigma_w = \pi w_0^2/2$  with  $w_0$  as the beam waist radius. For interaction on resonance, this is usually much larger than the atomic scattering cross section  $\sigma_d = 3\lambda^2/2\pi$ , except in a few diffraction-limited systems [75, 197–199]. Using a cavity with  $n_{rt}$  photon round trips, the scattering probability is thus enhanced with a factor of

$$\eta = 2n_{rt} \frac{\sigma_d}{\sigma_w} = \frac{6\mathcal{F}\lambda^2}{\pi^3 w_0^2} \quad (1.12)$$

with a factor of 2 as the photon “meets” the atom twice every round trips [200]. This enhancement or cooperativity factor  $\eta$  is also called the Purcell factor [73, 201].

In the second picture, coherent interaction requires the atom-cavity coupling strength to exceed the cavity and atomic dissipation losses. The coupling strength  $g$ , given in Equation 1.6, has a dependence with the cavity mode volume  $V$ . In the paraxial approximation with a Gaussian mode profile, assuming that the atom is placed at the focal point and the antinode of the standing wave (see Appendix A for more details), the mode volume is given by

$$V = \frac{1}{2}\sigma_w L = \frac{1}{4}\pi w_0^2 L . \quad (1.13)$$

The cavity field decay rate  $\kappa$  describes how fast a cavity losses a photon, and amounts to half the cavity bandwidth  $\delta\nu$  expressed in units of angular frequency,

$$\kappa = 2\pi \frac{\delta\nu}{2} = \frac{\pi c}{2L\mathcal{F}} , \quad (1.14)$$

where we have used the first equality in Equation 1.11 – longer or higher-finesse cavities store photons for a much longer time and have a much lower decay rate  $\kappa$ . The atomic decay rate  $\gamma$  is due to the coupling of the atomic dipole to the free-space modes [202] (spontaneous emission), and is given by

$$\gamma = \frac{d_a^2 \omega_a^3}{6\pi\epsilon_0 \hbar c^3} . \quad (1.15)$$

The degree of coherence is usually expressed in terms of a cooperativity factor,

$$C = \frac{g^2}{2\kappa\gamma} = \frac{3\mathcal{F}\lambda^2}{\pi^3 w_0^2} \quad (1.16)$$

assuming on-resonance condition ( $\omega_a = \omega_c$ ). Comparing with the first picture, this cooperativity factor  $C$  is just a factor of 2 smaller than the Purcell factor  $\eta$  defined in Equation 1.12 [203]. The author notes that  $C$  is conventionally defined with a factor of 2 in the denominator [18], though sometimes it is also expressed without such factor [200, 204], i.e.  $C = g^2/\kappa\gamma$ , in which case  $C = \eta$ .

The inverse of  $C$  is also known as the critical atom number, which is the number of atoms necessary to significantly modify the cavity transmission. For the case of  $C \gg 1$ , the presence of a single atom provides deterministic atom-light interaction. However, to observe Rabi oscillations, the hallmark of a coherent interaction, the

atom-cavity coupling has to exceed both the atom and cavity decay rates, i.e.  $g/\gamma \gg 1$  and  $g/\kappa \gg 1$  – this regime is called the strong-coupling regime. Another regime of interest is the so-called fast cavity regime, where the cavity decay rate dominates, i.e.  $\kappa \gg g \gg \gamma$  with  $C \gg 1$ . Due to the strong decay pathway through the cavity output mode, this regime is commonly used to produce single photons [120, 205]. Even though Rabi oscillation is not observable in this regime, coherence still presents itself in the form of induced transparencies [204], and it is also possible to construct high-fidelity quantum gates in this regime [206, 207].

### 1.4.3 Different Regimes of Fabry-Perot Cavity

A Fabry-Perot cavity with curved mirrors can form stable cavity modes in some geometrical regimes. These modes retain their sizes and divergences even after countless back and forth reflection, and thus have negligible diffraction losses [13]. With the mirror radii of  $R_1$  and  $R_2$ , and the mirror spacing of  $L$ , the stability criterion [208] is given by

$$0 < \left(1 - \frac{L}{R_1}\right) \left(1 - \frac{L}{R_2}\right) < 1 . \quad (1.17)$$

Defining the stability parameters  $g_1 = 1 - L/R_1$  and  $g_2 = 1 - L/R_2$ , the stability criterion can be rewritten as

$$0 < g_1 g_2 < 1 . \quad (1.18)$$

Figure 1.3 shows the stable regime for some configurations of Fabry-Perot cavities and their corresponding mode shape. The modes are a family of Gaussian beams due to the spherical boundary conditions imposed by the mirrors.

We focus on a class of symmetrical cavities ( $R_1 = R_2 = R$ ). Near-concentric cavities are located very close to the concentric point ( $g_1 = g_2 = -1$ ), towards the stable region – the distance away from the critical mirror separation is characterised by the critical distance  $d = 2R - L$ , with the stability parameter  $g = -1 + d/R$ .

The cavity length  $L$  for symmetrical cavities affects both the atom-cavity coupling strength  $g$  and cavity decay rate  $\kappa$ . For the coupling strength  $g \propto 1/\sqrt{V}$ , the length  $L$  affects the mode volume  $V = \pi w_0^2 L/4$ , with the cavity waist radius  $w_0$  given by

$$w_0^2 = \frac{\lambda L}{2\pi} \sqrt{\frac{2R}{L} - 1} . \quad (1.19)$$

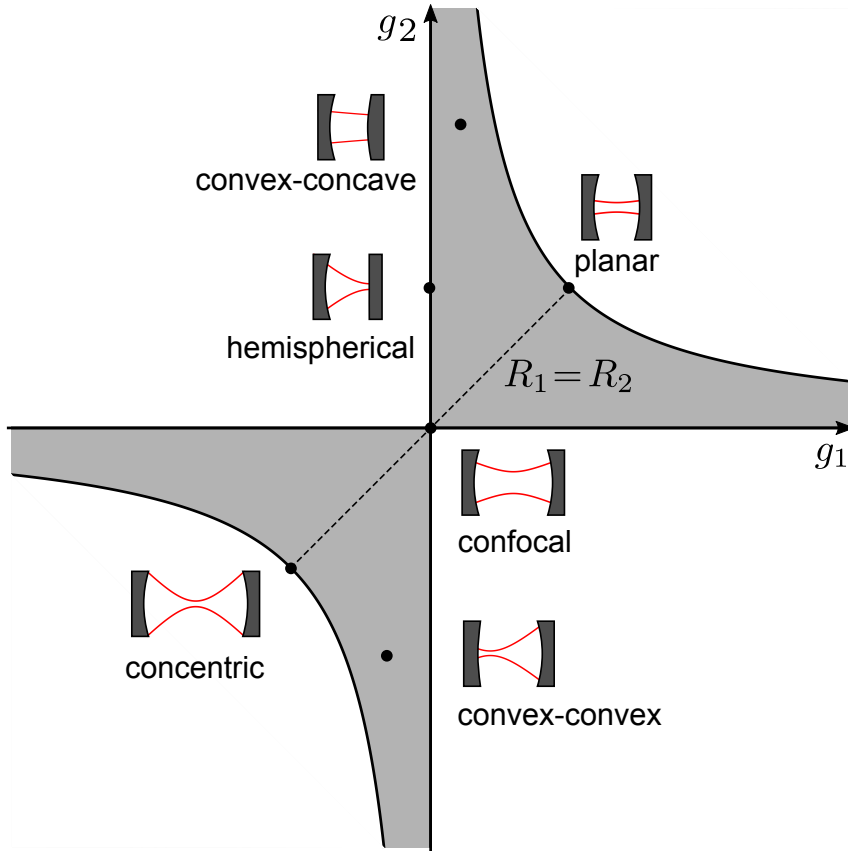


Figure 1.3: Stability diagram for Fabry-Perot cavities. The stable regime is indicated by the shaded region. Symmetrical cavities ( $R_1 = R_2$ ) lies on the shaded line. The concentric cavity is located at  $g_1 = g_2 = -1$  and is only marginally stable with isotropically radial modes. Near-concentric cavities are located very close to this concentric point in the stable region.

To get a large coupling strength  $g$ , the mode volume  $V$  has to be small, which can be achieved with either a near-planar or near-concentric configuration (see Figure 1.4). For near-planar cavities ( $R \gg L$ ), the expression for the mode volume  $V$  approximates to

$$V_{pl} \approx \frac{\lambda}{8} \sqrt{2RL^3}, \quad (1.20)$$

and is usually limited by the mirror spacing and the penetration of cavity modes inside the mirror coatings [209]. Using a typical values of  $L \approx 20\lambda$  and  $R/\lambda \approx 10^4$ , the mode volume is  $V_{pl} \approx 1600\lambda^3$ . For near-concentric cavities with small critical

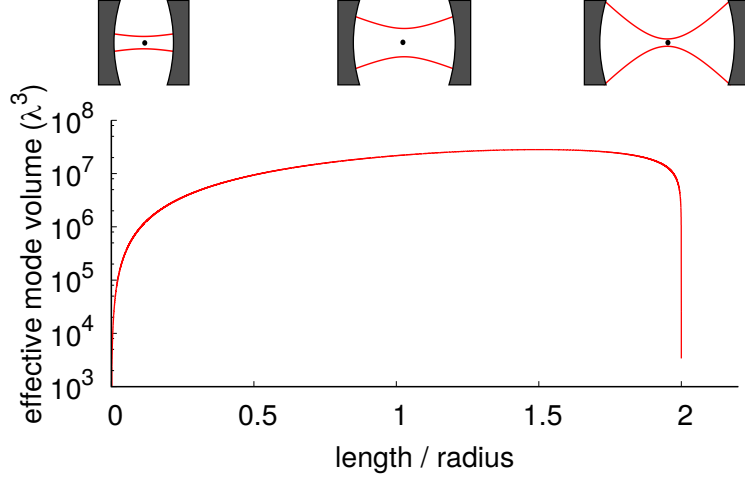


Figure 1.4: Mode volume of symmetrical cavities as a function of their length. The mirror radius and wavelength are  $R = 5.5$  mm and  $\lambda = 780$  nm. The effective mode volume  $V$  reduces to  $\lesssim 10^4 \lambda^3$  at both the near-planar and near-concentric regimes.

distances ( $d \ll R$ ), the expression for the mode volume approximates to

$$V_{nc} \approx \frac{\pi}{4} \left( \frac{\lambda}{\pi} \sqrt{\frac{Rd}{2}} \right) L, \quad (1.21)$$

assuming that the cavity mode is still paraxial – with a smaller critical distance  $d$ , the cavity modes diverges with a larger angle, and the paraxial approximation starts to break down. Assuming that the smallest achievable focal spot amounts to the atomic cross section, a limit that is being approached in several free-space experiments [75, 199, 210], the limit to the near-concentric cavity mode volume is

$$V_{nc}^{limit} = \frac{\pi}{2} \sigma_d L = \frac{3\lambda^2 R}{2\pi}. \quad (1.22)$$

Using a typical value of  $R/\lambda \approx 10^4$ , the mode volume is limited to  $V_{nc}^{limit} \approx 4800\lambda^3$ , which can be reduced further with smaller mirror radii.

The mode volumes of near-concentric cavities are typically higher than, but on the same order as the mode volume of near-planar cavities. Hence, near-concentric cavities are suitable for strong atom-cavity coupling, particularly in the case where a large physical space between the mirrors is necessary. Furthermore, an excellent advantage of near-concentric cavities is the lower requirement for the cavity finesse. From Equation 1.14,  $\mathcal{F} \propto 1/L$  for a particular value of  $\kappa$ . Using the typical values

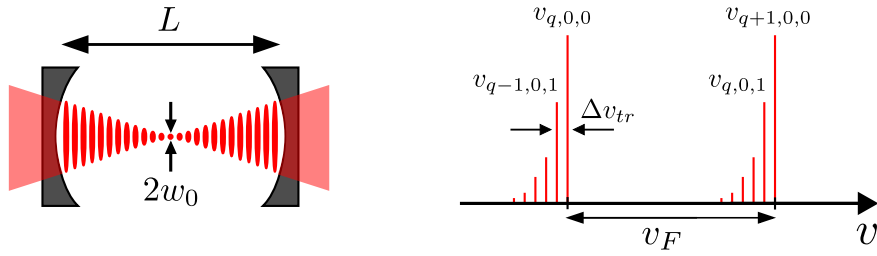


Figure 1.5: (Left) The standing-wave modes of a near-concentric cavity are strongly focused, with waist radius  $w_0$  approaching the light wavelength  $\lambda$ . (Right) An illustration of the cavity transmission spectrum displaying the cavity transverse mode resonances, which are near degenerate with a frequency spacing  $\Delta\nu_{tr} \ll \nu_F$ . With a good cavity alignment and mode-matching to the fundamental mode  $\nu_{q,0,0}$ , coupling and transmission of the higher-order transverse modes would be minimised.

above, the cavity finesse required for near-concentric cavities is  $\sim 500$  times smaller than the near-planar cavities.

Apart from the near-planar or near-concentric cavity configurations, some other geometries of Fabry-Perot cavity have also been explored to provide strong atom-photon interaction. Geometrically asymmetrical cavities provide a similar coupling strength with a better misalignment stability than near-concentric cavities [211]. Fiber-based cavities allow for a much smaller mirror radius  $\sim 50\mu\text{m}$  to be machined on the fiber tip, potentially reducing the mode volume to  $V \approx 10\lambda^3$  [212]. Tapered fiber cavities, with integrated bragg gratings mirrors, couple with atoms through the evanescent field modes, and have relatively low mode volumes due to the tight transverse confinement [213]. Besides Fabry-Perot cavities, there are also efforts to engineer atom-photon interaction in whispering-gallery-mode microresonators [214, 215], photonic crystal cavities [216], and ring cavities [217–219].

#### 1.4.4 Near-concentric cavity

A near-concentric cavity has strong focusing standing-wave modes, as shown in Figure 1.5 (left). Our cavity, with a length  $L$  of around 1 cm, has approximately  $q \approx 30000$  standing wave antinodes – the quantity  $q$  is also known as the longitudinal mode number. With the strong focusing geometry, the waist radius  $w_0$  can be extremely small, depending on the critical distance  $d$ . For our system, it is estimated to be a few  $\mu\text{m}$  in size, and is about 100 times smaller than the mode radius on the

mirror. The cavity output mode is thus strongly diverging, and we use an anastigmatic lens-mirror design to facilitate mode matching (see Chapter 2).

Besides the fundamental Gaussian mode, the cavity also supports a set of Gaussian-family modes (see Appendix A for the theoretical description). This results in many transverse mode resonances within a cavity free spectral range, as depicted in Figure 1.5 (right). The modes of a concentric cavity are degenerate, as the Gouy phase shifts of the transverse modes are multiples of  $\pi$ . Thus, for the near-concentric cavity, the frequency spacing between the transverse modes  $\Delta\nu_{tr}$  are pretty small. In our system,  $\Delta\nu_{tr}$  is on the order of 100 MHz, about 100 times smaller than the free spectral range  $\nu_F$ . The value of  $\Delta\nu_{tr}$  depends strongly on the critical distance  $d$ , and provides a straightforward measurement of  $d$  (see Section 3.4.3). The near-degeneracy of the cavity transverse modes is unique only to the near-concentric and near-confocal cavities, with potentially far-reaching applications (see Chapter 5).

## Chapter 2

# Design of a Near-Concentric Optical Cavity

This chapter describes the design of our near-concentric cavity. As the near-concentric modes have large divergences, we opt to use an anaclastic lens-mirror design which allows the mode outputs to be collimated. This design choice allows us to move extremely close to the critical point – in fact, up to the last stable resonance as shown in Chapter 7. In this near-concentric regime, the atom-cavity coupling exceeds the natural dipole decay of the atom, which is demonstrated with a corresponding measurement in Chapter 4.

A near-concentric cavity is very sensitive to longitudinal and transversal misalignment, and requires vacuum-compatible mechanical stages capable of moving in three directions. We have varying degrees of success with a few piezoelectric-driven translation stages and mechanical mounts, with each iteration ironing out a few issues of the preceding one. Last, we describe the procedure that we develop to align and mount the near-concentric cavity.

### 2.1 Cavity Mirrors

The idea of using a near-concentric cavity is inspired by the demonstration of strong atom-light interaction with a tight focusing geometry without a cavity [75]. In this free-space system, the ratio of scattered photons is around 10%, which later improves to around 40% with better lenses and illumination from both sides [199]. In this tight geometry, a deterministic interaction would be obtained by passing the light a few more times through the atom. Hence, using a cavity system in a tight

focusing geometry surpasses unit cooperativity with finesse on the order of tens.

High numerical aperture lenses can be obtained using a single aspheric element with low optical aberrations. A high quality aspheric lens can be produced with a diamond turning process [220], following any predefined surface profile with roughness on the order of 20 nm or less.

A cavity setup requires two optical components: highly reflective curved mirrors and mode-matching lenses. We combine both components into one optical element with a high numerical aperture – one side with a spherical profile and coated with highly reflective dielectric stacks, and the other side with an aspherical profile for mode-matching. We refer to this optical element as anaclastic lens-mirror, which has a long history dating back to ancient Baghdad [221, 222]. This anaclastic design allows a straightforward mode matching of a collimated input mode to a strongly focusing cavity mode, in the near-concentric regime.

### 2.1.1 Anaclastic Lens-Mirror Design

The anaclastic lens-mirror consists of two air-glass interfaces (see Figure 2.1). The spherical side satisfies the boundary condition of a paraxial cavity mode, and is coated with dielectric stacks to produce a mirror with curvature radius of 5.5 mm and reflectivity of around 99.5% at 780 nm. The aspherical side follows an elliptical profile, given by

$$h(r) = \frac{r^2}{R_{as} + \sqrt{R_{as}^2 - (1+k)r^2}} \quad (2.1)$$

with  $h$  as the height of the aspheric interface at radius  $r$  from the optical axis, and  $R_{as}$  and  $k$  are the mode-matching parameters that depend on the refractive index and ray tracing – an incoming ray parallel to the optical axis, upon hitting the aspherical surface, refracts towards and normal to the spherical surface. Owing to this configuration, aberration corrections of the aspherical profile on the order of  $r^4$  and higher are not necessary [223]. The aspherical interface is also anti-reflection coated at 780 nm, with transmission loss less than 0.5 %.

The anaclastic lens-mirror is produced and coated by Asphericon GmbH according to specification. The root mean square surface deviation is measured to be 19 nm on the aspherical side. The clear aperture diameter is 7.8 mm on both sides, but due to the ray configuration, it is effectively 4.07 mm on the mirror side ( $NA = 0.37$ ).

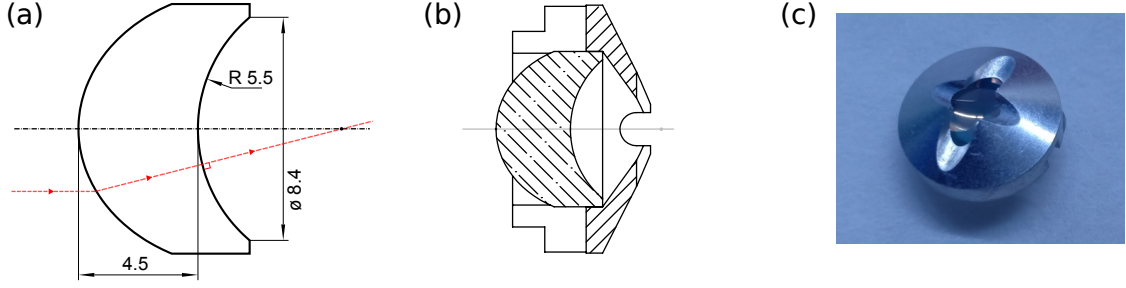


Figure 2.1: A schematic of the anaclastic lens-mirror. The lens-mirror design (a) with an example of ray propagation in red. The size unit is in mm. The lens-mirror is mounted inside a mirror shield (b), with a corresponding photo (c).

The anaclastic-lens mirror is mounted inside a mirror mount, which also acts as a mirror shield, with an ultrahigh-vacuum compatible epoxy glue (Torr Seal). The shield protects the mirror from the line-of-sight between the atomic source and the cavity mirror (see Section 3.2) and accidental contact during handling. The crevasses on the mirror shield allow horizontal and vertical laser beams, with diameter less than 2 mm, to pass through the centre of the cavity – the laser beams are used in Section 4.1.1 to form a magneto-optical-trap (MOT) cloud of cold atoms.

### 2.1.2 Estimation of Cavity Performance

With the two anaclastic lens-mirrors forming a near-concentric cavity, depicted in Figure 2.2 (a), the performance of the atom-cavity interaction, in terms of the coupling and cooperativity, is estimated using the theoretical framework described in Section 1.4. First, we define a critical distance  $d = 2R - L$  as the distance of the mirror spacing away from the critical point ( $L = 2R$ ). The values of  $d$  are positive for smaller cavity length (in the stable region). The stability parameter is  $g = -1 + d/R$  correspondingly. As our near-concentric cavity is operated extremely close to the critical point, we can assume that  $d \ll R$  for the subsequent calculations. Assuming the cavity mode profile is Gaussian, using Equation 1.19, the cavity waist radius  $w_0$  is given by

$$w_0^2 = \frac{\lambda(2R - d)}{2\pi} \sqrt{\frac{d}{2R - d}} \approx \frac{\lambda}{\pi} \sqrt{\frac{Rd}{2}}. \quad (2.2)$$

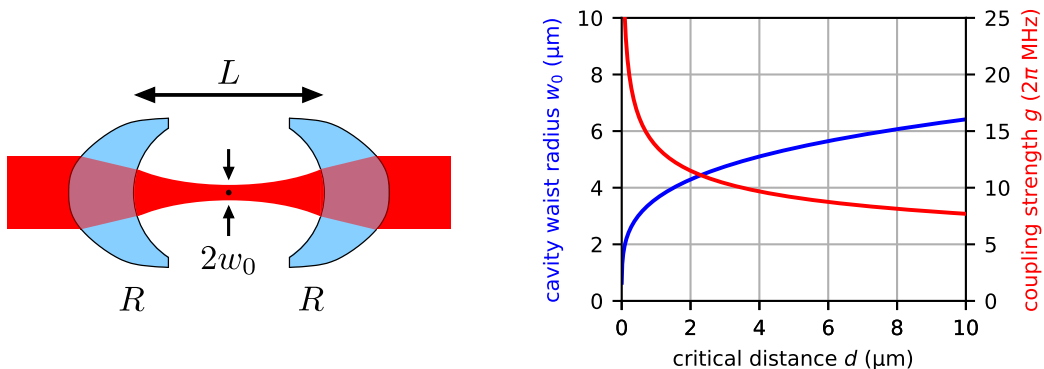


Figure 2.2: (Left) An illustration of a near-concentric cavity system formed by two mirrors with radius  $R$ , spacing  $L$  and cavity waist radius  $w_0$ . (Right) The cavity waist radius  $w_0$  and atom-cavity coupling strength  $g$  as a function of the critical distance  $d = 2R - L$ .

The atom-cavity coupling  $g$  can be evaluated using Equation 1.6 with the effective mode volume  $V = \pi w_0^2 L / 4$  given in Equation 1.21, and approximates to

$$g \approx \frac{d_a}{\lambda} \sqrt{\frac{2\pi c}{\hbar \epsilon_0}} \left( \frac{2}{R^3 d} \right)^{1/4}, \quad (2.3)$$

which gets larger for smaller mirror radius  $R$  and critical distance  $d$ .

To evaluate the values of atom-cavity coupling relevant to this thesis, we note that the atom species used is Rubidium 87 ( $^{87}\text{Rb}$ ), and the target atomic transition is the  $D_2$  line ( $5^2S_{1/2} \rightarrow 5^2P_{3/2}$ ) with  $\lambda = 780.24$  nm. The electric dipole moment for a cycling transition ( $|F = 2, m_F = \pm 2\rangle \rightarrow |F' = 3, m'_F = \pm 3\rangle$ ) is  $d_a = 2.99 e a_0$ , with  $e$  as the electron charge and  $a_0$  as the Bohr's radius. The excited states of the  $D_2$  line have a population decay rate of  $\Gamma = 2\gamma = 2\pi \times 6.07$  MHz and a lifetime of  $\tau = 26.2$  ns [224]. The values of the cavity waist radius  $w_0$  and atom-cavity coupling  $g$ , evaluated for the corresponding  $^{87}\text{Rb}$  atomic transition, is plotted in Figure 2.2 as a function of the critical distance.

There are two decoherence mechanisms in this system. First, the atomic excitation decay rate  $\gamma = 2\pi \times 3.03$  MHz is related to the atomic dipole moment  $d_a$  of the  $D_2$  transition through Equation 1.15. Second, the estimated cavity decay rate  $\kappa = 2\pi \times 10.9$  MHz is evaluated using Equation 1.14, with the cavity length of  $L \approx 2R = 11$  mm and the cavity finesse of  $\mathcal{F} = 627$  for the specified mirror reflectivities of  $\mathcal{R}_1 = \mathcal{R}_2 = 99.5\%$  for both mirrors.

**Achieving strong coupling** The requirements for a strongly coupled atom-cavity system are  $g/\gamma \gg 1$  and  $g/\kappa \gg 1$ . Our near-concentric cavity system could reach this regime, albeit with quite a small margin – with a critical distance of  $d = 1 \mu\text{m}$ , the atom cavity coupling is  $g = 2\pi \times 13.7 \text{ MHz}$ , resulting in  $g/\gamma = 4.5$ ,  $g/\kappa = 1.3$ , and cooperativity  $C = g^2/2\kappa\gamma = 2.8$ . The margin for  $g/\kappa$  can be readily improved with a higher cavity finesse  $\mathcal{F}$ , say to a few thousands, though it may be limited by the aperture size (see Section 8.2.2 for a more thorough discussion).

The more important ratio to consider is  $g/\gamma$ , as it can only be improved with a higher atom-cavity coupling  $g$ , as the atomic decay rate  $\gamma$  is fixed for a particular atomic transition. In addition, both the strong coupling and fast cavity regimes require  $g/\gamma \gg 1$  as a necessary condition. In fact,  $g/\gamma > 1$  for a near-concentric cavity requires a small mirror radius  $R$  and a short critical distance  $d$  – to the best of our knowledge, it has not been reached in other near-concentric cavity experiments, i.e.  $g/\gamma = [0.12, 0.25]$  in Ref. [84, 90]. Due to the anaclastic design, our cavity system is well within this regime, and we demonstrate  $g/\gamma = 1.7(1)$  experimentally at  $d = 1.7(1) \mu\text{m}$ , averaging over random dipole orientations (see Section 4.2.3).

Figure 2.3 (left) shows the “threshold distance”  $d_{th}$  as a function of mirror radius  $R$ . We define the threshold distance as the maximum critical distance  $d$  to reach the  $g/\gamma > 1$  regime. Below  $R = 4.25 \text{ mm}$ , the condition  $g/\gamma > 1$  always applies for any cavity length, which is a strong motivation to use mirrors with smaller radii, but with a compromise of a smaller physical space between the mirrors. In our system ( $R = 5.5 \text{ mm}$ ), the threshold distance  $d_{th} = 0.47 \text{ mm}$  has a pretty large margin. This margin decays rapidly to  $d_{th} = 4.5 \mu\text{m}$  for a  $5 \text{ cm}$  length cavity .

**Limit of the atom-cavity coupling** In an experimental setting of atom-cavity resonance, the available values of the critical distances  $d$  are discretised to the cavity free spectral range. This sets the lower bound of  $d$  to be approximately  $\lambda/2$  from the critical distance – the exact value of which depends on the effective mirror radii  $R_1$  and  $R_2$ , i.e.  $d_{min} = R_1 + R_2 \bmod (\lambda/2)$ . Aligning the cavity in the  $d \ll \lambda/2$  regime, where the atom-cavity coupling explodes to extremely high values, may not be trivial and will be discussed in Section 7.2.3.

It is useful to take  $d_{min} = \lambda/2$  as a lower bound of the critical distance. This assumption provides an estimate to the atom-cavity coupling  $g$  for a cavity setup

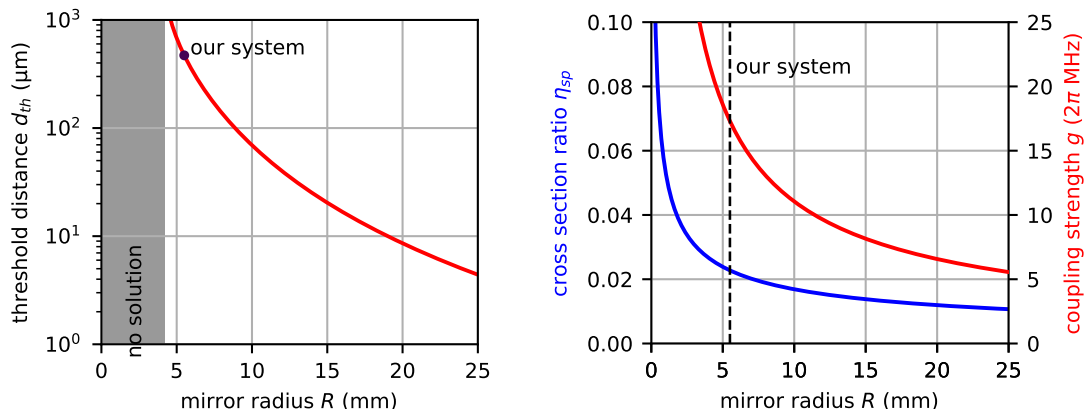


Figure 2.3: (Left) The threshold distance  $d_{th}$  as a function of the mirror radius  $R$ , signifying the regime where the coupling strength  $g$  exceeds the atomic decay rate  $\gamma$ . In the shaded region,  $g > \gamma$  applies for any cavity length. (Right) The atom-cavity coupling strength  $g$  and the ratio of the atomic cross section to the focal spot  $\eta_{sp}$ , both evaluated at  $d = \lambda/2$ , as a function of the mirror radius  $R$ . These values estimate the performance of cavity systems operated at the last stable resonance.

operated at the last stable resonance in the  $0 < d < \lambda/2$  regime (see Section 7.1). Figure 2.3 (right) shows the atom-cavity coupling  $g$  at  $d = \lambda/2$  as a function of the mirror radius  $R$ . In our current system,  $g = 2\pi \times 17.3$  MHz with  $C = 4.6$  serves as an estimate on the achievable coupling strength, with the system operated at the last stable resonance and targeting a cycling transition.

**Comparison with the lens systems** We compare the performance of the near-concentric cavity with the lens system. A relevant quantity to examine is the ratio of the atomic cross section to the focal spot, described previously in Equation 1.12,

$$\eta_{sp} = \frac{\sigma_d}{\sigma_w} = \frac{3\lambda^2}{\pi^2 w_0^2}, \quad (2.4)$$

where the subscript refers to a single pass of the light through the atom, in the case of a focused lens system. In the cavity system, this factor is enhanced by the number of photon round trips, and is equal to the cavity cooperativity factor. The ratio  $\eta_{sp}$  as a function of the mirror radius  $R$ , evaluated at  $d = \lambda/2$ , is plotted in Figure 2.3 (right). The single-pass cross section ratio  $\eta_{sp} = 0.023$  of our system, estimated at the last stable resonance, is smaller than the focused lens systems with similar focal lengths, i.e  $\eta_{sp} = [0.11, 0.27]$  in Ref. [75, 199]. To obtain a comparable

value of  $\eta_{sp} = 0.1$ , the cavity has to be aligned at  $d = 20$  nm.

With this comparison, we surmise that a near-concentric cavity can reach a similar single-pass performance with the focused lens system, but only at very short critical distances. Nevertheless, besides the technical hurdle to operate the cavity  $\sim 20$  nm away from the critical point in the  $d \ll \lambda/2$  regime, the paraxial approximation may no longer be valid. In the lens system, the electric field at the centre of the focal spot for  $\eta_{sp} = 0.1$ , calculated using the paraxial model, differs by about 3% compared with the full mode decomposition-propagation model [225]. This difference accumulates over multiple back-and-forth reflections of the cavity, which may result in cavity eigenmodes with non-spherical wavefronts [226–229], and may require cavity mirrors with special shapes.

## 2.2 Mechanical Stages

The operation of a near-concentric cavity relies on an accurate relative positioning between the two mirrors. The tight focusing geometry of the cavity mode requires alignment in both the longitudinal and the two transverse directions – either with translation or rotation (see Appendix B). We use stacked piezoelectric elements to provide movement in three orthogonal directions. The piezoelectric elements provide a small movement with an applied voltage, typically on the order of 0.5 nm/V, ideal for nanopositioning in an ultrahigh vacuum environment [230]. They are typically made from lead zirconate titanate ceramic, with a chemical formula of  $\text{Pb}[\text{Zr}_x\text{Ti}_{(1-x)}]\text{O}_3$  (also known as PZT). We use a few types of piezoelectric-based actuators, and develop different mounting strategies, to satisfy the demanding requirement of operating the cavity with low mechanical noise in ultrahigh vacuum.

The mechanical structure of the cavity follows a particular size constraint, as it has to fit within a glass cuvette of size  $150 \times 25 \times 25$  mm. This design choice allows us to use a smaller vacuum chamber with smaller pumps and smaller magnetic coils, and provides optical access in virtually any direction (see Section 3.2). Though, the variety of options for the translation stages and mounting methods become limited to a certain extent.

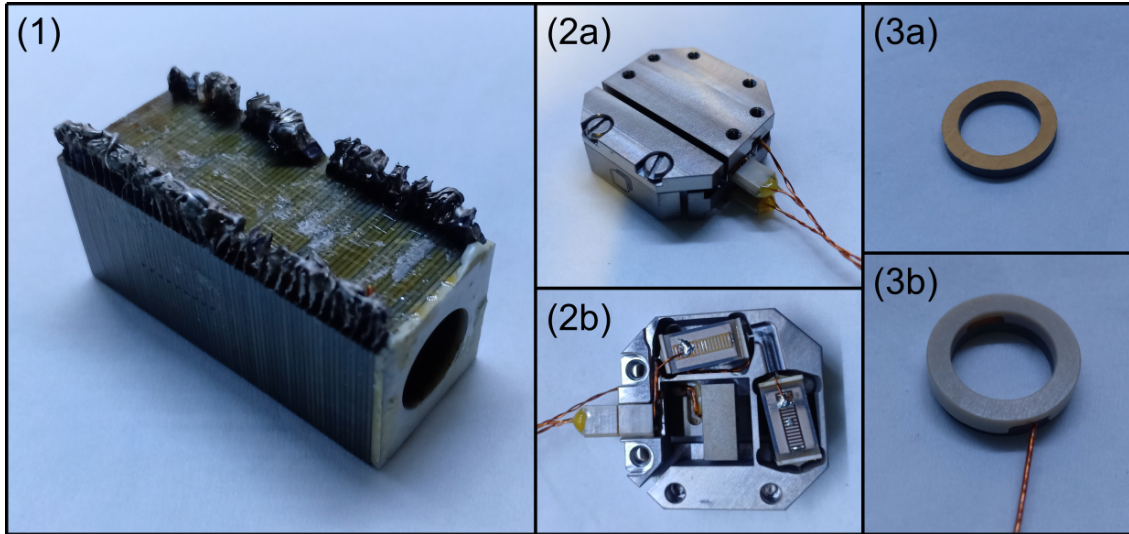


Figure 2.4: Pictures of the actuators and translation stages used in the thesis. (1) The three directional piezo stack actuator with a through hole for optical access. (2a) The flexural-based translation stage with 6 threaded holes for mounting. The flexural mechanism can be seen from the bottom of the translation stage (2b), where thin metal flexures on both sides of the piezos bend as the piezo elongates. (3a) The ring piezo to implement fast movement on one mirror. A spacer is added on top of the piezo (3b) to electrically isolate the high voltage part of the electrode.

### 2.2.1 Translation Stages and Actuators

In the first iteration of the mechanical design, we use a piezo stack actuator (P-153.10H, Physik Instrumente) consisting of 72 shear-piezo layers glued together. The actuator with size  $16 \times 16 \times 40$  mm has a cylindrical hole of 10-mm diameter through its centre for optical access. The bipolar actuator allows translation movement of  $\pm 5 \mu\text{m}$  in three directions, with a maximum supply voltage of  $\pm 250$  V. The resonance frequency of the actuator with no extra load is around 30 kHz.

After a few iterations, we identify the need for an actuator with a larger travel distance. We use a flexural-guided nanopositioner, which exploits a flexible joint to provide a mechanical amplification to the piezo movement [231]. The flexural-based translation stage (ANSxyz100, Attocube) with size  $25 \times 25 \times 10$  mm provides three dimensional translation movement up to  $50 \times 50 \times 24 \mu\text{m}$ , with unipolar operation and maximum supply voltage of 60 V. Due to the large movement range, the resonance frequency of the translation stage is much lower, typically less than 1 kHz.

## CHAPTER 2. DESIGN OF A NEAR-CONCENTRIC OPTICAL CAVITY

Version	1a	1b	2a	2b
Actuator type	piezo stack		flexural stage	
Movement range	$\pm 5 \mu\text{m}$		$50 \times 50 \times 24 \mu\text{m}$	
Actuator mounting method	epoxy	screws		
Easy to reconfigure	no	yes		
Extra mounted components	-			frc. dmp.
Post-baking misalg. (max)	$\sim 5 \mu\text{m}$	$> 5 \mu\text{m}$	$\sim 5 \mu\text{m}$	
Ultrahigh vacuum operation	yes	no	yes	
Mechanical noise (passive)	$\sim 0.2 \text{ nm}$		$\sim 1 \text{ nm}$	0.17(2) nm
Mechanical noise (w/ a.n.c.)	-		$\sim 0.4 \text{ nm}$	0.16(2) nm
Operating finesse	138(2)	606(3)	275(9)	484(9)
Noise effect factor $\xi_{noise}$	$\sim 0.07$	$\sim 0.3$	$\sim 0.3$	$\sim 0.2$
Experiment with atoms	yes	no	likely	
Publication	[79]	[80]	[81]	soon

Table 2.1: Summary of the cavity mechanical design development. List of Abbrev: frc. dmp. – friction damper; misalg. – misalignment; a.n.c. – active noise cancellation.

Alternatively, another common approach to increase the movement range is by using a piezo slip-stick actuator. The actuator exploits different driving signals on the piezo to move a stage along a rail through a slip-stick mechanism [232]. Although the actuator has a large movement range, limited only by the rail length, commercially available actuators with three directional movement do not fit within our size constraint. They are also more expensive compared to the flexural stages.

On top of the piezo stack actuator and the flexural stage, we also use another piezo to implement a fast movement along the cavity axis with a finer resolution. This ring-shaped piezo (PZT-4 compressional crystal, Boston Piezo-Optics) is glued to one of the cavity mirror mounts, with the high-voltage electrode protected by a spacer. The 2-mm thick piezo has a maximum travel range of 0.27 nm and an unloaded axial resonance frequency of  $\sim 1 \text{ MHz}$ . Figure 2.4 shows the pictures of all the translation stages and actuators used in the thesis.

### 2.2.2 Development of the Cavity Mechanical Designs

Table 2.1 captures the development of the cavity mechanical designs, spanning 4 versions. We describe below the main features and technical challenges associated with each version, and the improvement that we implement with each iteration.

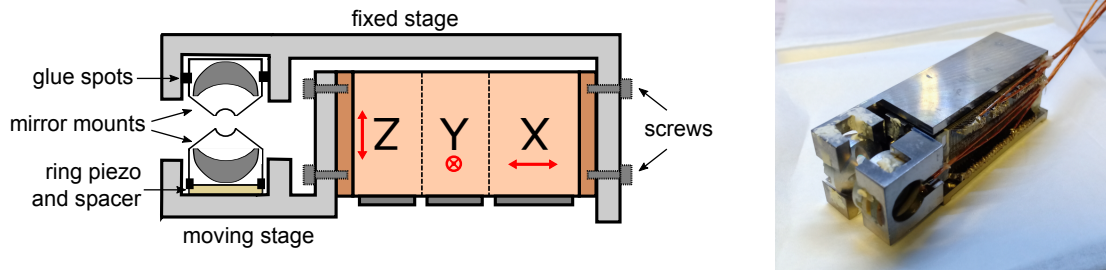


Figure 2.5: Schematic of the cavity mechanical design version 1 (left), where the piezo stack actuator is attached with epoxy glue in version 1a, and screws in version 1b. A corresponding picture of the setup is shown (right).

**Version 1** In design version 1a (see Figure 2.5), the piezo stack actuator is glued between the fixed and moving stages using epoxy (Torr Seal). The cavity mirror mounts are placed on each respective stage using the same epoxy, following the cavity alignment procedure (see Section 2.2.3). After the epoxy is cured, the cavity is almost aligned at a critical distance of around  $1 \mu\text{m}$  with zero input voltage. The cavity can then be aligned at different critical distances, by applying different voltages on the piezos and monitoring the transmission spectrum.

The setup is then placed in a vacuum chamber, and baked with a high temperature for a few weeks to reach ultrahigh vacuum (see Section 3.2). This baking process typically misaligns the cavity, up to around  $5 \mu\text{m}$  in version 1a, due to the effect of the temperature cycling on the epoxy glue in vacuum. With the piezo stack moving range of  $\pm 5 \mu\text{m}$ , the alignment and baking process may have to be performed a few times to get the cavity aligned in ultrahigh vacuum environment.

The downside of version 1a is that the setup is not easy to reconfigure, as the piezo stack is glued on the stage. In fact, in some of the realignment process, due to the mechanical stress induced during epoxy removal, the piezo stack broke up into two pieces. Hence, it became apparent that we require a design where some of the parts can be disassembled and reconfigured easily, with a much lower risk of physically destroying the actuator.

In design version 1b, we mount the actuators to the stages with screws (see Figure 2.5), which allows ease of reassembly. However, the effect of the temperature cycling during the vacuum baking process misaligns the cavity by more than the

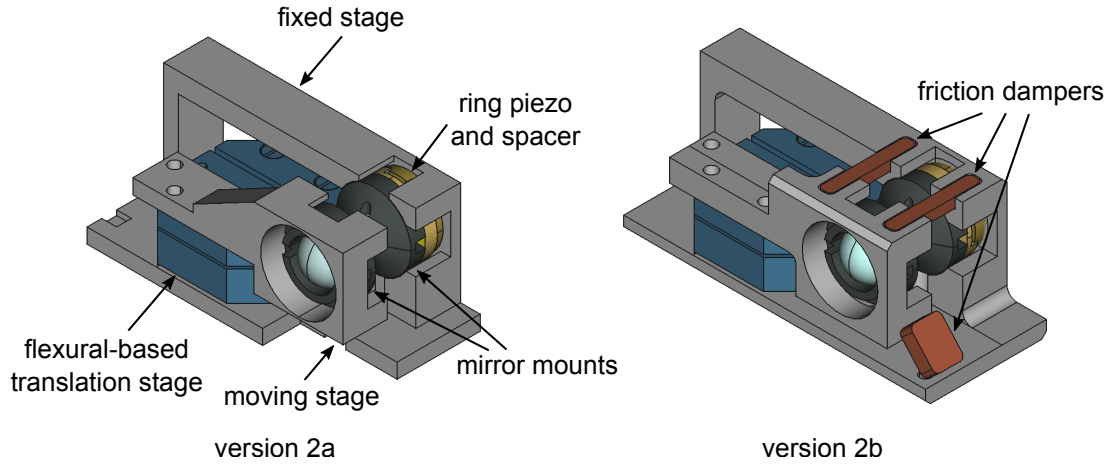


Figure 2.6: Schematic of the cavity mechanical design version 2a (left) and version 2b (right), in 3D drawing. Friction dampers are mounted in version 2b to reduce the cavity mechanical noise.

piezo stack movement range. Even after multiple tries and preemptive corrections to the expected misalignment behaviour, the cavity can no longer be aligned in the ultrahigh vacuum environment. We hypothesise that the misalignment is exacerbated as the stack piezo and screws are mounted horizontally – a small strain on the back screws, induced by some tension relaxation, would result in a large displacement on the moving stage.

**Version 2** In design version 2a, to counteract the post-baking misalignment issues, we use a flexural-based translation stage which has a larger moving range (see Figure 2.6), up to  $50\ \mu\text{m}$  horizontally and  $24\ \mu\text{m}$  vertically. The moving stage is screwed vertically to the translation stage. As the flexural stage requires unipolar operation, during the cavity alignment process, we apply a voltage bias to position the stage on the middle of the operating range. The maximum misalignment figure after a baking process is  $\sim 5\ \mu\text{m}$ , and there is typically no need to repeat the aligning and baking cycle in this design version.

However, the main drawback of design version 2a, which we have started to learn since version 1a and 1b, is the mechanical noise of the cavity. The mechanical noise varies, depending on the environment and platform noise. In a typical experimental setting, i.e. the cavity mount is placed inside a glass cuvette attached to a vacuum

## CHAPTER 2. DESIGN OF A NEAR-CONCENTRIC OPTICAL CAVITY

chamber on an optical table, the mechanical noise is around 0.2 nm for version 1a and 1b, and around 1 nm for version 2a. The noise is higher with the flexural stage, which is likely due to a more complex mechanical structure with flexural mechanical amplification, forming a system of “stacked cantilevers”.

We quantify how much the mechanical noise affects the operation of the atom-cavity system with a “noise effect factor”,

$$\xi_{noise} = \frac{\delta\omega_c}{2\kappa} = \frac{\delta L}{\lambda/2} \mathcal{F}, \quad (2.5)$$

which is how much the cavity resonance shakes,  $\delta\omega_c$ , with respect to the full-width half maximum of the cavity transmission,  $2\kappa$ . This factor is also equivalent to the ratio of mechanical noise (standard deviation of the cavity length) to the half-wavelength, multiplied by the cavity finesse. Here, we propose a figure of  $\xi_{noise} \lesssim 0.2$  as the noise target – the mechanical noise mostly contributes to 20% of the cavity linewidth. For a nominal cavity finesse of  $\mathcal{F} = 627$ , this corresponds to mechanical noise of at most 0.12 nm.

The noise effect factor  $\xi_{noise}$  for version 2a starts at around 0.7, which may be too high for any experiments with atom. Though, the noise is still tolerable for some experiments that do not require the cavity to be stabilised at its resonance. We develop a method to perform active noise cancellation based on control theory (see Section 6.1), and manage to reduce the noise to around  $\xi_{noise} = 0.3$ . This noise figure may be acceptable for atom-cavity experiments, but may require some further post-selection on the data, based on the time-varying cavity detuning. We didn’t proceed with this setup as we discover a way to passively damp the mechanical noise of the system using friction dampers (see Section 6.2).

In design version 2b, we introduce friction dampers to the mechanical design to reduce the mechanical noise of the cavity. The friction dampers are mounted on the pockets (see Figure 2.6, right) to prevent accidental dismounting, and rest with only their weights (no glue or screws). With a higher operating finesse at  $\mathcal{F} = 484(9)$ , the mechanical noise starts at around  $\delta L = 0.17(2)$  nm with  $\xi_{noise} = 0.22(3)$ , and reduces slightly to  $\delta L = 0.16(2)$  nm with  $\xi_{noise} = 0.20(3)$  with the active noise cancellation. The resultant noise effect factor is within our target of  $\xi_{noise} \lesssim 0.2$  for atom-cavity experiments, but slightly on the high side.

**Version 3** In future experiments, higher values of atom-cavity cooperativities can be reached with higher finesse cavities, which require much lower mechanical noise – for a cavity finesse of  $\mathcal{F} = 5000$ , the mechanical noise should be limited at  $\delta L \lesssim 16$  pm. This would require a radical redesign of the mechanical setup. We are developing a method to mount the cavity with higher inherent stability, by connecting the corners of the mirror mounts with small piezo stacks with large travel range. The mechanical design and preliminary results are provided in Section 8.2.1.

### 2.2.3 Cavity Alignment Procedure

With limited movement ranges of the translation stages, the cavity mirrors are first aligned using external translation stages with tip and tilt adjustment. Once the cavity is aligned in the correct regime, the mirrors are glued in place with an epoxy (Torr Seal). We describe the procedure in detail, for version 2b, below.

**Preparing the stages and mirrors** First, we stack the right mirror mount with the spacer and ring piezo, and glue them together with an epoxy (Torr Seal). The ground electrode of the ring piezo, at the bottom of the stack, is attached to the fixed stage with a silver epoxy (H21D, EPO-TEK). Then, we attach the flexural-based translation stage (ANSxyz100, Attocube) and the moving stage onto the fixed stage with screws, and put the friction dampers in position. We mount the whole setup on a tip-tilt platform (KM200PM, Thorlabs), on a 3-axis manual translation stage (PT3, Thorlabs). This concludes the preparation for the right cavity mirror.

On the left side, we hold the left mirror mount with a home-built mechanical tweezer by friction force. The tweezer is locked into its place with screws, and can be released by unscrewing. The tweezer is then mounted on another tip-tilt platform, on an external 3-axis piezo translation stage with 100- $\mu\text{m}$  moving range (Tritor 101 CAP, Piezosystem Jena), on another 3-axis manual translation stage. This concludes the preparation for the left cavity mirror.

The axes of the cavity mirrors should coincide. To achieve this, we prepare a reference axis with two fibre couplers facing each other, using the aligning mirrors (see Figure 2.7). By maximising the coupling of the right and left propagating laser beams to the right and left fibre respectively, the left and right propagating beam axes coincide, establishing the reference axis. Then, we align the axes of the cavity

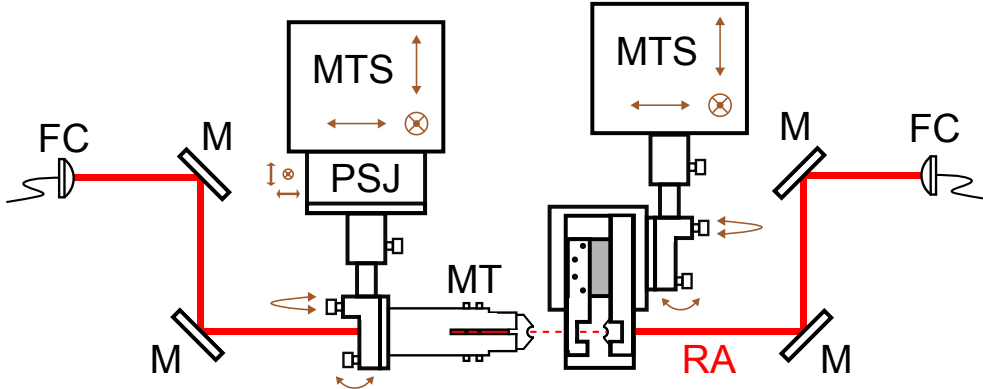


Figure 2.7: The alignment setup of the near-concentric cavity. The reference axis (RA) is formed by two fiber couplers (FC) with aligning mirrors (M). The right cavity mirror is mounted on the cavity setup, while the left cavity mirror is mounted on a mechanical tweezer (MT). Initially, both mirrors are aligned to retroreflect the laser beams back to the fiber coupler, using the manual translation stages (MTS) and the tip-tilt platforms. Then, they are brought together to form a cavity in the stable regime, with fine positional adjustments provided by the Piezosystem Jena (PSJ) translation stage.

mirrors to coincide with the reference axis, using the tip-tilt platform and the 3-axis manual translation stage. Due to the anaclastic design, collimated beams on the reference axis also collimate on the back-reflection path upon hitting the cavity mirrors. By monitoring and maximising the back-reflected fibre coupling efficiency, the tip and tilt misalignment can be corrected. The transverse off-axis misalignment can be corrected by observing the back-reflection mode of a slightly focused reference beam, which produces a small aberration in the off-axis case. Though, the transverse misalignment will become much more obvious once the cavity is formed.

**Forming the cavity** The next step of the procedure is to bring the cavity mirrors close to each other, by adjusting the manual translation stages. It is important to monitor the back-reflected fibre coupling efficiencies during this process, as the left mirror mount might knock on the moving stage and misalign the setup.

We first bring the mirrors together with their spacing smaller than the concentric length – in this stable regime, the cavity is more easily aligned. We observe the cavity mode and the transmission spectrum using a camera (USB2 CCD Monochrome, Point Grey) and an amplified photodiode (PDA36A2, Thorlabs), by sending a slow-

## CHAPTER 2. DESIGN OF A NEAR-CONCENTRIC OPTICAL CAVITY

varying frequency modulation (stimulation input) on the laser (see Section 3.1.1). We correct for the off-axis misalignment using the external 3-axis piezo translation stage, by maximising the coupling to the fundamental cavity mode and minimising the coupling to the non cylindrically-symmetric cavity transverse modes. At this point, the manual translation stage would be too coarse for such alignment. We slowly bring the cavity mirrors further apart, and approach the critical point.

The critical distance can be estimated from the frequency spacing of the cavity transverse modes (see Section 3.4). At the critical point, the transverse modes start to overlap at the same frequency. In addition, the transmission of the fundamental mode reduces and the linewidth increases, due to higher diffraction loss (see Section 7.1). We align the cavity at around 2 or 3 half-wavelengths away from the critical point (critical distance of  $\sim 1 \mu\text{m}$ ), and apply voltages to move the flexural-based translation stage to the centre of its operation ranges.

**Fixing the position of the cavity mirrors** After the cavity is aligned at the correct position, we put a small amount of epoxy (Torr Seal) at a few spots to attach the left mirror mount to the moving stage. The epoxy takes about 2 hours to harden, and more than 24 hours to fully cure. Within the first 2 hours, we monitor the cavity mode and spectrum, and compensate for any misalignment that occurs within this time.

About 2 days later, we unscrew the mechanical tweezer to release the left mirror mount, which now stays on the moving stage. This concludes the cavity alignment procedure. The cavity misalignment that accumulates up to this point is typically around  $1 \mu\text{m}$ , which can be readily compensated with the flexural-based translation stage. Much larger misalignment occurs during the baking process in vacuum (up to  $\sim 5 \mu\text{m}$ ), which is still within the operating range of the translation stage.

## Chapter 3

# Experimental Setup and Techniques

The experimental setup and techniques to operate a near-concentric cavity in an ultrahigh vacuum environment are described in this chapter. This includes the laser system and spectroscopy techniques, vacuum system, cavity stabilisation, and measurement of cavity parameters. Most of the techniques described here are standard resources found in typical quantum optics laboratories, except the transverse alignment stabilisation of a near-concentric cavity (Section 3.3.2).

### 3.1 Laser Systems and Spectroscopy Techniques

The laser system forms the main backbone of the cavity experiments. We use a home-built external cavity diode laser (ECDL), which is frequency-tunable over a large range with a relatively narrow linewidth. By probing the atomic transition, the frequency of the ECDL can be stabilised to the resonance of the atomic transition, or slightly detuned from it, through spectroscopy techniques.

#### 3.1.1 External Cavity Diode Laser

Our external cavity diode lasers (ECDL) are constructed in a Littrow configuration [233, 234] inside an enclosed box with temperature stabilisation. Collimated light from a commercial laser diode, upon hitting a reflective grating, diffracts part of the light back onto the laser diode, modifying its spectral properties (see Figure 3.1). Meanwhile, part of the light which is not diffracted, reflects off the grating and forms the ECDL output.

The spectral properties of the ECDL is modified by the grating in three steps.

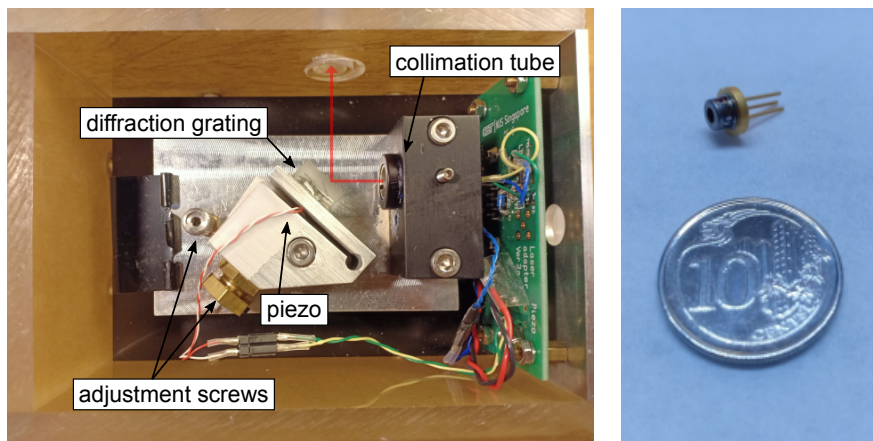


Figure 3.1: A picture of the external cavity diode laser setup (left), located inside an acrylic box with size  $120 \times 80 \times 50$  mm. The red laser beam path is drawn as a visual aid. The laser diode (right) is mounted inside the collimation tube. The diameter of a Singaporean dime is 18.5 mm for a size reference.

First, the diffraction angle selects part of the laser operating wavelength that feeds back on the laser diode. Second, the external feedback increases the overall gain of the system and reduces the laser threshold. Third, the spacing between the laser diode and the grating forms an “external cavity”, accumulating a phase difference on the feedback path – this changes the laser frequency and decreases the laser linewidth. With the external cavity length of  $\sim 3$  cm and diffraction efficiency of  $\sim 20\%$ , our ECDL linewidth is typically less than 1 MHz, much narrower compared to the atomic or cavity linewidth.

There are 4 ways to tune the frequency of an ECDL. Starting from the coarsest way, they are (1) the diffraction angle, via an adjustment screw on the grating mount, (2) the temperature of the ECDL, via a peltier element, (3) the laser current, and (4) the change of the external cavity length in  $\sim \text{nm}$  scale, via a piezoelectric element attached to the grating mount. To probe the frequency response of an experimental system, i.e. in atomic or cavity spectroscopy, we send a periodic stimulation input (stim-in) signal to the piezo, which varies the laser frequency over a small range, and monitor the response with an oscilloscope.

**Laser sources in our setup** We use ECDLs for 3 different wavelengths – 780 nm and 795 nm lasers to target the  $D_2$  and  $D_1$  transition of  $^{87}\text{Rb}$  atom, and an 810 nm

laser to provide a far off resonant light to the near-concentric cavity. The laser diodes are commercially available (780 nm – GH0781RA2C, Sharp; 795 nm & 810 nm – LD808-SA100, Thorlabs), with their output mode collimated by aspheric lenses (C220TMD-B, Thorlabs) and directed towards a holographic grating (GH13-18V, Thorlabs). The ECDL output passes through an optical isolator (780 nm & 795 nm – IOT-5-780-VLP, Thorlabs; 810 nm –  $2\times$  IO-3D-830-VLP, Thorlabs) to prevent any back-propagating beam, from further on, to affect the operation of the ECDL. The laser beam is then coupled to a single-mode fiber (FOP-78-x, AFW Technologies), which spatially filters the mode to a Gaussian profile.

### 3.1.2 Atomic Spectroscopy for Laser Stabilisation

The atomic species used for cavity-atom interaction experiments is Rubidium 87 ( $^{87}\text{Rb}$ ), which belongs to the alkali metal group, and is hydrogen-like due to a lone outermost electron on the s-orbital. The atomic dipole transition of interest is the  $D_2$  line ( $5^2S_{1/2} \rightarrow 5^2P_{3/2}$ ), with a centre transition frequency of 384.23 THz and wavelength of 780.24 nm in vacuum [224]. In the  $D_2$  line, it is possible to form a cycling transition between the  $|F = 2, m_F = \pm 2\rangle$  and  $|F' = 3, m'_F = \pm 3\rangle$  states, realising a two level system. In addition, the other fine structure doublet, the  $D_1$  line ( $5^2S_{1/2} \rightarrow 5^2P_{3/2}$ ), has a centre transition frequency of 377.11 THz and wavelength of 794.98 nm in vacuum. An energy level structure of the  $^{87}\text{Rb}$  D line transitions is shown in Figure 3.2.

The frequency of the EDCL can be stabilised to a particular atomic transition, by first generating an error signal using a frequency modulation (FM) spectroscopy [235, 236] of the atoms, and implementing a control-loop feedback on the ECDL piezo. We use two different types of atomic FM spectroscopy – saturation absorption spectroscopy [237] and modulation transfer spectroscopy [238], which share a very similar setup arrangement (see Figure 3.3). The modulation transfer spectroscopy has a strong signal only in a closed atomic transition, i.e. the  $F = 2 \rightarrow F' = 3$  transition of the  $D_2$  line, but provides a background-free error signal.

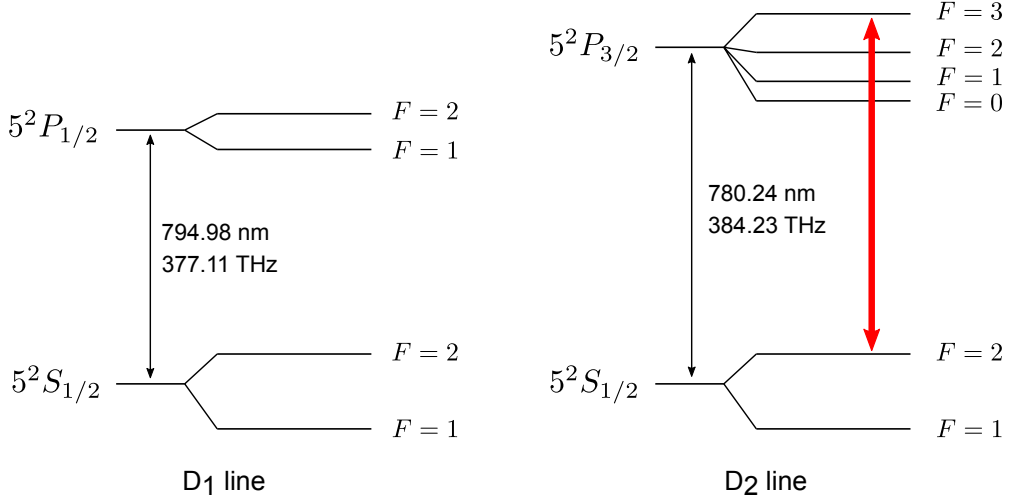


Figure 3.2: Energy level structure of  $^{87}\text{Rb}$   $D_1$  and  $D_2$  line transitions. The targeted transition for the atom-cavity interaction is  $F = 2$  to  $F' = 3$  on the  $D_2$  line (red).

### 3.1.3 Laser frequency detuned from atomic transition

We use an acoustic optical modulator (AOM) to detune the ECDL frequency away from an atomic transition. The AOM creates different diffraction orders off the main beam, with their frequencies shifted by integer multiples of the AOM driving frequency. The diffraction efficiency onto either the +1 or -1 order can be maximised up to  $\sim 85\%$  efficiency, by varying the tilt angle of the AOM. The AOM can be operated in either a single-pass or double-pass configuration [239]. Our AOMs, with centre frequencies of 80MHz (3080-122, Crystal Technology) and 200 MHz (3200-124, Crystal Technology), provide a range of frequency shifts, from 70 MHz up to  $2 \times 230$  MHz. The output of the AOM can be switched on/off with a rise/fall time of less than 100 ns, enacting a switching mechanism in implementing the experimental sequences.

Alternatively, similar frequency detuning can also be provided by a phase electro-optical modulator (EOM) with a large frequency range. The phase EOM generates frequency sidebands on the main laser frequency, with the spacing determined by the EOM modulation frequency. By locking the sideband to an atomic transition, the main frequency of the ECDL can be tuned by changing the driving frequency. Using a large bandwidth waveguide phase EOM (10 GHz Phase Modulator, EOspace), the modulation or detuning frequency can be tuned from DC up to 10 GHz, although

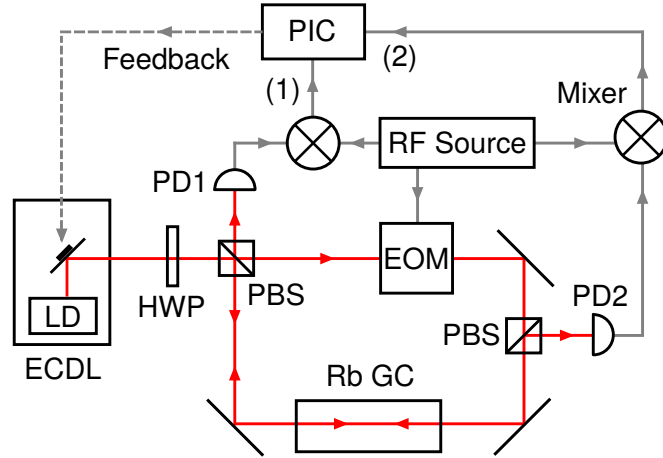


Figure 3.3: Atomic FM spectroscopy setup for ECDL stabilisation. The radio-frequency (RF) source modulates a laser beam with a frequency of 20 MHz via an electro-optical modulator (EOM). The half-wave plate (HWP) and polarising beam-splitter (PBS) divides the ECDL output into a pump and probe paths. The modulated intensities of the probe are measured by photodetectors (PD1 or PD2), and mixed with the RF source to produce error signals, which provide feedback to the ECDL piezo via a proportional-integral control (PIC).

In the saturation absorption spectroscopy (1), the probe (horizontal) is modulated, while the pump (vertical) saturates the Rubidium gas cell (Rb GC), such that the spectroscopy signal is provided by zero-velocity atoms.

In the modulation transfer spectroscopy (2), the probe (vertical) is not modulated initially, but the modulated pump (horizontal) transfer the modulation to the probe, via a near-resonant four-wave mixing process.

the tuning range is usually also limited by the bandwidth of the RF source and amplifier.

### 3.1.4 Detecting Single Photons and Running Experimental Sequences

The interaction between the atom and cavity photons is observed in the single-photon regime. We use a silicon avalanche photodiode (home-built) as the single-photon detector with detector efficiency of around 45 – 50% at 780 nm. The photodetection signals are recorded by a timestamp unit (home-built), which outputs either a list of the photodetection time or the number of photons within a set time period.

The photon count rates are used to trigger the start of an experiment sequence

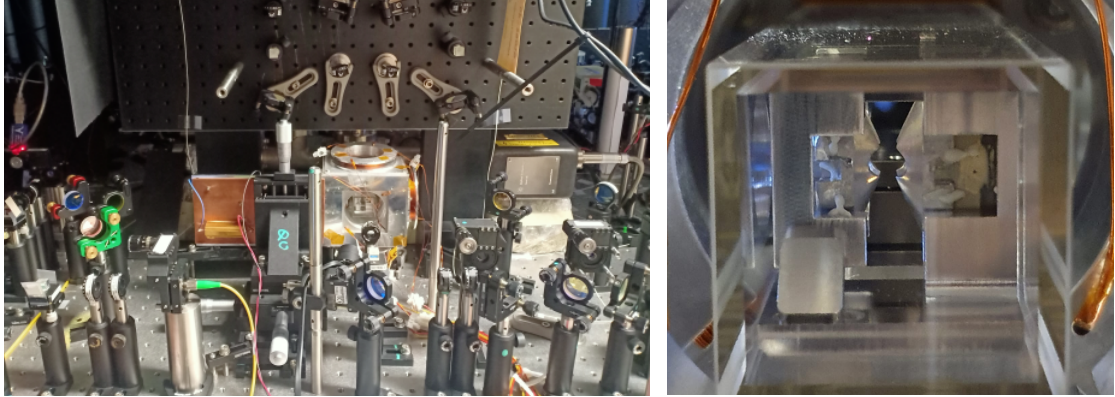


Figure 3.4: Pictures of the cavity setup inside the vacuum chamber. The cavity setup is mounted inside a cuvette (right, zoomed in) attached to a relatively small vacuum chamber, and surrounded by magnetic coils and optical components (left).

– if the rate exceeds a certain threshold that indicates atom loading, a preloaded experimental sequence is run by a digital pattern generator (home-built). Data collected during the experimental sequences are processed with computer programs, typically written in C or Python.

## 3.2 Vacuum System

The cavity setup is placed inside an ultrahigh vacuum (UHV) environment, with pressure lower than  $10^{-8}$  Torr, to limit collision of random particles with the trapped atoms. We use a small vacuum chamber, and put our setup inside a glass cuvette of size  $100 \times 25 \times 25$  mm with excellent optical access (see Figure 3.4). The cuvette is externally coated with anti-reflective coating, which reduces the optical loss through the cuvette to around 8%, and limits the etalon effect from the cuvette wall interfaces [240].

We connect the electrical wires of the translation stage and piezo actuator, with a UHV-compatible cable (Cable In-Vacuum, Type-D 9 Pins, MDC Precision) and externally with an electrical feedthrough (Multipin Feedthrough, Conflat Flange, MDC Precision). The source of rubidium atom is a getter dispenser (Rubidium AMD, SAES), which is placed facing the cavity, but not at line-of sight with the mirrors, protected by the mirror mount-shields. The dispenser is powered by an

## CHAPTER 3. EXPERIMENTAL SETUP AND TECHNIQUES

external power supply with an operating current of around 2.5 A.

**Pumping down** Besides the aforementioned components, the main vacuum chamber also consists of an ion pump (Vaclon Plus 20, Agilent), an ionisation gauge (UHV-24, Varian), titanium sublimation pump (TSP Cartridge Filament Source, Agilent), and a valve (Angle Valve 1.5", All Metal, MDC Precision) which connects to an external vacuum chamber which consists of a turbomolecular pump (HiCube 80 Classic, with rotary vane backup pump, Pfeiffer Vacuum) and a compact vacuum gauge (PKR 251, Pirani and cold cathode combined gauges, Pfeiffer Vacuum). After the installation of the cavity setup, the chamber is first pumped down with a turbomolecular pump, reaching pressure of around  $10^{-6}$  Torr after 1 day of pumping. During the pumping down process, the titanium sublimation pump is outgassed at a pressure below  $10^{-2}$  Torr by running a current of 40 A for 1 min on each filament. Thereafter, we switch on the ion pump, which pumps the main chamber indefinitely.

There are three methods to monitor the pressure of our vacuum chamber. The thermistor/pirani gauge is located at the external vacuum chamber, and can be used to monitor the pressure down to  $10^{-7}$  Torr while opening the valve. The ionisation gauge measures vacuum pressure down to  $10^{-11}$  Torr, and is the main pressure gauge we use. The current of the ion pump can also be used to estimate the vacuum pressure down to around  $5 \times 10^{-9}$  Torr, but it has to be calibrated with the ionisation gauge beforehand. We use this method occasionally, as continuous operation of the ionisation gauge shakes the vacuum chamber and introduces additional mechanical noise to the cavity.

**Baking the vacuum chamber** To lower the vacuum pressure considerably, we bake the vacuum chamber to accelerate the evacuation of volatile materials inside the chamber. The vacuum chamber is covered with heat tapes and layers of aluminium foils which provide thermal isolation. The temperature of the chamber is increased slowly, while monitoring the vacuum chamber pressure to not exceed  $5 \times 10^{-6}$  Torr. The target baking temperature is  $120^\circ\text{C}$ , which is limited by the maximum baking temperature of Torr Seal. The baking is stopped once the vacuum chamber pressure drops very slowly, i.e. less than  $\sim 5\%$  drop after a full baking day. The temperature of the vacuum chamber is then lowered slowly, to minimise excessive temperature

## CHAPTER 3. EXPERIMENTAL SETUP AND TECHNIQUES

gradients which might crack the cuvette. We close the valve separating the main and external vacuum chamber at temperature of around  $100^{\circ}\text{C}$ , and wait until the vacuum chamber cools down to the room temperature.

If there is no significant leak or excessive outgassing, the pressure of the main vacuum chamber should reach around  $8 \times 10^{-9}$  Torr. We can lower the pressure to less than  $2 \times 10^{-9}$  Torr by running the titanium sublimation pump with a current of 42 A for 1 min. This process may have to be repeated every few months, as the vacuum pressure climbs back up. The target operating pressure is  $3 \times 10^{-9}$  Torr, which gives an atomic loss rate of around  $0.2 \text{ s}^{-1}$  from a magneto-optical trap [241], and a single atom trapping lifetime of around 1 s from a dipole trap [242], due to background gas pressure.

**Rubidium dispenser and the decrease of cavity finesse** The rubidium dispenser is the main source of the rubidium atoms. We operate it at around 2.5 A, by heating it up to a temperature of around 600 K. At this temperature, a large amount of rubidium atoms and other volatile materials are released by the dispenser, which might condense on the mirror surface and reduce the cavity finesse. In the past, we have observed the cavity finesse reducing from around 600 to 138 (version 1a) and 275 (version 2a), which we hypothesise to be mostly contributed by the operation of the rubidium dispenser.

In the most recent experiment (version 2b), we monitor the cavity finesse closely during the whole vacuum operation. The initial cavity finesse of  $\mathcal{F} = 545(11)$  drops to  $\mathcal{F} = 503(11)$  after a series of vacuum procedures, which include baking the vacuum chamber and running the titanium sublimation pump. Then, we ramp the rubidium dispenser current slowly to 2.5 A, while keeping the main chamber pressure below  $3 \times 10^{-8}$  Torr, as the dispenser outgasses quite appreciably. The finesse is still maintained during this process, but later drops to  $\mathcal{F} = 484(9)$  as we increase the dispenser current to 2.8 A intermittently for short periods of time (less than one hour in total) to search for the formation of the rubidium cloud (see Section 4.1.1). This corresponds to a cumulative increase of the mirror scattering loss of about 740(160) ppm. To prevent further deterioration, we have developed and implemented a method to infer the cloud formation without a camera (see the last paragraph of Section 4.1.1), which allows us to keep the dispenser at the operating

current (2.4 A) without increasing it further. The cavity finesse still maintains at  $\mathcal{F} = 484(9)$  after a few weeks of operation.

The increase in the cavity scattering loss will be an issue in future experiments with higher finesse cavities – a similar mirror scattering loss of 740 ppm corresponds to a finesse drop from  $\mathcal{F} = 5000$  to  $\mathcal{F} = 2300$ . Besides the method described above, we are currently developing another method to reduce condensation of volatile materials on the mirror surface, by using a shield to protect the cavity setup while the hot elements, i.e. rubidium dispenser and titanium sublimation pump, are outgassing. The shield can then be opened once the setup is ready for experiments.

**Magnetic field coils** We use magnetic field coils to generate homogeneous and quadrupole magnetic field inside the cavity setup. The homogeneous magnetic field in three directions are generated with three pairs of coils, arranged close to a Helmholtz configuration – not exactly Helmholtz due to space considerations, but the magnetic field is very homogeneous in the vicinity of the atomic cloud ( $\sim 0.2$  mm in size). This is used to compensate external magnetic fields, i.e. from earth, ion pump, etc, and to create Zeeman-level splitting of the atom.

The quadrupole magnetic field is generated by a pair of anti-Helmholtz coils, and is used to create large magnetic field gradients to form the cold rubidium cloud, typically on the order of 20 G/cm. In a small vacuum chamber, such field gradients can be generated with a relatively small coil setup with a diameter of 6 cm and coil spacing of 3 cm, and each coil consisting of 160 turns of AWG 22 copper wire. The coil setup is run with a current of about 1 A, and generates heat of about 3.2 W. Generate the same field gradient in a larger vacuum system requires higher current or more coil windings, which scale quadratically with the size of the coil setup. It may also be important to consider heat management of the coil setup – for example, scaling the coil setup and wire diameter by a factor of two requires a current of 4 A to generate a similar field gradient, while dissipating around 26 W of heat.

### 3.3 Stabilisation of Near-Concentric Cavity

To observe atom-cavity interaction, the near-concentric cavity has to be stabilised in both the longitudinal and transverse directions, corresponding to the cavity length

and transverse alignment respectively. In the longitudinal direction, the degree of stability is specified by the noise effect factor (see Equation 2.5), which quantifies how much the cavity resonance fluctuates with respect to the cavity linewidth. Long term fluctuations of the cavity resonance can be addressed by stabilising the cavity length to an atomic transition, which is extremely stable across time. However, short term fluctuations, arising from mechanical vibrations of the cavity setup, is ever-present and requires a few additional techniques (see Chapter 6).

Cavity misalignment in the transverse directions changes the mode-matching condition and hence the cavity transmission and fibre coupling. Such misalignment is typically due to changes in temperature, which expands or contracts the mechanical stages. As it progresses quite slowly, in the timescale of minutes, the misalignment can be corrected using a computer algorithm, by moving the translation stage back to the spot with higher transmission. The transverse alignment stabilisation method has been published in [80].

### 3.3.1 Far Off Resonant Lock and Transfer Cavity

To stabilise the near-concentric cavity length, we send a laser to probe the cavity resonance, and create an error signal with the frequency modulation technique [236, 243]. The error signal is then used to implement a proportional-integral (PI) control on the cavity axis direction of the translation stage. To prevent any near-resonant interaction of the locking laser with the atom, the laser used has a frequency that is far away from any atomic resonances. The locking laser has a long-term stability derived from the atomic transition, through the use of a transfer cavity. The locking laser is also used as a far off-resonant trap (FORT) to trap single atoms (see Section 4.1.2).

Figure 3.5 shows the schematic of the transfer cavity setup. We use a 780 nm laser, which is already stabilised to one of the  $^{87}\text{Rb}$  transitions, and a 810 nm laser, which is far-off resonant with rubidium transitions, to lock the near-concentric cavity length. The transfer cavity is made from two mirrors with reflectivity  $R > 99.9\%$  (ATFilms), separated by an Invar spacer and a piezo tube. The cavity is near-planar with length 1.17 cm, corresponding to a free spectral range of 12.8 GHz and linewidth of 2.8 MHz. The cavity is placed inside a high vacuum (HV) environment with a

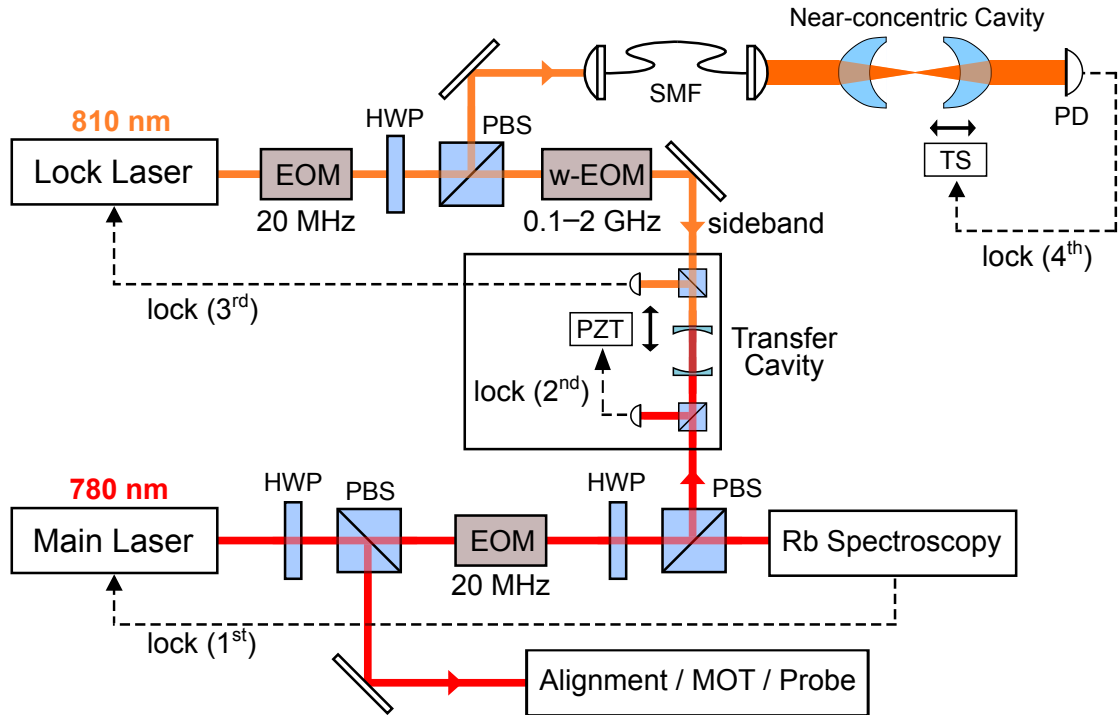


Figure 3.5: Schematic of the transfer cavity setup. The stabilisation sequence consists of a series of four locks (1<sup>st</sup> to 4<sup>th</sup>). First, the 780 nm laser is locked (1<sup>st</sup>) to the  $^{87}\text{Rb}$  transition via atomic spectroscopy. Then, the length of the transfer cavity is locked (2<sup>nd</sup>) to the 780 nm laser via a piezo (PZT). The waveguide electro-optical modulator (w-EOM) generates a frequency sideband of 0.1 to 2 GHz on the 810 nm laser, which is then locked (3<sup>rd</sup>) to the transfer cavity to stabilise the 810 nm laser. Finally, the near-concentric cavity is locked (4<sup>th</sup>) to the 810 nm laser via the translation stage (TS). The length of the near-concentric cavity can be varied by changing the modulation frequency of the w-EOM.

pressure of  $5 \times 10^{-6}$  mbar, and the vacuum chamber is temperature-stabilised with a heating coil, to reduce cavity fluctuations.

The transfer cavity length is locked to the 780 nm laser frequency using the piezo tube, transferring the long term stability of the atomic resonance to the transfer cavity. We use a waveguide EOM (10 GHz Phase Modulator, EOspace) to generate frequency sidebands of around 0.1 to 2 GHz on the 810 nm laser, and lock one of the 810 nm laser sideband to the transfer cavity. This process effectively transfers the long term stability of the atomic resonance to the 810 nm laser. The locking of the sideband, instead of the mainband, of the 810 nm laser frequency is necessary for

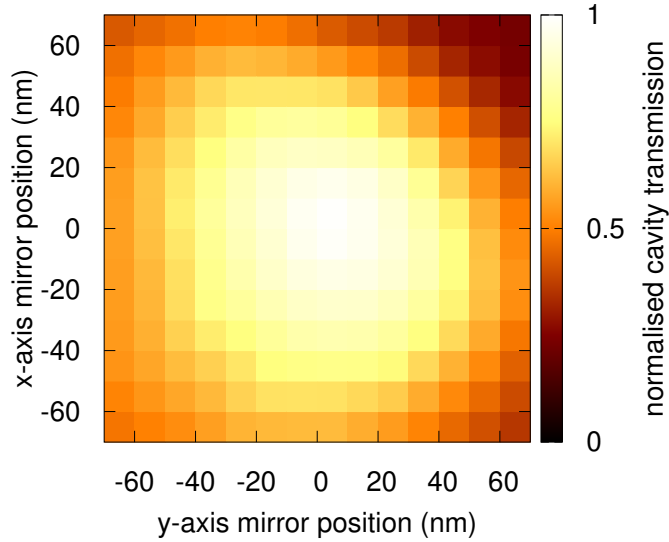


Figure 3.6: Cavity transmission at different transverse positions of a cavity mirror. By moving the translation stage in the transverse directions (x and y axes), the cavity transmission coupled through a single mode fibre drops, with a full width at half maximum (FWHM) of  $59(3)$  nm.

the tunability of the near-concentric cavity resonance, via the modulation frequency of the waveguide EOM.

### 3.3.2 Transverse Alignment Stabilisation

Transverse alignment is very important in a near-concentric cavity. Figure 3.6 shows the cavity transmission after coupling to a single-mode fibre, by moving the translation stage in the two transverse directions, while locking the cavity in the longitudinal direction. With a critical distance of  $1.7(1)$   $\mu\text{m}$ , the cavity transmission through a single-mode fibre loses half its initial value with only around 30 nm of cavity misalignment (FWHM =  $59(3)$  nm). The transverse alignment is even more sensitive for smaller critical distances.

A small change in temperature expands or contracts the cavity setup slightly, which can misalign the cavity in the transverse directions. The difference in the thermal expansion of the cavity stages (aluminium,  $\alpha = 23 \times 10^{-6} \text{ K}^{-1}$ ) and the translation stage (titanium,  $\alpha = 8.6 \times 10^{-6} \text{ K}^{-1}$ ), say for a length of 2 cm, causes misalignment of about 290 nm/K. The day and night temperature cycle of the laboratory, and thus our cavity setup, is around 1 K. We lower this down by putting

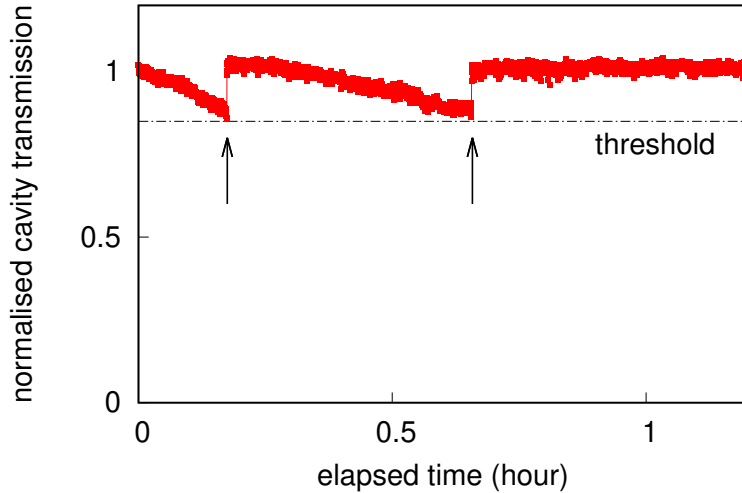


Figure 3.7: Transverse alignment stabilisation via the cavity transmission. Over time, on the order of minutes, the near-concentric cavity accumulates misalignment in the transverse directions. Once the transmission drops below a threshold, or by an amount of  $\delta T_{tr}$ , the stabilisation algorithm maximises the cavity transmission back to its initial value, as indicated by the arrows.

an enclosure on the whole vacuum chamber and the surrounding optics, and control the temperature inside by actuating the air conditioner via an air duct. Nevertheless, there are other thermal sources, i.e. rubidium dispenser and the quadrupole coils, which also affect the temperature of the cavity setup.

To counteract the issue of the transverse misalignment, we monitor the transmission of the locking laser through a single-mode fibre, and implement a stabilisation mechanism once the transmission drops by a set amount  $\delta T_{tr}$ . Below the transmission threshold, the computer moves the translation stage in the transverse directions to compensate for the misalignment, and find the location with the original transmission value – the algorithm scans the surrounding area in a fine step, and implement movement in the direction of the steepest ascent.

Figure 3.7 shows an implementation of the transverse stabilisation mechanism in a near-concentric cavity with a critical distance of 207(13) nm. The temperature drift is on the order of tens of minutes, while the stabilisation mechanism typically only requires a few seconds. The degree of transverse stability is characterised by  $\delta T_{tr}$ , which can be set very low, but with a smaller experiment duty cycle.

## 3.4 Measurement of Cavity Parameters

This section describes methods to measure relevant cavity parameters, including the free spectral range, cavity length, finesse, cavity decay rates, and mode matching. These can be measured via a frequency reference and the cavity spectra. Particularly for a near-concentric cavity, another important cavity parameter is the critical distance, which can be determined by the frequency spacing of the transverse modes. The method to measure critical distances has been published in [80]. Characterisation experiments in subsequent chapters follow the method described in this section.

### 3.4.1 Free spectral range and cavity length

For our near-concentric cavity, the cavity length is  $L = 2R - d$ , with mirror radii  $R$  and critical distance  $d$ . As the operating critical distance is at most a few  $\mu\text{m}$  ( $d/L \sim 10^{-4}$ ), and the radius of curvature is set by the manufacturing and coating process ( $\delta R/R \lesssim 10^{-4}$ ), we take  $L = 11.000$  mm with a free spectral range of  $\nu_F = c/2L = 13.627$  GHz in vacuum, with an uncertainty of around  $10^{-4}$ . These values have been verified experimentally, but with a higher uncertainty (see below).

Alternatively, the free spectral ranges can be determined by a wavelength meter (WS7-60, HighFinesse), which outputs the frequency of the laser up 60 MHz absolute accuracy with 10 MHz resolution. First, we find the resonance frequency to the fundamental mode of the cavity, and then tune the laser frequency one free spectral range away, either up or down, to find the next resonance frequency of the cavity fundamental mode. We repeat the process a few times, in both frequency directions, to estimate the uncertainty – typically around  $10^{-3}$  to  $10^{-2}$ . Using the free spectral range, the cavity length in vacuum can then be determined using the formula  $L = c/2\nu_F$ . For cavities not in vacuum, the cavity length is slightly shorter, due to the air index of refraction of around 1.0003. A lower uncertainty can be obtained by sending another resonant laser at different frequency to lock the cavity length, eliminating the cavity temperature fluctuation during the measurement period.

### 3.4.2 Finesse, decay rates, and mode matching

Characterisation of the cavity finesse, decay rates and mode matching can be performed using the cavity transmission and reflection spectra, following the

## CHAPTER 3. EXPERIMENTAL SETUP AND TECHNIQUES

technique described in [209]. Here, we assume that both cavity mirrors have the same transmission. The transmission of the laser power through the cavity, or the cavity transmission spectrum, is given by

$$T(\omega) = \frac{P_t(\omega)}{P_{in}} = \eta \frac{\kappa_m^2}{(\kappa_m + \kappa_l)^2 + (\omega - \omega_0)^2}, \quad (3.1)$$

where  $P_t(\omega)$  is the laser power transmitted through the cavity,  $P_{in}$  is the input power,  $\eta$  is the spatial mode matching efficiency,  $\omega_0$  is the cavity resonance frequency, and  $\kappa_m$  and  $\kappa_l$  are the cavity decay rates due to the mirror transmission and scattering losses, respectively. On the other hand, the fraction of laser power reflected back from the cavity, or the cavity reflection spectrum, is given by

$$R(\omega) = \frac{P_r(\omega)}{P_{in}} = 1 - \eta \frac{\kappa_m^2 + 2\kappa_m\kappa_l}{(\kappa_m + \kappa_l)^2 + (\omega - \omega_0)^2}, \quad (3.2)$$

where  $P_r(\omega)$  is the laser power reflected by the cavity. The cavity finesse  $\mathcal{F} = \pi\nu_F/\kappa$ , is determined from the total cavity decay rate,  $\kappa = \kappa_m + \kappa_l$ .

**Obtaining the cavity spectra** To obtain the cavity transmission and reflection spectra, we use a stimulation-input (stim-in) signal either on the ECDL or cavity piezos, generating a periodic and near-linear variations on the laser frequency or cavity length, respectively. With the same stim-in signal, we obtain a frequency reference, either via the atomic spectroscopy signal or the EOM modulation frequency. The frequency reference allows us to map and express the cavity spectra in terms of laser frequency  $\omega$  or cavity resonance detuning  $\omega_0 = \omega + \delta\omega$ , provided that the scanning range is mostly linear. Both scanning methods, either in laser frequency or cavity length, are almost equivalent, except for a very minute change of the free spectral range while varying the cavity length.

The non-linearity in the scanning arises when the stim-in voltages on the ECDL and cavity piezos do not correspond linearly with the laser frequency and cavity movement. In some cases, the stim-in voltages are set to be sinusoidal in time, as the ramp or triangular signal might have different gains for the higher harmonics, due to piezo mechanical resonances. We reduce the degree of non-linearity by only performing the measurement within a “near-linear window” – within this window, the maximum and minimum measured values of the spectral width or the frequency

## CHAPTER 3. EXPERIMENTAL SETUP AND TECHNIQUES

reference only vary by at most 5%. We repeat the measurement a few times and at different spots within the near-linear window to provide an error estimate.

A lower uncertainty can be obtained by locking the cavity length with another laser, and obtain the transmission and reflection spectra with a probe laser. The frequency of the probe laser can be varied across the cavity resonance, either using an AOM or EOM (see Section 3.1.3). As the probe frequency in a single measurement does not vary over time, we use this method to probe the atom-cavity spectra, which require a much longer integration time for each probe frequency (see Section 4.2).

It is important to recognise that both the transmission and reflection spectra are normalised, i.e. the measured power spectra are to be divided by the input power. Thus, in determining the transmission spectrum, one has to factor in losses from the optical components before and after the cavity, in particular the cuvette loss (around 5% on each side). For the reflection spectrum, the normalisation to the input power is already given in the far-off detuning case, i.e.  $R(\omega) \rightarrow 1$  for  $|\omega - \omega_0| \gg \kappa$ .

**Determining the finesse** The finesse is determined by fitting either the measured transmission or reflection spectra to either Equation 3.1 or Equation 3.2, and evaluating the total decay rate  $\kappa = \kappa_m + \kappa_l$  via a frequency reference. The finesse is then given by  $\mathcal{F} = \pi v_F / \kappa$ .

**Determining the cavity decay rates** First, we define a parameter  $\alpha$  to represent the effectiveness of the cavity transmission. The parameter  $\alpha$  is measured from the cavity transmission and reflection at resonance,

$$\alpha = \frac{T(\omega_0)}{1 - R(\omega_0)} = \frac{\kappa_m}{2\kappa_l + \kappa_m} . \quad (3.3)$$

It is interesting to note that  $\alpha$  is nominally determined by the cavity decay rates, and thus is a physical property of the cavity mirrors – for mirrors with no scattering losses,  $\alpha = 1$ . The cavity decay rates due to the mirror transmission and scattering losses can then be evaluated with

$$\kappa_m = \frac{2\kappa\alpha}{1 + \alpha} , \quad (3.4)$$

$$\kappa_l = \frac{\kappa(1 - \alpha)}{1 + \alpha} , \quad (3.5)$$

from measured values of  $\kappa$  and  $\alpha$ .

**Determining the mode matching efficiency** The mode matching efficiency  $\eta$  quantifies how well the mode of the input beam matches the cavity mode – a perfect mode matching results in  $\eta = 1$ . It can be evaluated by substituting Equation 3.4 and Equation 3.5 to Equation 3.1 on cavity resonance, given by

$$\eta = \frac{(1 + \alpha)^2}{(2\alpha)^2} T(\omega_0) . \quad (3.6)$$

### 3.4.3 Critical distance

The critical distance of the near-concentric cavity can be measured by the frequency spacing of the cavity transverse modes. In a near-concentric symmetrical cavity, the frequency spacing between two consecutive transverse modes,  $LG_{00}$  and  $LG_{01}$ , is evaluated using Equation A.3 (see Appendix A) and given by

$$\Delta v_{tr} = v_{q,0,0} - v_{q-1,0,1} = \frac{v_F}{\pi} \cos^{-1} \left( 1 - \frac{d}{R} \right) , \quad (3.7)$$

where  $\Delta v_{tr} \rightarrow 0$  as  $d \rightarrow 0$ . The frequency spacing  $\Delta v_{tr}$  is measured via a frequency reference as described previously, and Equation 3.7 is inverted to determine the critical distance  $d$ .

The mode matching to the  $LG_{01}$  is very small in a well-aligned near-concentric cavity with an input beam mode that nearly matches the cavity fundamental mode. Hence, it may be necessary to slightly misalign the input beam to couple some light into the  $LG_{01}$  mode. This slight misalignment on the input beam does not change the cavity length or the critical distance.

Figure 3.8 shows a measurement of the transverse mode spacing over critical distances that are separated by half-wavelengths, by fixing the laser frequency. The data points are fitted with Equation 3.7, with the critical distance of the first data point (the last stable resonance) as the only fitting parameter. The data points follow the theoretical line closely, indicating that the method of using the transverse mode spacing to determine the critical distance is valid in this region. From the fitting, the critical distance of the last stable resonance is  $d = 207(13)$  nm, the implication of which will be explored further in Section 7.1.

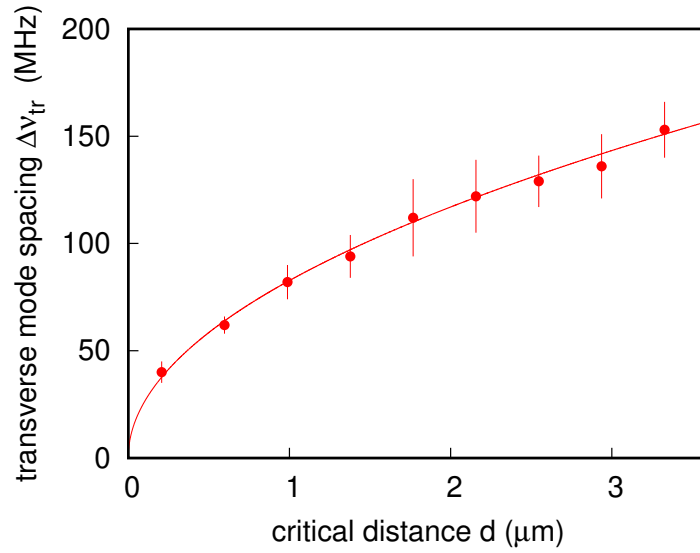


Figure 3.8: Cavity transverse mode spacing  $\Delta v_{tr}$  at different fitted critical distances  $d$ . All data points are spaced  $\lambda/2$  apart, initially at some arbitrary distance. After fitting, we determine the critical distance of the first data point at  $d = 207(13)$  nm. The error bars indicate the standard deviation of each measurement.

## Chapter 4

# Observation of Atom-Cavity Interaction

This chapter outlines the procedure to trap a single  $^{87}\text{Rb}$  atom from a cold atomic cloud, in an intra-cavity trap of a near-concentric cavity. With the single atom trapped, we probe the atom-cavity spectra to estimate the atom-cavity coupling strength and cooperativity. This work has been published in [79].

### 4.1 Trapping Single Atoms

To trap single atoms inside our cavity, we first prepare a cold  $^{87}\text{Rb}$  atomic cloud with a magneto-optical trap (MOT). The atomic cloud provides a reservoir of cold atoms to be loaded into the single atom traps, formed by an intra-cavity far-off resonant trap (FORT). The atomic fluorescence signal exhibits discrete jumps once an atom is loaded on a trapping site, which allows us to determine the presence of a single atom inside a cavity mode, and measure the trap lifetime.

#### 4.1.1 Magneto-optical trap

The MOT uses a red-detuned radiation pressure force and a quadrupole magnetic field to cool and confine the atoms [244]. The counter-propagating circularly polarised beams in three different directions cool the atoms preferentially towards the centre of the MOT, by exploiting a spatially-varying atomic Zeeman shift due to the quadrupole magnetic field. The MOT has a trap depth on the order of Kelvins, and a size on the order of millimetres. This allows a large number of atoms, up to  $10^{10}$  atoms in some setups [245], to be cooled and confined in a small region, serving as a

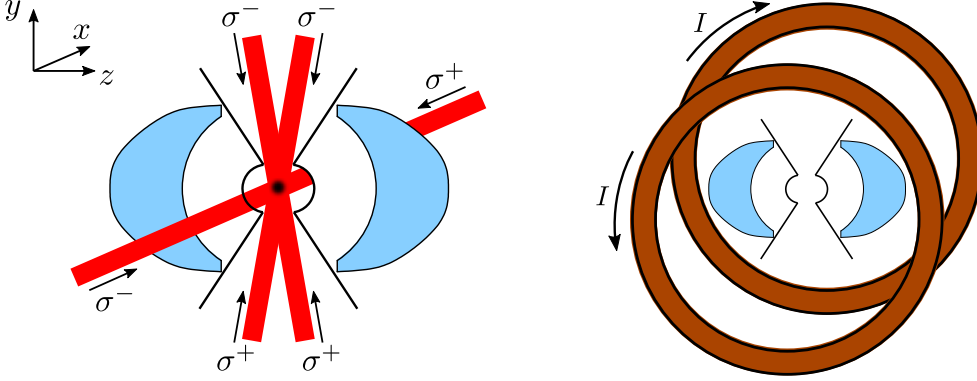


Figure 4.1: Schematic of the magneto-optical trap setup to form a  $^{87}\text{Rb}$  atomic cloud at the centre of the cavity. Three counter-propagating circularly polarised beams, one along the  $x$ -axis and two on the  $yz$ -plane, pass through the openings of the mirror shields (left). A pair of anti-Helmholtz coils (right) provides quadrupole magnetic field at the cavity centre.

reservoir of cold atoms with  $\sim\text{mK}$  temperatures.

**The MOT setup** Figure 4.1 shows the setup of the MOT. The cold atomic cloud can be formed directly inside the cavity, due to a large physical spacing between the cavity mirrors – the cavity length is 11 mm, and the mirror shields provide an aperture size of around 2 mm for the MOT beams. This removes the requirement to deliver atoms from the MOT to the cavity trapping sites, which is common in small cavity systems [246, 247].

The MOT beams consist of light from a cooling laser and a repump laser. The cooling laser is red-detuned from the  $D_2$  line  $F = 2$  to  $F' = 3$  closed transition by around 10 MHz. The repump laser tuned to the  $D_1$  line  $F = 1$  to  $F' = 2$  transition brings some atoms off-resonantly transferred to the ground  $F = 1$  state, back to the  $F = 2$  state and continue on the closed transition cycles. To cool the atomic motion in all directions, one MOT beam is placed in the horizontal direction perpendicular to the cavity axis, and two MOT beams are placed vertically with tilt angles of approximately  $\pm 10^\circ$ . The three beams overlap at the centre of the cavity, guided by the mirror shields. In each beam, the cooling and repump laser powers are set to be around  $100 \mu\text{W}$  and  $30 \mu\text{W}$ , respectively, with beam diameter of around 1 mm.

The cooling beams are either left ( $\sigma^-$ ) or right ( $\sigma^+$ ) circularly polarised, de-

pending on the gradient of the quadrupole magnetic field. We use a quarter-wave plate to convert a linearly polarised cooling beam to circularly polarised. On the back-reflection path, the handedness is reversed with a quarter-wave plate and mirror combination. The polarisation of the repump beams is not critical.

The quadrupole magnetic field is generated by a pair of coils in anti-Helmholtz configuration (see Section 3.2), which produce magnetic field gradient of around 20 G/cm along the coil axis, and -10 G/cm in perpendicular directions at the centre of the coil setup with zero magnetic field. As the atomic cloud forms around this zero point, we use a 3-axis manual translation stage to move the position of the coil centre to coincide with the centre of the overlapping MOT beams. In addition, we use three Helmholtz coil pairs to compensate for external magnetic fields.

**Observing the cold  $^{87}\text{Rb}$  cloud** The formation of an atomic cloud with a MOT can be observed using a camera, as the cold atoms scatter the light from the MOT beams in all directions. To verify that it is indeed an atomic cloud, and not some imaging artefacts, we block the repump beam which would disperse the cloud. In our system, a clear visual of the cloud, with a diameter of around 0.2 mm, can be seen with a rubidium dispenser current exceeding 3.2 A. However, operating the dispenser at such a high current reduces the cavity finesse significantly (see Section 3.2). The cloud is barely observable as a faint flickering spot at a dispenser current of 2.8 A and below, due to a much lower number of atoms.

The alignment of the MOT beams and coils are critical to observe the atomic cloud. First, the number of atoms in a MOT approximately scales with the fourth power of the size of the overlapping MOT beams [248], which is around 1 mm or less. Second, the location of the zero magnetic field has to be located within the overlap region. While the MOT beams and magnetic field overlaps are not yet optimised, the formation of the cloud might only be observable at a higher dispenser current. Thus, any attempts to align the MOT setup and search for the cloud formation so far have resulted in a varying degree of mirror finesse decrease.

To counteract this issue, we can choose to protect the cavity finesse from being contaminated by skipping this step entirely, as the visual verification of the atomic cloud is not necessary to proceed on trapping a single atom with an intra-cavity FORT. Instead, if single atoms are successfully loaded into the trap, observed via

the atomic fluorescence signal on the cavity output, we can infer that a cold atomic cloud must have been formed, though not visually seen. Thus, we align and optimise the MOT setup by looking at the trapped atom signals, while ensuring that every elements of the MOT and FORT setups are working as intended. This allows us to keep the dispenser current at the operating current of around 2.5 A.

### 4.1.2 Far-off resonant trap

The FORT exploits a far-detuned dipole interaction between atom and light, which shifts the atomic ground state energy depending on the light intensity [242] – a phenomenon known as ac Stark shift. For a two level system, the energy level shift is given by

$$\Delta E(\mathbf{r}) = \frac{3\pi c^2}{2\omega_0^3} \frac{\Gamma}{\Delta} I(\mathbf{r}), \quad (4.1)$$

with  $\omega_0$  the atomic resonance,  $\Gamma = 2\gamma$  the atomic population decay rate,  $\Delta = \omega - \omega_0$  the laser detuning from the atomic resonance, and  $I(\mathbf{r})$  the location-dependent intensity of the laser beam. For a red-detuned laser beam, the sign of  $\Delta$  is negative, which shifts the ground state lower with higher laser intensity. This results in conservative potential well to trap atoms at the centre of the beam [249]. A semi-classical way to view this process is that the atom has a small frequency-varying index of refraction (dispersion), which refracts the FORT laser and inflicts a restoring force on the atom towards the beam centre. The scattering rate from this process is given by

$$R_{sc}(\mathbf{r}) = \frac{3\pi c^2}{2\hbar\omega_0^3} \frac{\Gamma^2}{\Delta^2} I(\mathbf{r}) \quad (4.2)$$

which scales as  $\Gamma^2/\Delta^2$ . Compared with the dispersive energy level shift which scales as  $\Gamma/\Delta$ , the FORT laser detuning is chosen to be much larger than the atomic linewidth, typically on the order of 10 THz, to minimise the scattering rate.

The FORT is formed in a fundamental cavity mode by a laser which is far-off resonant with the atomic transitions [65]. The FORT laser is also used concurrently to stabilise the cavity length (see Section 3.3.1). The atoms are trapped at the antinodes of the intra-cavity standing wave, where the laser intensity has local maxima. The trapping sites are pretty small – in the axial direction, each neighbouring sites are separated by  $\lambda/2$  distance, while in the radial direction, the trapping region is

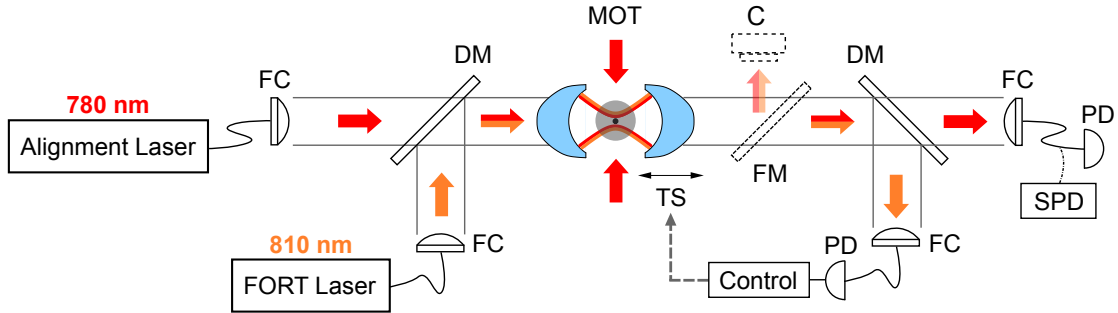


Figure 4.2: Schematic of the far-off resonant trap (FORT) setup. A collimated FORT laser beam, from a fibre coupler (FC) output, is coupled to the fundamental mode of the near-concentric-cavity. To assist the alignment process, we use a flip mirror (FM) to observe the cavity modes with a camera (C). The cavity output is then fibre-coupled to a photodetector (PD) for cavity stabilisation via the translation stages (TS). We use an alignment beam along the same path of the FORT beam, combined using a dichroic mirror (DM), to couple to the cavity mode resonant with the atoms. To observe the atomic fluorescence signal from the MOT cooling beams, we block the alignment laser path, and measure the photodetection rate with a single-photon detector (SPD).

limited by the cavity mode waist. Thus, each trapping site can be occupied by a single atom or none due to the light-assisted collisional blockade effect [250].

Atoms are loaded probabilistically to the FORT sites with  $\sim$ mK trap depth, directly from the neighbouring reservoir of cold atoms produced by the MOT [251]. As there are many trapping sites, more than one atom can be trapped, but at different sites. However, as each loading event happens randomly and can be observed with a clear step-function signal due to a low loading rate, we can identify whether the trap holds a single atom or more. The atom-cavity coupling strength varies with different trapping locations, as the antinodes of the FORT and the atom-resonant cavity standing waves do not coincide. Nevertheless, sites with higher or near-maximum atom-cavity coupling strength can be chosen based on the strength of the signal.

**The FORT setup** Figure 4.2 shows the setup of the FORT. The linearly-polarized 810 nm FORT laser is combined with a 780 nm alignment laser resonant to the main atomic transition using a dichroic mirror. Both lasers are aligned to the same fundamental mode of the cavity – the cavity axes coincide, but with different node

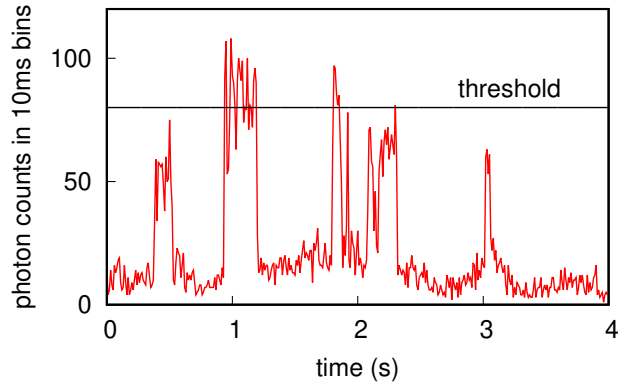


Figure 4.3: A typical trace of the atomic fluorescence signal, sorted into 10 ms time bins. The threshold for a fluorescence trigger is set at around 8 counts/ms.

spacings and mode waists due to different laser frequencies. The cavity length is stabilised by the FORT laser via a transfer cavity (see Section 3.3.1), and is simultaneously resonant with both lasers. From the cavity input and output power of the FORT laser ( $P_{in} = 2.6$  mW,  $P_{out} = 100$   $\mu$ W) and the cavity finesse at 810 nm ( $\mathcal{F} = 100$ ), the trap depth and scattering rate are estimated to be about 27 MHz and  $11$  s $^{-1}$ , respectively.

On the cavity output, both the FORT and alignment lasers are split by another dichoric mirror, and coupled separately to two single-mode fibres as spatial mode filters. The FORT laser component is used to generate an error signal for cavity stabilisation, and also to monitor the cavity transmission for transverse alignment stabilisation (see Section 3.3.2). The alignment laser component is used to observe the on-resonant cavity output mode, and connected to a single-photon detector after the alignment laser is blocked.

**Atomic fluorescence signal** Atoms trapped in the FORT sites scatter photons from the red-detuned MOT beams into the on-resonant cavity output. This atomic fluorescence signal is observed by a single-photon detector, and exhibits discrete jumps which signal a single atom loading event, as shown in Figure 4.3. The loading rate depends on the MOT parameters, which affect the density, location, and temperature of the cold atom reservoir. Typically, it can range from 0.1 to 10 loading events per second. Experimental sequences, generated by a pattern generator, are started when the atomic fluorescence signal exceeds a certain threshold of detection

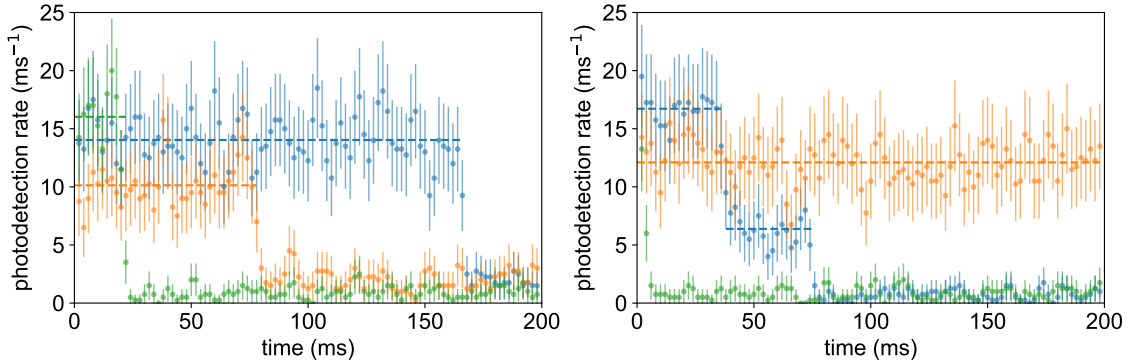


Figure 4.4: Triggered fluorescence of single atom (left) and indeterminate (right) traces, with 1 ms time binning. For the single atom traces, the fluorescence signal strengths vary and display discrete drops as the single atoms disappear. In addition, the indeterminate traces consist of atoms with very short lifetimes (green), atoms with lifetime longer than the observation period (orange), and atoms trapped in multiple locations indicated by two or more drops (blue). Error bars are estimates from Poissonian statistics.

events – we call this the “fluorescence trigger”. After each fluorescence trigger, the quadrupole magnetic field is switched off to disperse the atomic cloud and prevent further atomic loading.

### 4.1.3 Single atom trace and trap lifetime

Figure 4.4 shows some typical traces of the trapped atom fluorescence, after the fluorescence trigger. The strength of the single atom fluorescence signals varies, which we attribute to the variation of the atom trapping sites and the maximum atom-cavity coupling sites, as described previously. The fluorescence trigger threshold can be set higher to select loading of sites with higher coupling strengths, though with a lower experimental duty cycle. In addition, we also observe atoms with very short and long lifetimes, and events with more than one atom loaded at different sites. The fluorescence signal allows us to post-select cases with a clear single atom trace, and will be discussed further in Section 4.2.2.

Figure 4.5 shows the “dark lifetime” (lifetime without laser cooling) of the trapped atoms. After the fluorescence trigger, the MOT cooling beams are switched off for a duration of  $\tau$ , and the atom does not emit fluorescence signal. Then, the MOT cooling beams are switched back on to check whether the atom is still trapped. The survival probability fits an exponential curve with a decay time of around 230(30) ms.

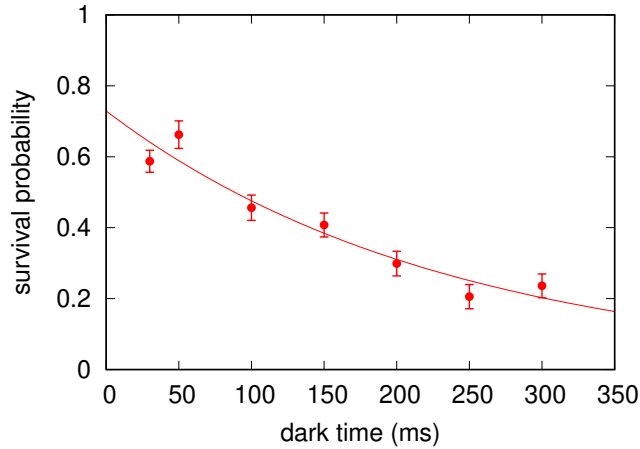


Figure 4.5: Trapped atom lifetime with MOT cooling beams switched off. The survival probabilities of atoms in the FORT fit an exponential curve with a time constant of 230(30) ms and a y-intercept of 0.73(5). Error bars are estimates from Binomial statistics.

This dark lifetime is mainly limited by the intensity noise of the FORT [252] due to the cavity noise, while the upper bound is determined the background pressure of the vacuum system [242].

## 4.2 Probing Atom-Cavity Response

With a single atom trapped inside the near-concentric cavity mode, we probe the response of the atom-cavity system through the transmission and reflection spectra of the cavity. This allows us to determine the atom-cavity coupling strength and cooperativity. The cavity transmission spectrum, probed by a weak coherent beam [18], is given by

$$T_{ac}(\omega) = \left| \frac{\kappa_m(i\Delta_a + \gamma)}{(i\Delta_c + \kappa)(i\Delta_a + \gamma) + g^2} \right|^2, \quad (4.3)$$

with the laser detuning of  $\Delta_{c(a)} = \omega - \omega_{c(a)}$  with respect to the cavity (atom) resonance. This expression assumes that both mirrors have the same transmission  $\kappa_{m1} = \kappa_{m2} = \kappa_m/2$ , and the total cavity decay rate  $\kappa = \kappa_m + \kappa_l$  also includes mirror losses  $\kappa_l$ , as described previously in Section 3.4.2. On the other hand, the reflection

spectrum is given by

$$R_{ac}(\omega) = \left| 1 - \frac{\kappa_m(i\Delta_a + \gamma)}{(i\Delta_c + \kappa)(i\Delta_a + \gamma) + g^2} \right|^2. \quad (4.4)$$

In experiments with imperfect mode matching, the equations above have to be modified to capture the spatial mode-matching efficiency  $\eta$ ,  $T_{ac}^{exp}(\omega) = \eta T_{ac}(\omega)$  and  $R_{ac}^{exp}(\omega) = (1 - \eta) + \eta R_{ac}(\omega)$ . These equations reproduce the “empty” cavity transmission and reflection spectra ( Equation 3.1 and Equation 3.1) in absence of an atom-cavity coupling, by setting  $g = 0$ .

### 4.2.1 Experimental setup

Figure 4.6 shows the experimental setup to probe the atom-cavity response. A weak coherent 780 nm probe is generated by attenuating a frequency-tunable laser beam with neutral density filters (NExA-B, Thorlabs), so that the intra-cavity photon number is much less than one. This is to ensure that the atom-cavity system is not saturated during the weak probing experiment. The frequency tunability of the probe is achieved by varying the EOM modulation frequency with its sideband locked to an atomic transition (see Section 3.1.3). In addition, there is light from an alignment laser on the same fibre-coupled path of the probe beam, which can be utilised as needed, but is blocked during the experimental sequences. The purpose of the alignment laser is to ensure that the weak probe beam couples well to the cavity mode and to the single-mode fibres afterwards.

The linearly-polarised probe beam is combined with a linearly-polarised FORT beam with a dichoric mirror before entering the cavity. The FORT cavity mode is used to both trap single atoms (see Section 4.1.2), and to stabilise the cavity length and transverse misalignment (see Section 3.3). The cavity transmission and reflection of the probe beam are coupled to single-mode fibres and detected with single-photon detectors SPD<sub>1</sub> and SPD<sub>2</sub>.

**Experimental sequence** The experimental sequence is shown in Figure 4.7. After each successful atom-loading event, indicated by a fluorescence trigger, we switch off the quadrupole magnetic field to prevent further atom loading events. Then, the MOT cooling beams and the probe beam are pulsed alternately, each with a time window of 1 ms. The sequence repeats for a total duration of 200 ms. The purpose

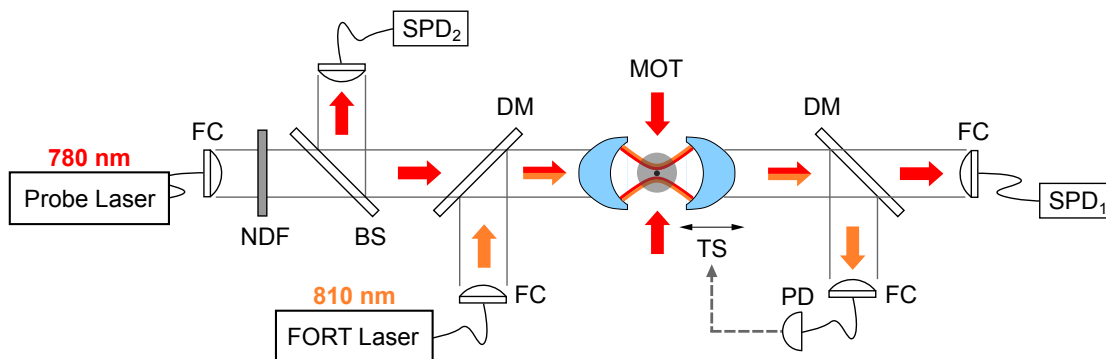


Figure 4.6: Schematic of the setup to probe the atom-cavity response. A weak probe beam, attenuated with a neutral density filter (NDF), and the FORT beam, are coupled to the same fundamental mode of the near-concentric cavity with a dichroic mirror (DM). The cavity transmission and reflection of the weak probe beam are measured with the single photon detectors ( $\text{SPD}_1$  and  $\text{SPD}_2$ ).

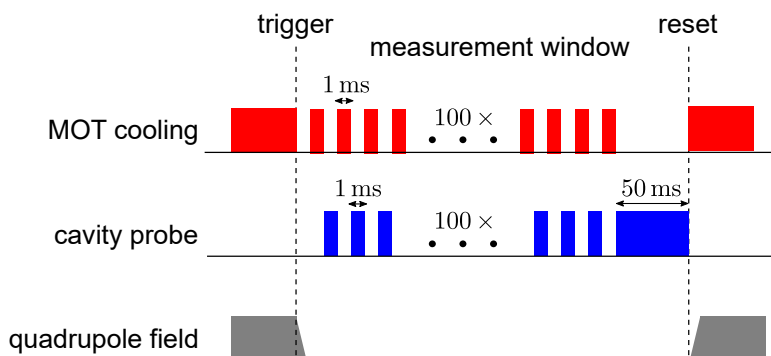


Figure 4.7: Experimental sequence of the cavity probe experiment. The measurement window consists of 200-ms long alternating periods of atomic fluorescence and cavity probe measurements, and 50-ms long “empty” cavity probe. The MOT repump and FORT laser beams are continuously switched on.

of this repeating pattern is to probe the atom-cavity system while ensuring that a single atom is still trapped – with this pattern, we can determine whether a loading event consists of exactly one atom, and when the atom escapes from the trap.

Figure 4.8 shows a sample trace of the atomic fluorescence and cavity probe transmission, obtained by counting the number of photons detected by  $D_1$  in each respective 1 ms time bin. The trace clearly indicates a discrete jump in the fluorescence and transmission level at around 100 ms, as the single atom escapes from

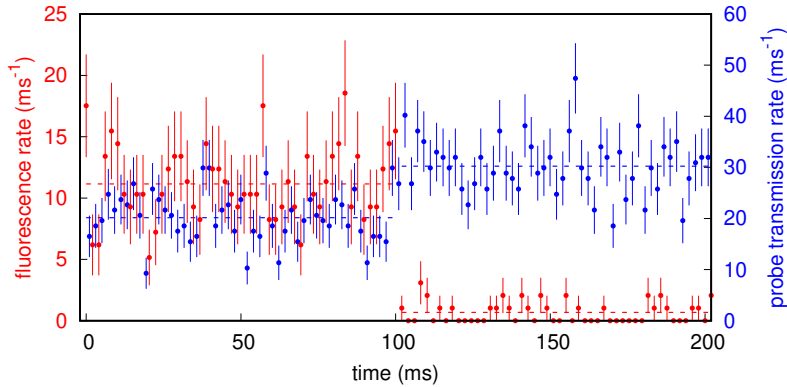


Figure 4.8: A sample trace of the alternating fluorescence and transmission signal. The MOT cooling beams and cavity probe are switched on and off alternately every 1 ms for a total of 200 ms, which provide the atomic fluorescence (red) and cavity probe transmission (blue) signals, as measured by the single photon detector. At around 100 ms, the atom escapes, indicated by the sudden drop in the fluorescence rate, while the probe transmission changes at the same moment.

the trap. To ensure that the atom-cavity coupling is observed with a single atom, we impose a post-selection criteria based on the fluorescence trace (see Section 4.2.2). On the same sequence, the cavity probe reflection is also recorded using the time-binned photon numbers on detector  $D_2$ .

After the measurement of the alternating fluorescence and cavity probe traces, the probe beam is switched on for another 50 ms to measure the transmission and reflection of an “empty” cavity as a reference. The experimental sequence is completed at this point, and the pattern reverts back and waits for the next loading event to trigger.

**Setting a critical distance** In this experiment, we set the cavity critical distance to be around 5 half-wavelengths away from the critical point. This is mainly limited by the cavity linewidth of around 100 MHz, as it becomes hard to distinguish higher-order transverse modes from the fundamental mode. At this distance, the transverse mode spacing is measured to be  $\Delta v_{tr} = 109(2)$  MHz, which corresponds to a critical distance of  $d = 1.7(1)$   $\mu\text{m}$ .

### 4.2.2 Single atom post-selection criteria

A successful loading event does not guarantee that only a single atom is trapped, as shown in Figure 4.4 (left). However, as the atoms load into the traps probabilistically and at random times, we can classify loading events by analysing the statistics of the fluorescence time trace. We post-select only on events classified as single atom, to obtain the cavity spectra and determine the atom-cavity coupling.

To determine the type of an atomic loading event, we fit the fluorescence trace  $F(t)$  to a single-atom escape model described by a Gauss error function,

$$F(t) = A - C \operatorname{erf}\left(\frac{t - t_{esc}}{\tau}\right), \quad (4.5)$$

with an initial high fluorescence level of  $h = A + C$ , a background fluorescence level of  $b = A - C$ , and the atom escape time and duration of  $t_{esc}$  and  $\tau$ , respectively. While in reality the atom escapes almost instantaneously, the variable  $\tau$  captures the artefact of such instantaneous escape within a time bin, where the fluorescence level of the escape bin has a value between  $h$  and  $b$ . We limit the parameter  $\tau$  to be less than 2 ms, which is the spacing between respective fluorescence time bins.

The objective of the fitting is to minimise the value of the reduced chi-square, defined as

$$\chi_\nu^2 = \frac{1}{\nu} \sum_i \frac{(F(t_i) - D_i)^2}{F(t_i)}, \quad (4.6)$$

where  $\nu = 100 - 4 = 96$  is the degree of freedom for 100 data points and 4 fitted parameters,  $D_i$  are the data points from the fluorescence trace, and we assume that the fluorescence levels have a Poissonian distribution, with variances of  $\sigma_i^2 = F(t_i)$ .

We use an upper-tail critical value of  $\chi_\nu^2 = 1.25$  ( $\alpha = 0.025$ ) to post-select the single-atom cases apart from the multi-atom or inconclusive cases. With this definition, around 97.5% of traces described by the single-atom escape model have  $\chi_\nu^2 \leq 1.25$ , whereas  $\chi_\nu^2 > 1.25$  typically indicates non single-atom traces. The type I error, where single-atom traces are classified as non single-atom traces, is around 5%. However, the type II error, where non single-atom traces are classified as single atom traces, is hard to quantify, but we expect it to be relatively low with the following consideration. Multiple atom traces with  $\chi_\nu^2 \leq 1.25$  are most likely contributed by a collection from one strongly coupled atom with one or a few weakly coupled atoms, with escape timings that are spaced close apart. In a cavity system with a strongly

## CHAPTER 4. OBSERVATION OF ATOM-CAVITY INTERACTION

coupled atom, other atoms weakly coupled to the cavity would only have limited impact on the operation of the atom-cavity system.

Based on the reduced chi-square of  $\chi_\nu^2$ , and the fitted parameters of  $t_{esc}$ ,  $h$ , and  $b$ , we classify each atomic loading event into 5 different types, as follows.

- Non single-atom traces ( $\sim 29\%$  of the traces). The criteria is  $\chi_\nu^2 > 1.25$ , which indicates that the traces are most likely not single atom traces. These traces are typically due to multiple atoms, or a single atom hopping between different sites or having erratic dynamics with the fluorescence and probe beams.
- Single atom traces ( $\sim 44\%$  of the traces). The criteria is  $\chi_\nu^2 \leq 1.25$  with an escape time of  $t_1 < t_{esc} < t_2$ , and fluorescence levels of  $h > h_{th}$  and  $b < b_{th}$ . A monitoring window of atom escape between  $t_1 = 10$  ms and  $t_2 = 190$  ms is selected to allow for enough statistics (at least 5 time bins) to estimate the value of  $h$  and  $b$ . Furthermore, the high or atom-loaded fluorescence level  $h$  has to be higher than a set threshold of  $h_{th} = 8$  ms<sup>-1</sup> and the background or “empty” fluorescence level has to be lower than a set threshold of  $b_{th} = 3$  ms<sup>-1</sup>. This is to ensure that the single atom has a discrete and verifiable jump.
- Short atom traces ( $\sim 23\%$  of the traces). The criteria is  $\chi_\nu^2 \leq 1.25$  with either an escape time of  $t_{esc} < t_1$  or a high fluorescence levels of  $h < h_{th}$ . These traces indicate that the atom escapes very fast, with less than  $t_1 = 10$  ms of trap lifetime. The proportion of short atoms agrees with the no-waiting-time triggering success probability of 73(5)% as indicated in Figure 4.5.
- Long atom traces ( $\sim 3\%$  of the traces). The criteria is  $\chi_\nu^2 \leq 1.25$  with either an escape time of  $t_{esc} > t_2$  or a background fluorescence levels of  $b > b_{th}$ . These traces indicate that the atom stays in the trap for a very long time, with more than  $t_2 = 190$  ms of trap lifetime. These may well be single atoms, but one can not rule out the possibility of them being multiple atom traces.
- Inconclusive traces ( $\lesssim 1\%$  of the traces). The criteria is  $\chi_\nu^2 \leq 1.25$ , but are not classified as either single, short, or long atom traces.

The requirement to perform a post-selection procedure on single atom traces is necessary, as we are characterising the atom-cavity coupling based of a trapped single

atom with a relatively short lifetime, typically less than 200 ms with the probe beam on. Furthermore, the on-resonance transmission “extinction” is pretty small (around 25%) due to a low atom-cavity cooperativity (see the next section), which precludes atom-triggering based on the probe transmission. In an atom-cavity system with a longer trap lifetime and high atom-cavity cooperativity, such post-selection might no longer be necessary, or can be built into the triggering mechanism, due to a higher time-accumulative signal-to-noise ratio for each atom loading event.

### 4.2.3 Transmission and reflection spectra

The measured cavity transmission and reflection spectra, without and with a trapped single atom, is shown in Figure 4.9. Each probe detuning frequency has around 250 single atom events. The empty cavity spectra fit to Lorentzian profiles, while the cavity spectra with a trapped single atom fit to Equation 4.3 and Equation 4.4 in good agreement as well.

From the fitting of the “empty” cavity transmission and reflection spectrum, we determine cavity linewidths of  $2\kappa = 2\pi \times 99(1)$  MHz and  $2\kappa = 2\pi \times 95(3)$  MHz, respectively. The cavity transmission and reflection at resonance, normalised to the input power, is measured to be  $T(\omega_c) = 4.6(2)\%$  and  $R(\omega_c) = 58.3(5)\%$ . In determining  $T(\omega_c)$ , we take into account various optical losses and the coupling efficiency of 29(2)% from the cavity output to the single-mode fiber. From these fitted values, with a conservative estimate of the cavity linewidth of 99(1) MHz, we determine the cavity finesse of  $\mathcal{F} = 138(2)$  and the cavity decay rates of  $\kappa_m = 2\pi \times 9.8(5)$  MHz and  $\kappa_l = 2\pi \times 40(2)$  MHz, using Equation 3.4 and 3.5. The cavity decay rate due to mirror transmission  $\kappa_m$  agrees with the design value of  $2\pi \times 10.9$  MHz. However, the cavity decay rate due to mirror scattering losses  $\kappa_l$  is much higher, and contributes to a drop in finesse from  $\mathcal{F} = 627$  to  $\mathcal{F} = 138(2)$ . We attribute the source of the mirror scattering losses to the deposition and adsorption of rubidium atoms and other volatile materials on the mirror surfaces (see Section 3.2).

From the fitting of the cavity transmission spectrum with a trapped single atom, we determine the atom-cavity coupling strength of  $g = 2\pi \times 5.0(2)$  MHz with a small frequency offset of  $\omega_{ca} = \omega_c - \omega_a = 2\pi \times 3.4(3)$  MHz between the atom and cavity resonance. Similar values are also obtained by fitting the cavity reflection

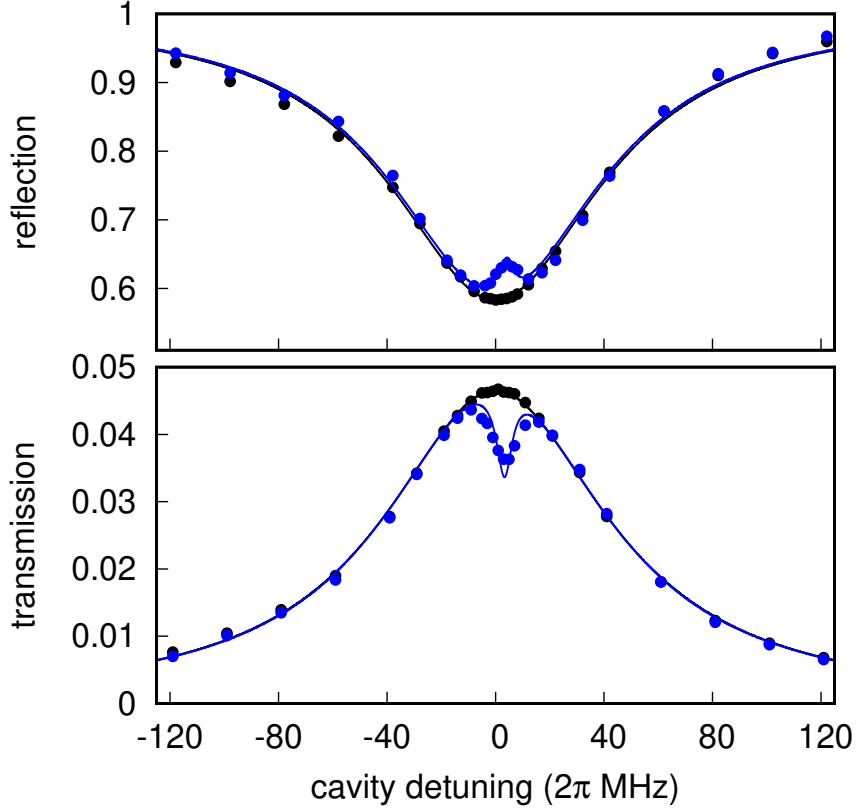


Figure 4.9: Cavity reflection (top) and transmission (bottom) spectra with a trapped single atom (blue trace). The spectra reveal an onset of the normal-mode splitting, and indicate that the single atom is coupled to the near-concentric cavity. The cavity spectra without a trapped single atom, i.e. “empty” cavity, is provided as a reference (black trace).

spectra, with the atom-cavity coupling strength of  $g = 2\pi \times 4.6(4)$  MHz and the frequency offset of  $\omega_{ca} = 2\pi \times 4.4(7)$  MHz.

**Atom-cavity coupling and cooperativity** The atom-cavity coupling strength  $g = 2\pi \times 5.0(2)$  MHz measured from the transmission spectrum is lower than the theoretical coupling strength of  $g_{ideal} = 2\pi \times 12$  MHz, calculated using Equation A.13 and A.19, at a critical distance of  $d = 1.7 \mu\text{m}$ . This is of course expected, as the atom is prepared in a random spin polarisation, and probed with a linearly polarised light. The expected maximum coupling strength is thus  $g_{max} = g_{ideal}/\sqrt{2} = 2\pi \times 8.5$  MHz, after averaging over the Clebsch-Gordan coefficients. Furthermore, the atoms are loaded at different trapping sites not coinciding with the standing-wave cavity modes,

which may explain how the measured value is around 40% lower than expected in a randomly polarised system.

The atom-cavity coupling strength  $g$  exceeds the atomic dipole decay rate of  $\gamma = 2\pi \times 3.03$  MHz by a factor of  $g/\gamma = 1.7(1)$ . Though, with a relatively large cavity linewidth of  $2\kappa = 2\pi \times 99(1)$  MHz, the corresponding atom-cavity cooperativity is calculated to be  $C = g^2/2\kappa\gamma = 0.084(4)$ . We expect this value to increase in newer designs with lower cavity linewidths – at least by a factor of 3 in cavity design version 2b (see Section 2.2.2) with a linewidth of  $2\kappa = 2\pi \times 28.2(6)$  MHz. In addition, lower-linewidth cavities also allow for smaller critical distances, as the higher order transverse modes are still well-resolved even at the last stable resonance. The atom-cavity coupling strength can increase by about 50% as a result. Another factor of 2 increase in the cooperativity can be achieved by targeting the  $^{87}\text{Rb}$  atom cycling transition of  $|F = 2, m_F = \pm 2\rangle$  and  $|F' = 3, m'_F = \pm 3\rangle$  in the  $D_2$  line with a circularly polarised probe. By implementing these enhancements, the atom-cavity cooperativity can reach  $C > 1$  with our current system, though it will be limited to around  $C \lesssim 5$  (see Section 2.1.2).

#### 4.2.4 Summary and Outlook

We demonstrate that near-concentric cavities provide atom-cavity coupling strength of  $g = 2\pi \times 5.0(2)$  MHz which exceeds the atomic decay rate of  $\gamma = 2\pi \times 3.0$  MHz, at the critical distance of  $1.7(1)$   $\mu\text{m}$ . This coupling strength is comparable to some of the state-of-the-art small cavities [18], due to the tight focusing geometry. However, the measured cooperativity  $C = 0.084(4)$  is lower than the design value due to a reduced mirror finesse of  $\mathcal{F} = 138(2)$ , corresponding to a cavity decay rate of  $\kappa = 2\pi \times 49(1)$  MHz (cavity design version 1a). The performance is expected to improve in the newer versions.

In future experiments (see Section 8.2.2), using a cavity with a higher finesse of  $\mathcal{F} = 5000$  and a corresponding linewidth of  $2\kappa = 2\pi \times 2.7$  MHz would put the system straight in a strong coupling regime, even at the current critical distance and operating conditions, with  $g/\gamma \approx 1.7$  and  $g/\kappa \approx 3.7$ .

## Chapter 5

# Coupling to Near-Concentric Transverse Modes

Transverse modes of paraxial beams are a set of unique field patterns perpendicular to the propagation of electromagnetic waves. They have a wide range of applications, such as increasing the information-carrying capacity in free-space [253] and fibre [254, 255] communications, creating smaller focal volumes to achieve superresolution imaging [256], utilizing orbital angular momentum (OAM) for quantum key distribution [257], and producing highly-entangled states [258]. In optical cavities, transverse modes have been used to track atomic position via the observed mode pattern [259–261], and to help enhancing the cooling process in atomic ensembles [130, 132, 262]. Optical cavities with near-degenerate transverse modes have also been used to engineer inter-mode coupling [263, 264], and to study crystallization domains in Bose-Einstein condensates (BEC) [140, 141, 265, 266]. Furthermore, transverse modes can be chosen as a degree of freedom for field quantization, along with wavelength and polarization, and can be utilized to explore atom-photon interaction as building blocks of a quantum network.

The near-degeneracy of transverse modes in an optical cavity arises in the region where the Gouy phase shifts of the cavity modes are fractions of  $\pi$ , notably in the confocal and concentric region [208, 267]. Cavity modes in the near-confocal region have relatively large mode volume, which is suitable to explore multi-mode interaction in large atomic ensemble such as BEC [266, 267]. On the other hand, cavity modes in the near-concentric region have small mode volumes with a beam waist on the order of the atomic cross section, and thus show potential for strong interaction between light and single atoms [72, 78, 90] (and see Chapter 4). The

spatial resolution of the transverse modes can also be utilized to trap and couple selectively to small ensemble of single atoms. In centimetre-sized near-concentric cavities, the frequency spacing of the transverse modes ranges between  $\sim 0.01$  to 1 GHz – the lower limit is set by the last stable resonance from the critical point, which is less than half a wavelength away (see Chapter 7). Unlike planar cavities, the frequency spacing is on the order of the hyperfine or the Zeeman level splitting of the atoms. This allows to explore single-quanta atomic nonlinearities with multiple optical modes coupled to different hyperfine or magnetic energy levels simultaneously, which has been previously demonstrated with two atomic transitions with  $\sim 10$  THz spacing using planar cavities [268].

The transverse modes of a cavity can be excited by modifying the wavefront of the incoming Gaussian beam in a  $\text{TE}_{00}$  mode to match the transverse spatial profile of the modes. In this chapter, we use a liquid-crystal spatial light modulator (SLM) to perform mode conversion by modulating the spatial phase profile. This enables coupling of a SLM-converted beam to a specific mode or a superposition of transverse modes in a near-concentric cavity. Previously, such phase SLM have been utilized to excite the transverse modes of multimode fibres [269], while excitation of cavity transverse modes in a near-confocal regime has been implemented with a digital micromirror device (DMD) – a type of binary-mask amplitude SLM [267]. Compared with amplitude SLMs, phase SLMs can ideally perform mode conversion and coupling with higher overall efficiency as it does not require parts of the beam to be attenuated or diverted away. While the near-concentric cavities exhibit some technical complexities specific to the highly diverging modes in approaching the critical point, an efficient mode conversion enables interfacing of atomic qubits with multiple near-degenerate photonic modes. This work has been published in [81].

## 5.1 Mode Preparation with a Spatial Light Modulator

The transverse modes of the near-concentric cavity are well described by the paraxial approximation up to the last stable resonance, and consist of Laguerre-Gaussian (LG) beams that forms standing-wave cavity modes in a cylindrically symmetric system (see Appendix A for a detailed description of the modes). In

this section, we describe a method to prepare the LG modes using an SLM, and to quantify the mode-matching to the transverse modes of the near-concentric cavity.

The LG cavity modes are distinguished by their radial and azimuthal mode indices,  $p$  and  $l$ , and denoted by  $\text{LG}_{p,l}$ . The resonance frequencies of the LG modes depend on the mode indices  $p$  and  $l$ , as described by Equation A.3. In the near-concentric cavity, the detuning of a neighbouring  $\text{LG}_{p,l}$  mode with respect to the fundamental Gaussian  $\text{LG}_{0,0}$  mode is given by

$$\Delta v_{p,l} = -(2p + l)\Delta v_{tr} , \quad (5.1)$$

where  $\Delta v_{tr}$  is the transverse mode spacing defined in Equation 3.7, with a negative sign to indicate that the higher-order neighbouring transverse modes have lower resonance frequencies than the fundamental mode.

Out of the LG modes, radial transverse modes (LG modes with  $l = 0$ ) are particularly interesting to us, as they have identical effective mode volumes  $V_m$  at a particular critical distance  $d$  (see Appendix A for a more detailed calculation). This allows coupling between an atom and cavity modes with equal strengths across all radial transverse modes – even though higher order radial modes appear to be “larger”, their intensity cross-section areas remain the same. On the other hand, LG modes with  $l \neq 0$  have zero electric field amplitude at their mode centre, and require the atom to be either slightly displaced from, or distributed around, the cavity axis.

### 5.1.1 Beam Shaping with a Spatial Light Modulator

To prepare LG beams and couple to the transverse modes of the near-concentric cavity, we use a liquid-crystal phase SLM to perform mode conversion from a collimated single mode fibre output (approximating a Gaussian beam). Such a transformation can be performed with a spatial filter which modulates both the amplitude and the phase of the incoming mode, and described by a generalized filter function  $T(\mathbf{x}) = M(\mathbf{x}) \exp(i\Phi(\mathbf{x}))$ . However, a liquid-crystal phase SLM only modulates the phase of the incoming beam and hence only provides the transformation  $T(\mathbf{x}) = \exp(i\Phi(\mathbf{x}))$ .

There are several methods to perform both amplitude and phase modulation using only a phase SLM. In one method, the SLM can be operated in a phase-grating configuration – this produces both the carrier and first-order diffraction beams, where

phase and amplitude can be varied using the modulation angle and the modulation depth, respectively [270, 271]. This method typically requires a high-resolution SLM to encode the phase and amplitude information sufficiently precise with the phase grating. However, recent works explored encoding techniques with different sets of amplitude modulation bases which allow the usage of a low-resolution phase SLM [272–275]. Another method relies on using two SLMs with a polarizer to modulate the amplitude and phase of the incoming beam independently [276–278].

Here, we use a much simpler technique that does not require parts of the beam to be diverted away or attenuated, because LG modes with relatively high purity can be created by spatially modulating the incoming Gaussian beam with only the phase component of the desired LG modes [279–281]. The cavity then acts as a filter to attenuate the remaining off-resonant LG mode components, while transmitting the desired LG mode. The SLM phase function for this transformation is given by

$$\Phi(\rho, \phi) = \arg [U_{p,l}(\rho, \phi, 0)] = \arg \left[ \mathcal{L}_p^l \left( \frac{2\rho^2}{w^2} \right) \right] - l\phi, \quad (5.2)$$

with the mode function  $U_{p,l}(\rho, \phi, 0)$  given by Equation A.1.

The mode overlap is defined as  $\int (d\sigma) U_1^*(\rho, \phi) U_2(\rho, \phi)$ , evaluated over the cross section at position  $z = 0$ , where  $U_1(\rho, \phi) = A_0 \exp(-\rho^2/w_0^2) \exp[i\Phi(\rho, \phi)]$  is the SLM-modulated output of the incoming Gaussian mode, and  $U_2(\rho, \phi)$  is the targeted LG mode, while the normalization coefficients  $A_0$  and  $A_{p,l}$  are chosen such that the modes are normalized, i.e.  $\int (d\sigma) U_i^*(\rho, \phi) U_i(\rho, \phi) = 1$ . Thus, the modulus square of the mode overlap is equivalent to the mode matching efficiency  $\eta$  as defined in Equation 3.6. The ratio between the targeted LG mode waist and the incoming Gaussian mode waist  $w/w_0$  can also be varied to maximize the mode overlap. For relatively small mode indices  $p$  and  $l$ , the mode matching efficiencies of the same LG modes are relatively high, with low mode matching efficiencies to different LG modes (see Table 5.1). Due to the simplicity of the phase function, this technique can also be implemented using physical phase plates [282, 283].

### 5.1.2 Experimental Setup

Figure 5.1 shows the experimental setup to couple to the LG modes of the near-concentric cavity. Mode conversion from a fibre output to a relevant LG mode is performed with a spatial light modulator, and coupled to the near-concentric

SLM output	$w/w_0$	Mode matching efficiencies					
		LG <sub>00</sub>	LG <sub>10</sub>	LG <sub>20</sub>	LG <sub>30</sub>	LG <sub>40</sub>	LG <sub>50</sub>
LG <sub>10</sub>	0.57	0.1%	<b>81.2%</b>	0.0%	2.4%	1.3%	0.7%
LG <sub>20</sub>	0.45	1.3%	0.1%	<b>76.9%</b>	0.1%	1.6%	4.5%
LG <sub>30</sub>	0.39	0.4%	1.2%	0.5%	<b>74.6%</b>	0.3%	0.9%
LG <sub>40</sub>	0.35	0.2%	0.4%	1.2%	0.8%	<b>73.2%</b>	0.5%

Table 5.1: Calculated values of the mode matching efficiencies  $\eta$  between the SLM output and the radial transverse modes (LG modes with  $l = 0$ ), up to LG<sub>50</sub>. Mode-matching to modes higher than LG<sub>50</sub> are smaller (not shown in table), and the cumulative efficiencies sum up to unity asymptotically. The model does not incorporate pixellation and aperture effects caused by a real SLM.

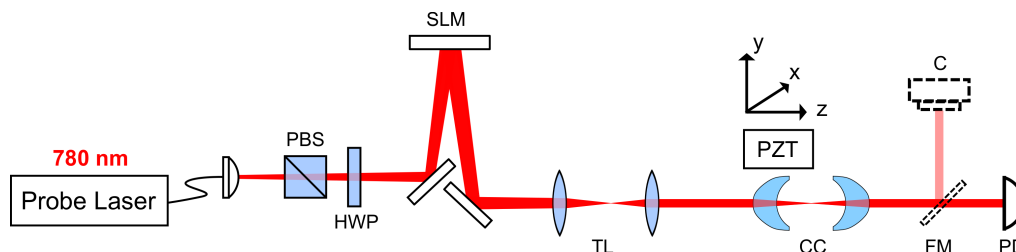


Figure 5.1: Experimental setup for coupling to higher-order transverse modes. A spatial light modulator (SLM) transforms light emerging from a single mode optical fibre to couple to the LG modes of the near concentric cavity (CC). A telescope (TL) facilitates mode matching between the SLM output and the cavity – the cavity requires collimated input modes with beam sizes depending on the transverse mode profiles and critical distances. Cavity transmission is monitored using either a photodetector (PD) or mode camera (C), selected by a flip mirror (FM).

cavity. The performance of a mode conversion and coupling to the cavity transverse mode is characterised by the mode-matching efficiency  $\eta$ .

**Converting the fibre output mode with a SLM** We use a liquid-crystal phase SLM (Meadowlark HV 512 DVI) with an active area of  $12.8 \text{ mm} \times 12.8 \text{ mm}$  and resolution of  $512 \times 512$  pixels. As this SLM only modulates light with a particular linear polarization, a sequence of a polarizing beam-splitter (PBS) and a half-wave plate (HWP) prepares the correct polarization to match the SLM polarization axis. We minimize the pixelation artifact by using a significant portion of the SLM area. To achieve this, we prepare a slightly divergent beam by tuning the focal length of the single-mode fibre-coupler. The beam has a diameter ( $1/e^2$  width) ranging from 3 to 7 mm at the SLM.

## CHAPTER 5. COUPLING TO NEAR-CONCENTRIC TRANSVERSE MODES

The phase modulation applied on the SLM consists of three components: the LG mode-generating phase pattern as described in Equation 5.2, the correction phase pattern provided by the manufacturer, and a quadratic phase pattern which effectively acts as a Fresnel lens with variable focal length. The combination of the Fresnel lens and the telescope with variable focal lengths creates a collimated LG beam with tunable size, which matches the cavity input mode – the appropriate values for the Fresnel lens and telescope parameters are obtained with ray-tracing simulations. In addition, the SLM-generated Fresnel lens also helps in suppressing the unmodulated light on the SLM output (more commonly done with a blazed grating pattern [281]).

The overall diffraction efficiency of the SLM due to the aforementioned phase modulation is measured to be around 60%, similar for different LG mode-generating phase patterns, which can potentially improve with better SLM designs. Thus, the overall fibre-to-cavity coupling efficiency is only limited by the SLM diffraction efficiency, losses due to on-path optical elements, and the measured mode matching efficiencies  $\eta$ . This is much better than using the DMD-based devices which have much higher loss due to the amplitude mask [284, 285]. We did not employ any feedback methods or optimisation algorithms to maximise the coupling efficiency, and the mode patterns are calculated prior to the experiment.

**Obtaining the cavity spectra** After the near-concentric cavity is well aligned, the transmission and reflection spectra are obtained by measuring the light intensity with a photodetector while varying the cavity length linearly over time. The detuning from the cavity resonance is expressed in corresponding units of light frequency – the frequency detuning is calibrated using the spacing of the frequency sideband generated with an electro-optical modulator (see Section 3.4.2).

**Measuring the mode matching efficiencies** The mode matching efficiency  $\eta$ , as defined in Equation 3.6, quantifies how well the input mode couples to the cavity mode. It only depends on the resonant power transmission at resonance  $T(\omega_0)$  and the effective transmission coefficient  $\alpha$  in Equation 3.3. We use cavity version 2a in this experiment (see Section 2.2.2). We characterise the value of  $\alpha$  by coupling a Gaussian beam (from a collimated single mode fibre output mode) into the cavity

without the SLM. From the fitting of the transmission and reflection spectra, we obtain  $T(\omega_0) = 19.5(1)\%$ ,  $R(\omega_0) = 33.6(2)\%$ , and  $\kappa = 2\pi \times 24.8(8)$  MHz, which corresponds to a cavity finesse of  $\mathcal{F} = 275(9)$ . From these parameters, we estimate  $\alpha = 0.294(2)$ , which results in a mode matching efficiency of  $\eta = 94(1)\%$  for Gaussian beam, and cavity decay rates of  $\kappa_m = 2\pi \times 11.3(4)$  MHz and  $\kappa_l = 2\pi \times 13.5(4)$  MHz.

To estimate the mode matching efficiencies for SLM-generated LG modes, we obtain the cavity transmission spectrum  $T(\omega)$  and multiply it with  $(1 + \alpha)^2 / (2\alpha)^2$  (the prefactor in Equation 3.6) to obtain the mode transmission spectrum  $\eta(\omega)$ . We fit this spectrum with a Lorentzian profile, and estimate the mode matching efficiency  $\eta = \eta(\omega_0)$  from the fit amplitude. The parameters from the ray-tracing simulation helps to start the coupling procedure, and we fine-tune these values further to maximize the mode matching efficiency.

## 5.2 Mode Matching to Cavity Transverse Modes

In this section, we present the measurement of the mode matching efficiencies  $\eta$  of a SLM-transformed input mode into various LG modes of the near-concentric cavity. The cavity is located at a critical distance of  $d = 4.8(2)\mu\text{m}$  with stability parameter  $g = -0.99912(4)$ , corresponding to a measured transverse mode spacing of  $\Delta v_{tr} = v_F(1 - \Delta\zeta/\pi) = 182(5)$  MHz between adjacent LG modes.

### 5.2.1 Mode-matching to single LG modes

We use the SLM to generate a single LG mode and couple it to the corresponding LG mode of a near concentric cavity. The cavity spectra and the camera-captured output modes are depicted in Figure 5.2 for LG modes with no angular momentum ( $l = 0$ ), and in Figure 5.3 for LG modes with angular momentum ( $l \neq 0$ ). The measured mode matching efficiencies are close to the simulated values (see Table 5.2), although they decrease with higher mode indices. We attribute this to limited SLM pixel resolution, axial mismatch between the cavity and the anaclastic lens axis due to tip-tilt misalignment, and a mirror surface deviation from a perfect spherical profile. These factors also contribute to some irregularities on the mode transmission spectra and the output modes observed with the camera.

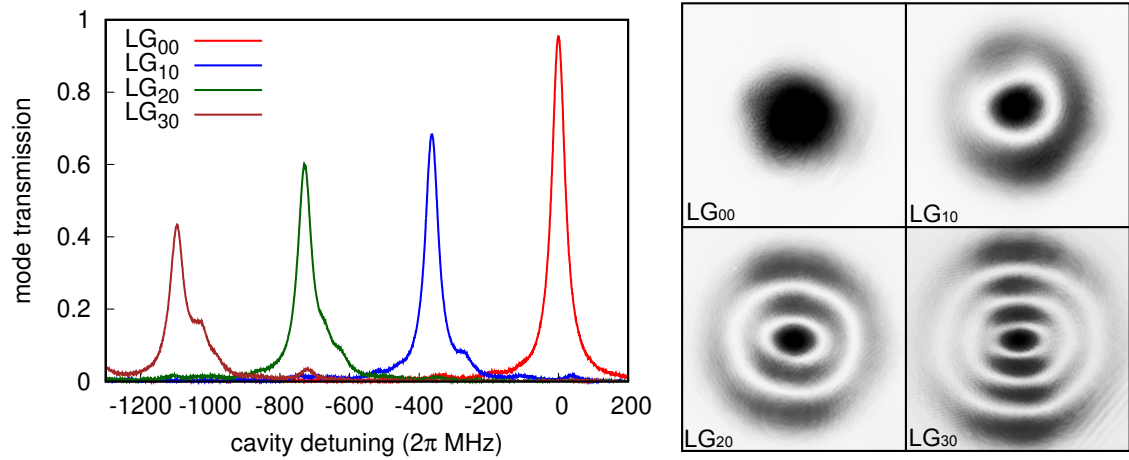


Figure 5.2: Mode-matching spectra for LG modes with  $l = 0$ . (Left) measured cavity transmission for radial transverse modes. The detuning is defined with respect to the LG<sub>00</sub> resonance; higher order the modes are spaced  $2\Delta\nu_{tr}$  apart. (Right) the corresponding cavity output mode observed with the mode camera.

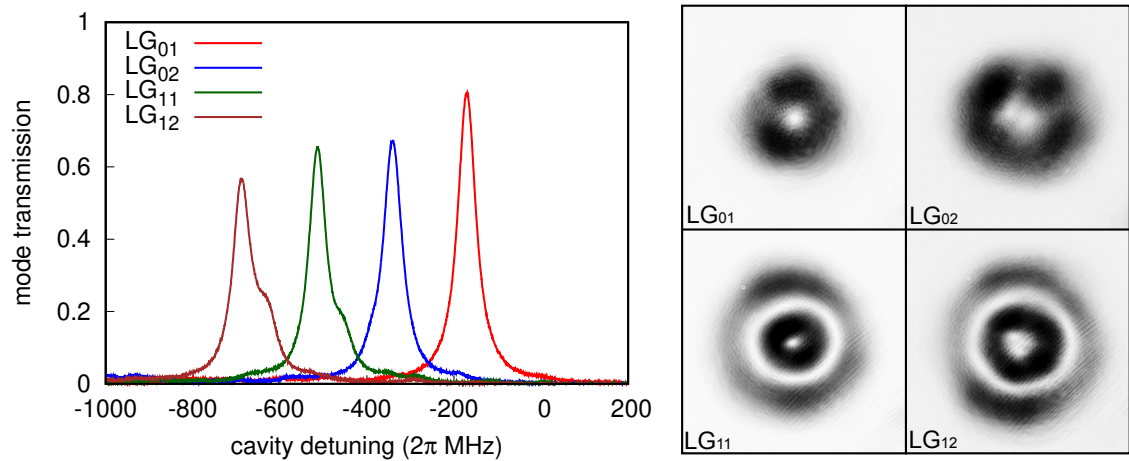


Figure 5.3: Mode-matching spectra for LG modes with  $l \neq 0$ . (Left) measured cavity transmission for LG modes with low angular momentum ( $l = 1$  and  $l = 2$ ). (Right) the corresponding cavity output mode.

### 5.2.2 Mode-matching to a superposition of LG modes

Superpositions of cavity modes provide an interesting avenue to explore multi-photon interaction with atomic medium [42]. Such multi-photon nonlinear interaction with a single atom has been implemented using two longitudinal cavity modes [268]. The transverse modes of a cavity form a separate degree of freedom and can be utilised for such interaction as well.

Mode	Sim.	Exp.	Mode	Sim.	Exp.
LG <sub>00</sub>	100%	96(1)%	LG <sub>01</sub>	93.1%	81(1)%
LG <sub>10</sub>	81.2%	68(1)%	LG <sub>02</sub>	84.4%	67(1)%
LG <sub>20</sub>	76.9%	57(1)%	LG <sub>11</sub>	81.8%	63(1)%
LG <sub>30</sub>	74.7%	38(1)%	LG <sub>12</sub>	79.8%	53(1)%

Table 5.2: Comparison of mode matching efficiencies between simulation and experiment for single LG modes.

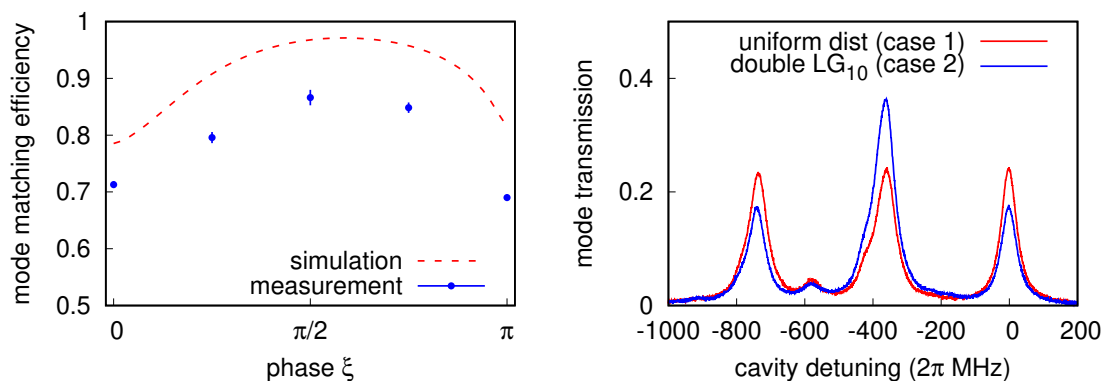


Figure 5.4: Mode-matching to a superposition of LG modes. (Left) Coupling to equal parts of LG<sub>00</sub> and LG<sub>10</sub> while varying their phase difference. (Right) Coupling to a superposition of LG<sub>00</sub>, LG<sub>10</sub> and LG<sub>20</sub>.

We demonstrate the coupling of the SLM-generated beam to an arbitrary superposition of LG modes. We use the method described in Section 5.1.1 by considering the resultant mode as a superposition of individual LG modes,

$$U_{res} = \sum A_{p,l} \exp(i\xi_{p,l}) LG_{pl} , \quad (5.3)$$

where  $A_{p,l}$  is the amplitude of each constituting LG mode and  $\xi_{p,l}$  is the relative phase of the LG mode.

Figure 5.4 (left) shows the mode matching efficiency in coupling the SLM-generated beam to the cavity superposition mode  $U_{\{00,10\}} = (LG_{00} + e^{i\xi} LG_{10}) / \sqrt{2}$  with a varying relative phase angle  $\xi$ . To obtain a balanced distribution of LG<sub>00</sub> and LG<sub>10</sub>, we introduce a mode amplitude  $A_{10}$  to the SLM spatial phase pattern,

$$\Phi = \arg [U_{\{00,10\}}] = \arg \left[ \frac{LG_{00} + A_{10} e^{i\xi} LG_{10}}{\sqrt{1 + A_{10}^2}} \right] , \quad (5.4)$$

and vary the amplitude  $A_{10}$  and  $w/w_0$ , maximising the mode matching efficiency subject to the balanced distribution constraint. The mode matching efficiency  $\eta$

is obtained by adding the mode transmission amplitudes of both the  $LG_{00}$  and  $LG_{10}$  modes, while ensuring that they are balanced within  $\sim 1\%$ . The measured values follow a similar trend with the simulated values, with some offset ( $\sim 10\%$ ) attributable to the SLM pixel size and the mirror irregularities as described previously. The highest mode matching efficiency ( $\eta = 87(1)\%$ ) occurs around  $\xi = \pi/2$ , in which case the  $LG_{00}$  mode is encoded with no phase shift with respect to the SLM output (in the “in-phase” component), while the  $LG_{10}$  mode is encoded with a  $\pi/2$  phase shift with respect to the SLM output (in the “quadrature” component).

Figure 5.4 (right) shows the transmission spectra of a superposition of three modes. Modes  $LG_{00}$ ,  $LG_{10}$ , and  $LG_{20}$  are superposed with a relative phase difference of  $2\pi/3$  to distribute the phases evenly on the complex plane. The corresponding SLM spatial pattern is given by

$$\Phi = \arg [U_{\{00,10,20\}}] = \arg \left[ \frac{LG_{00} + A_{10}e^{i2\pi/3}LG_{10} + A_{20}e^{i4\pi/3}LG_{20}}{\sqrt{1 + A_{10}^2 + A_{20}^2}} \right], \quad (5.5)$$

where  $A_{10}$ ,  $A_{20}$  and  $w/w_0$  are parameters to be varied to obtain the desired mode distribution and the efficiency. Two cases are illustrated in Figure 5.4 (right): (1) equally distributed modes, i.e.  $U_{\{00,10,20\}} = (LG_{00} + e^{i2\pi/3}LG_{10} + e^{i4\pi/3}LG_{20})/\sqrt{3}$ , and (2)  $LG_{10}$  content double the content of the other modes, i.e.  $U_{\{00,10,20\}} = (LG_{00} + \sqrt{2}e^{i2\pi/3}LG_{10} + e^{i4\pi/3}LG_{20})/2$ . The theoretical efficiencies under optimized parameters are 95.6% and 97.2% for case (1) and (2), while the measured efficiencies are 71(1)% and 70(1)%, respectively. We attribute this discrepancy to the imperfections of the SLM and cavity as discussed previously in Section 5.2.1, and in particular when coupling to the superposition component with higher mode indices.

### 5.2.3 Summary and Outlook

We present a mode-matching procedure to excite several transverse modes of a near-concentric cavity with a relatively high conversion efficiency. We use an SLM to engineer the spatial phase of an input Gaussian beam to selectively match a specific LG mode, and observe experimental mode matching efficiencies close to theoretical predictions for several low-order LG modes, despite the imperfections in the cavity alignment and mirror surface, and the limited resolution of the SLM. We

## CHAPTER 5. COUPLING TO NEAR-CONCENTRIC TRANSVERSE MODES

also demonstrate that a superposition of cavity modes can be generated with a high fidelity.

The near-concentric regime of an optical cavity supports transverse modes which are spaced close to one another, on the same order of the magnetic level or hyperfine splitting of the atoms. Exciting the transverse modes in such a regime is a step towards exploring interaction between atoms and strongly focused near-degenerate spatial modes. The nonlinearity arising from multiple photons interacting with single atoms can therefore provide a building block for quantum gates with multiple photonic channels.

## Chapter 6

# Noise Reduction Techniques

The operation of an optical resonator requires a good amount of noise isolation to achieve length stability. In a Fabry-Perot resonator with finesse  $\mathcal{F}$ , the mirror spacing needs to be stabilised to a small fraction of  $\lambda/2\mathcal{F}$ . Large optical resonators such as LIGO, with separate mounting of mirrors, use a combination of stabilisation techniques on stacked pendulum systems [286, 287]. On the other hand, small cavities used in quantum optics experiments are typically operated in a low vibration environment; they are also usually constructed with rigid structures [288–290], mounted in a symmetric configuration [291, 292] with high bandwidth piezos [293, 294], or controlled with additional gain filters [295, 296].

Some cavity systems [80, 297] may require a relatively large movement (more than  $10\ \mu\text{m}$ ) between the two mirrors in three directions. In these systems, mechanical noise sources can couple easily to the cavity system, due to (a) the number of components necessary to actuate three directional movements, which precludes a rigid structure, and (b) the necessity for piezos with large movement range, which can lower the resonance frequency of the system [231]. Large movement ranges with a piezo can be achieved by either using a slip-stick mechanism [298, 299] or a flexure-based mechanical amplification [300, 301]. Stacked translation stages based on slip-stick mechanism have been used to align a microcavity in three directions, with a relatively low mechanical noise [297]. However, it might not be as compact or cost-effective as flexure-based stages which can implement up to three directional movements with a single stage. These flexural stages are sometimes used in scanning probe microscopy (SPM) experiments [231]. However, they have a relatively low resonance frequency (typically less than 1 kHz), and hence

couple easily to acoustic noise. This limits their scanning speed and movement resolution [300, 302], which can be improved with well-designed control systems [295, 303–305], improved vibration isolation system [306, 307], counter balancing [308, 309], mechanical rearrangement [310], symmetrical flexure arrangement [311], or adding a clay damper [312].

We propose two methods to reduce the mechanical noise of the flexural stages in optical resonator systems by (1) implementing active noise cancellation with a digital filter, and (2) placing friction dampers made from thin pieces of aluminium. We quantify the performance of the noise reduction strategies with the noise effect factor, as defined in Equation 2.5,

$$\xi_{noise} = \frac{\delta\omega_c}{2\kappa} = \frac{\delta L}{\lambda/2} \mathcal{F}, \quad (6.1)$$

which quantifies the mechanical noise in the cavity length  $\delta L$ , and affects how much the cavity resonance  $\delta\omega_c$  varies with respect to the cavity linewidth  $2\kappa$ . We propose a target performance figure of  $\xi_{noise} \lesssim 0.2$ , which can be reached with one or a combination of the methods, depending on the finesse  $\mathcal{F}$ . We have also explored a few other noise reduction methods, which work to some extent (see Appendix D).

**Basic ideas of the noise reduction techniques** In the first method, active noise cancellation, we use a digital filter board to modify the phase of the control feedback, which could decrease significantly the mechanical noise in some specific regions. In our setup, most of the noise comes from the first mechanical resonance, and is eliminated with this approach. However, the amount of overall noise reduction is limited by the mechanical resonances at higher frequencies, which may have uncontrollable phase delay.

In the second method, friction damping, we install thin metal strips across the two mirrors, which are supported by gravity and friction forces. In the small movement range, on the order of the mechanical noise, the metal strips restrict the movement between the mirrors, and result in lower cavity noise. In the larger movement range, the metal strips would slip and allow for three-dimensional alignment between the mirrors.

## 6.1 Active Noise Cancellation

In this section, we describe a noise reduction mechanism which employs a digital filter. This method allows us to reduce the mechanical noise in cavity version 2a from  $\delta L \sim 1$  nm ( $\xi_{noise} \sim 0.7$ ) to  $\delta L \sim 0.4$  nm ( $\xi_{noise} \sim 0.3$ ). There have been similar efforts to use digital filters to compensate for acoustic resonances in optical interferometer systems, by using a finite impulse response (FIR) filter [295] and an infinite impulse response (IIR) filter [296]. The implementation of the digital filters allows them to “cancel” the acoustic resonance and obtain a relatively flat actuator response, which results in a higher control bandwidth.

Our near-concentric cavity setup has different operating conditions and design constraints. First, the mechanical noise of our cavity is much higher, on the order of the cavity linewidth, and requires a substantial noise reduction. Second, our cavity is always kept at a constant length and does not require fast control. This is in contrast with the SPM experiments, where the moving stages follow some predefined movement functions, which require a relatively high control bandwidth. Third, our cavity setup displays a lot of mechanical resonances tightly cramped across a relatively large range, with phase delays beyond  $2\pi$ . The resonance frequencies may also vary slightly over time, which complicated the modelling process.

Instead, we implement a digital filter strategy which specifically reduces the noise amplitudes on some of the noisier peaks. As the cavity does not require fast control, the strategy does not attempt to obtain a flat actuator response, so that it can focus exclusively on “cancelling” the noise peaks. The active noise cancellation strategy and its limitations are discussed in the next few sections. To implement the strategy, we use IIR digital filters which run on home-built field-programmable gate array (FPGA) boards.

### 6.1.1 Experimental setup and noise measurement

We implement the active noise cancellation on the cavity setup version 2a. There are two actuators in the setup, the flexural translation stage (ANSxyz100, Attocube) for large movement, and the ring piezo (PZT-4, Boston Piezo-Optics) for fast and small movement. We focus on describing the noise cancellation strategy on the z-axis of the translation stage, on the direction along the cavity axis. The ring piezo is

used thereafter to enhance the noise cancellation in a similar way (see Section 6.1.4).

**Measuring noise spectral density** The mechanical noise of the cavity setup is characterised by first obtaining the cavity error signal with the frequency modulation technique (see Section 3.3.1). We use a control loop with a low integral gain to lock a stabilised laser to the cavity resonance via the error signal. This weak lock keeps the cavity resonant with the laser in the long term, but does not feedback on the cavity on short timescales. As a result, any frequency detuning  $\delta\omega_c$  between the cavity and the laser that arises due to the mechanical noise remains uncorrected, allowing us to measure the mechanical noise  $\delta L$  by monitoring the error signal.

Typically, a stable cavity is operated in the linear region of the error signal, where it is one-to-one (injective), hence one value of frequency detuning  $\delta\omega_c$  corresponds to only one value of the error signal. Consequently, we can simply invert the error signal to find the frequency detuning. In our case, the noise of the cavity is relatively high, and causes the error signal to sometimes go beyond the linear region. Thus, to determine the frequency detuning more accurately, we corroborate the error signal with the cavity transmission signal to estimate the frequency detuning, as each value of the transmission signal gives a unique value of frequency detuning up to a sign ambiguity. This process of error signal “linearisation” results in a time trace of  $\delta L(t)$ , and the mechanical noise spectral density can be obtained by performing a discrete Fourier transform on the time trace. The total mechanical noise can be obtained by integrating the noise power spectral density across the whole frequency range. Alternatively, it is also equivalent to the standard deviation of the time trace.

Figure 6.1 shows a typical mechanical noise spectral density for our cavity setup (version 2a). The total integrated root mean square (RMS) noise is 1.4(2) nm, with most of the noise power ( $\sim 59\%$ ) contributed by Peak A (290–330 Hz). The second and third places are taken by Peak B (600–630 Hz) and C (255–385 Hz), which contribute noise power with a much smaller amount of  $\sim 4.3\%$  and  $\sim 3.8\%$ , respectively. We suspect that Peak B is a harmonic of Peak A, based on their frequencies and peak shapes. It may well be an artefact of the error signal generation and processing, with Peak A being very strong and the error signal exceeding the linear region.

Noise spikes with electrical origins can be identified by their much smaller

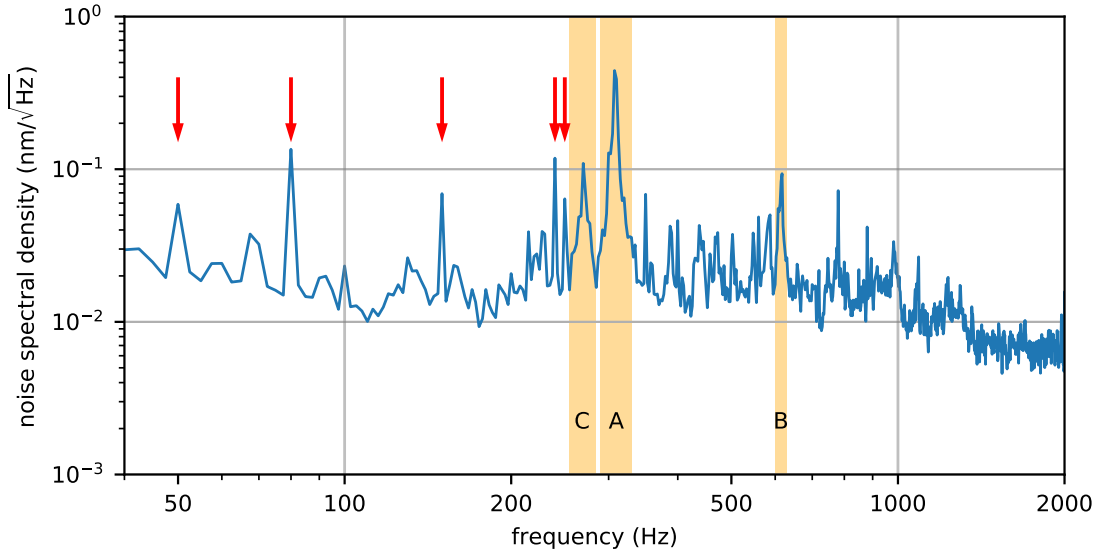


Figure 6.1: A typical mechanical noise spectral density in cavity version 2a (averaged over 5 traces). Most of the noise is contributed by the A, B, and C noise peaks. Noise spikes of electrical origin are indicated by the red arrows.

linewidths, which are Fourier-transform limited in Figure 6.1 (red arrows). With a much longer measurement window, these spikes are identified by having linewidths smaller than 1 Hz. Their frequencies are 50 Hz, 80 Hz and their odd harmonics. The first five noise spikes, as indicated by the red arrows, contribute to only around 2.3% of the total noise.

**Measuring the gain-phase response** The frequency responses in our system are characterised by measuring the gain and phase of an output signal with respect to an input signal, as a function of frequency. In particular, measurement of the gain-phase response of the cavity translation stage, reveals the corresponding acoustical resonances and informs the noise cancellation strategy. The input signal is connected to the actuator voltage input, while the output signal is typically obtained from a linear error signal of the cavity.

However, the stimulus input typically induces vibration beyond the linear regime of the error signal in our cavity setup. Thus, we use a Michelson interferometer setup, with one arm on the actuator-mounted cavity mirror, and the other arm on another mirror fixed to the optical table. The output signal is then obtained via the

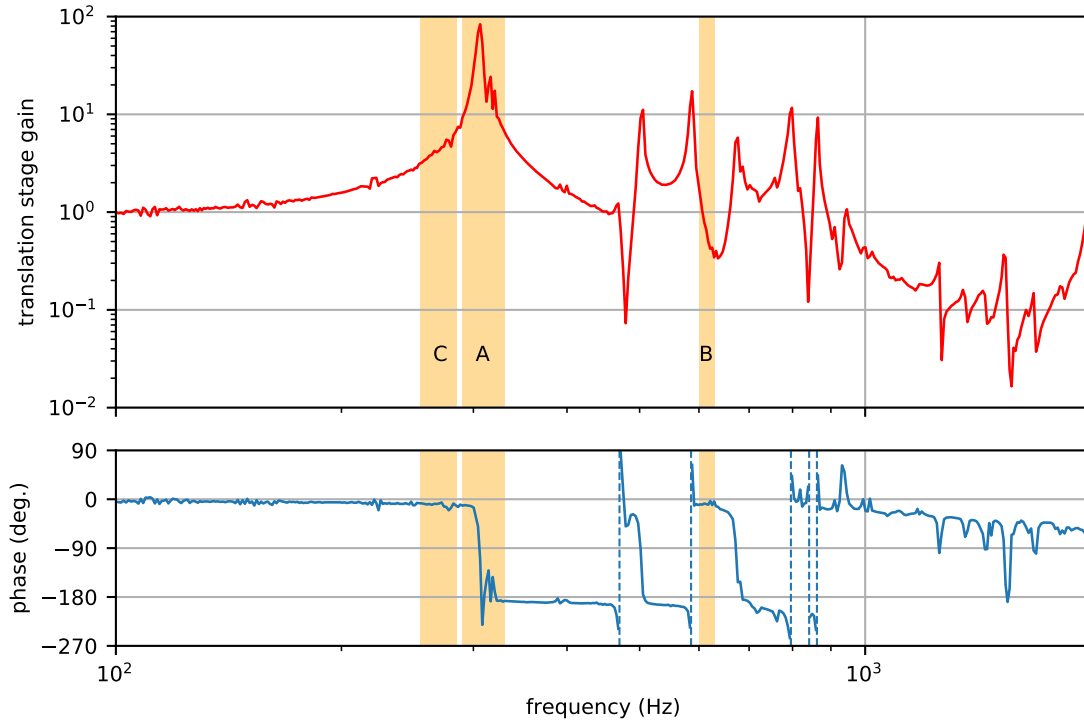


Figure 6.2: The gain-phase response of the cavity translation stage, via a Michelson interferometer setup. The shaded regions correspond to the noise peaks of Figure 6.1. The gain is normalised to one at zero frequency (DC). Dashed vertical lines in the phase plot indicate phases beyond the plot region, with subsequent phases plotted in the modulus  $2\pi$  region.

slope of the interferometric fringes, which relates the cavity mirror movement with the fringe intensity. The gain-phase response of the translation stage is measured with the low frequency gain-phase test ports of a network analyser (E5061B, Agilent). The intermediate frequency bandwidth (IFBW) for each stimulus frequency is set to be 10 Hz, which significantly reduces noise contribution from other frequencies.

Figure 6.2 shows the gain-phase response of the cavity translation stage. Besides the main resonance peak at 310 Hz, the gain-phase profile displays numerous and densely spaced mechanical resonances, with phase delays beyond  $2\pi$ . This indicates that the flexural translation stage, along with the mirror mounting structures, is mechanically pretty complex. We postulate that Peak A, the highest noise peak in Figure 6.1, is contributed by the main resonance at 310 Hz. Meanwhile, Peak C might be contributed by an acoustical resonance of another part of the structure,

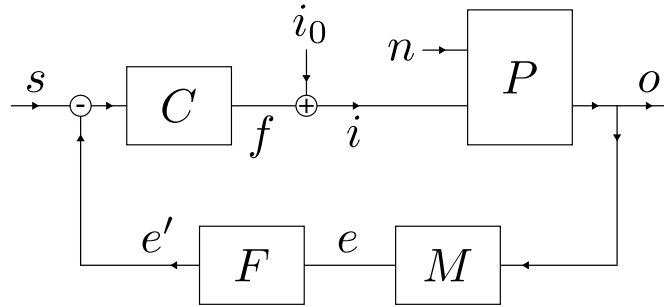


Figure 6.3: A block diagram for cavity translation stage actuation and control.

which does not correspond to the z-axis actuation of the translation stage.

### 6.1.2 Noise cancellation strategy

The noise cancellation strategy that we employ mainly focuses on Peak A (see Figure 6.1), where most of the mechanical noise ( $\sim 59\%$  of the noise power) resides. A digital filter is used to shift the phase of the feedback signal to a region where the noise can be reduced. Along with a large gain from the translation stage resonance, the noise is effectively “cancelled” by the feedback loop. The strategy can be tweaked to also cancel other noise peaks and regions, and later incorporated with a parallel noise cancellation using a separate ring piezo actuator (see Section 6.1.4).

Figure 6.3 shows a simple block diagram of the actuation and control of the cavity translation stage. The response of the translation stage can be modelled with a transfer function  $P$ , that acts on an voltage input  $i$  and mechanical noise  $n$ . The output signal  $o$  represents the cavity resonant length, which is measured with  $M$  to obtain an error signal  $e$ . The digital filter  $F$  shapes this error signal to  $e'$ , in such a way that allows noise cancellation. The proportional-integral (PI) control filter  $C$  acts on the signal  $s - e'$  with set-point  $s = 0$ , and provides a feedback signal  $f$ , which is added with a voltage input offset  $i_0$  to stabilise the cavity length.

For the case of Peak A and other similar peaks, the mechanical noise source is coupled strongly to the translation stage response. With no apparent acoustical vibration source at 310 Hz, the spectral density of the noise  $n$  would be relatively flat, which is later amplified by the translation stage resonance on the output  $o$ . Thus, with no control ( $C = 0$ ), we model the translation stage response with a

simple relation,

$$o = i_0 P + nP . \quad (6.2)$$

On the other hand, for the case of Peak C and other similar peaks, the mechanical noise source is amplified by some other acoustical resonances, and does not correlate with the translation stage response. In the block model, we assume these noise contributions  $m$  to come after the translation stage, as addition to the output signal. The output signal fluctuation due only to mechanical noise can thus be written as

$$o_n = nP + m . \quad (6.3)$$

**The effect of a control loop** With the control loop switched on, the output signal fluctuation is modified to be

$$o'_n = \frac{o_n}{1 + PMFC} \quad (6.4)$$

where  $o_n$  is the initial mechanical noise without any control loop, and  $o'_n$  is the resulting noise after switching on the control. Noise reduction for a particular frequency requires  $|1 + PMFC| > 1$  as a condition. Meanwhile, if  $PMFC = -1$ , the noise explodes and the system becomes inherently unstable.

Figure 6.4 shows the area in the complex plane of  $PMFC$  where the noise gets reduced and amplified. An effective noise reduction strategy rely on shaping the phase of  $PMFC$  to be between  $-\pi/2$  and  $\pi/2$ , as the noise is suppressed by any magnitude of  $|PMFC|$ . In some systems, it is not possible to shape the  $PMFC$  phase inside the  $[-\pi/2, \pi/2]$  range for all frequencies, particularly in systems with phase delays exceeding  $2\pi$ . Hence, there are always some frequency regions where the noise is amplified, and care must be taken to ensure that either  $|PMFC| \ll 1$ , or  $o_n$  is very small, in those regions.

**Noise reduction using PI control** The main components in the noise reduction strategy are the PI control  $C$  and the IIR digital filter  $F$ . We assume that the measurement  $M$  of the cavity length is performed with a constant gain and without any delay. In this part, we consider the case where the IIR digital filter does not modify the error signal, by setting  $F = 1$ .

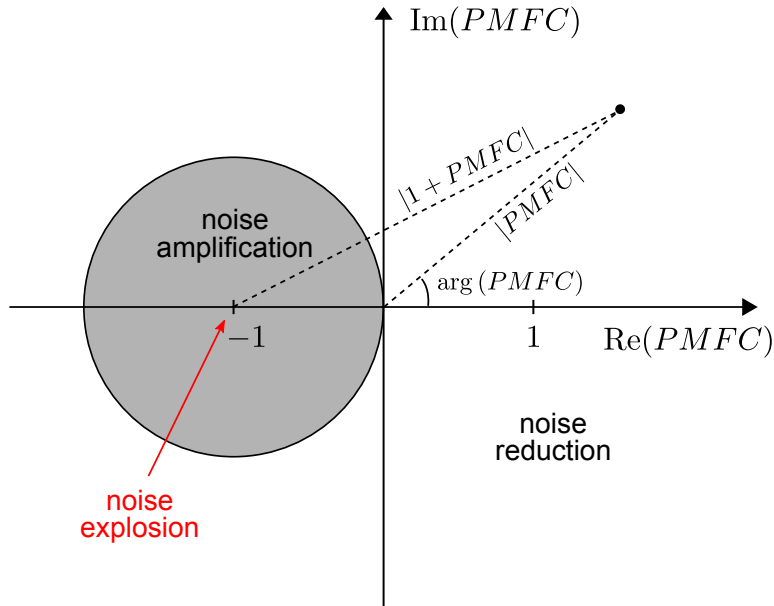


Figure 6.4: The area in  $PMFC$  complex plane suitable for noise reduction. The grey-shaded area indicates the region where the noise is amplified, with the unstable point located at  $PMFC = -1$ . The noise is reduced in the unshaded area.

The PI control can be described with a transfer function [313]

$$C(s) = K_P + \frac{K_I}{s}, \quad (6.5)$$

where  $s = \sigma + i\omega$  is a Laplace frequency parameter, and  $K_P > 0$  and  $K_I > 0$  are the proportional and integral control gain. As we are mostly concerned with the steady-state behaviour of the noise, we remove the transient frequency component, setting  $\sigma = 0$ , and the Laplace frequency parameter is effectively  $s = i\omega$ , with  $\omega = 2\pi f$  as the steady-state frequency.

The PI control has the following characteristics. At low frequencies, the integral term ( $-i K_I/\omega$ ) dominates, with the phase approaching  $-\pi/2$ . This behaviour is very useful for long-term stability. At high frequencies, the proportional term ( $K_P$ ) dominates, with the phase approaching zero. Thus, the PI control has a phase in the  $[-\pi/2, 0]$  range (see Figure 6.5).

From Figure 6.2, the first resonance of the translation stage  $P$ , corresponding to noise Peak A, has a phase of  $-\pi/2$ . Thus, with the PI control, the phase of  $PMFC$  at resonance is lower than  $-\pi/2$ , and the mechanical noise would be amplified near the resonance frequency. To counteract this, the  $PMFC$  phase near the resonance

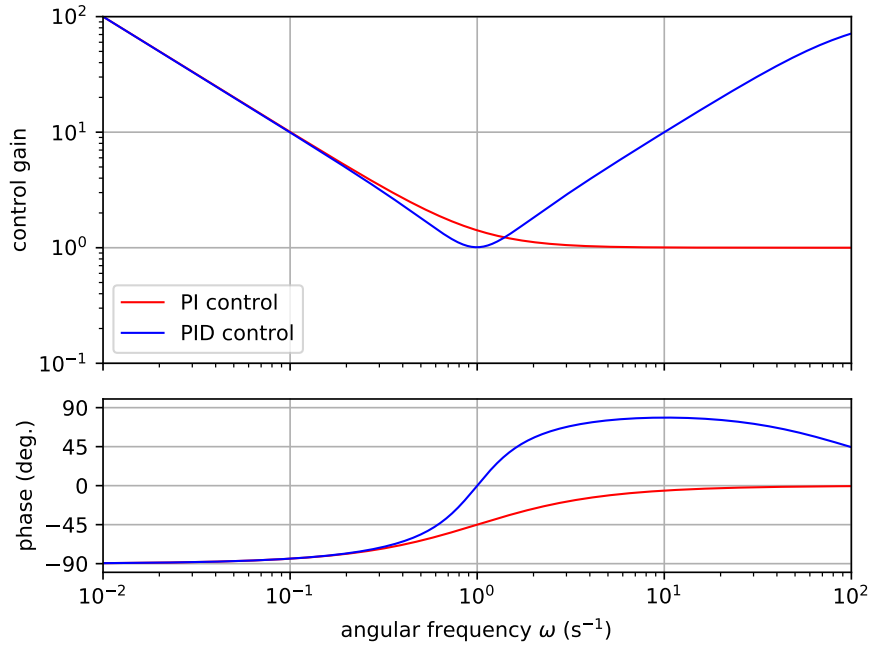


Figure 6.5: A typical gain-phase response of a PI (red) and PID (blue) control, with  $K_P = 1$ ,  $K_I = 1 \text{ s}^{-1}$ ,  $K_D = 1 \text{ s}$ , and  $\omega_c = 100 \text{ s}^{-1}$ .

has to increase beyond  $-\pi/2$ , and implies that the phase of the combined *FC* filter has to be larger than zero – implementing the phase-lead operation.

A common approach is to add a derivative component to the PI control, resulting in a PID control with a transfer function

$$C(s) = K_P + \frac{K_I}{s} + \frac{sK_D}{(1 + s/\omega_c)^n}, \quad (6.6)$$

noting that the action of derivative control is limited up to a cut-off frequency  $\omega_c$  with  $n$  low-pass filters, to prevent high-frequency sensor noise amplification [313]. A typical gain-phase response of a PID control is shown in Figure 6.5. In some high frequency regions, the phase of the PID control is in the  $[0, \pi/2]$  range, and the mechanical noise contributions near the resonance frequency can be reduced. However, such PID control acts on a relatively broad frequency range, and works only for one or a few resonances with phase delays not exceeding  $\pi$ . We choose not to add a derivative component in our PI control, and instead delegating the phase-lead operation to the IIR digital filter.

**IIR digital filter as a toolbox for noise reduction** An IIR digital filter allows us to construct a gain-phase response that follows a simple transfer function  $F(s) = N(s)/D(s)$ , with polynomial numerator  $N(s)$  and denominator  $D(s)$ . The roots of the  $N(s)$  and  $D(s)$  polynomial are known as zeros and poles, respectively. To implement the filter digitally, the transfer function  $F(s)$  is mapped from the continuous-time domain to the discrete-time domain with a Bilinear transform [314]. The input signal is read by an analog-to-digital (ADC) converter, processed digitally within an FPGA, and the digital output is converted back to an analog signal.

In contrast with the FIR filter, which allows the gain-phase response to be shaped arbitrarily, the IIR filter has to follow a time-causality principle, and operates in a similar way as analog filters. Nevertheless, an IIR filter requires much fewer coefficients and operations than a FIR filter, resulting in a lower latency [296].

Our IIR filter consist of 6 cascaded digital biquad filters, each can be used to implement up to a second order polynomial in  $N(s)$  and  $D(s)$ , or up to two zeros and two poles. Implementing a higher-order polynomial is possible with factorisation. The latency of our IIR filter is around 10  $\mu$ s, as we did not use a fast ADC or a FPGA with dedicated multipliers. This sets an operating bandwidth of around 50 kHz for latency-induced phase delay not exceeding  $\pi$ , which is more than sufficient for noise cancellation at  $\lesssim 1$  kHz region.

The IIR filter can provide a phase-lead and a phase-lag in a small frequency region. The transfer function of such filter, in first-order polynomial, can be written as

$$F_{lc}^{(1)}(s) = \frac{s - z}{s - p}, \quad (6.7)$$

with  $z$  and  $p$  as the zero and the pole, which are typically negative real numbers. This filter is commonly known as the first-order lead or lag compensator [315]. To obtain a lead (lag) compensator, the pole has to be more (less) negative than the zero. The derivative component of a PID control described previously is a type of a lead compensator, with  $z = 0$  and  $p = -\omega_c$  (for  $n = 1$ ).

The performance of such lead (lag) compensator is quite limited in terms of the amount of phase lead (lag), up to a maximum value of  $\pi/2$  ( $-\pi/2$ ). The amount of phase shift also trades off with the frequency-range selectivity (see Figure 6.6). This is because the zero and pole are constrained on the real axis. Thus, we usually

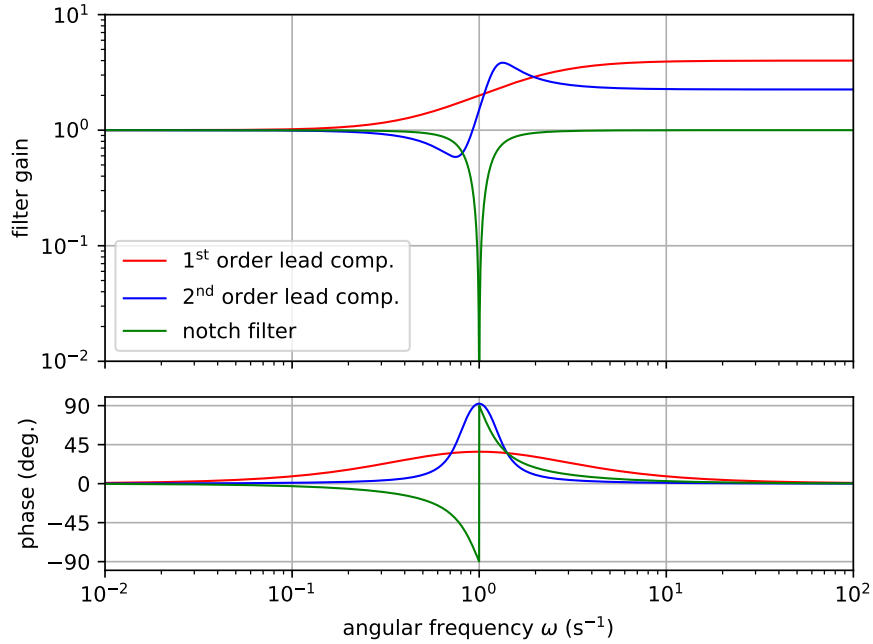


Figure 6.6: A typical gain-phase response of a lead compensator (1<sup>st</sup> order – red; 2<sup>nd</sup> order – blue) and notch filter (green). For the first-order lead compensator,  $z = -0.5 \text{ s}^{-1}$  and  $p = -2 \text{ s}^{-1}$ . For the second-order lead compensator,  $z = (i - 0.2)0.8 \text{ s}^{-1}$  and  $p = (i - 0.2)1.2 \text{ s}^{-1}$ . For the notch filter,  $\omega_n = 1 \text{ s}^{-1}$  and  $Q = 2$ .

implement a second-order lead or lag compensator, with a transfer function given by

$$F_{lc}^{(2)}(s) = \frac{(s - z)(s - \bar{z})}{(s - p)(s - \bar{p})}, \quad (6.8)$$

where  $(z, \bar{z})$  and  $(p, \bar{p})$  are complex conjugate pairs of the zeros and poles, respectively. The requirement of a complex conjugate pair is necessary for a real-valued implementation of the filter. For filter stability, the poles have to be located on the left of the imaginary axis. The second-order lead (lag) compensator provides a phase lead (lag) up to a maximum of  $\pi$  ( $-\pi$ ). Greater frequency-range selectivity can be achieved by increasing the slope of the phase response, by decreasing the real part in the zero and pole complex numbers. A typical gain-phase response of a second-order lead compensator is given in Figure 6.6.

The IIR filter can also be used to implement a notch filter, which is very useful for rejecting signal in a specific frequency range. The transfer function is given by

$$F_{no}(s) = \frac{s^2 + \omega_n^2}{s^2 + s\Delta\omega_n + \omega_n^2}, \quad (6.9)$$

where  $\omega_n$  is the notch frequency, and  $\Delta\omega_n = \omega_n/Q$  is the width of the rejection band, with  $Q$  as the quality factor of the notch filter. A typical gain-phase response of the notch filter is given in Figure 6.6.

**Active noise cancellation procedure** The PI control and the IIR filter work together to reduce noise in specific target regions, by achieving  $|1 + PMFC| > 1$  in those regions, and limiting noise amplification in other regions. We typically set the integral gain  $K_I$  of the PI control pretty low, that it affects minimally the gain-phase response in the noisy region – the  $K_I$  is used mainly for long-term stability, by reducing the noise in the sub-Hz frequency range. The main tuning component of the PI control is the proportional gain  $K_P$ . With an appropriately configured IIR filter, the  $K_P$  is slowly increased to obtain high values of  $|1 + PMFC|$  in the target regions, resulting in noise reduction in those regions.

We describe the step-by-step procedure for active noise cancellation as follows:

1. Identify a target region to implement the noise reduction strategy. Usually we choose the region with the highest noise content, i.e. Peak A in Figure 6.1.
2. Estimate the phase of the actuator in the target region. From Figure 6.2, the actuator phase is around  $-\pi/2$  at resonance and  $[-\pi, 0]$  around the resonance.
3. Identify the amount of phase lead (lag) to implement, and construct an appropriate lead (lag) compensator in the IIR digital filter. For Peak A, it is suitable to set a phase lead of around  $\pi/2$ .
4. Increase the proportional gain  $K_P$  of the PI control, until the noise in the target region is reduced. It is very common to observe noise in other regions being amplified during this process – stop before it is amplified too much.
5. Decide whether the amount of noise reduction is satisfactory. If yes, conclude the current cycle and go back to step 1 for other noise regions. If not, estimate the phase of the actuator in the noise amplification region.
6. Find out whether a lead or lag compensator can be implemented in the noise amplification region to change the overall  $PMFC$  phase and prevent noise

amplification. If not, implement a notch filter to achieve  $|PMFC| \ll 1$  in the noise amplification region.

7. If neither of the above work satisfactorily, one can try increasing the gain of the filter in the target region, or move the noise amplification region to a quieter place with small  $o_n$ .
8. If none of the above works, repeat the whole procedure with a slightly different pathways or parameter choices. There is some likelihood that one reaches the limit of the noise-cancelling capability at this point.

### 6.1.3 A toy model simulation

To gain more insights into the noise cancellation mechanism and its performance limitation, we present a simulation with two simplified translation stage responses: (1) a damped harmonic oscillator with a single resonance, and (2) a coupled harmonic oscillator with a double resonance. The gain-phase response of the toy models is shown in Figure 6.7. For the single-resonance model, we set the resonance at  $f_0 \approx 310$  Hz with a quality factor  $Q$ , similar to the main resonance in Figure 6.2. For the double-resonance model, we “add” another resonance of a similar quality factor, at around 3 times the first resonance. The double resonance model mimics to some extent the “forest of peaks” above the main resonance in Figure 6.2. The total phase delay of the double-resonance model is  $2\pi$  for high frequencies.

**Noise model** To keep the simulation simple, we assume that the noise  $n$  has a constant spectral density (white), and couples strongly to the translation stage response, producing a noise spectral density of  $o_n(\omega) = nP(\omega)$  with no control. The total noise can be obtained via integration over the whole frequency range. In particular, we take the square of the noise spectral density, with a  $[\text{Length}][\text{Frequency}]^{-1/2}$  dimension, and integrate it across  $\pm 2$  frequency decades from the main resonances, to obtain a measure of the noise power, up to a conversion factor. The total noise is thus obtained as the square-root of this noise power.

We simulate reduction on the total noise in these models, by implementing the PI control and suitable IIR filters (see Figure 6.8). For the PI control, we set a

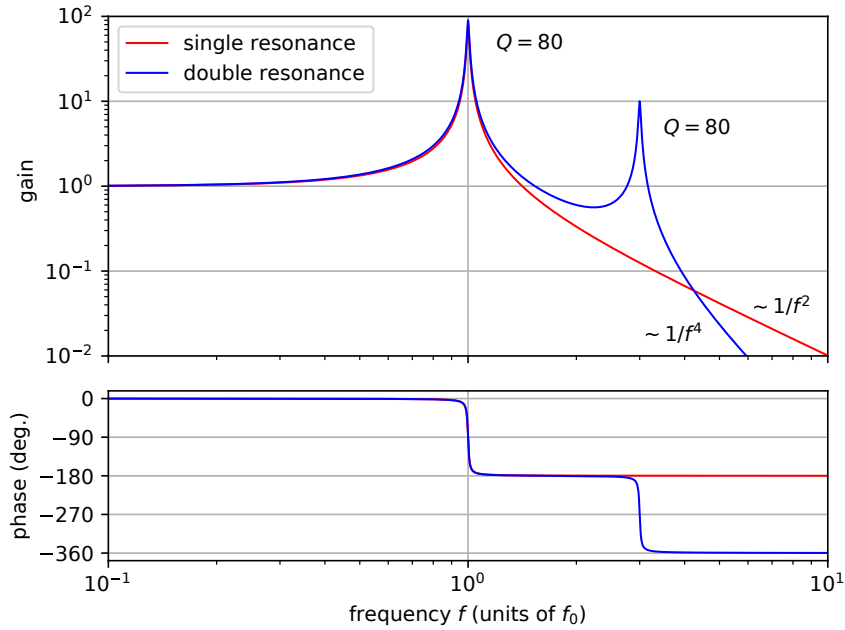


Figure 6.7: The gain-phase responses of the toy models: (1, red) single-resonance damped harmonic oscillator, and (2, blue) double-resonance coupled harmonic oscillator. The  $Q$ -factor of the resonance is set to 80, similar to our translation stage. At high frequencies, the gains decay with  $f^{-2}$  and  $f^{-4}$ , respectively.

small fixed value of  $K_I = 2\pi f_0 \times 0.01$  for noise reduction in the sub-Hz frequency range. Then, we vary  $K_P$  to observe overall noise reduction, and particularly near the resonances.

We first examine the scenarios with no digital filter ( $F = 1$ ), which are plotted with grey traces in Figure 6.8. At low values of  $K_P$ , even a small set value of  $K_I$  increases the total noise in the system, due to a high gain of the translation stage near resonance. Interestingly, for the single-resonance model, the noise reduces at high values of  $K_P$ . This simulated reduction is likely just a mathematical construct, as the  $PMFC$  phase of  $-\pi$  is only reached asymptotically at infinite frequency. By increasing  $K_P$ , the noise amplification region moves to higher frequencies, while following a diminished gain of  $f^{-2}$ , and resulting in a lower integrated noise. The behaviour of the double-resonance model is more typically observed in our experiments – the total noise stays roughly the same as  $K_P$  is increased, until the system hits an unstable point, where  $PMFC = -1$  at a particular frequency.

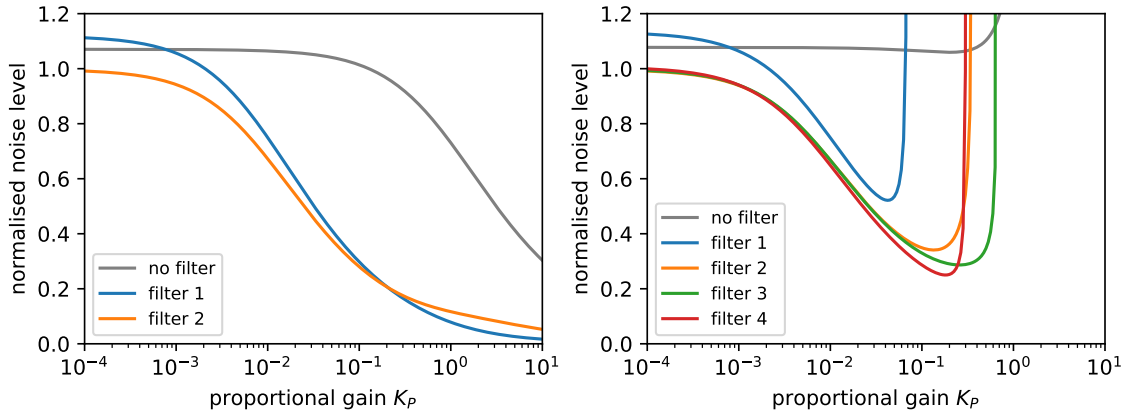


Figure 6.8: Noise reduction of the toy models by tuning  $K_P$ , with  $K_I = 2\pi f_0 \times 0.01$  fixed, for single-resonance (left) and double-resonance (right) model. With digital filters, the noise can be reduced. Filter 1 (blue) and filter 2 (orange) employ a first-order and a second-order lead compensator, respectively. For the double-resonance model, filter 3 (green) implements a notch filter with a second-order lead compensator, and filter 4 (red) implements a second order lead and lag compensators.

**Simulating lead compensators** We implement the first-order and second-order lead compensators of Figure 6.6 in the simulation, and observe noise reduction in Figure 6.8 – filter 1 (blue traces) and filter 2 (orange traces) denote the first-order and second-order lead compensator, respectively. For the single-resonance model, the total noise is reduced with higher  $K_P$  for both filters. The model indicates that filter 2 is better-performing at lower  $K_P$  values, likely due a higher phase lead at resonance. Interestingly, filter 1 outperforms filter 2 at higher  $K_P$  values. We suspect that, due to a relatively high frequency-range selectivity of filter 2, the noise reduction happens mostly inside a small frequency range. The noise spectral density of the single-resonance model, before and after active noise cancellation with filter 1, are shown in Figure 6.9 (red).

For the double-resonance model, the total noise is first reduced with higher  $K_P$  values, but increase significantly as it approaches the unstable point. Here, the filter 2 outperforms the filter 1, simply due to the fact that filter 2 has a high frequency-range selectivity, such that it only modifies the phase response of the first resonance without affecting the second resonance too much. With the best value of  $K_P$ , the total noise reduces by around 66% from the original noise – or equivalently, a reduction of 88% in the total noise power.

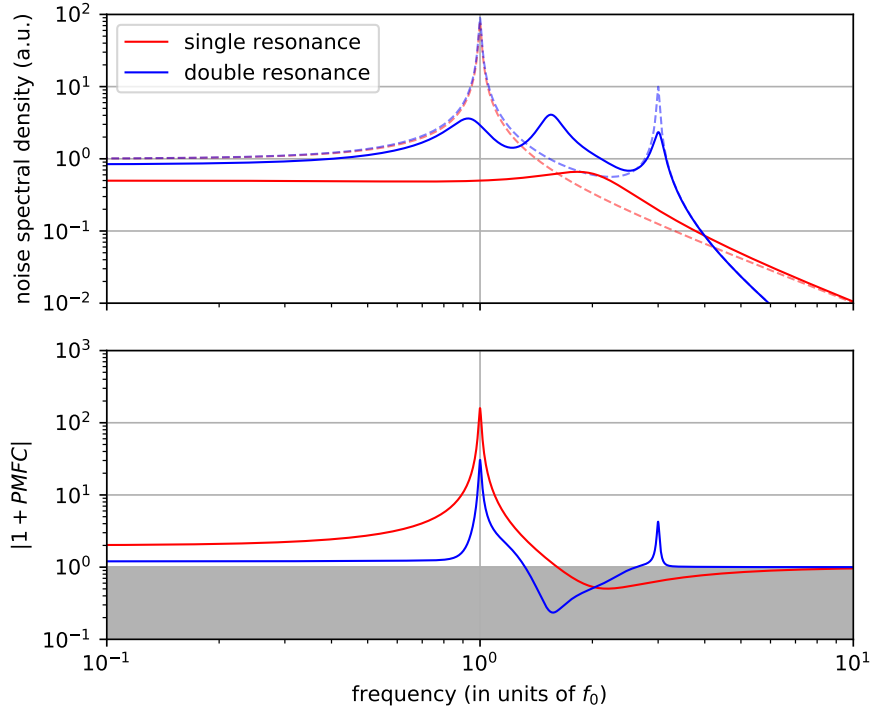


Figure 6.9: Noise spectral density of the toy models after noise cancellation (top), with the corresponding values of  $|1 + PMFC|$  (bottom), for the single-resonance (red) and double-resonance (blue) models – the single-resonance model employs filter 1 with  $K_P = 1$ , while the double-resonance model employs filter 4 with  $K_P = 0.2$ . The noise spectral density before noise cancellation is provided as dashed lines as reference. The grey-shaded area of  $|1 + PMFC| < 1$  indicates the region where the noise is amplified.

**Refining noise reduction strategies** A better performance in noise reduction for the double-resonance model can be achieved with some strategies that deal with the second resonance. One approach would be to additionally implement a notch filter of Figure 6.6 on the second resonance – here, the notch filter  $Q$ -factor is set to  $Q = 20$  for better frequency selectivity. This would reduce the  $PMFC$  gain near the second resonance, and effectively allows  $K_P$  to be increased further, before the system becomes unstable. The performance of this filter is shown in Figure 6.8 (filter 3, green), and exhibits a further  $\sim 16\%$  decrease in total noise compared with filter 2.

Another approach is to “cancel” the noise of the second resonance by additionally implementing a lag compensator. In this case, the first resonance is phase-led

by about  $\pi/2$ , while the second resonance is phase-lagged by about  $\pi/2$  as well. This strategy would reduce noise in both resonance peaks, but would inadvertently amplify the noise at the region in-between, due to the  $2\pi$  phase delay of the model response. The performance of such filter is shown in Figure 6.8 (filter 4, red), and the resulting noise spectral density is shown in Figure 6.9 (blue). This filter performs the best out of the others, with a total noise reduction of around 75%.

The resulting noise spectral density may suggest a noise-reduction limitation in systems with multiple resonances having  $\geq 2\pi$  phase delays. The phase response of *PMFC* in such systems would have to cross the  $-\pi$  phase at some frequencies, which would make the system unstable with high enough  $K_P$ . Thus, it becomes a matter of compromise – how much noise reduction is achieved in the noisy regions, and how much noise amplification can be tolerated in the  $-\pi$  phase-crossing regions.

#### 6.1.4 Active noise cancellation in cavity version 2a

We applied the noise cancellation strategy on cavity version 2a, by actuating on the translation stage and targeting to mainly reduce noise from Peak A. The total noise reduced from 1.4(2) nm to 0.63(2) nm, or equivalent to  $\sim 78\%$  reduction in the noise power. The resulting noise spectral density is shown in Figure 6.10 (orange). Peak A and B diminished, while Peak C stayed the same. This was expected, as Peak B is likely a harmonic of Peak A, and Peak C does not correspond to any actuator resonances.

Besides the translation stage, the cavity length can also be actuated in a small movement range by a ring piezo, with resonance peaks starting at around 1 kHz. The gain response before the resonance peaks is pretty flat, which provides some flexibility in the IIR filter design. We shaped the filter to provide a relatively high gain near Peak A and C, to target further noise reduction in those areas. We managed to implement active noise cancellation with both actuators, and observed a further noise reduction to 0.38(2) nm, corresponding to  $\sim 92\%$  cumulative reduction in the noise power. The resulting noise spectral density (see Figure 6.10, green) shows a significant reduction in all of the identified noise peaks, with the noise spikes of electrical origins becoming a more significant noise component.

After some investigations, we managed to identify and resolve some of the

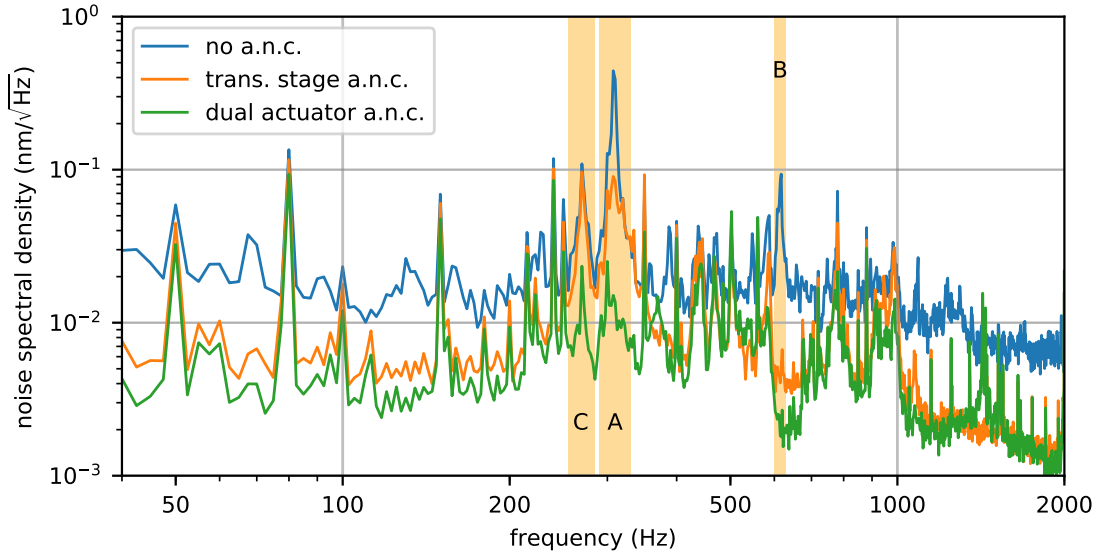


Figure 6.10: Noise spectral density of cavity version 2a after noise cancellation: (orange) with only the translation stage actuation, and (green) with both the translation stage and ring piezo actuation.

electrical and mechanical noise sources (see Appendix D). The initial noise without any control became smaller, at  $0.8(1)$  nm. With active noise cancellation, the noise is reduced to  $0.35(2)$  nm by using both actuators, corresponding to  $\sim 82\%$  cumulative reduction in the noise power. We suspect that the system is close to the limit of the noise reduction capability, as none of the remaining noise peaks dominates – the highest noise peak only contributes to around  $15\%$  of the total noise power.

## 6.2 Friction Damping

In this section, we describe a noise reduction mechanism which employs thin metal strips as friction dampers to restrict the relative motion between the mirrors, particularly along the cavity axis. This method inspired the design of cavity setup version 2b, with a relatively low passive noise (see Section 6.2.4). Such friction-based damping elements have also been used to damp resonant stresses in gas-turbine blades [316, 317] and to dissipate earthquake energy from building structures [318, 319]. Due to the relative ease of application and its compactness, this method can potentially be applied to any position-sensitive systems requiring further noise

isolation, particularly in interferometric system with less rigid structures, in atomic-scale microscopy, or in compact systems with no separate vibration isolation.

### 6.2.1 Experimental setup

We use the cavity mechanical design version 2a (see Figure 2.6), and replace the cavity mirrors with less curved ones and higher reflectivities, such that the cavity operates in the planar regime with finesse in the thousands. The higher finesse is useful in increasing the sensitivity of the cavity to the mechanical noise according to Equation 6.1 so that the noise present and any subsequent improvement of the passive stability are more readily observed. We characterise the noise using the method described in Section 6.1.1.

The noise of the planar cavity system mainly comes from the inherent mechanical vibration of the translation stage (ANSxyz100, Attocube), which we have measured to be  $\sim 1$  nm along the cavity axis, similar to Section 6.1. The noise spectrum of this mechanical vibration exhibits several resonances in the 100-1000 Hz band (black line in Figure 6.12). The noise from this band contributes significantly to the fluctuation in cavity length. Once they are suppressed, the passive stability of the cavity is greatly improved. We have also observed environmental noise coupling into the cavity through the structure housing the set-up. The contribution from the environmental noise is typically lower.

### 6.2.2 Friction dampers and noise reduction

Due to the unique mechanical design requirements of the near-concentric cavity, we are unable to incorporate a spacer made out of ultralow expansion glass (ULE) or fused silica (FS) to provide stability against thermal and vibration drifts and achieve a low noise effect factor  $\xi_{noise}$  [320]. Instead, we aim to “stiffen” the mechanical modes by introducing friction dampers to reduce the mechanical vibrations. These friction dampers are thin light strips of aluminum which we cut from a larger sheet and milled to the desired thickness and weight. They are then placed across the moving stage and the fixed stage of the cavity structure.

With strategically chosen points of placement, we find that we can suppress the noise by an order of magnitude to  $\sim 0.1$  nm [98]. We observe an improvement in the

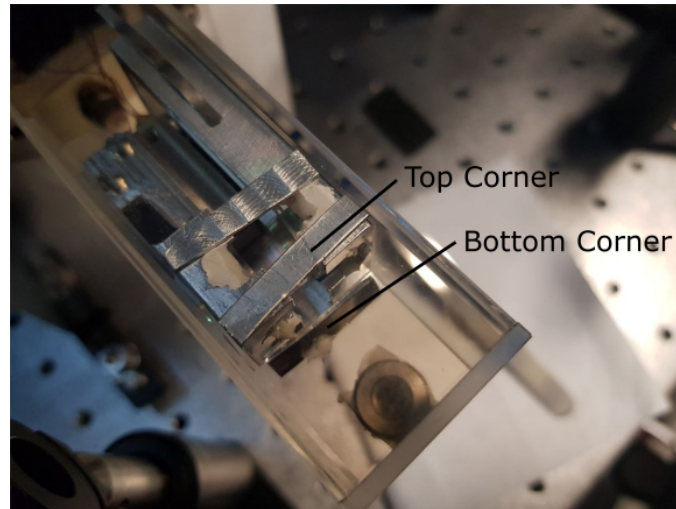


Figure 6.11: Placements of friction dampers on the cavity structure for mechanical noise reduction (top view). The friction dampers are placed on the cavity structure housed inside a cuvette – two at the top corners, and one at the bottom corner. The dampeners weigh around 0.2 g, and have a thickness of approximately 0.5 mm to fit within the 1 mm gap between the cavity structure and the cuvette.

suppression as the number of dampers increase, with a maximal improvement with three friction dampers. The ideal locations of the dampers are shown in Figure 6.11. We observe that populating the top of the structure with more than two dampers did not yield any discernible improvements. It is important to note that the dampers are effective only when they are in contact with both mirrors.

This approach is advantageous for several reasons. Firstly, the friction dampers are very lightweight and compact. They weigh a mere 0.2 g and have a thickness of around 0.5 mm. Hence, they do not restrict the movement range of the piezo translation stages and are easily implemented in systems that face stringent space or load constraints. Secondly, they are readily available at practically no cost since they are made from a common material, and they do not require any technical expertise to prepare. Lastly, it is a vacuum-compatible material, which is crucial for applications where the system will be placed in a vacuum, such as ours.

We use this approach to construct the cavity mechanical design version 2b, where the friction dampers are placed in their respective pockets, to prevent them from accidental displacement and detachment from the structure. The performance of friction dampers in cavity version 2b, along with a combined implementation of the

active noise cancellation, is discussed in Section 6.2.4.

### 6.2.3 Understanding the noise isolation mechanism

To understand the noise isolation mechanism of the friction dampers, we need to measure the cavity noise in a controlled fashion. We achieve this by placing the cavity apparatus on a vibrating platform, which is driven along the cavity axis at a known voltage and frequency using a piezo translation stage (Tritor 101 CAP, Piezosystem Jena). The noise isolation performance is deduced from the gain ratio  $VG(f) = x(f)/a(f)$  between the cavity and the platform vibration amplitudes,  $x(f)$  and  $a(f)$  respectively, across different driving frequencies  $f$ . We obtain  $x(f)$  via the gain-phase response measurement technique described in Section 6.1.1, but using the error signal of another cavity with a lower finesse to observe a larger range of the movement (up to  $\sim 5$  nm). On the other hand, the platform vibration  $a(f)$  is determined from the movement of the fixed-stage cavity mirror with respect to the optical table via a Michelson interferometer setup. We placed the friction dampers with mass around 1 g either to a top corner site (one damper case) or to all three sites (3 dampers case) and compare the gain ratios with the case without any friction dampers. As the cavity and platform vibration amplitudes span around 5 orders of magnitude, we drive the piezo translation stage with different amplitudes and reconstruct the gain ratio correspondingly.

Figure 6.12 shows the vibration gain ratio  $VG$  of the cavity system with different driving frequencies. Without any damper, there is a peak of  $VG \approx 100$  at 320 Hz, which we attribute to the “tuning-fork” mechanical resonance of the cavity structure. The dampers restrict this “tuning-fork” motion and reduce the gain ratio on this resonance by a factor of  $\sim 100$ . Furthermore, the dampers also provide further noise isolation for frequencies lower than  $\sim 400$  Hz. The three-damper configuration also provides additional noise isolation at  $\sim 600$  Hz, compared with the one-damper configuration, as they restrict more modes due to the inclusion of the damper at the bottom corner. For higher frequencies, the dampers no longer provide any noise isolation, which may be due to the structure resonating at higher harmonics.

**Stick to slip transition** Having demonstrated the noise isolation obtained from adding the friction dampers, we show that the damper friction force acts on the

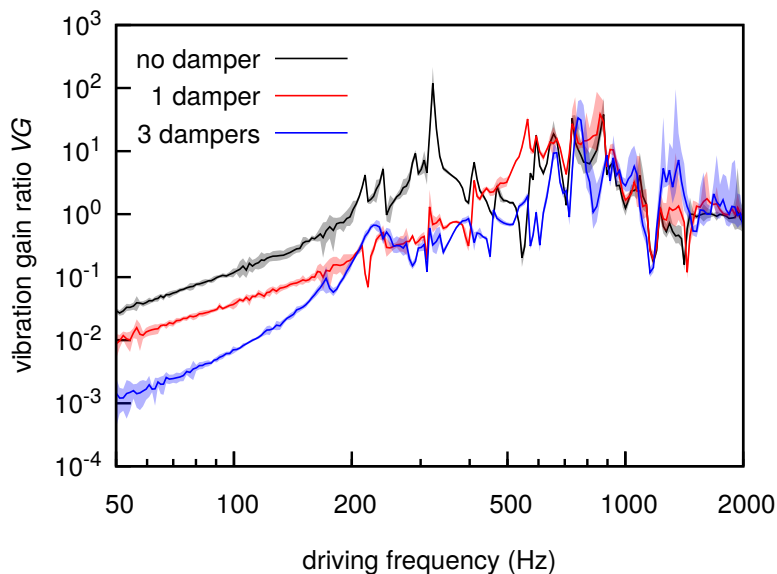


Figure 6.12: Frequency-dependent gain ratio  $VG$  between the cavity and the platform vibration amplitudes for three different friction damper configurations: no damper (top black line), one damper (middle red line), and three dampers (bottom blue line). The shaded regions represent an estimate of the standard deviation over repeated measurements.

cavity structure in the stick regime. We place a friction damper with masses ranging from 0.03 g to 0.17 g on the top corner site, and monitor the vibration amplitudes of both mirrors, representing the cavity moving-stage and platform vibrations, via two Michelson interferometers. Figure 6.13 shows that, near the “tuning-fork” mechanical resonance, the cavity moving-stage vibration amplitude increases with higher platform vibration, until around 15 to 20 nm where it abruptly jumps to significantly higher values. We identify this as the stick-to-slip transition of the friction regime. As the noise isolation mechanism for our cavity works at much lower vibration amplitudes ( $\lesssim 1$  nm), the friction dampers stick on their contact points and reduce motional modes along the dampers, similar to a caged system, when operating at small deviations from the set point. Furthermore, the slipping mechanism of the friction dampers allow large movements necessary for the alignment of the mirrors.

Furthermore, Figure 6.13 also indicates that the friction damping increases with larger damper mass, which we suspect to be due to a combination of following two factors. First, friction dampers with higher mass have higher cross-section areas,

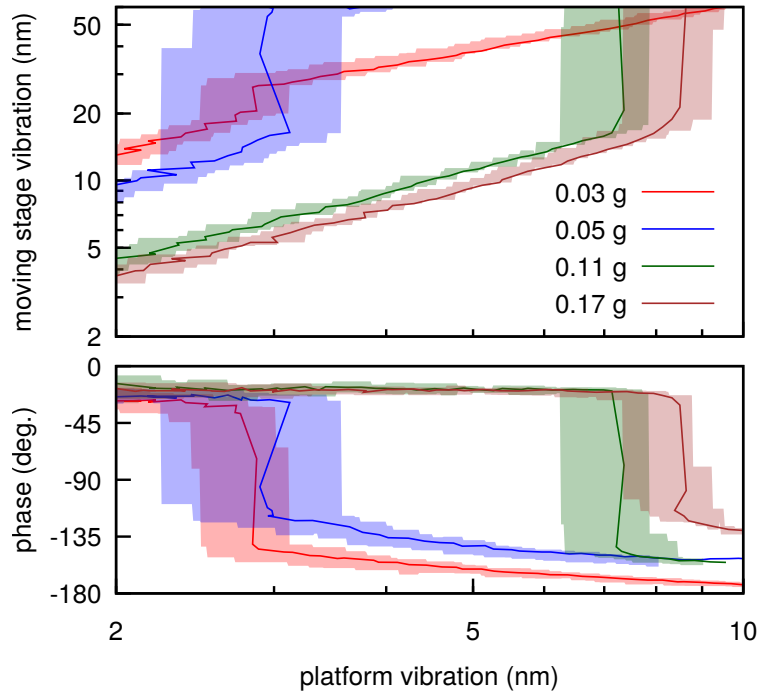


Figure 6.13: Probing the stick to slip transition of the friction dampers. By driving the cavity structure near its mechanical resonance (330 Hz) with increasing platform vibration, we observe a jump in the vibration amplitudes of the moving stage (top) and in their relative phases (bottom). The solid lines and the shaded regions represent the medians and the ranges of values observed over seven repeated measurements, with increasing damper masses (from left to right). The measurement of the vibration amplitudes is limited to the linear region of the interferometric intensity, around  $\lambda/4\pi \approx 60$  nm.

increasing its stiffness. In the stick regime, the movement between the two contact points can be effectively reduced with higher damper stiffness. Second, the effective areas of contact between the friction damper and the stages increase with larger normal force from heavier damper mass [321].

**Damping effect with different masses** It is difficult to model the interplay between these factors with a relatively complex structure that includes the flexural translation stages and the moving stage with a mounted cavity mirror. Instead, we examine experimentally the effect of using different damper masses, placing one on the top corner site, on two relevant parameters – DC gain of the cavity translation stage and total vibration noise (see Figure 6.14). To measure the DC gain of the

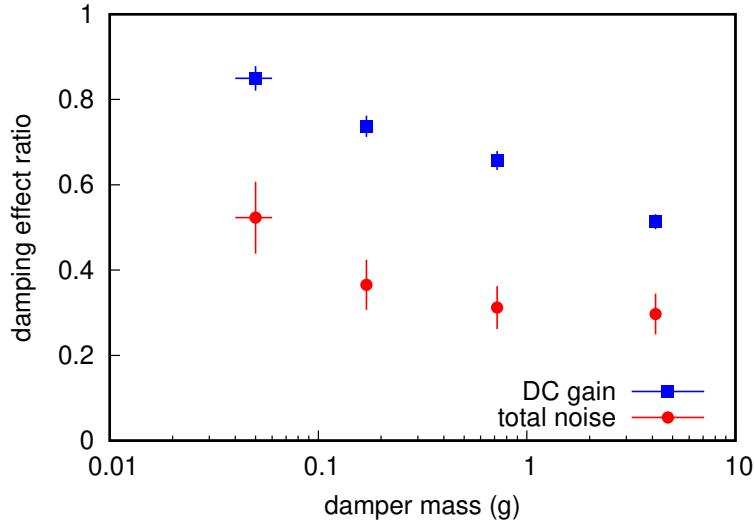


Figure 6.14: Damping effect of different friction damper masses on the translation stage DC gain (blue square) and the total vibration noise (red circle), with one friction damper placed on the top corner site. The DC gain and total noise are normalised to the case without any friction dampers.

translation stage, we drive the translation stage in the direction of the cavity axis in the low frequency regime ( $\sim 10$  Hz), well below any mechanical resonances, and measure the corresponding vibration amplitude. We observe a reduction of the DC gain after placing the friction dampers, which is expected as the damper restricts some movement between the cavity stages in the stick friction regime.

Next, we quantify the total vibration noise using the technique described in Section 6.1.1, by integrating the linearised noise spectral density across the whole frequency range. We observe a significant reduction in the total noise, even just by placing one 0.05 g friction damper on one corner site. This damping effect seems to saturate at around 1 g of damper mass, with a noise reduction of around 70%, or equivalently around 90% reduction of the noise power.

#### 6.2.4 Combining friction damping and active noise cancellation in cavity version 2b

In cavity version 2b (see Figure 2.6), we designed a few pockets on the mechanical structure to place the friction dampers, at the three sites identified in Section 6.2.2. The friction dampers were made out of stainless steel, and each weighs around 1 g.

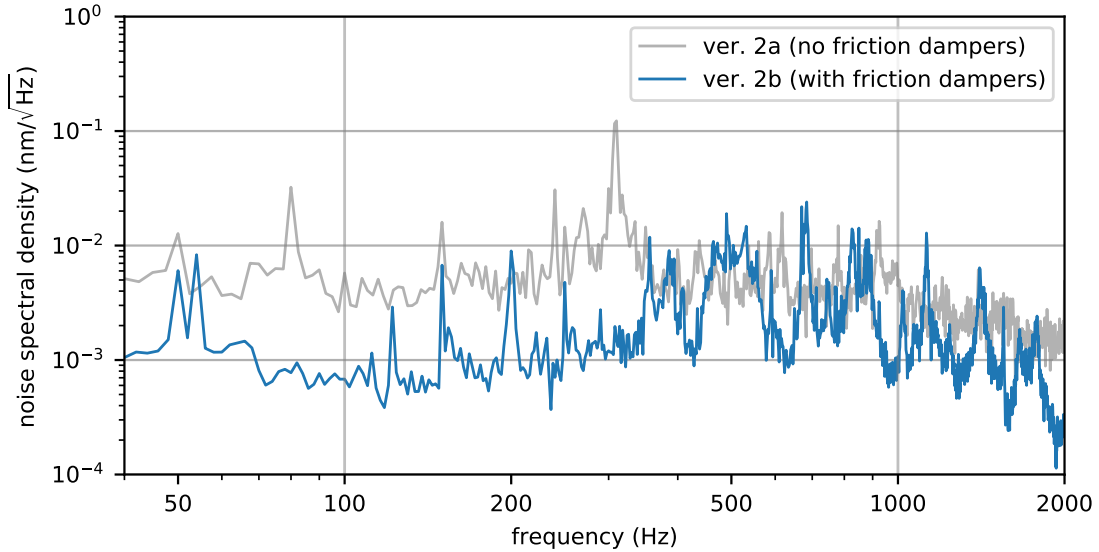


Figure 6.15: A typical mechanical noise spectral density in cavity version 2b (blue, averaged over 5 traces), after installing the friction dampers. A typical noise spectral density without any friction dampers, i.e. in cavity version 2a from Figure 6.1, is provided as a reference (grey).

After putting the friction dampers, the mechanical noise reduced from  $\sim 1$  nm to around  $0.17(2)$  nm, inside a cuvette and under ultrahigh vacuum condition. The noise spectral density is given in Figure 6.15.

We have also tried to implement active noise cancellation on the setup, and observed a modest decrease in the mechanical noise. The total noise power reduced by around 15% via the translation stage actuation, resulting in a mechanical noise of around  $0.16(2)$  nm and a noise effect factor of  $\xi_{noise} \sim 0.2$  with a cavity finesse of  $\mathcal{F} = 484(9)$ . This was likely due to the friction damper setup no longer having a particularly noisy region, e.g. the noise Peak A in cavity version 2a, and the mechanical resonances are spaced relatively close to each other. A similar amount of noise reduction was also observed with the ring piezo actuation.

### 6.2.5 Summary and Outlook

We have successfully demonstrated mechanical noise reduction in our cavity setup with two different methods. First, we use an IIR digital filter to modify the control response, and reduce the total noise from about 1 nm to 0.4 nm. Second, we use

## CHAPTER 6. NOISE REDUCTION TECHNIQUES

friction dampers in our cavity setup to achieve a much higher passive stability, with noise of about 0.17 nm. To achieve the target noise of  $\xi_{noise} \lesssim 0.2$ , the supported cavity finesse ranges are  $\mathcal{F} \lesssim 220$  and  $\mathcal{F} \lesssim 460$ , with the two methods, respectively.

With these noise figures, it is likely for us to perform experiment with atoms – we have managed to trap atoms with cavity version 2b. Though the noise level can probably reduce a bit further, by refining the techniques or discovering new methods, operating a cavity with finesse of thousands or more may require a completely different approach.

Recently, we examine a different cavity mounting technique which could potentially provide a higher mechanical stability. The piezo actuators are mounted in-between the mirror mounts without any mounting screws, with any movements along the cavity axis restricted by the tensile modulus of the actuators. Transverse misalignment corrections are provided by the tip and tilt piezo actuation. This scheme will be discussed further in Section 8.2.2.

## Chapter 7

# Discursion around the Critical Point

A unique feature of a near-concentric cavity is its proximity to the unstable regime, where the cavity length is longer than the critical length  $L = 2R$ . In the region surrounding the critical point, the cavity modes are highly focused, with mode widths that vary rapidly over small length changes. In this chapter, we examine the behaviour of the near-concentric cavity modes close to this critical point. With the observation of the diffraction losses, we infer the aperture size of our cavity, which may provide insights on the mirror imperfections. We conclude with a discussion on operating optical resonators on and beyond the critical point.

### 7.1 Last Stable Resonance

We find that our near-concentric cavity can be aligned extremely close to the critical point. With a fixed laser frequency, the cavity resonances are half-wavelength separated. By adjusting the cavity resonant length by half-wavelengths, there exists a cavity length with the “last stable resonance”, just before the it enters the unstable regime. This point is particularly interesting, as it allows the highest on-resonant atom-cavity coupling in near-concentric cavity systems (see Section 2.1.2). In this section, we aligned our cavity at the last stable resonance, and observed that the fundamental mode is well supported with virtually no diffraction loss. This work has been published in [80].

The critical distance  $d = 2R - L$ , which characterises the distance of the cavity length to the critical point, can be measured via the transverse mode spacing method described in Section 3.4.3, and the last stable resonance described here refers to the first point in Figure 3.8. For this experiment we use the cavity setup version 1b (see

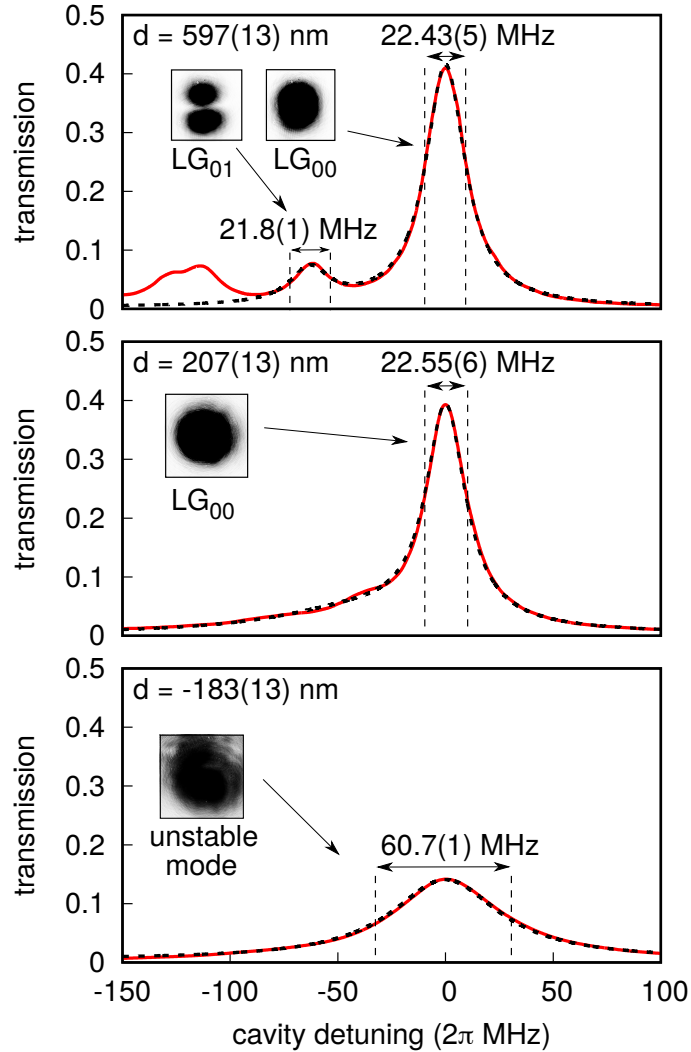


Figure 7.1: Cavity transmission spectra at the penultimate stable resonance with (top), last stable resonance (middle), and the first unstable resonance (bottom). The camera-captured transmitted mode profiles are shown in the insets (partially saturated). The transmission spectra are fitted to a sum of two Lorentzian functions, which model the resonances of the  $_{10}$  and  $LG_{10}$  modes (dashed lines).

Section 2.2.2), which is not put under a vacuum condition and thus has a relatively pristine finesse of  $606(3)$ , just slightly below the nominal finesse of  $627$ .

Figure 7.1 shows the transmission spectra of the cavity at the penultimate stable resonance (top), last stable resonance (middle), and the first unstable resonance (bottom). These corresponds to critical distances of  $597$  nm,  $207$  nm, and  $-183$  nm, respectively, with an uncertainty of  $13$  nm obtained from the fit of Figure 3.8.

## CHAPTER 7. DISCURSION AROUND THE CRITICAL POINT

At the last stable resonance, the linewidth of the fundamental cavity mode (LG<sub>00</sub>) is still maintained at  $2\kappa = 2\pi \times 22.55(6)$  MHz, barely drops from the linewidth at the penultimate stable resonance of 22.43(5) MHz. However, the linewidth of the LG<sub>01</sub> transverse mode is difficult to identify, as the transverse mode spacing becomes smaller and the transmission profile smears out. Just one half-wavelength into to the unstable regime at  $d = -183(13)$  nm, the linewidth of the “fundamental” mode broadens to 60.7(2) MHz, with mode that no longer looks Gaussian.

The absence of finesse loss in the cavity fundamental mode, even at the last stable resonance, contrasts with other cavity systems, as their finesse drop significantly as they approach the critical point [264, 322]. We believe that this is due to the design of the anaclastic lens-mirrors, which allows ease of alignment, as the highly-divergent near-concentric modes are transformed into collimated modes on the cavity input and output. Furthermore, a high-quality large-angle spherical surfaces of the lens-mirrors allows the near-concentric modes to be well supported.

At the last stable resonance with  $d = 207(13)$  nm, the cavity waist radius is calculated to be  $w_0 = 2.44(4)$   $\mu\text{m}$  using paraxial approximation. The cavity mode  $1/e^2$ -width for LG<sub>00</sub> mode on the mirror is calculated to be  $2w_m = 1.12(2)$  mm – the  $1/e^2$ -width is equivalent to  $2w(z)$  defined in Equation A.1. Thus, with virtually no diffraction loss on the LG<sub>00</sub> mode at the last stable resonance, the effective aperture diameter of the anaclastic lens-mirror is at least the size of the  $1/e^2$ -width  $2w_m$ .

It is interesting to comment on the validity of the paraxial approximation in this regime. Several theoretical works in cavities with highly divergent eigenmodes [226, 227] have shown that the calculated cavity eigenmodes formed with spherical mirrors agrees closely with the free-space paraxial modes, even at small critical distances. On the other hand, cavity eigenmodes formed with parabolic mirrors differ from the free-space modes, with larger cavity mode waists, even at large critical distances ( $d/R \sim 10^{-4}$ ). This may indicate that spherical mirrors are more suitable to form highly-divergent cavity modes. This is reminiscent of a similar observation in the focused lens systems, where a spherical wavefront produces a much tighter focus compared to a parabolic wavefront [225].

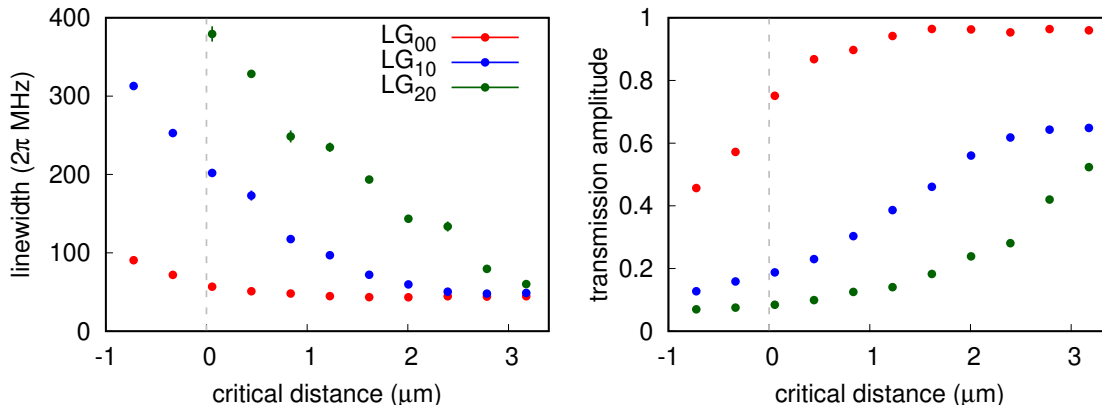


Figure 7.2: Cavity transverse modes linewidths (left) and transmission amplitudes (right) at different critical distances. The linewidth is obtained from the fit of transmission spectrum. The transmission amplitudes are normalised to the cavity transmission with a perfect mode matching – without diffraction loss, the transmission amplitudes are equivalent to the mode-matching efficiency  $\eta$  as defined previously in Section 3.4.2.

## 7.2 Diffraction Loss and Aperture Size

With the techniques developed in Chapter 5, we can couple to the cavity transverse modes with high mode-matching efficiencies. In this section, we study how the transverse modes and their mode matching perform close to the critical point. Contrary to the fundamental cavity mode, the higher order transverse modes display relatively high diffraction losses as they approach the critical point, which suggest an effective aperture diameter smaller than the nominal value. These observations have been published in [81].

We use the SLM to couple to  $\text{LG}_{00}$ ,  $\text{LG}_{10}$ , and  $\text{LG}_{20}$  transverse modes of the near-concentric cavity, and obtain the cavity transmission spectra at different critical distances. We demonstrate this experiment using the cavity setup version 2a under vacuum conditions, with a reduced finesse of 275(5) for the fundamental mode. We obtain the critical distance of the penultimate stable point as  $d = 0.45(3) \mu\text{m}$  via the transverse mode spacing measurement. By changing the cavity length and fixing the laser frequency, we obtain neighbouring cavity spectra spaced half-wavelengths apart.

Figure 7.2 shows the cavity transverse mode linewidths and transmission amplitudes for various critical distances. Our near-concentric cavity supports several LG

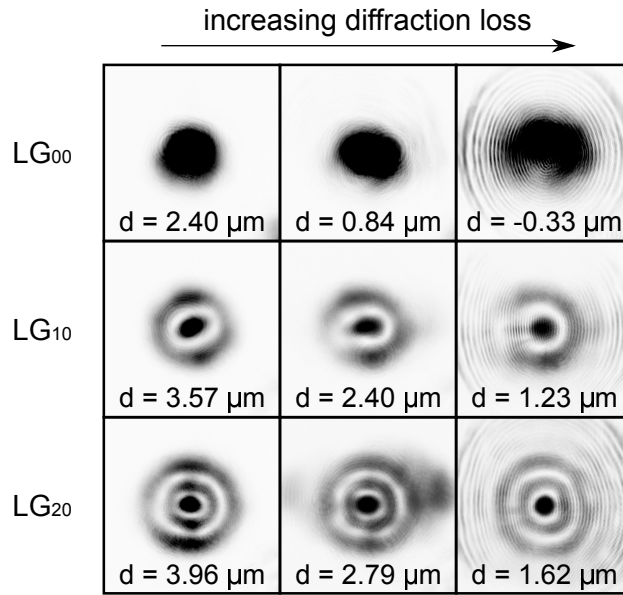


Figure 7.3: Camera-captured spatial profiles of the cavity transmission modes (partially saturated). For a small critical distance, diffraction loss becomes significant and distorts the mode profile. The diffraction rings are caused by the aperture of the anastigmatic lens.

modes reasonably close ( $\sim$  a few  $\mu\text{m}$ ) to the critical point. However, the LG modes start to exhibit diffraction losses at some critical distances, as the mode sizes on the cavity mirrors start to exceed the cavity effective aperture size. This results in a corresponding increase of cavity linewidths and decrease in cavity transmission amplitudes. Figure 7.3 shows the spatial profile of the cavity transmission, captured with the mode camera. Diffraction rings become visible at the critical distances where the linewidths start to increase.

### 7.2.1 Estimating the aperture size

The performance of the cavity mirrors can be characterised with an effective aperture size – for every round trip, the cavity mode is clipped by a circular aperture with diameter  $a$  on the mirror, effectively blocking some outer parts of the beam. As a first-order approximation, we assume the LG modes to be unperturbed after subsequent round trips. To estimate the onset of the diffraction loss, we choose an aperture size that blocks  $\sim 1\%$  of the mode, which contributes to an additional diffraction loss of  $\kappa_{ap} \approx 2\pi \times 10 \text{ MHz}$ . This is on the same order as the mirror

## CHAPTER 7. DISCURSION AROUND THE CRITICAL POINT

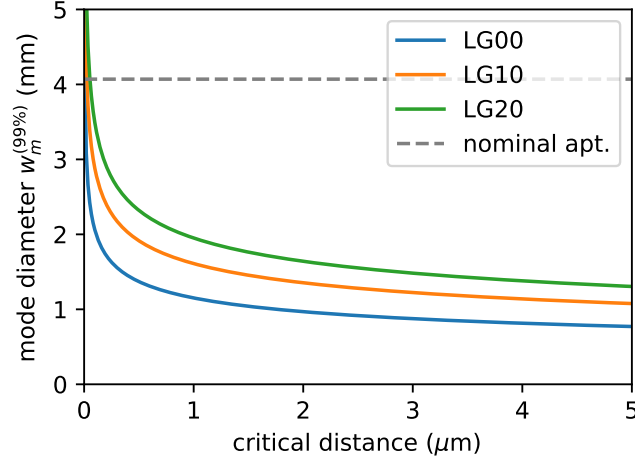


Figure 7.4: The diameters of the transverse modes on the cavity mirror  $2w_m^{(99\%)}$  which contains 99% of the total power. The nominal aperture size of our mirror is also given as a reference.

transmission and scattering losses,  $\kappa_m = 2\pi \times 11.3(4)$  MHz and  $\kappa_l = 2\pi \times 13.5(4)$  MHz (see Section 5.1.2), which are not expected to change with different critical distances.

Due to the diffraction loss  $\kappa_{ap}$ , the cavity linewidth increases by around 20 MHz. From Figure 7.2 (right), we estimate this increase to happen at critical distances of  $d_{ap,10} \approx 1.7 \mu\text{m}$  and  $d_{ap,20} \approx 2.9 \mu\text{m}$  for the LG<sub>10</sub> and LG<sub>20</sub> modes, respectively. We do not consider the corresponding estimate using the LG<sub>00</sub> mode, as it yields a negative critical distance.

Figure 7.4 shows the mode diameters on the mirror which contain 99% of the total power  $2w_m^{(99\%)}$ , for different paraxial transverse modes and critical distances. Based on the critical distance estimates where  $\sim 1\%$  of the mode is blocked, and assuming that the modes are centred on a circular aperture, we estimate that the LG<sub>10</sub> and LG<sub>20</sub> modes have effective aperture diameters of  $a_{10} \approx 1.4$  mm and  $a_{20} \approx 1.5$  mm, respectively. These values are comparatively lower than the nominal aperture of our anastigmatic lens-mirrors  $a_{\text{nom}} = 4.07$  mm. While these discrepancies may be due to some nonparaxial effects of the cavity modes, particularly for the higher-order transverse modes, we suspect that it is more likely to be due to mirror imperfections (see Appendix C for a list of them).

### 7.2.2 Numerical calculation of the cavity eigenmodes

It is interesting to numerically calculate the cavity eigenmodes formed with a circular aperture, which may provide some intuition on how diffraction losses affect the formation of the cavity modes in the near-concentric regime. To reduce the complexity of the model, we make the following assumptions. First, the mirrors are ideally spherical, with a circular aperture centred on one of the mirrors. Second, we use paraxial approximation on both the modes and propagation operators – this may not be entirely unwarranted, as paraxial free-space modes closely approximate the eigenmodes of a spherical cavity (see the last paragraph of Section 7.1). Third, we assume that the circular aperture perfectly blocks all the light outside the aperture.

In a paraxial system, the diffraction integral of a light propagation can be written in terms of the matrix optics, in a formalism known as the Collins' integral [323]. After one round trip of the cavity, the integral equation can be written [324] as

$$\gamma E(\eta_2, \theta_2) = N \int_0^{2\pi} \int_0^1 E(\eta_1, \theta_1) K(\eta_2, \eta_1, \theta_2, \theta_1) \eta_1 d\eta_1 d\theta_1, \quad (7.1)$$

with  $\gamma$  an eigenvalue which characterises the resonator aperture loss  $\mathcal{L}_{ap} = 1 - \gamma\bar{\gamma}$ ,  $E(\eta_i, \theta_i)$  the eigenmode distribution,  $\eta_i = \rho_i/a_r$  a normalised radial coordinate with aperture radius  $a_r$ , and  $N = a^2/2\lambda L|g|$  the Fresnel number with the stability parameter  $g = -1 + d/R$ . The kernel  $K(\eta_2, \eta_1, \theta_2, \theta_1)$  is given by

$$K(\eta_2, \eta_1, \theta_2, \theta_1) = \exp \left[ i\pi N(2g^2 - 1)(\eta_1^2 + \eta_2^2) - 2i\pi N\eta_1\eta_2 \cos(\theta_1 - \theta_2) \right]. \quad (7.2)$$

In a radially symmetric system, the integral equation simplifies to

$$\gamma E(\eta_2) = N \int_0^1 E(\eta_1) 2\pi J_0(-2\pi N\eta_1\eta_2) \exp \left[ i\pi N(2g^2 - 1)(\eta_1^2 + \eta_2^2) \right] \eta_1 d\eta_1, \quad (7.3)$$

where  $J_0$  is the Bessel function of the first kind.

The diffraction integral of Equation 7.3 can be written as a matrix eigenequation  $\mathbf{M}\mathbf{u} = \gamma\mathbf{u}$  by discretising the eigenmode  $E(\eta)$  to the eigenvector  $\mathbf{u}$  with enough sampling points – systems with large Fresnel number  $N$  require finer discretisation due to the oscillatory behaviour of the complex exponential term. We set the number of points to be at least 10 times the Fresnel number, and verify that the result does not vary too much with a different number of points. The matrix  $\mathbf{M}$  can be obtained by applying Newton-Cotes formula for  $n = 2$  (also known as Simpson's rule) on the diffraction integral with equally spaced points.

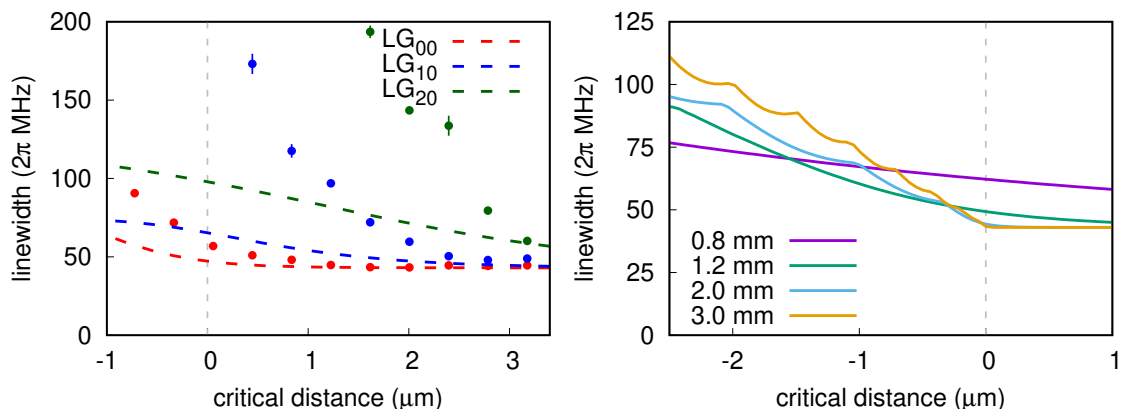


Figure 7.5: Numerical calculation of the cavity linewidth using the Prony's method, with the paraxial approximation. A circular hard-edge aperture is centred on one mirror. (Left) the dashed lines are the estimated linewidths for the radial modes with an aperture diameter of 1.4 mm. The experimental data points, obtained from Figure 7.2, are much larger than the estimated values in the high diffraction regime. (Right) the estimated linewidths for the  $LG_{00}$  mode, with different aperture diameters indicated by the legend.

The matrix eigenequation is then solved using the Prony's method described in [325], which gives a set of eigenvectors with the eigenvalues  $\gamma \leq 1$ , ranked from the largest eigenvalue. These correspond to a set of cavity radial eigenmodes with relatively low losses – in the near-concentric case, these are the radial  $LG_{i0}$  modes with diffraction losses  $\mathcal{L}_{ap} = 1 - \gamma\bar{\gamma}$ . These losses add to the cavity decay rate  $\kappa$  and increase the cavity linewidth.

Figure 7.5 (left) shows the expected cavity linewidths obtained with this numerical calculation, as a function of the critical distances. We use an aperture diameter of 1.4 mm, estimated from the previous section. These values can be treated as lower-bound estimates on the cavity linewidth, as the cavity eigenmodes are no longer Laguerre-Gaussian and the mode-matching procedure cannot be performed effectively. Furthermore, our cavity does not have a fixed aperture size with a circular shape, and currently the diffraction loss mechanism in our cavity is not entirely understood.

It may be interesting to note that the diffraction loss for the fundamental mode does not increase significantly with smaller critical distance, even at the critical point. Figure 7.5 (right) shows the expected cavity linewidths for the fundamental mode with different aperture sizes. With a relatively large aperture size, the diffraction

loss only starts to increase in the unstable regime, which is consistent with our experimental observations. This result may be an interesting starting point for future research, which takes the nonparaxial nature of the cavity eigenmodes into account, with the mode-propagation model valid even at extremely small critical distances ( $d \ll \lambda$ ).

### 7.2.3 Summary and outlook

Owing to the anaclastic lens-mirror design, we managed to align the near-concentric cavity at the last stable resonance, with virtually no diffraction loss on the fundamental mode. The diffraction loss observed with higher-order transverse modes yields an effective aperture diameter of around 1.4 mm, which is lower than the nominal value of 4.07 mm due to mirror imperfections.

**Approaching concentricity** The atom-cavity coupling is expected to increase significantly when operated very close to the critical point, in the  $d \ll \lambda/2$  regime (see Section 2.1.2). The measurement of atom-cavity coupling may have to be performed dispersively, as it may not be possible to tune the cavity to be resonant with the atom. However, it is not clear to what extent realistic mirrors can increase the coupling strength through reduction in the cavity mode waist, considering their imperfections (see Appendix C). Thus, it may be prudent to first design and perform an experiment to measure the cavity mode waist in-situ, similar to the knife-edge technique in focused lens systems [326]. In addition, it is advantageous to understand why the effective aperture size is currently limited to around 1.4 mm, as smaller mode waists require larger apertures. Higher finesse mirrors may allow for a better mode discrimination and provide further insights into the limitations and imperfections of our lens-mirrors.

**Beyond concentricity** It is a rather surprising observation that the diffraction loss is still relatively low for the fundamental mode in the beyond-concentric regime. It may be interesting to engineer atom-cavity coupling with this “beyond-concentric cavity”, and examine the difference, if any, with the stable cavities.

# Chapter 8

## Outlook and Future Studies

The thesis has so far investigated a few aspects and features of a near-concentric cavity. It may be a good exercise to evaluate the current state of the project and how to proceed. Weighing in some of the technical challenges, I propose to redesign the mechanical structures and the cavity mirrors, which would expedite future explorations. Finally, I give a brief outlook on how near-concentric cavities can be applied in various systems.

### 8.1 Current and Future Capabilities

With the latest cavity design version 2b, we have managed to trap atoms in the intra-cavity trapping sites. The cavity finesse is 484(9), which is the highest achieved yet for our near-concentric cavity under vacuum conditions. With the same operating conditions in Chapter 4, we expect a cooperativity of  $C = 0.3$ . This value can be further enhanced to  $C > 1$  by operating the cavity at the last stable resonance and targeting the atomic cycling transition (see Section 4.2.3).

Owing to the passive damping technique with appropriately placed friction dampers (see Section 6.2), the mechanical noise of the cavity is around 0.16 nm, with a noise effect factor of around 0.2 (see Equation 2.5). This noise level is within our target, but slightly on the high side – the next step is to examine to what extent this noise level affects the atom-cavity experiment.

We have developed a method to efficiently couple an external light to the cavity transverse modes (see Chapter 5). With the current system, it would be very interesting to examine the atom-cavity coupling with a few of the near-degenerate transverse modes. It would also be beneficial to understand further how the current

mirror aperture size is limited (see Chapter 7), which may allow the atom-cavity coupling with the transverse modes to be performed at the last stable resonance.

**Towards a near-concentric cavity quantum gate** A significant milestone to reach with the near-concentric cavity is the implementation of a quantum gate between two qubits. A control phase-flip gate between two single photons can be implemented via a cavity with a trapped single atom [327] – along with single qubit gates, the control phase-flip gate forms a set of universal quantum gates. Such quantum gates have been demonstrated recently in small cavities, first between a photon and an atom [106], and later between two photons [107].

The implementation of a quantum gate typically employs an asymmetric cavity, where one mirror has a much higher reflectivity than the other mirror, which allows one-sided cavity input/output channel. Furthermore, an asymmetric cavity system straightforwardly implements a control phase-flip – if the cavity is resonant with the atom, an incoming resonant photon acquires an additional  $\pi$  phase shift upon reflection. Thus, to use our cavity system as a quantum gate, we would need to replace one of the cavity mirror with another mirror of a much higher reflectivity. With this adjustment, the cavity decay rate would reduce by half, and our cavity would most likely operate in a fast cavity regime ( $\kappa \gg g \gg \gamma$  with  $C \gg 1$ ).

Even though being in a strong-coupling regime ( $g \gg \kappa, \gamma$ ) is beneficial for quantum gates, it may not be necessary. Several quantum gate proposals do not strictly require strong coupling, and can be operated in the fast cavity regime as only high cooperativity ( $C \gg 1$ ) is necessary [207, 328]. Furthermore, some probabilistic implementations of a control phase gate only require a relatively low cooperativity of  $C > 0.5$ , with a success probability that increases for higher cooperativity values [329]. This may not be entirely surprising, as a “deterministic” atom-light interaction is reached with high cooperativity (see Section 1.4.2), and the coherence of the quantum system can still be observed despite a high cavity decoherence [204].

## 8.2 Cavity Setup and Mirror Redesign

The main technical challenge in operating the near-concentric cavity setup is the mechanical noise. To address that, we have developed two noise reduction methods

(see Chapter 6) which result in a tolerable noise level for our current setup. However, the noise level may not be low enough to operate a near-concentric cavity with a higher finesse. We recently examined a different cavity mounting strategy, which displays a much lower mechanical noise in some of the preliminary measurements. The setup is pretty compact, and uses inexpensive actuators. This forthcoming redesign may allow us to operate a near-concentric cavity with much higher finesse.

### 8.2.1 Mechanical structure redesign

The earlier cavity mechanical designs used three-dimensional translation stages (see Section 2.2.2). This resulted in relatively bulky designs, with the moving arms projected outwards and supported only at one end. This cantilever mounting strategy typically displays “tuning-fork” modes, with one of them vibrating along the cavity axis. The flexural translation stages used for cavity version 2 designs in particular bore cantilever structures on each of the actuation directions. These design choices might have not been optimal, but were necessary due to the required movement ranges and space constraints.

Previous experiments in our group show that a much lower cavity mechanical noise can be achieved with a cage or cage-like structure (see Chapter 5 in Ref. [98]). Thus, it would be appropriate to mount the near-concentric cavity as such and without any cantilever, while allowing for three directional movement. Recently, we discovered a cavity mounting strategy with cage support, which provides translation movement along the cavity axis and rotation movements in the transverse directions.

Figure 8.1 shows a prototypical design of the cavity mechanical structure with such mounting strategy. Three linear actuators are placed in-between the mirror mounts, on three corners. Translation along the cavity axis is provided by extending the length of all three actuators, while rotations on the two transverse directions (tip and tilt) are provided by differentially extending the length of the actuators. A “fourth” linear actuator, on the remaining corner, is not necessary, as its length is already predetermined by the other three actuators. In the near-concentric cavity, any transverse misalignment can be corrected by rotational alignment, and vice versa (see Appendix B). Thus, a set of linear, tip and tilt actuations would provide all the necessary degrees of freedom for near-concentric cavity alignment.

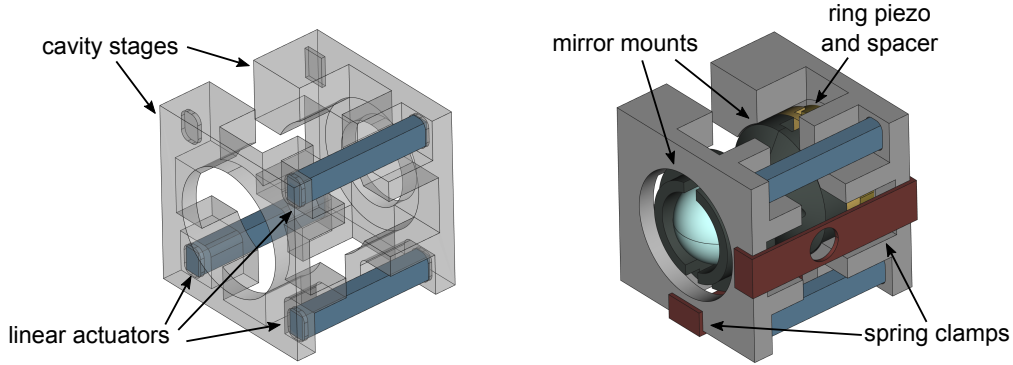


Figure 8.1: Prototype of the cavity mechanical redesign, with the placement of the actuators (left) and the assembled setup (right). The setup is held together by the spring clamps, and the ring piezo may be optional.

The linear actuators suitable for the setup require small cross sections and are capable of producing large movements. We use a stack multilayer piezo actuator (P-882.51, Physik Instrumente) with size  $3 \times 2 \times 18$  mm and a maximum linear travel range of  $18 \mu\text{m}$ . With a designed spacing between the corners of 16 mm, this setup could provide tip and tilt rotation up to  $\delta\alpha = 1.1$  mrad – equivalent to a transverse misalignment correction of around  $6.2 \mu\text{m}$ . A larger range of rotational movement can be achieved by lowering the spacing between the actuators, or by using actuators with larger travel ranges.

There are several methods to mount the actuators. One method is to spring-load the setup to provide compression forces along the actuators. In Figure 8.1 (right), the springs are made from bent metal sheets with a spring constant of around  $70 \text{ N/mm}$ , which could produce a compression force of 70 N for a spring length extension of 1 mm. Nevertheless, it is not yet known whether the alignment can withstand a large impact force or temperature cycling during the vacuum bake-out procedure. Alternatively, the actuators can be glued on the mirror mounts with an epoxy. Even though there is a chance of breaking the actuators while disassembling the setup, the replacement cost of the actuator is pretty inexpensive.

To characterise a typical mechanical noise of such setup, we build a test cavity using less-curved mirrors with higher reflectivities. The test cavity is operated in the near-planar regime with a measured finesse of  $\mathcal{F} = 5600(200)$ . Figure 8.2 shows the noise spectral density of the test cavity, obtained using the method described in

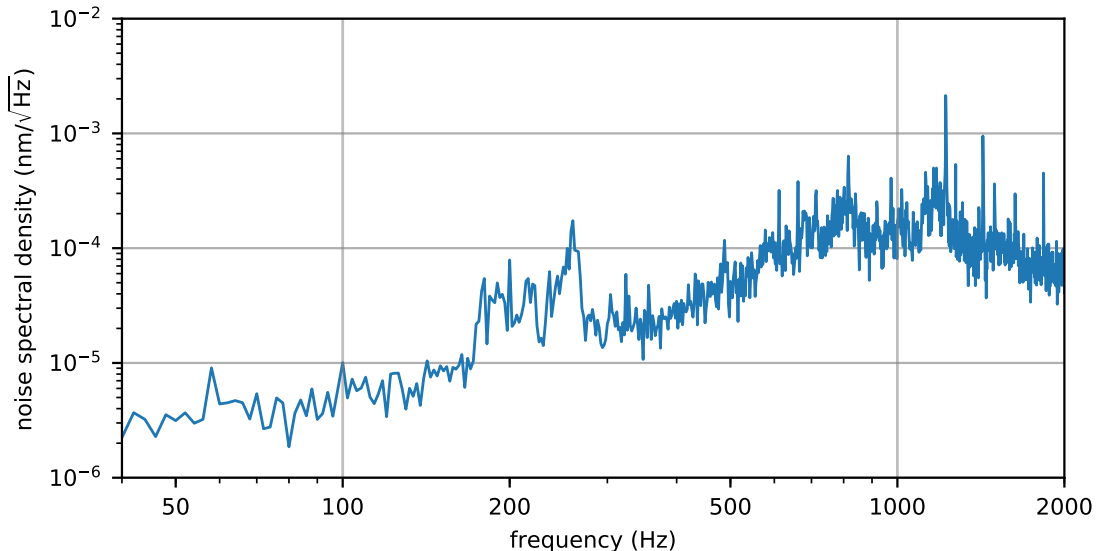


Figure 8.2: A typical mechanical noise spectral density in cavity version 3 (averaged over 5 traces), obtained with a PI control loop on the actuators. The noise around the 1 kHz region is due to the laser frequency noise.

Section 6.1.1. The total mechanical noise is around  $10(1)$  pm without the active and passive noise reduction techniques described in Chapter 6, and is much lower than in previous design versions. With such a low mechanical noise, we can operate a near-concentric cavity up to around  $\mathcal{F} = 8000$  to keep within the target noise level.

Interestingly, the ECDL used for the noise measurement (see Section 3.1.1) has a frequency noise of around 0.5 MHz, which limits the noise measurement resolution to be around 10 pm. This indicates that the real mechanical noise of the cavity is most likely lower than 10 pm, and we probably need a laser with a much lower frequency noise.

## 8.2.2 Cavity mirror redesign

Increasing the finesse of the cavity allows us to reduce the cavity decay rate  $\kappa$  and obtain higher atom-cavity cooperativity  $C$ . With the mechanical structure redesign, a cavity with a finesse of  $\mathcal{F} = 8000$  allows the system to be operated in the strong coupling regime – with the same operating condition in Section 4.2.3, the cavity parameters are  $[g, \kappa, \gamma] \approx 2\pi \times [5, 0.9, 3]$  MHz with  $C \approx 4.6$ . With the

maximum estimated atom-cavity coupling  $g = 2\pi \times 17.3$  MHz at the last stable resonance (see Section 2.1.2), the cooperativity is estimated to reach  $C \approx 55$ .

Due to the optical coating deposition, the curved mirror does not have consistently high reflectivity over the whole surface, as the thickness of the optical coating decreases at larger ray angle (see Appendix C). In an optical coating simulation (see Figure C.2), the effective finesse drops to half at about 20 degrees of the ray angle. Meanwhile, the effective aperture size of the cavity mirrors is currently limited to around 1.4 mm (see Section 7.2.1), which corresponds to only around 7.5 degrees of the ray angle. With a further understanding on how the aperture size is limited, it may be possible to design optical surfaces or coatings which allow for a larger effective aperture size. On the other hand, it is probably not unreasonable to use cavity mirrors with small aperture sizes, due to the relative ease of manufacturing.

Furthermore, it would also be interesting to vary the mirror radii in future designs, as the atom-cavity coupling strength at the last stable resonance varies as  $g \propto R^{-3/4}$  with the mirror radii  $R$  (see Equation 2.3). A larger mirror radii allows a larger mirror separation with lower coupling strength as a trade-off, and vice versa. Alternatively, using cavity mirrors with different radii might also be beneficial for some applications – for example, a geometrically asymmetrical cavity provides a much higher misalignment tolerance compared to the near-concentric cavity [211].

### 8.3 Near-Concentric Cavity Pathways

In this section, we present a few possible research directions where a near-concentric cavity might play a significant role. First, we note that near-concentric cavities can function like any small cavities with high atom-cavity coupling, which would make them a viable alternative for quantum information processing applications. On top of that, near-concentric cavities have a few additional features: (1) a large physical separation between the cavity mirrors, (2) a lower requirement for the cavity finesse with a strong-focusing geometry, and (3) the near-degeneracy of the cavity transverse modes. By pairing them with various systems, we can form a matrix of possible areas that can benefit from near-concentric cavities, as summarised in Table 8.1.

There are a few entries in the matrix that are particularly thought-provoking.

## CHAPTER 8. OUTLOOK AND FUTURE STUDIES

First, deep optical dipole traps can be used to study the nonlinear breakdown of the atomic hyperfine structure [330], and to trap ions [331, 332] or molecules [333] optically. Typically, trapping ions with optical dipole force requires a high-powered laser ( $\sim 10$  W) with a large detuning ( $\sim 10^6\gamma$ ), and focused down to a small beam waist ( $\sim 1$   $\mu\text{m}$ ) to produce a trap depth on the order of 10 mK [334, 335]. A near-concentric cavity could be an appropriate choice to produce such deep dipole traps with a much lower laser power, due to the intra-cavity light amplification and small beam waist, and with an added benefit of a strong coupling.

Second, owing to the small beam waist of the near concentric cavity, the cavity transverse modes can be used to generate trapping sites for atomic arrays. The spacing between the sites is on the order of wavelengths, and the trapping potential can be varied by sending in a superposition of transverse modes. The trap array can be useful to study long-range interaction between Rydberg atoms.

Another intriguing use of a near-concentric optical cavity is in biochemical sensing application, particularly in the current global situation [336]. Optical cavities were used to enhance the sensitivity of Raman spectroscopy [337]. Subsequently, cavity ringdown spectroscopy has been used for breath analysis [338], and detection of explosives [339] and laboratory gas samples [340]. Recently, there are efforts to apply near-concentric cavities to enhance the detection of biochemical samples [341, 342]. It would be pretty amusing to utilise near-concentric cavities, with much smaller beam waists, to help identifying some infectious agents with much higher sensitivities.

Applications	Near-concentric cavity features			Transverse modes near-degeneracy
	High atom-cavity coupling strength	Large cavity mirror separation	Lower finesse req. & focusing geometry	
Quantum interfaces	Quantum info. processing	Ions and Rydberg atoms in a cavity	Higher tolerance for mirror losses; deep optical dipole traps	Multi-channel photonic modes
Single-photon sources	Photon temporal profile shaping			
Atomic ensembles	Strongly-coupled atomic arrays	Large atomic ensemble size	Trapping sites with transverse modes	Degenerate interaction
Pseudo-atomic systems	Quantum info. processing	Ease of implementation in some systems		All of the above
Cavity opto-mechanical systems	Coherent interaction with mesoscopic objects			

Table 8.1: Explorations pathways in near-concentric cavities, with their features exhibited in various systems (non-exhaustive). List of abbreviations: req. – requirements, info. – information.

# Chapter 9

## Conclusion

In the study of atom-light interaction, optical resonators are immensely useful. They preserve the system coherence, enabling quantum information processing, and various other applications. Emerging in different forms and geometries, they satisfy various constraints and functions, creating new possibilities for a society of explorers.

Amidst near-concentric optical cavities, atoms can be addressed and manipulated, with tightly focused optical modes, and in a large physical space.

The finesse can be relatively small, easing the mirror specification.

The resonances can be near-degenerate, with new potentials for multi-mode interactions.

In this thesis, we have described the design of the near-concentric optical cavity (Chapter 2). The optical cavity is formed by two anaclastic lens-mirrors with a relatively low finesse of  $\sim 630$ . Even with this finesse, the estimated atom-cavity coupling strength and cooperativity is comparable to the state-of-the-art planar cavities with micron-sized lengths. To align the cavity, we used a translation stage that can move in three directions – piezo stack actuators (version 1 designs)

and flexural translation stage (version 2 designs). The experimental setup and techniques to operate the cavity are presented in Chapter 3, whereas the transverse alignment stabilisation and the critical distance measurement are specific only to the near-concentric cavity.

We observed strong interaction with single atoms using our near-concentric cavity (Chapter 3). Owing to a large physical space, a cold atomic cloud was produced at the centre of the cavity with a magneto-optical trap. A single atom can then be loaded into the trapping sites along the cavity mode, with a far-off resonant trap. The presence of single atom inside the cavity mode modified the cavity transmission and reflection spectra. From these spectra, we characterised atom-cavity coupling strength of  $g = 2\pi \times 5.0(2)$  MHz, which exceeds the natural atomic decay. Unfortunately, we accidentally contaminated the cavity mirrors and decreased the cavity finesse to  $138(2)$ , resulting in a relatively low atom-cavity cooperativity of  $0.084(4)$ . In subsequent iterations, the cooperativity will increase with higher-finesse cavities.

The transverse modes of the near-concentric cavity are near-degenerate, with frequency spacings on the order of the hyperfine or Zeeman splitting of the atoms. Radial modes are particularly interesting, as they have the same atom-cavity coupling strength as the fundamental mode. We explore this feature by exciting the transverse modes of our near-concentric cavity using a spatial light modulator (Chapter 5). We managed to achieve mode-matching efficiencies close to the theoretical predictions, on both single and superposition of the transverse modes.

To reduce the mechanical noise of the near-concentric cavity, we have developed two noise reduction methods (Chapter 6). First, we developed a digital filter to shape the phase of the error signal, and reduce the noise via a control loop. We managed to observe noise reduction from  $\sim 1$  nm to  $\sim 0.4$  nm. Second, we achieved a higher passive stability of  $\sim 0.17$  nm by installing friction dampers across the cavity mirror mounts. The noise reduction allows us to perform experiment with atoms using higher finesse cavities.

Our near-concentric cavity can be operated extremely close to the critical point (Chapter 7). We successfully aligned our near-concentric cavity at the last stable resonance, with a relatively low diffraction loss for the fundamental mode. Diffraction losses of the higher-order transverse modes revealed an effective aperture diameter of

around 1.4 mm. These discussions around the critical point allow us to understand the limits of the near-concentric cavity, and suggest possible improvements and upgrades in future designs.

Our current setup is a proof-of-concept and testbed for a versatile and robust quantum system employing a near-concentric geometry. We discuss future plans for this project in Chapter 8. In the near-future, we plan on improving the design of the cavity mirrors and mechanical structures, and exploring some quantum nonlinear properties with the near-concentric cavity modes. We conclude with an outlook of the project, on how it can be potentially applied in various systems and disciplines.

With every bit of new understanding,  
sparking fresh perspectives and insights,  
rediscovering previously forgotten,  
time-invariant are quantum technologies. □

# Bibliography

- <sup>1</sup>A. Perot and C. Fabry, “On the application of interference phenomena to the solution of various problems of spectroscopy and metrology”, *The Astrophysical Journal* **9**, 87 (1899).
- <sup>2</sup>J. Strong, “On a method of decreasing the reflection from nonmetallic substances”, *JOSA* **26**, 73–74 (1936).
- <sup>3</sup>A. Thelen, “The pioneering contributions of w. geffcken”, *Thin Films on Glass*. Springer-Verlag, 227–239 (1997).
- <sup>4</sup>A. Macleod, “The early days of optical coatings”, *Journal of Optics A: Pure and Applied Optics* **1**, 779 (1999).
- <sup>5</sup>F. Abels, “Recherches sur la propagation des ondes electromagnetiques sinusoidales dans les milieux stratifies - application aux couches minces”, *Ann. Phys.* **12**, 596–640 (1950).
- <sup>6</sup>M. Banning, “Practical methods of making and using multilayer filters”, *JOSA* **37**, 792–797 (1947).
- <sup>7</sup>A. Turner, “Some current developments in multilayer optical films”, *J. phys. radium* **11**, 444–460 (1950).
- <sup>8</sup>T. H. Maiman, “Stimulated optical radiation in ruby”, *Nature* **187**, 493–494 (1960).
- <sup>9</sup>R. N. Hall, G. E. Fenner, J. Kingsley, T. Soltys, and R. Carlson, “Coherent light emission from gaas junctions”, *Physical Review Letters* **9**, 366 (1962).
- <sup>10</sup>A. L. Schawlow and C. H. Townes, “Infrared and optical masers”, *Physical Review* **112**, 1940 (1958).
- <sup>11</sup>G. D. Boyd and J. P. Gordon, “Confocal multimode resonator for millimeter through optical wavelength masers”, *Bell System Technical Journal* **40**, 489–508 (1961).

## BIBLIOGRAPHY

- <sup>12</sup>A. G. Fox and T. Li, “Resonant modes in a maser interferometer”, *Bell System Technical Journal* **40**, 453–488 (1961).
- <sup>13</sup>G. D. Boyd and H. Kogelnik, “Generalized confocal resonator theory”, *Bell System Technical Journal* **41**, 1347–1369 (1962).
- <sup>14</sup>H. Kogelnik and T. Li, “Laser beams and resonators”, *Applied optics* **5**, 1550–1567 (1966).
- <sup>15</sup>J. Sites, P. Gilstrap, and R. Rujkorakarn, “Ion beam sputter deposition of optical coatings”, *Optical Engineering* **22**, 224447 (1983).
- <sup>16</sup>G. Rempe, R. Thompson, H. J. Kimble, and R. Lalezari, “Measurement of ultralow losses in an optical interferometer”, *Optics letters* **17**, 363–365 (1992).
- <sup>17</sup>R. Thompson, G. Rempe, and H. Kimble, “Observation of normal-mode splitting for an atom in an optical cavity”, *Physical review letters* **68**, 1132 (1992).
- <sup>18</sup>A. Reiserer and G. Rempe, “Cavity-based quantum networks with single atoms and optical photons”, *Reviews of Modern Physics* **87**, 1379 (2015).
- <sup>19</sup>J. Ye and T. W. Lynn, “Applications of optical cavities in modern atomic, molecular, and optical physics”, *Advances in Atomic, Molecular, and Optical Physics* **49**, 1–83 (2003).
- <sup>20</sup>N. Hinkley, J. A. Sherman, N. B. Phillips, M. Schioppo, N. D. Lemke, K. Beloy, M. Pizzocaro, C. W. Oates, and A. D. Ludlow, “An atomic clock with 10–18 instability”, *Science* **341**, 1215–1218 (2013).
- <sup>21</sup>R. Wagner, F. Guzman, A. Chijioke, G. K. Gulati, M. Keller, and G. Shaw, “Direct measurement of radiation pressure and circulating power inside a passive optical cavity”, *Optics express* **26**, 23492–23506 (2018).
- <sup>22</sup>R. A. Wolthuis, G. L. Mitchell, E. Saaski, J. C. Hartl, and M. A. Afromowitz, “Development of medical pressure and temperature sensors employing optical spectrum modulation”, *IEEE Transactions on Biomedical Engineering* **38**, 974–981 (1991).
- <sup>23</sup>M. Singh, C. Tuck, and G. Fernando, “Multiplexed optical fibre fabry-perot sensors for strain metrology”, *Smart materials and structures* **8**, 549 (1999).

## BIBLIOGRAPHY

- <sup>24</sup>M. J. Thorpe, D. Balslev-Clausen, M. S. Kirchner, and J. Ye, “Cavity-enhanced optical frequency comb spectroscopy: application to human breath analysis”, *Optics Express* **16**, 2387–2397 (2008).
- <sup>25</sup>G. Gagliardi and H.-P. Loock, “Cavity-enhanced spectroscopy and sensing”, Vol. 179 (Springer, 2014).
- <sup>26</sup>C. Eisele, A. Y. Nevsky, and S. Schiller, “Laboratory test of the isotropy of light propagation at the 10- 17 level”, *Physical Review Letters* **103**, 090401 (2009).
- <sup>27</sup>A. Abramovici, W. E. Althouse, R. W. Drever, Y. Gursel, S. Kawamura, F. J. Raab, D. Shoemaker, L. Sievers, R. E. Spero, K. S. Thorne, et al., “Ligo: the laser interferometer gravitational-wave observatory”, *science* **256**, 325–333 (1992).
- <sup>28</sup>B. P. Abbott, R. Abbott, T. Abbott, M. Abernathy, F. Acernese, K. Ackley, C. Adams, T. Adams, P. Addesso, R. Adhikari, et al., “Gw150914: the advanced ligo detectors in the era of first discoveries”, *Physical review letters* **116**, 131103 (2016).
- <sup>29</sup>E. Schrödinger, “Are there quantum jumps? part ii”, *The British Journal for the Philosophy of science* **3**, 233–242 (1952).
- <sup>30</sup>J.-M. Raimond, M. Brune, and S. Haroche, “Manipulating quantum entanglement with atoms and photons in a cavity”, *Reviews of Modern Physics* **73**, 565 (2001).
- <sup>31</sup>S. Haroche, “Nobel lecture: controlling photons in a box and exploring the quantum to classical boundary”, *Reviews of Modern Physics* **85**, 1083 (2013).
- <sup>32</sup>M. Gross, P. Goy, C. Fabre, S. Haroche, and J. Raimond, “Maser oscillation and microwave superradiance in small systems of rydberg atoms”, *Physical Review Letters* **43**, 343 (1979).
- <sup>33</sup>D. Meschede, H. Walther, and G. Müller, “One-atom maser”, *Physical review letters* **54**, 551 (1985).
- <sup>34</sup>M. Brune, F. Schmidt-Kaler, A. Maali, J. Dreyer, E. Hagley, J. Raimond, and S. Haroche, “Quantum rabi oscillation: a direct test of field quantization in a cavity”, *Physical review letters* **76**, 1800 (1996).

## BIBLIOGRAPHY

- <sup>35</sup>M. Brune, E. Hagley, J. Dreyer, X. Maitre, A. Maali, C. Wunderlich, J. Raimond, and S. Haroche, “Observing the progressive decoherence of the “meter” in a quantum measurement”, *Physical Review Letters* **77**, 4887 (1996).
- <sup>36</sup>T. Meunier, S. Gleyzes, P. Maioli, A. Auffeves, G. Nogues, M. Brune, J. Raimond, and S. Haroche, “Rabi oscillations revival induced by time reversal: a test of mesoscopic quantum coherence”, *Physical review letters* **94**, 010401 (2005).
- <sup>37</sup>S. Gleyzes, S. Kuhr, C. Guerlin, J. Bernu, S. Deleglise, U. B. Hoff, M. Brune, J.-M. Raimond, and S. Haroche, “Quantum jumps of light recording the birth and death of a photon in a cavity”, *Nature* **446**, 297–300 (2007).
- <sup>38</sup>S. Deleglise, I. Dotsenko, C. Sayrin, J. Bernu, M. Brune, J.-M. Raimond, and S. Haroche, “Reconstruction of non-classical cavity field states with snapshots of their decoherence”, *Nature* **455**, 510–514 (2008).
- <sup>39</sup>X. Maitre, E. Hagley, G. Nogues, C. Wunderlich, P. Goy, M. Brune, J. Raimond, and S. Haroche, “Quantum memory with a single photon in a cavity”, *Physical review letters* **79**, 769 (1997).
- <sup>40</sup>A. Rauschenbeutel, G. Nogues, S. Osnaghi, P. Bertet, M. Brune, J.-M. Raimond, and S. Haroche, “Coherent operation of a tunable quantum phase gate in cavity qed”, *Physical Review Letters* **83**, 5166 (1999).
- <sup>41</sup>A. Rauschenbeutel, G. Nogues, S. Osnaghi, P. Bertet, M. Brune, J.-M. Raimond, and S. Haroche, “Step-by-step engineered multiparticle entanglement”, *Science* **288**, 2024–2028 (2000).
- <sup>42</sup>D. E. Chang, V. Vuletić, and M. D. Lukin, “Quantum nonlinear optics—photon by photon”, *Nature Photonics* **8**, 685–694 (2014).
- <sup>43</sup>R. Schoelkopf and S. Girvin, “Wiring up quantum systems”, *Nature* **451**, 664–669 (2008).
- <sup>44</sup>M. H. Devoret and R. J. Schoelkopf, “Superconducting circuits for quantum information: an outlook”, *Science* **339**, 1169–1174 (2013).
- <sup>45</sup>F. Arute, K. Arya, R. Babbush, D. Bacon, J. C. Bardin, R. Barends, R. Biswas, S. Boixo, F. G. Brandao, D. A. Buell, et al., “Quantum supremacy using a programmable superconducting processor”, *Nature* **574**, 505–510 (2019).

## BIBLIOGRAPHY

- <sup>46</sup>D. Leibfried, R. Blatt, C. Monroe, and D. Wineland, “Quantum dynamics of single trapped ions”, *Reviews of Modern Physics* **75**, 281 (2003).
- <sup>47</sup>D. J. Wineland, “Nobel lecture: superposition, entanglement, and raising schrodinger’s cat”, *Reviews of Modern Physics* **85**, 1103 (2013).
- <sup>48</sup>W. Neuhauser, M. Hohenstatt, P. Toschek, and H. Dehmelt, “Optical-sideband cooling of visible atom cloud confined in parabolic well”, *Physical Review Letters* **41**, 233 (1978).
- <sup>49</sup>D. J. Wineland, R. E. Drullinger, and F. L. Walls, “Radiation-pressure cooling of bound resonant absorbers”, *Physical Review Letters* **40**, 1639 (1978).
- <sup>50</sup>F. Diedrich, J. Bergquist, W. M. Itano, and D. Wineland, “Laser cooling to the zero-point energy of motion”, *Physical Review Letters* **62**, 403 (1989).
- <sup>51</sup>D. Meekhof, C. Monroe, B. King, W. M. Itano, and D. J. Wineland, “Generation of nonclassical motional states of a trapped atom”, *Physical Review Letters* **76**, 1796 (1996).
- <sup>52</sup>J. I. Cirac and P. Zoller, “Quantum computations with cold trapped ions”, *Physical review letters* **74**, 4091 (1995).
- <sup>53</sup>C. Monroe, D. M. Meekhof, B. E. King, W. M. Itano, and D. J. Wineland, “Demonstration of a fundamental quantum logic gate”, *Physical review letters* **75**, 4714 (1995).
- <sup>54</sup>K. Wright, K. Beck, S. Debnath, J. Amini, Y. Nam, N. Grzesiak, J.-S. Chen, N. Pimenti, M. Chmielewski, C. Collins, et al., “Benchmarking an 11-qubit quantum computer”, *Nature communications* **10**, 1–6 (2019).
- <sup>55</sup>N. M. Linke, D. Maslov, M. Roetteler, S. Debnath, C. Figgatt, K. A. Landsman, K. Wright, and C. Monroe, “Experimental comparison of two quantum computing architectures”, *Proceedings of the National Academy of Sciences* **114**, 3305–3310 (2017).
- <sup>56</sup>S. Blinov, B. Wu, and C. Monroe, “Comparison of cloud-based ion trap and superconducting quantum computer architectures”, arXiv preprint arXiv:2102.00371 (2021).

## BIBLIOGRAPHY

- <sup>57</sup>G. Rempe, R. Thompson, R. Brecha, W. Lee, and H. Kimble, “Optical bistability and photon statistics in cavity quantum electrodynamics”, *Physical Review Letters* **67**, 1727 (1991).
- <sup>58</sup>R. Brecha, L. Orozco, M. Raizen, M. Xiao, and H. Kimble, “Observation of oscillatory energy exchange in a coupled-atom-cavity system”, *JOSA B* **12**, 2329–2339 (1995).
- <sup>59</sup>C. Hood, M. Chapman, T. Lynn, and H. Kimble, “Real-time cavity qed with single atoms”, *Physical review letters* **80**, 4157 (1998).
- <sup>60</sup>J. Childs, K. An, M. Otteson, R. Dasari, and M. Feld, “Normal-mode line shapes for atoms in standing-wave optical resonators”, *Physical review letters* **77**, 2901 (1996).
- <sup>61</sup>S. Mielke, G. Foster, and L. Orozco, “Nonclassical intensity correlations in cavity qed”, *Physical review letters* **80**, 3948 (1998).
- <sup>62</sup>M. Hennrich, A. Kuhn, and G. Rempe, “Transition from antibunching to bunching in cavity qed”, *Physical review letters* **94**, 053604 (2005).
- <sup>63</sup>Q. A. Turchette, C. J. Hood, W. Lange, H. Mabuchi, and H. J. Kimble, “Measurement of conditional phase shifts for quantum logic”, *Physical Review Letters* **75**, 4710 (1995).
- <sup>64</sup>P. Münstermann, T. Fischer, P. Maunz, P. Pinkse, and G. Rempe, “Dynamics of single-atom motion observed in a high-finesse cavity”, *Physical review letters* **82**, 3791 (1999).
- <sup>65</sup>J. Ye, D. Vernooy, and H. Kimble, “Trapping of single atoms in cavity qed”, *Physical Review Letters* **83**, 4987 (1999).
- <sup>66</sup>C. J. Hood, T. Lynn, A. Doherty, A. Parkins, and H. Kimble, “The atom-cavity microscope: single atoms bound in orbit by single photons”, *Science* **287**, 1447–1453 (2000).
- <sup>67</sup>P. Pinkse, T. Fischer, P. Maunz, and G. Rempe, “Trapping an atom with single photons”, *Nature* **404**, 365–368 (2000).

## BIBLIOGRAPHY

- <sup>68</sup>J. McKeever, J. Buck, A. Boozer, A. Kuzmich, H.-C. Nägerl, D. Stamper-Kurn, and H. Kimble, “State-insensitive cooling and trapping of single atoms in an optical cavity”, *Physical review letters* **90**, 133602 (2003).
- <sup>69</sup>S. Nußmann, K. Murr, M. Hijlkema, B. Weber, A. Kuhn, and G. Rempe, “Vacuum-stimulated cooling of single atoms in three dimensions”, *Nature Physics* **1**, 122–125 (2005).
- <sup>70</sup>A. Boca, R. Miller, K. Birnbaum, A. Boozer, J. McKeever, and H. Kimble, “Observation of the vacuum rabi spectrum for one trapped atom”, *Physical Review Letters* **93**, 233603 (2004).
- <sup>71</sup>P. Maunz, T. Puppe, I. Schuster, N. Syassen, P. W. Pinkse, and G. Rempe, “Normal-mode spectroscopy of a single-bound-atom–cavity system”, *Physical review letters* **94**, 033002 (2005).
- <sup>72</sup>S. Morin, C. Yu, and T. Mossberg, “Strong atom-cavity coupling over large volumes and the observation of subnatural intracavity atomic linewidths”, *Physical review letters* **73**, 1489 (1994).
- <sup>73</sup>E. M. Purcell, H. C. Torrey, and R. V. Pound, “Resonance absorption by nuclear magnetic moments in a solid”, *Physical review* **69**, 37 (1946).
- <sup>74</sup>D. Kleppner, “Inhibited spontaneous emission”, *Physical review letters* **47**, 233 (1981).
- <sup>75</sup>M. K. Tey, Z. Chen, S. A. Aljunid, B. Chng, F. Huber, G. Maslennikov, and C. Kurtsiefer, “Strong interaction between light and a single trapped atom without the need for a cavity”, *Nature Physics* **4**, 924–927 (2008).
- <sup>76</sup>S. A. Aljunid, M. K. Tey, B. Chng, T. Liew, G. Maslennikov, V. Scarani, and C. Kurtsiefer, “Phase shift of a weak coherent beam induced by a single atom”, *Physical review letters* **103**, 153601 (2009).
- <sup>77</sup>S. A. Aljunid, B. Chng, J. Lee, M. Paesold, G. Maslennikov, and C. Kurtsiefer, “Interaction of light with a single atom in the strong focusing regime”, *Journal of Modern Optics* **58**, 299–305 (2011).
- <sup>78</sup>K. Durak, C. H. Nguyen, V. Leong, S. Straupe, and C. Kurtsiefer, “Diffraction-limited fabry–perot cavity in the near concentric regime”, *New Journal of Physics* **16**, 103002 (2014).

## BIBLIOGRAPHY

- <sup>79</sup>C. H. Nguyen, A. N. Utama, N. Lewty, K. Durak, G. Maslennikov, S. Straupe, M. Steiner, and C. Kurtsiefer, “Single atoms coupled to a near-concentric cavity”, *Physical Review A* **96**, 031802 (2017).
- <sup>80</sup>C. H. Nguyen, A. N. Utama, N. Lewty, and C. Kurtsiefer, “Operating a near-concentric cavity at the last stable resonance”, *Physical Review A* **98**, 063833 (2018).
- <sup>81</sup>A. N. Utama, C. H. Chow, C. H. Nguyen, and C. Kurtsiefer, “Coupling light to higher order transverse modes of a near-concentric optical cavity”, *Optics Express* **29**, 8130–8141 (2021).
- <sup>82</sup>A. N. Utama, J. P. N. Chen, and C. Kurtsiefer, “Passive stabilization of optical interferometers with friction dampers”, *Manuscript in preparation*, 2021.
- <sup>83</sup>M. Harlander, M. Brownnutt, W. Hänsel, and R. Blatt, “Trapped-ion probing of light-induced charging effects on dielectrics”, *New Journal of Physics* **12**, 093035 (2010).
- <sup>84</sup>A. Stute, B. Casabone, B. Brandstätter, D. Habicher, H. Barros, P. Schmidt, T. Northup, and R. Blatt, “Toward an ion–photon quantum interface in an optical cavity”, *Applied Physics B* **107**, 1145–1157 (2012).
- <sup>85</sup>A. Stute, B. Casabone, B. Brandstätter, K. Friebe, T. Northup, and R. Blatt, “Quantum-state transfer from an ion to a photon”, *Nature photonics* **7**, 219–222 (2013).
- <sup>86</sup>B. Casabone, K. Friebe, B. Brandstätter, K. Schüppert, R. Blatt, and T. Northup, “Enhanced quantum interface with collective ion-cavity coupling”, *Physical review letters* **114**, 023602 (2015).
- <sup>87</sup>M. Lee, K. Friebe, D. A. Fioretto, K. Schüppert, F. R. Ong, D. Plankensteiner, V. Torggler, H. Ritsch, R. Blatt, and T. E. Northup, “Ion-based quantum sensor for optical cavity photon numbers”, *Physical review letters* **122**, 153603 (2019).
- <sup>88</sup>V. Krutyanskiy, M. Meraner, J. Schupp, V. Krcmarsky, H. Hainzer, and B. Lanyon, “Light-matter entanglement over 50 km of optical fibre”, *npj Quantum Information* **5**, 1–5 (2019).

## BIBLIOGRAPHY

- <sup>89</sup>M. Meraner, A. Mazloom, V. Krutyanskiy, V. Krcmarsky, J. Schupp, D. Fioretto, P. Sekatski, T. Northup, N. Sangouard, and B. Lanyon, “Indistinguishable photons from a trapped-ion quantum network node”, *Physical Review A* **102**, 052614 (2020).
- <sup>90</sup>E. J. Davis, G. Bentsen, L. Homeier, T. Li, and M. H. Schleier-Smith, “Photon-mediated spin-exchange dynamics of spin-1 atoms”, *Physical review letters* **122**, 010405 (2019).
- <sup>91</sup>E. J. Davis, A. Periwal, E. S. Cooper, G. Bentsen, S. J. Evered, K. Van Kirk, and M. H. Schleier-Smith, “Protecting spin coherence in a tunable heisenberg model”, *Physical Review Letters* **125**, 060402 (2020).
- <sup>92</sup>K. Ott, S. Garcia, R. Kohlhaas, K. Schüppert, P. Rosenbusch, R. Long, and J. Reichel, “Millimeter-long fiber fabry-perot cavities”, *Optics express* **24**, 9839–9853 (2016).
- <sup>93</sup>G. K. Gulati, H. Takahashi, N. Podoliak, P. Horak, and M. Keller, “Fiber cavities with integrated mode matching optics”, *Scientific reports* **7**, 1–6 (2017).
- <sup>94</sup>R. J. Barbour, P. A. Dalgarno, A. Curran, K. M. Nowak, H. J. Baker, D. R. Hall, N. G. Stoltz, P. M. Petroff, and R. J. Warburton, “A tunable microcavity”, *Journal of Applied Physics* **110**, 053107 (2011).
- <sup>95</sup>R. Albrecht, A. Bommer, C. Deutsch, J. Reichel, and C. Becher, “Coupling of a single nitrogen-vacancy center in diamond to a fiber-based microcavity”, *Physical review letters* **110**, 243602 (2013).
- <sup>96</sup>K. Durak, “A diffraction limited fabry-perot cavity with a strongly focused mode”, PhD thesis (National University of Singapore, 2014).
- <sup>97</sup>C. H. Nguyen, “Single atoms coupled to a near-concentric cavity”, PhD thesis (National University of Singapore, 2018).
- <sup>98</sup>J. P. N. Chen, “Passive stabilisation of optical cavity mounted on 3d piezo scanner”, Bachelor thesis (National University of Singapore, 2020).
- <sup>99</sup>T. Wilk, S. C. Webster, A. Kuhn, and G. Rempe, “Single-atom single-photon quantum interface”, *Science* **317**, 488–490 (2007).

## BIBLIOGRAPHY

- <sup>100</sup>B. B. Blinov, D. L. Moehring, L.-M. Duan, and C. Monroe, “Observation of entanglement between a single trapped atom and a single photon”, *Nature* **428**, 153–157 (2004).
- <sup>101</sup>J. Volz, M. Weber, D. Schlenk, W. Rosenfeld, J. Vrana, K. Saucke, C. Kurtsiefer, and H. Weinfurter, “Observation of entanglement of a single photon with a trapped atom”, *Physical review letters* **96**, 030404 (2006).
- <sup>102</sup>B. Weber, H. P. Specht, T. Müller, J. Bochmann, M. Mücke, D. L. Moehring, and G. Rempe, “Photon-photon entanglement with a single trapped atom”, *Physical review letters* **102**, 030501 (2009).
- <sup>103</sup>H. P. Specht, C. Nölleke, A. Reiserer, M. Uphoff, E. Figueroa, S. Ritter, and G. Rempe, “A single-atom quantum memory”, *Nature* **473**, 190–193 (2011).
- <sup>104</sup>S. Ritter, C. Nölleke, C. Hahn, A. Reiserer, A. Neuzner, M. Uphoff, M. Mücke, E. Figueroa, J. Bochmann, and G. Rempe, “An elementary quantum network of single atoms in optical cavities”, *Nature* **484**, 195–200 (2012).
- <sup>105</sup>H. J. Kimble, “The quantum internet”, *Nature* **453**, 1023–1030 (2008).
- <sup>106</sup>A. Reiserer, N. Kalb, G. Rempe, and S. Ritter, “A quantum gate between a flying optical photon and a single trapped atom”, *Nature* **508**, 237–240 (2014).
- <sup>107</sup>B. Hacker, S. Welte, G. Rempe, and S. Ritter, “A photon–photon quantum gate based on a single atom in an optical resonator”, *Nature* **536**, 193–196 (2016).
- <sup>108</sup>S. Daiss, S. Langenfeld, S. Welte, E. Distante, P. Thomas, L. Hartung, O. Morin, and G. Rempe, “A quantum-logic gate between distant quantum-network modules”, *Science* **371**, 614–617 (2021).
- <sup>109</sup>M. Steiner, H. M. Meyer, C. Deutsch, J. Reichel, and M. Köhl, “Single ion coupled to an optical fiber cavity”, *Physical review letters* **110**, 043003 (2013).
- <sup>110</sup>B. Brandstatter, A. McClung, K. Schuppert, B. Casabone, K. Friebe, A. Stute, P. O. Schmidt, C. Deutsch, J. Reichel, R. Blatt, et al., “Integrated fiber-mirror ion trap for strong ion-cavity coupling”, *Review of scientific instruments* **84**, 123104 (2013).
- <sup>111</sup>H. Takahashi, E. Kassa, C. Christoforou, and M. Keller, “Strong coupling of a single ion to an optical cavity”, *Physical review letters* **124**, 013602 (2020).

## BIBLIOGRAPHY

- <sup>112</sup>P. Kobel, M. Breyer, and M. Köhl, “Deterministic spin-photon entanglement from a trapped ion in a fiber fabry–perot cavity”, *npj Quantum Information* **7**, 1–7 (2021).
- <sup>113</sup>J. McKeever, A. Boca, A. Boozer, R. Miller, J. Buck, A. Kuzmich, and H. Kimble, “Deterministic generation of single photons from one atom trapped in a cavity”, *Science* **303**, 1992–1994 (2004).
- <sup>114</sup>R. H. Brown and R. Q. Twiss, “Correlation between photons in two coherent beams of light”, *Nature* **177**, 27–29 (1956).
- <sup>115</sup>T. Wilk, S. C. Webster, H. P. Specht, G. Rempe, and A. Kuhn, “Polarization-controlled single photons”, *Physical review letters* **98**, 063601 (2007).
- <sup>116</sup>M. Keller, B. Lange, K. Hayasaka, W. Lange, and H. Walther, “Continuous generation of single photons with controlled waveform in an ion-trap cavity system”, *Nature* **431**, 1075–1078 (2004).
- <sup>117</sup>H. Barros, A. Stute, T. Northup, C. Russo, P. Schmidt, and R. Blatt, “Deterministic single-photon source from a single ion”, *New Journal of Physics* **11**, 103004 (2009).
- <sup>118</sup>P. Michler, A. Kiraz, C. Becher, W. Schoenfeld, P. Petroff, L. Zhang, E. Hu, and A. Imamoglu, “A quantum dot single-photon turnstile device”, *science* **290**, 2282–2285 (2000).
- <sup>119</sup>C. Santori, D. Fattal, J. Vuckovic, G. S. Solomon, and Y. Yamamoto, “Indistinguishable photons from a single-photon device”, *nature* **419**, 594–597 (2002).
- <sup>120</sup>A. Kuhn and D. Ljunggren, “Cavity-based single-photon sources”, *Contemporary Physics* **51**, 289–313 (2010).
- <sup>121</sup>P. B. Nisbet-Jones, J. Dille, D. Ljunggren, and A. Kuhn, “Highly efficient source for indistinguishable single photons of controlled shape”, *New Journal of Physics* **13**, 103036 (2011).
- <sup>122</sup>O. Morin, M. Körber, S. Langenfeld, and G. Rempe, “Deterministic shaping and reshaping of single-photon temporal wave functions”, *Physical review letters* **123**, 133602 (2019).

## BIBLIOGRAPHY

- <sup>123</sup>H. P. Specht, J. Bochmann, M. Mücke, B. Weber, E. Figueroa, D. L. Moehring, and G. Rempe, “Phase shaping of single-photon wave packets”, *Nature Photonics* **3**, 469–472 (2009).
- <sup>124</sup>P. G. Kwiat, K. Mattle, H. Weinfurter, A. Zeilinger, A. V. Sergienko, and Y. Shih, “New high-intensity source of polarization-entangled photon pairs”, *Physical Review Letters* **75**, 4337 (1995).
- <sup>125</sup>B. Srivathsan, G. K. Gulati, B. Chng, G. Maslennikov, D. Matsukevich, and C. Kurtsiefer, “Narrow band source of transform-limited photon pairs via four-wave mixing in a cold atomic ensemble”, *Physical review letters* **111**, 123602 (2013).
- <sup>126</sup>C. Schuck, F. Rohde, N. Piro, M. Almendros, J. Huwer, M. Mitchell, M. Hennrich, A. Haase, F. Dubin, and J. Eschner, “Resonant interaction of a single atom with single photons from a down-conversion source”, *Physical Review A* **81**, 011802 (2010).
- <sup>127</sup>E. Meyer-Scott, N. Montaut, J. Tiedau, L. Sansoni, H. Herrmann, T. J. Bartley, and C. Silberhorn, “Limits on the heralding efficiencies and spectral purities of spectrally filtered single photons from photon-pair sources”, *Physical Review A* **95**, 061803 (2017).
- <sup>128</sup>B. Srivathsan, G. K. Gulati, A. Cere, B. Chng, and C. Kurtsiefer, “Reversing the temporal envelope of a heralded single photon using a cavity”, *Physical review letters* **113**, 163601 (2014).
- <sup>129</sup>M. A. Seidler, X. J. Yeo, A. Cerè, and C. Kurtsiefer, “Spectral compression of narrowband single photons with a resonant cavity”, *Physical Review Letters* **125**, 183603 (2020).
- <sup>130</sup>H. Ritsch, P. Domokos, F. Brennecke, and T. Esslinger, “Cold atoms in cavity-generated dynamical optical potentials”, *Reviews of Modern Physics* **85**, 553 (2013).
- <sup>131</sup>P. Maunz, T. Puppe, I. Schuster, N. Syassen, P. W. Pinkse, and G. Rempe, “Cavity cooling of a single atom”, *Nature* **428**, 50–52 (2004).
- <sup>132</sup>A. T. Black, H. W. Chan, and V. Vuletić, “Observation of collective friction forces due to spatial self-organization of atoms: from rayleigh to bragg scattering”, *Physical review letters* **91**, 203001 (2003).

## BIBLIOGRAPHY

- <sup>133</sup>B. Nagorny, T. Elsässer, and A. Hemmerich, “Collective atomic motion in an optical lattice formed inside a high finesse cavity”, *Physical review letters* **91**, 153003 (2003).
- <sup>134</sup>S. Gupta, K. L. Moore, K. W. Murch, and D. M. Stamper-Kurn, “Cavity nonlinear optics at low photon numbers from collective atomic motion”, *Physical review letters* **99**, 213601 (2007).
- <sup>135</sup>F. Brennecke, T. Donner, S. Ritter, T. Bourdel, M. Köhl, and T. Esslinger, “Cavity qed with a bose–einstein condensate”, *Nature* **450**, 268–271 (2007).
- <sup>136</sup>Y. Colombe, T. Steinmetz, G. Dubois, F. Linke, D. Hunger, and J. Reichel, “Strong atom–field coupling for bose–einstein condensates in an optical cavity on a chip”, *Nature* **450**, 272–276 (2007).
- <sup>137</sup>F. Brennecke, S. Ritter, T. Donner, and T. Esslinger, “Cavity optomechanics with a bose-einstein condensate”, *Science* **322**, 235–238 (2008).
- <sup>138</sup>K. Baumann, C. Guerlin, F. Brennecke, and T. Esslinger, “Dicke quantum phase transition with a superfluid gas in an optical cavity”, *nature* **464**, 1301–1306 (2010).
- <sup>139</sup>J. Léonard, A. Morales, P. Zupancic, T. Esslinger, and T. Donner, “Supersolid formation in a quantum gas breaking a continuous translational symmetry”, *Nature* **543**, 87–90 (2017).
- <sup>140</sup>V. D. Vaidya, Y. Guo, R. M. Kroeze, K. E. Ballantine, A. J. Kollar, J. Keeling, and B. L. Lev, “Tunable-range, photon-mediated atomic interactions in multimode cavity qed”, *Physical Review X* **8**, 011002 (2018).
- <sup>141</sup>Y. Guo, R. M. Kroeze, V. D. Vaidya, J. Keeling, and B. L. Lev, “Sign-changing photon-mediated atom interactions in multimode cavity quantum electrodynamics”, *Physical review letters* **122**, 193601 (2019).
- <sup>142</sup>I. D. Leroux, M. H. Schleier-Smith, and V. Vuletić, “Implementation of cavity squeezing of a collective atomic spin”, *Physical Review Letters* **104**, 073602 (2010).
- <sup>143</sup>O. Hosten, R. Krishnakumar, N. J. Engelsen, and M. A. Kasevich, “Quantum phase magnification”, *Science* **352**, 1552–1555 (2016).

## BIBLIOGRAPHY

- <sup>144</sup>M. P. Baden, K. J. Arnold, A. L. Grimsmo, S. Parkins, and M. D. Barrett, “Realization of the dicke model using cavity-assisted raman transitions”, *Physical review letters* **113**, 020408 (2014).
- <sup>145</sup>Z. Zhiqiang, C. H. Lee, R. Kumar, K. Arnold, S. J. Masson, A. Parkins, and M. Barrett, “Nonequilibrium phase transition in a spin-1 dicke model”, *Optica* **4**, 424–429 (2017).
- <sup>146</sup>M. A. Norcia, R. J. Lewis-Swan, J. R. Cline, B. Zhu, A. M. Rey, and J. K. Thompson, “Cavity-mediated collective spin-exchange interactions in a strontium superradiant laser”, *Science* **361**, 259–262 (2018).
- <sup>147</sup>C. Weisbuch, M. Nishioka, A. Ishikawa, and Y. Arakawa, “Observation of the coupled exciton-photon mode splitting in a semiconductor quantum microcavity”, *Physical Review Letters* **69**, 3314 (1992).
- <sup>148</sup>G. Khitrova, H. Gibbs, F. Jahnke, M. Kira, and S. W. Koch, “Nonlinear optics of normal-mode-coupling semiconductor microcavities”, *Reviews of Modern Physics* **71**, 1591 (1999).
- <sup>149</sup>B. Riel, “An introduction to self-assembled quantum dots”, *American Journal of Physics* **76**, 750–757 (2008).
- <sup>150</sup>K. J. Vahala, “Optical microcavities”, *nature* **424**, 839–846 (2003).
- <sup>151</sup>J. P. Reithmaier, G. Sek, A. Löffler, C. Hofmann, S. Kuhn, S. Reitzenstein, L. Keldysh, V. Kulakovskii, T. Reinecke, and A. Forchel, “Strong coupling in a single quantum dot–semiconductor microcavity system”, *Nature* **432**, 197–200 (2004).
- <sup>152</sup>T. Yoshie, A. Scherer, J. Hendrickson, G. Khitrova, H. Gibbs, G. Rupper, C. Ell, O. Shchekin, and D. Deppe, “Vacuum rabi splitting with a single quantum dot in a photonic crystal nanocavity”, *Nature* **432**, 200–203 (2004).
- <sup>153</sup>E. Peter, P. Senellart, D. Martrou, A. Lemaitre, J. Hours, J. Gérard, and J. Bloch, “Exciton-photon strong-coupling regime for a single quantum dot embedded in a microcavity”, *Physical review letters* **95**, 067401 (2005).
- <sup>154</sup>K. Hennessy, A. Badolato, M. Winger, D. Gerace, M. Atature, S. Gulde, S. Falt, E. L. Hu, and A. Imamoglu, “Quantum nature of a strongly coupled single quantum dot–cavity system”, *Nature* **445**, 896–899 (2007).

## BIBLIOGRAPHY

- <sup>155</sup>P. Lodahl, S. Mahmoodian, and S. Stobbe, “Interfacing single photons and single quantum dots with photonic nanostructures”, *Reviews of Modern Physics* **87**, 347 (2015).
- <sup>156</sup>D. D. Awschalom, R. Hanson, J. Wrachtrup, and B. B. Zhou, “Quantum technologies with optically interfaced solid-state spins”, *Nature Photonics* **12**, 516–527 (2018).
- <sup>157</sup>W. Gao, A. Imamoglu, H. Bernien, and R. Hanson, “Coherent manipulation, measurement and entanglement of individual solid-state spins using optical fields”, *Nature Photonics* **9**, 363–373 (2015).
- <sup>158</sup>G. Fuchs, G. Burkard, P. Klimov, and D. Awschalom, “A quantum memory intrinsic to single nitrogen–vacancy centres in diamond”, *Nature Physics* **7**, 789–793 (2011).
- <sup>159</sup>T. H. Taminiau, J. Cramer, T. van der Sar, V. V. Dobrovitski, and R. Hanson, “Universal control and error correction in multi-qubit spin registers in diamond”, *Nature nanotechnology* **9**, 171 (2014).
- <sup>160</sup>A. Faraon, P. E. Barclay, C. Santori, K.-M. C. Fu, and R. G. Beusoleil, “Resonant enhancement of the zero-phonon emission from a colour centre in a diamond cavity”, *Nature Photonics* **5**, 301 (2011).
- <sup>161</sup>D. Riedel, I. Söllner, B. J. Shields, S. Starosielec, P. Appel, E. Neu, P. Maletinsky, and R. J. Warburton, “Deterministic enhancement of coherent photon generation from a nitrogen-vacancy center in ultrapure diamond”, *Physical Review X* **7**, 031040 (2017).
- <sup>162</sup>A. Dorsel, J. D. McCullen, P. Meystre, E. Vignes, and H. Walther, “Optical bistability and mirror confinement induced by radiation pressure”, *Physical Review Letters* **51**, 1550 (1983).
- <sup>163</sup>P.-F. Cohadon, A. Heidmann, and M. Pinard, “Cooling of a mirror by radiation pressure”, *Physical Review Letters* **83**, 3174 (1999).
- <sup>164</sup>C. H. Metzger and K. Karrai, “Cavity cooling of a microlever”, *Nature* **432**, 1002–1005 (2004).
- <sup>165</sup>D. Kleckner and D. Bouwmeester, “Sub-kelvin optical cooling of a micromechanical resonator”, *Nature* **444**, 75–78 (2006).

## BIBLIOGRAPHY

- <sup>166</sup>H. Rokhsari, T. J. Kippenberg, T. Carmon, and K. J. Vahala, “Radiation-pressure-driven micro-mechanical oscillator”, *Optics Express* **13**, 5293–5301 (2005).
- <sup>167</sup>M. Tomes and T. Carmon, “Photonic micro-electromechanical systems vibrating at x-band (11-ghz) rates”, *Physical review letters* **102**, 113601 (2009).
- <sup>168</sup>Y.-S. Park and H. Wang, “Resolved-sideband and cryogenic cooling of an optomechanical resonator”, *Nature physics* **5**, 489–493 (2009).
- <sup>169</sup>L. Ding, C. Baker, P. Senellart, A. Lemaitre, S. Ducci, G. Leo, and I. Favero, “High frequency gaas nano-optomechanical disk resonator”, *Physical review letters* **105**, 263903 (2010).
- <sup>170</sup>M. Eichenfield, R. Camacho, J. Chan, K. J. Vahala, and O. Painter, “A picogram- and nanometre-scale photonic-crystal optomechanical cavity”, *nature* **459**, 550–555 (2009).
- <sup>171</sup>M. Eichenfield, J. Chan, R. M. Camacho, K. J. Vahala, and O. Painter, “Optomechanical crystals”, *Nature* **462**, 78–82 (2009).
- <sup>172</sup>E. Gavartin, R. Braive, I. Sagnes, O. Arcizet, A. Beveratos, T. J. Kippenberg, and I. Robert-Philip, “Optomechanical coupling in a two-dimensional photonic crystal defect cavity”, *Physical review letters* **106**, 203902 (2011).
- <sup>173</sup>G. Anetsberger, O. Arcizet, Q. P. Unterreithmeier, R. Rivière, A. Schliesser, E. M. Weig, J. P. Kotthaus, and T. J. Kippenberg, “Near-field cavity optomechanics with nanomechanical oscillators”, *Nature Physics* **5**, 909–914 (2009).
- <sup>174</sup>G. S. Wiederhecker, L. Chen, A. Gondarenko, and M. Lipson, “Controlling photonic structures using optical forces”, *Nature* **462**, 633–636 (2009).
- <sup>175</sup>Y.-G. Roh, T. Tanabe, A. Shinya, H. Taniyama, E. Kuramochi, S. Matsuo, T. Sato, and M. Notomi, “Strong optomechanical interaction in a bilayer photonic crystal”, *Physical Review B* **81**, 121101 (2010).
- <sup>176</sup>J. Thompson, B. Zwickl, A. Jayich, F. Marquardt, S. Girvin, and J. Harris, “Strong dispersive coupling of a high-finesse cavity to a micromechanical membrane”, *Nature* **452**, 72–75 (2008).

## BIBLIOGRAPHY

- <sup>177</sup>I. Favero, S. Stapfner, D. Hunger, P. Paulitschke, J. Reichel, H. Lorenz, E. M. Weig, and K. Karrai, “Fluctuating nanomechanical system in a high finesse optical microcavity”, *Optics express* **17**, 12813–12820 (2009).
- <sup>178</sup>J. Gieseler, B. Deutsch, R. Quidant, and L. Novotny, “Subkelvin parametric feedback cooling of a laser-trapped nanoparticle”, *Physical review letters* **109**, 103603 (2012).
- <sup>179</sup>S. Kuhn, B. A. Stickler, A. Kosloff, F. Patolsky, K. Hornberger, M. Arndt, and J. Millen, “Optically driven ultra-stable nanomechanical rotor”, *Nature communications* **8**, 1–5 (2017).
- <sup>180</sup>U. Delic, M. Reisenbauer, D. Grass, N. Kiesel, V. Vuletić, and M. Aspelmeyer, “Cavity cooling of a levitated nanosphere by coherent scattering”, *Physical review letters* **122**, 123602 (2019).
- <sup>181</sup>K. W. Murch, K. L. Moore, S. Gupta, and D. M. Stamper-Kurn, “Observation of quantum-measurement backaction with an ultracold atomic gas”, *Nature Physics* **4**, 561–564 (2008).
- <sup>182</sup>M. H. Schleier-Smith, I. D. Leroux, H. Zhang, M. A. Van Camp, and V. Vuletić, “Optomechanical cavity cooling of an atomic ensemble”, *Physical review letters* **107**, 143005 (2011).
- <sup>183</sup>R. W. Andrews, R. W. Peterson, T. P. Purdy, K. Cicak, R. W. Simmonds, C. A. Regal, and K. W. Lehnert, “Bidirectional and efficient conversion between microwave and optical light”, *Nature Physics* **10**, 321–326 (2014).
- <sup>184</sup>K. C. Balram, M. I. Davanco, J. D. Song, and K. Srinivasan, “Coherent coupling between radiofrequency, optical and acoustic waves in piezo-optomechanical circuits”, *Nature photonics* **10**, 346–352 (2016).
- <sup>185</sup>M. Mirhosseini, A. Sipahigil, M. Kalaei, and O. Painter, “Superconducting qubit to optical photon transduction”, *Nature* **588**, 599–603 (2020).
- <sup>186</sup>M. Aspelmeyer, T. J. Kippenberg, and F. Marquardt, “Cavity optomechanics”, *Reviews of Modern Physics* **86**, 1391 (2014).
- <sup>187</sup>M. Ludwig, B. Kubala, and F. Marquardt, “The optomechanical instability in the quantum regime”, *New Journal of Physics* **10**, 095013 (2008).

## BIBLIOGRAPHY

- <sup>188</sup>G. Brawley, M. Vanner, P. E. Larsen, S. Schmid, A. Boisen, and W. Bowen, “Nonlinear optomechanical measurement of mechanical motion”, *Nature communications* **7**, 1–7 (2016).
- <sup>189</sup>J. Chan, T. M. Alegre, A. H. Safavi-Naeini, J. T. Hill, A. Krause, S. Gröblacher, M. Aspelmeyer, and O. Painter, “Laser cooling of a nanomechanical oscillator into its quantum ground state”, *Nature* **478**, 89–92 (2011).
- <sup>190</sup>J. D. Teufel, T. Donner, D. Li, J. W. Harlow, M. Allman, K. Cicak, A. J. Sirois, J. D. Whittaker, K. W. Lehnert, and R. W. Simmonds, “Sideband cooling of micromechanical motion to the quantum ground state”, *Nature* **475**, 359–363 (2011).
- <sup>191</sup>S. Hong, R. Riedinger, I. Marinković, A. Wallucks, S. G. Hofer, R. A. Norte, M. Aspelmeyer, and S. Gröblacher, “Hanbury brown and twiss interferometry of single phonons from an optomechanical resonator”, *Science* **358**, 203–206 (2017).
- <sup>192</sup>I. Marinković, A. Wallucks, R. Riedinger, S. Hong, M. Aspelmeyer, and S. Gröblacher, “Optomechanical bell test”, *Physical review letters* **121**, 220404 (2018).
- <sup>193</sup>R. Riedinger, A. Wallucks, I. Marinković, C. Löschnauer, M. Aspelmeyer, S. Hong, and S. Gröblacher, “Remote quantum entanglement between two micromechanical oscillators”, *Nature* **556**, 473–477 (2018).
- <sup>194</sup>E. T. Jaynes and F. W. Cummings, “Comparison of quantum and semiclassical radiation theories with application to the beam maser”, *Proceedings of the IEEE* **51**, 89–109 (1963).
- <sup>195</sup>B. W. Shore and P. L. Knight, “The jaynes-cummings model”, *Journal of Modern Optics* **40**, 1195–1238 (1993).
- <sup>196</sup>S. Van Enk and H. Kimble, “Single atom in free space as a quantum aperture”, *Physical Review A* **61**, 051802 (2000).
- <sup>197</sup>G. Wrigge, I. Gerhardt, J. Hwang, G. Zumofen, and V. Sandoghdar, “Efficient coupling of photons to a single molecule and the observation of its resonance fluorescence”, *Nature Physics* **4**, 60–66 (2008).

## BIBLIOGRAPHY

- <sup>198</sup>R. Maiwald, A. Golla, M. Fischer, M. Bader, S. Heugel, B. Chalopin, M. Sondermann, and G. Leuchs, “Collecting more than half the fluorescence photons from a single ion”, *Physical Review A* **86**, 043431 (2012).
- <sup>199</sup>Y.-S. Chin, M. Steiner, and C. Kurtsiefer, “Nonlinear photon-atom coupling with 4pi microscopy”, *Nature communications* **8**, 1–5 (2017).
- <sup>200</sup>P. Horak, B. G. Klappauf, A. Haase, R. Folman, J. Schmiedmayer, P. Domokos, and E. Hinds, “Possibility of single-atom detection on a chip”, *Physical Review A* **67**, 043806 (2003).
- <sup>201</sup>M. Motsch, M. Zeppenfeld, P. W. Pinkse, and G. Rempe, “Cavity-enhanced rayleigh scattering”, *New Journal of Physics* **12**, 063022 (2010).
- <sup>202</sup>R. Loudon, “The quantum theory of light”, (OUP Oxford, 2000).
- <sup>203</sup>H. Tanji-Suzuki, I. D. Leroux, M. H. Schleier-Smith, M. Cetina, A. T. Grier, J. Simon, and V. Vuletić, “Interaction between atomic ensembles and optical resonators: classical description”, *Advances in atomic, molecular, and optical physics* **60**, 201–237 (2011).
- <sup>204</sup>Y.-H. Lien, G. Barontini, M. Scheucher, M. Mergenthaler, J. Goldwin, and E. Hinds, “Observing coherence effects in an overdamped quantum system”, *Nature Communications* **7**, 1–7 (2016).
- <sup>205</sup>M. D. Eisaman, J. Fan, A. Migdall, and S. V. Polyakov, “Invited review article: single-photon sources and detectors”, *Review of scientific instruments* **82**, 071101 (2011).
- <sup>206</sup>B.-C. Ren, G.-Y. Wang, F.-G. Deng, et al., “Universal hyperparallel hybrid photonic quantum gates with dipole-induced transparency in the weak-coupling regime”, *Physical Review A* **91**, 032328 (2015).
- <sup>207</sup>A. Borne, T. E. Northup, R. Blatt, and B. Dayan, “Efficient ion-photon qubit swap gate in realistic ion cavity-qed systems without strong coupling”, *Optics express* **28**, 11822–11839 (2020).
- <sup>208</sup>B. E. Saleh and M. C. Teich, “Fundamentals of photonics”, (John Wiley & Sons, 2019).

## BIBLIOGRAPHY

- <sup>209</sup>C. J. Hood, H. Kimble, and J. Ye, “Characterization of high-finesse mirrors: loss, phase shifts, and mode structure in an optical cavity”, *Physical Review A* **64**, 033804 (2001).
- <sup>210</sup>M. Sondermann and G. Leuchs, “Photon-atom coupling with parabolic mirrors”, in *Engineering the atom-photon interaction* (Springer, 2015), pp. 75–98.
- <sup>211</sup>A. Kawasaki, B. Braverman, E. Pedrozo-Peñafiel, C. Shu, S. Colombo, Z. Li, Ö. Özel, W. Chen, L. Salvi, A. Heinz, et al., “Geometrically asymmetric optical cavity for strong atom-photon coupling”, *Physical Review A* **99**, 013437 (2019).
- <sup>212</sup>D. Hunger, T. Steinmetz, Y. Colombe, C. Deutsch, T. W. Hänsch, and J. Reichel, “A fiber fabry–perot cavity with high finesse”, *New Journal of Physics* **12**, 065038 (2010).
- <sup>213</sup>S. Kato and T. Aoki, “Strong coupling between a trapped single atom and an all-fiber cavity”, *Physical review letters* **115**, 093603 (2015).
- <sup>214</sup>C. Junge, D. O’shea, J. Volz, and A. Rauschenbeutel, “Strong coupling between single atoms and nontransversal photons”, *Physical review letters* **110**, 213604 (2013).
- <sup>215</sup>I. Shomroni, S. Rosenblum, Y. Lovsky, O. Bechler, G. Guendelman, and B. Dayan, “All-optical routing of single photons by a one-atom switch controlled by a single photon”, *Science* **345**, 903–906 (2014).
- <sup>216</sup>T. Tiecke, J. D. Thompson, N. P. de Leon, L. Liu, V. Vuletić, and M. D. Lukin, “Nanophotonic quantum phase switch with a single atom”, *Nature* **508**, 241–244 (2014).
- <sup>217</sup>K. C. Cox, D. H. Meyer, N. A. Schine, F. K. Fatemi, and P. D. Kunz, “Increased atom-cavity coupling and stability using a parabolic ring cavity”, *Journal of Physics B: Atomic, Molecular and Optical Physics* **51**, 195002 (2018).
- <sup>218</sup>S. Ruddell, K. Webb, I. Herrera, A. Parkins, and M. Hoogerland, “Collective strong coupling of cold atoms to an all-fiber ring cavity”, *Optica* **4**, 576–579 (2017).
- <sup>219</sup>A. Johnson, M. Blaha, A. E. Ulanov, A. Rauschenbeutel, P. Schneeweiss, and J. Volz, “Observation of collective superstrong coupling of cold atoms to a 30-m long optical resonator”, *Physical review letters* **123**, 243602 (2019).

## BIBLIOGRAPHY

- <sup>220</sup>T. T. Saito, “Diamond turning of optics: the past, the present, and the exciting future”, *Optical Engineering* **17**, 176570 (1978).
- <sup>221</sup>I. Sahl, “On burning mirrors and lenses”, *Baghdad Court* **984**.
- <sup>222</sup>R. Rashed, “A pioneer in anaclastics: ibn sahl on burning mirrors and lenses”, *Isis* **81**, 464–491 (1990).
- <sup>223</sup>G.-I. Kweon and C.-H. Kim, “Aspherical lens design by using a numerical analysis”, *Journal of the Korean Physical Society* **51**, 93–103 (2007).
- <sup>224</sup>D. A. Steck, “Rubidium 87 d line data”, 2001.
- <sup>225</sup>M. K. Tey, G. Maslennikov, T. C. Liew, S. A. Aljunid, F. Huber, B. Chng, Z. Chen, V. Scarani, and C. Kurtsiefer, “Interfacing light and single atoms with a lens”, *New Journal of Physics* **11**, 043011 (2009).
- <sup>226</sup>H. Laabs and A. T. Friberg, “Nonparaxial eigenmodes of stable resonators”, *IEEE journal of quantum electronics* **35**, 198–207 (1999).
- <sup>227</sup>F. Zomer, V. Soskov, and A. Variola, “On the nonparaxial modes of two-dimensional nearly concentric resonators”, *Applied optics* **46**, 6859–6866 (2007).
- <sup>228</sup>M. Zeppenfeld and P. W. Pinkse, “Calculating the fine structure of a fabry-perot resonator using spheroidal wave functions”, *Optics express* **18**, 9580–9591 (2010).
- <sup>229</sup>M. Jaffe, L. Palm, C. Baum, L. Taneja, and J. Simon, “Aberrated optical cavities”, *arXiv preprint arXiv:2105.05235* (2021).
- <sup>230</sup>S. Dong, “Review on piezoelectric, ultrasonic, and magnetoelectric actuators”, *Journal of Advanced Dielectrics* **2**, 1230001 (2012).
- <sup>231</sup>Y. Yong, S. R. Moheimani, B. J. Kenton, and K. Leang, “Invited review article: high-speed flexure-guided nan positioning: mechanical design and control issues”, *Review of scientific instruments* **83**, 121101 (2012).
- <sup>232</sup>P. Pan, F. Yang, Z. Wang, B. Zhong, L. Sun, and C. Ru, “A review of stick–slip nan positioning actuators”, *Nan positioning Technologies*, 1–32 (2016).
- <sup>233</sup>L. Ricci, M. Weidemüller, T. Esslinger, A. Hemmerich, C. Zimmermann, V. Vuletic, W. König, and T. W. Hänsch, “A compact grating-stabilized diode laser system for atomic physics”, *Optics communications* **117**, 541–549 (1995).

## BIBLIOGRAPHY

- <sup>234</sup>A. Arnold, J. Wilson, and M. Boshier, “A simple extended-cavity diode laser”, *Review of Scientific Instruments* **69**, 1236–1239 (1998).
- <sup>235</sup>G. C. Bjorklund, “Frequency-modulation spectroscopy: a new method for measuring weak absorptions and dispersions”, *Optics letters* **5**, 15–17 (1980).
- <sup>236</sup>E. D. Black, “An introduction to pound–drever–hall laser frequency stabilization”, *American journal of physics* **69**, 79–87 (2001).
- <sup>237</sup>J. Hall, L. Hollberg, T. Baer, and H. Robinson, “Optical heterodyne saturation spectroscopy”, *Applied Physics Letters* **39**, 680–682 (1981).
- <sup>238</sup>D. McCarron, S. King, and S. Cornish, “Modulation transfer spectroscopy in atomic rubidium”, *Measurement science and technology* **19**, 105601 (2008).
- <sup>239</sup>E. Donley, T. Heavner, F. Levi, M. Tataw, and S. Jefferts, “Double-pass acousto-optic modulator system”, *Review of Scientific Instruments* **76**, 063112 (2005).
- <sup>240</sup>B. I. Lange, T. Brendel, and G. Hüttmann, “Temperature dependence of light absorption in water at holmium and thulium laser wavelengths”, *Applied optics* **41**, 5797–5803 (2002).
- <sup>241</sup>T. Arpornthip, C. Sackett, and K. Hughes, “Vacuum-pressure measurement using a magneto-optical trap”, *Physical Review A* **85**, 033420 (2012).
- <sup>242</sup>R. Grimm, M. Weidemüller, and Y. B. Ovchinnikov, “Optical dipole traps for neutral atoms”, *Advances in atomic, molecular, and optical physics* **42**, 95–170 (2000).
- <sup>243</sup>R. Drever, J. L. Hall, F. Kowalski, J. Hough, G. Ford, A. Munley, and H. Ward, “Laser phase and frequency stabilization using an optical resonator”, *Applied Physics B* **31**, 97–105 (1983).
- <sup>244</sup>E. Raab, M. Prentiss, A. Cable, S. Chu, and D. E. Pritchard, “Trapping of neutral sodium atoms with radiation pressure”, *Physical Review Letters* **59**, 2631 (1987).
- <sup>245</sup>G. Labeyrie, F. Michaud, and R. Kaiser, “Self-sustained oscillations in a large magneto-optical trap”, *Physical review letters* **96**, 023003 (2006).
- <sup>246</sup>S. Nussmann, M. Hijlkema, B. Weber, F. Rohde, G. Rempe, and A. Kuhn, “Submicron positioning of single atoms in a microcavity”, *Physical review letters* **95**, 173602 (2005).

## BIBLIOGRAPHY

- <sup>247</sup>K. M. Fortier, S. Y. Kim, M. J. Gibbons, P. Ahmadi, and M. S. Chapman, “Deterministic loading of individual atoms to a high-finesse optical cavity”, *Physical review letters* **98**, 233601 (2007).
- <sup>248</sup>G. Gattobigio, T. Pohl, G. Labeyrie, and R. Kaiser, “Scaling laws for large magneto-optical traps”, *Physica Scripta* **81**, 025301 (2010).
- <sup>249</sup>S. Chu, J. Bjorkholm, A. Ashkin, and A. Cable, “Experimental observation of optically trapped atoms”, *Physical review letters* **57**, 314 (1986).
- <sup>250</sup>N. Schlosser, G. Reymond, and P. Grangier, “Collisional blockade in microscopic optical dipole traps”, *Physical review letters* **89**, 023005 (2002).
- <sup>251</sup>N. Schlosser, G. Reymond, I. Protsenko, and P. Grangier, “Sub-poissonian loading of single atoms in a microscopic dipole trap”, *Nature* **411**, 1024–1027 (2001).
- <sup>252</sup>T. Savard, K. O’hara, and J. Thomas, “Laser-noise-induced heating in far-off resonance optical traps”, *Physical Review A* **56**, R1095 (1997).
- <sup>253</sup>J. Wang, J.-Y. Yang, I. M. Fazal, N. Ahmed, Y. Yan, H. Huang, Y. Ren, Y. Yue, S. Dolinar, M. Tur, and A. E. Willner, “Terabit free-space data transmission employing orbital angular momentum multiplexing”, *Nature Photonics* **6**, 488 (2012).
- <sup>254</sup>N. Bozinovic, Y. Yue, Y. Ren, M. Tur, P. Kristensen, H. Huang, A. E. Willner, and S. Ramachandran, “Terabit-scale orbital angular momentum mode division multiplexing in fibers”, *Science* **340**, 1545–1548 (2013).
- <sup>255</sup>L. Zhu, J. Liu, Q. Mo, C. Du, and J. Wang, “Encoding/decoding using superpositions of spatial modes for image transfer in km-scale few-mode fiber”, *Optics Express* **24**, 16934–16944 (2016).
- <sup>256</sup>A. Hasnaoui, A. Bencheikh, M. Fromager, E. Cagniot, and K. Ait-Ameur, “Creation of a sharper focus by using a rectified temp0 beam”, *Optics Communications* **284**, 1331–1334 (2011).
- <sup>257</sup>M. Mafu, A. Dudley, S. Goyal, D. Giovannini, M. McLaren, M. J. Padgett, T. Konrad, F. Petruccione, N. Lütkenhaus, and A. Forbes, “Higher-dimensional orbital-angular-momentum-based quantum key distribution with mutually unbiased bases”, *Physical Review A* **88**, 032305 (2013).

## BIBLIOGRAPHY

- <sup>258</sup>R. Fickler, R. Lapkiewicz, W. N. Plick, M. Krenn, C. Schaeff, S. Ramelow, and A. Zeilinger, “Quantum entanglement of high angular momenta”, *Science* **338**, 640–643 (2012).
- <sup>259</sup>P. Horak, H. Ritsch, T. Fischer, P. Maunz, T. Puppe, P. W. Pinkse, and G. Rempe, “Optical kaleidoscope using a single atom”, *Physical Review Letters* **88**, 043601 (2002).
- <sup>260</sup>P. Maunz, T. Puppe, T. Fischer, P. W. Pinkse, and G. Rempe, “Emission pattern of an atomic dipole in a high-finesse optical cavity”, *Optics Letters* **28**, 46–48 (2003).
- <sup>261</sup>T. Puppe, P. Maunz, T. Fischer, P. W. Pinkse, and G. Rempe, “Single-atom trajectories in higher-order transverse modes of a high-finesse optical cavity”, *Physica Scripta* **2004**, 7 (2004).
- <sup>262</sup>M. Gangl, P. Horak, and H. Ritsch, “Cooling neutral particles in multimode cavities without spontaneous emission”, *Journal of Modern Optics* **47**, 2741–2753 (2000).
- <sup>263</sup>T. Klaassen, J. de Jong, M. van Exter, and J. Woerdman, “Transverse mode coupling in an optical resonator”, *Optics Letters* **30**, 1959–1961 (2005).
- <sup>264</sup>J. Benedikter, T. Hummer, M. Mader, B. Schlederer, J. Reichel, T. W. Hänsch, and D. Hunger, “Transverse-mode coupling and diffraction loss in tunable fabry–perot microcavities”, *New Journal of Physics* **17**, 053051 (2015).
- <sup>265</sup>S. Gopalakrishnan, B. L. Lev, and P. M. Goldbart, “Emergent crystallinity and frustration with bose–einstein condensates in multimode cavities”, *Nature Physics* **5**, 845–850 (2009).
- <sup>266</sup>A. J. Kollar, A. T. Papageorge, K. Baumann, M. A. Armen, and B. L. Lev, “An adjustable-length cavity and bose–einstein condensate apparatus for multimode cavity qed”, *New Journal of Physics* **17**, 043012 (2015).
- <sup>267</sup>A. T. Papageorge, A. J. Kollar, and B. L. Lev, “Coupling to modes of a near-confocal optical resonator using a digital light modulator”, *Optics Express* **24**, 11447–11457 (2016).

## BIBLIOGRAPHY

- <sup>268</sup>C. Hamsen, K. N. Tolazzi, T. Wilk, and G. Rempe, “Strong coupling between photons of two light fields mediated by one atom”, *Nature Physics* **14**, 885–889 (2018).
- <sup>269</sup>F. Dubois, P. Emplit, and O. Hugon, “Selective mode excitation in graded-index multimode fiber by a computer-generated optical mask”, *Optics Letters* **19**, 433–435 (1994).
- <sup>270</sup>J. P. Kirk and A. L. Jones, “Phase-only complex-valued spatial filter”, *JOSA* **61**, 1023–1028 (1971).
- <sup>271</sup>J. A. Davis, D. M. Cottrell, J. Campos, M. J. Yzuel, and I. Moreno, “Encoding amplitude information onto phase-only filters”, *Applied Optics* **38**, 5004–5013 (1999).
- <sup>272</sup>V. Arrizon, U. Ruiz, R. Carrada, and L. A. Gonzalez, “Pixelated phase computer holograms for the accurate encoding of scalar complex fields”, *JOSA A* **24**, 3500–3507 (2007).
- <sup>273</sup>T. Ando, Y. Ohtake, N. Matsumoto, T. Inoue, and N. Fukuchi, “Mode purities of laguerre–gaussian beams generated via complex-amplitude modulation using phase-only spatial light modulators”, *Optics Letters* **34**, 34–36 (2009).
- <sup>274</sup>T. W. Clark, R. F. Offer, S. Franke-Arnold, A. S. Arnold, and N. Radwell, “Comparison of beam generation techniques using a phase only spatial light modulator”, *Optics Express* **24**, 6249–6264 (2016).
- <sup>275</sup>A. Forbes, A. Dudley, and M. McLaren, “Creation and detection of optical modes with spatial light modulators”, *Advances in Optics and Photonics* **8**, 200–227 (2016).
- <sup>276</sup>R. D. Juday and J. M. Florence, “Full-complex modulation with two one-parameter slms”, in *Wave propagation and scattering in varied media ii*, Vol. 1558 (International Society for Optics and Photonics, 1991), pp. 499–504.
- <sup>277</sup>L. G. Neto, D. Roberge, and Y. Sheng, “Full-range, continuous, complex modulation by the use of two coupled-mode liquid-crystal televisions”, *Applied Optics* **35**, 4567–4576 (1996).

## BIBLIOGRAPHY

- <sup>278</sup>S. Reichelt, R. Haussler, G. Fütterer, N. Leister, H. Kato, N. Usukura, and Y. Kanbayashi, “Full-range, complex spatial light modulator for real-time holography”, *Optics Letters* **37**, 1955–1957 (2012).
- <sup>279</sup>J. Arlt, K. Dholakia, L. Allen, and M. Padgett, “The production of multiringed laguerre–gaussian modes by computer-generated holograms”, *Journal of Modern Optics* **45**, 1231–1237 (1998).
- <sup>280</sup>Y. Ohtake, T. Ando, N. Fukuchi, N. Matsumoto, H. Ito, and T. Hara, “Universal generation of higher-order multiringed laguerre-gaussian beams by using a spatial light modulator”, *Optics Letters* **32**, 1411–1413 (2007).
- <sup>281</sup>N. Matsumoto, T. Ando, T. Inoue, Y. Ohtake, N. Fukuchi, and T. Hara, “Generation of high-quality higher-order laguerre-gaussian beams using liquid-crystal-on-silicon spatial light modulators”, *JOSA A* **25**, 1642–1651 (2008).
- <sup>282</sup>K. Sueda, G. Miyaji, N. Miyanaga, and M. Nakatsuka, “Laguerre-gaussian beam generated with a multilevel spiral phase plate for high intensity laser pulses”, *Optics Express* **12**, 3548–3553 (2004).
- <sup>283</sup>A. Bencheikh, M. Fromager, and K. A. Ameer, “Generation of laguerre–gaussian lg p0 beams using binary phase diffractive optical elements”, *Applied Optics* **53**, 4761–4767 (2014).
- <sup>284</sup>B. Brown and A. Lohmann, “Computer-generated binary holograms”, *IBM Journal of research and Development* **13**, 160–168 (1969).
- <sup>285</sup>V. Lerner, D. Shwa, Y. Drori, and N. Katz, “Shaping laguerre–gaussian laser modes with binary gratings using a digital micromirror device”, *Optics letters* **37**, 4826–4828 (2012).
- <sup>286</sup>J. Giaime, P. Saha, D. Shoemaker, and L. Sievers, “A passive vibration isolation stack for ligo: design, modeling, and testing”, *Review of scientific instruments* **67**, 208–214 (1996).
- <sup>287</sup>J. Aasi, B. Abbott, R. Abbott, T. Abbott, M. Abernathy, K. Ackley, C. Adams, T. Adams, P. Addesso, R. Adhikari, et al., “Advanced ligo”, *Classical and quantum gravity* **32**, 074001 (2015).

## BIBLIOGRAPHY

- <sup>288</sup>M. Notcutt, L.-S. Ma, A. D. Ludlow, S. M. Foreman, J. Ye, and J. L. Hall, “Contribution of thermal noise to frequency stability of rigid optical cavity via hertz-linewidth lasers”, *Physical Review A* **73**, 031804 (2006).
- <sup>289</sup>T. Kessler, C. Hagemann, C. Grebing, T. Legero, U. Sterr, F. Riehle, M. Martin, L. Chen, and J. Ye, “A sub-40-mhz-linewidth laser based on a silicon single-crystal optical cavity”, *Nature Photonics* **6**, 687–692 (2012).
- <sup>290</sup>J. Gallego, S. Ghosh, S. K. Alavi, W. Alt, M. Martinez-Dorantes, D. Meschede, and L. Ratschbacher, “High-finesse fiber fabry–perot cavities: stabilization and mode matching analysis”, *Applied Physics B* **122**, 47 (2016).
- <sup>291</sup>M. Notcutt, L.-S. Ma, J. Ye, and J. L. Hall, “Simple and compact 1-hz laser system via an improved mounting configuration of a reference cavity”, *Optics letters* **30**, 1815–1817 (2005).
- <sup>292</sup>S. Webster, M. Oxborrow, and P. Gill, “Vibration insensitive optical cavity”, *Physical review A* **75**, 011801 (2007).
- <sup>293</sup>T. C. Briles, D. C. Yost, A. Cingoz, J. Ye, and T. R. Schibli, “Simple piezoelectric-actuated mirror with 180 khz servo bandwidth”, *Optics express* **18**, 9739–9746 (2010).
- <sup>294</sup>E. Janitz, M. Ruf, Y. Fontana, J. Sankey, and L. Childress, “High mechanical bandwidth fiber-coupled fabry-perot cavity”, *Optics express* **25**, 20932–20943 (2017).
- <sup>295</sup>A. Ryou and J. Simon, “Active cancellation of acoustical resonances with an fpga fir filter”, *Review of Scientific Instruments* **88**, 013101 (2017).
- <sup>296</sup>M. Okada, T. Serikawa, J. Dannatt, M. Kobayashi, A. Sakaguchi, I. Petersen, and A. Furusawa, “Extending the piezoelectric transducer bandwidth of an optical interferometer by suppressing resonance using a high dimensional iir filter implemented on an fpga”, *Review of Scientific Instruments* **91**, 055102 (2020).
- <sup>297</sup>L. Greuter, S. Starosielec, D. Najer, A. Ludwig, L. Duempelmann, D. Rohner, and R. J. Warburton, “A small mode volume tunable microcavity: development and characterization”, *Applied Physics Letters* **105**, 121105 (2014).
- <sup>298</sup>D. W. Pohl, “Dynamic piezoelectric translation devices”, *Review of scientific instruments* **58**, 54–57 (1987).

## BIBLIOGRAPHY

- <sup>299</sup>C. Renner, P. Niedermann, A. Kent, and O. Fischer, “A vertical piezoelectric inertial slider”, *Review of scientific instruments* **61**, 965–967 (1990).
- <sup>300</sup>F. E. Scire and E. C. Teague, “Piezodriven 50-um range stage with subnanometer resolution”, *Review of scientific Instruments* **49**, 1735–1740 (1978).
- <sup>301</sup>R. Yang, M. Jouaneh, and R. Schweizer, “Design and characterization of a low-profile micropositioning stage”, *Precision Engineering* **18**, 20–29 (1996).
- <sup>302</sup>X. Zhu, X. Xu, Z. Wen, J. Ren, and P. Liu, “A novel flexure-based vertical nan positioning stage with large travel range”, *Review of Scientific Instruments* **86**, 105112 (2015).
- <sup>303</sup>J. Dong, S. M. Salapaka, and P. M. Ferreira, “Robust control of a parallel-kinematic nanopositioner”, *Journal of dynamic systems, measurement, and control* **130** (2008).
- <sup>304</sup>A. J. Fleming, “Nanopositioning system with force feedback for high-performance tracking and vibration control”, *IEEE/Asme Transactions on Mechatronics* **15**, 433–447 (2009).
- <sup>305</sup>A. J. Fleming, S. S. Aphale, and S. R. Moheimani, “A new method for robust damping and tracking control of scanning probe microscope positioning stages”, *IEEE Transactions on Nanotechnology* **9**, 438–448 (2009).
- <sup>306</sup>J. H. Lee, H. Y. Kim, K. H. Kim, M. H. Kim, and S. W. Lee, “Control of a hybrid active-passive vibration isolation system”, *Journal of Mechanical Science and Technology* **31**, 5711–5719 (2017).
- <sup>307</sup>V. M. Ryaboy, P. S. Kasturi, A. S. Nastase, and T. K. Rigney, “Optical table with embedded active vibration dampers (smart table)”, in *Smart structures and materials 2005: industrial and commercial applications of smart structures technologies*, Vol. 5762 (International Society for Optics and Photonics, 2005), pp. 236–244.
- <sup>308</sup>T. Ando, N. Kodera, E. Takai, D. Maruyama, K. Saito, and A. Toda, “A high-speed atomic force microscope for studying biological macromolecules”, *Proceedings of the National Academy of Sciences* **98**, 12468–12472 (2001).

## BIBLIOGRAPHY

- <sup>309</sup>N. Kodera, H. Yamashita, and T. Ando, “Active damping of the scanner for high-speed atomic force microscopy”, *Review of scientific instruments* **76**, 053708 (2005).
- <sup>310</sup>C. Kim, J. Jung, W. Youm, and K. Park, “Design of mechanical components for vibration reduction in an atomic force microscope”, *Review of Scientific Instruments* **82**, 035102 (2011).
- <sup>311</sup>Y. K. Yong, S. S. Aphale, and S. R. Moheimani, “Design, identification, and control of a flexure-based xy stage for fast nanoscale positioning”, *IEEE Transactions on Nanotechnology* **8**, 46–54 (2008).
- <sup>312</sup>C. Carrasco, P. Ares, P. De Pablo, and J. Gomez-Herrero, “Cutting down the forest of peaks in acoustic dynamic atomic force microscopy in liquid”, *Review of Scientific Instruments* **79**, 126106 (2008).
- <sup>313</sup>J. Bechhoefer, “Feedback for physicists: a tutorial essay on control”, *Reviews of modern physics* **77**, 783 (2005).
- <sup>314</sup>A. V. Oppenheim, “Discrete-time signal processing”, (Pearson Higher Education, 2010).
- <sup>315</sup>N. S. Nise, “Control systems engineering”, (John Wiley & Sons, 2020).
- <sup>316</sup>J. H. Griffin, “Friction damping of resonant stresses in gas turbine engine airfoils”, *Journal of Engineering for Power* **102**, 329–333 (1980).
- <sup>317</sup>C.-H. Menq, J. Griffin, and J. Bielak, “The influence of microslip on vibratory response, part ii: a comparison with experimental results”, *Journal of Sound and Vibration* **107**, 295–307 (1986).
- <sup>318</sup>E. P. Popov, C. E. Grigorian, and T.-S. Yang, “Developments in seismic structural analysis and design”, *Engineering structures* **17**, 187–197 (1995).
- <sup>319</sup>W. Y. Loo, P. Quenneville, and N. Chow, “A new type of symmetric slip-friction connector”, *Journal of Constructional Steel Research* **94**, 11–22 (2014).
- <sup>320</sup>A. Didier, J. Millo, C. Lacroute, M. Ouisse, J. Delporte, V. Giordano, E. Rubiola, and Y. Kersale, “Design of an ultra-compact reference ule cavity”, *Journal of Physics: Conference Series* **723**, 012029 (2016).

## BIBLIOGRAPHY

- <sup>321</sup>J. Archard, “Elastic deformation and the laws of friction”, Proceedings of the Royal Society of London. Series A. Mathematical and Physical Sciences **243**, 190–205 (1957).
- <sup>322</sup>A. Haase, B. Hessmo, and J. Schmiedmayer, “Detecting magnetically guided atoms with an optical cavity”, Optics letters **31**, 268–270 (2006).
- <sup>323</sup>S. A. Collins, “Lens-system diffraction integral written in terms of matrix optics”, JOSA **60**, 1168–1177 (1970).
- <sup>324</sup>R. Hauck, N. Hodgson, and H. Weber, “Misalignment sensitivity of unstable resonators with spherical mirrors”, Journal of Modern Optics **35**, 165–176 (1988).
- <sup>325</sup>A. E. Siegman and H. Miller, “Unstable optical resonator loss calculations using the prony method”, Applied optics **9**, 2729–2736 (1970).
- <sup>326</sup>Y. Suzaki and A. Tachibana, “Measurement of the um sized radius of gaussian laser beam using the scanning knife-edge”, Applied optics **14**, 2809–2810 (1975).
- <sup>327</sup>L.-M. Duan and H. Kimble, “Scalable photonic quantum computation through cavity-assisted interactions”, Physical review letters **92**, 127902 (2004).
- <sup>328</sup>F. K. Asadi, S. Wein, and C. Simon, “Cavity-assisted controlled phase-flip gates”, Physical Review A **102**, 013703 (2020).
- <sup>329</sup>H. S. Borges and C. J. Villas-Bôas, “Quantum phase gate based on electromagnetically induced transparency in optical cavities”, Physical Review A **94**, 052337 (2016).
- <sup>330</sup>A. Neuzner, M. Körber, S. Dürr, G. Rempe, and S. Ritter, “Breakdown of atomic hyperfine coupling in a deep optical-dipole trap”, Physical Review A **92**, 053842 (2015).
- <sup>331</sup>C. Schneider, M. Enderlein, T. Huber, and T. Schätz, “Optical trapping of an ion”, Nature Photonics **4**, 772–775 (2010).
- <sup>332</sup>R. B. Linnet, I. D. Leroux, M. Marciante, A. Dantan, and M. Drewsen, “Pinning an ion with an intracavity optical lattice”, Physical review letters **109**, 233005 (2012).

## BIBLIOGRAPHY

- <sup>333</sup>J. G. Danzl, M. J. Mark, E. Haller, M. Gustavsson, R. Hart, J. Aldegunde, J. M. Hutson, and H.-C. Nägerl, “An ultracold high-density sample of rovibronic ground-state molecules in an optical lattice”, *Nature Physics* **6**, 265–270 (2010).
- <sup>334</sup>T. Schaetz, “Trapping ions and atoms optically”, *Journal of Physics B: Atomic, Molecular and Optical Physics* **50**, 102001 (2017).
- <sup>335</sup>A. Lambrecht, J. Schmidt, P. Weckesser, M. Debatin, L. Karpa, and T. Schaetz, “Long lifetimes and effective isolation of ions in optical and electrostatic traps”, *Nature Photonics* **11**, 704–707 (2017).
- <sup>336</sup>J. Lukose, S. Chidangil, and S. D. George, “Optical technologies for the detection of viruses like covid-19: progress and prospects”, *Biosensors and Bioelectronics*, 113004 (2021).
- <sup>337</sup>D. J. Taylor, M. Glugla, and R.-D. Penzhorn, “Enhanced raman sensitivity using an actively stabilized external resonator”, *Review of Scientific Instruments* **72**, 1970–1976 (2001).
- <sup>338</sup>C. Wang and P. Sahay, “Breath analysis using laser spectroscopic techniques: breath biomarkers, spectral fingerprints, and detection limits”, *Sensors* **9**, 8230–8262 (2009).
- <sup>339</sup>M. Snels, T. Venezia, and L. Belfiore, “Detection and identification of tnt, 2, 4-dnt and 2, 6-dnt by near-infrared cavity ringdown spectroscopy”, *Chemical Physics Letters* **489**, 134–140 (2010).
- <sup>340</sup>D. Paul, A. Furgeson, and H. D. Osthoff, “Measurements of total peroxy and alkyl nitrate abundances in laboratory-generated gas samples by thermal dissociation cavity ring-down spectroscopy”, *Review of Scientific Instruments* **80**, 114101 (2009).
- <sup>341</sup>D. Yang, J. Guo, C. Liu, Q. Liu, and R. Zheng, “A direct bicarbonate detection method based on a near-concentric cavity-enhanced raman spectroscopy system”, *Sensors* **17**, 2784 (2017).
- <sup>342</sup>J. Hayden, B. Baumgartner, J. P. Waclawek, and B. Lendl, “Mid-infrared sensing of co at saturated absorption conditions using intracavity quartz-enhanced photoacoustic spectroscopy”, *Applied Physics B* **125**, 1–11 (2019).

## BIBLIOGRAPHY

- <sup>343</sup>G. B. Arfken and H. J. Weber, “Mathematical methods for physicists”, 1999.
- <sup>344</sup>R. Hauck, H. Kortz, and H. Weber, “Misalignment sensitivity of optical resonators”, *Applied Optics* **19**, 598–601 (1980).
- <sup>345</sup>H. H. Karow, “Fabrication methods for precision optics”, *Fabrication methods for precision optics* (2004).
- <sup>346</sup>T. Legero, T. Kessler, and U. Sterr, “Tuning the thermal expansion properties of optical reference cavities with fused silica mirrors”, *JOSA B* **27**, 914–919 (2010).
- <sup>347</sup>P. R. Yoder, “Mounting optics in optical instruments”, Vol. 2 (SPIE, 2008).
- <sup>348</sup>H. A. Macleod and H. A. Macleod, “Thin-film optical filters”, (CRC press, 2010).
- <sup>349</sup>M. A. Bandres and J. C. Gutiérrez-Vega, “Ince-gaussian modes of the paraxial wave equation and stable resonators”, *JOSA A* **21**, 873–880 (2004).
- <sup>350</sup>R. K. Tyson, “Conversion of zernike aberration coefficients to seidel and higher-order power-series aberration coefficients”, *optics letters* **7**, 262–264 (1982).
- <sup>351</sup>N. W. Hagood and A. von Flotow, “Damping of structural vibrations with piezoelectric materials and passive electrical networks”, *Journal of sound and vibration* **146**, 243–268 (1991).
- <sup>352</sup>A. A. Eielson and A. J. Fleming, “Passive shunt damping of a piezoelectric stack nanopositioner”, in *Proceedings of the 2010 american control conference (IEEE, 2010)*, pp. 4963–4968.
- <sup>353</sup>A. J. Fleming and S. R. Moheimani, “Sensorless vibration suppression and scan compensation for piezoelectric tube nanopositioners”, *IEEE Transactions on Control Systems Technology* **14**, 33–44 (2005).

# List of Publications

- <sup>1</sup>C. H. Nguyen, A. N. Utama, N. Lewty, K. Durak, G. Maslennikov, S. Straupe, M. Steiner, and C. Kurtsiefer, “Single atoms coupled to a near-concentric cavity”, *Physical Review A* **96**, 031802 (2017).
- <sup>2</sup>C. H. Nguyen, A. N. Utama, N. Lewty, and C. Kurtsiefer, “Operating a near-concentric cavity at the last stable resonance”, *Physical Review A* **98**, 063833 (2018).
- <sup>3</sup>A. N. Utama, C. H. Chow, C. H. Nguyen, and C. Kurtsiefer, “Coupling light to higher order transverse modes of a near-concentric optical cavity”, *Optics Express* **29**, 8130–8141 (2021).
- <sup>4</sup>A. N. Utama, J. P. N. Chen, and C. Kurtsiefer, “Passive stabilization of optical interferometers with friction dampers”, Manuscript in preparation, 2021.

## Appendix A

# Theory of Near-Concentric Cavity Paraxial Modes

This appendix presents a theoretical description of the paraxial cavity modes in the near-concentric regime. From the interaction Hamiltonian of an atom-cavity system, we evaluate the atom-cavity coupling strength and mode volume for an atom placed at the centre of the radial transverse modes of the cavity.

Furthermore, we show that the radial transverse modes have the same effective mode volumes and coupling strengths, at any particular cavity length. This would allow an atom to have similar interaction with all of the radial transverse modes of the cavity.

**Transverse modes of a near-concentric cavity** The paraxial modes of a Fabry-Perot optical cavity belong to a family of Gaussian transverse electromagnetic modes, expressed with a scalar field and form standing waves [208]. In a cavity with cylindrical symmetry, the transverse mode profile can be described by a complex amplitude

$$U_{p,l}(\rho, \phi, z) = A_{p,l} \frac{w_0}{w(z)} \left( \frac{\rho}{w(z)} \right)^l \mathcal{L}_p^l \left( \frac{2\rho^2}{w^2(z)} \right) \exp \left( -\frac{\rho^2}{w^2(z)} \right) \exp(i\psi_{p,l}(\rho, \phi, z)) , \quad (\text{A.1})$$

where  $p$  and  $l$  are the radial and azimuthal mode numbers of the Laguerre-Gaussian (LG) beams,  $A_{p,l}$  is the normalization constant,  $w(z) = w_0 \sqrt{1 + (z/z_0)^2}$  is the beam radius along the  $z$  direction with  $z_0 = \pi w_0^2/\lambda$  as the Rayleigh range and  $w_0$  as the waist radius,  $\mathcal{L}_p^l$  is the generalized Laguerre polynomial, and  $\psi_{p,l}(\rho, \phi, z)$  is the

APPENDIX A. THEORY OF NEAR-CONCENTRIC CAVITY PARAXIAL  
MODES

real-valued phase of the LG beam, given by

$$\psi_{p,l}(\rho, \phi, z) = -kz - k\frac{\rho^2}{2R(z)} - l\phi + (2p + l + 1)\zeta(z), \quad (\text{A.2})$$

where  $R(z) = z + z_0^2/z$  is the curvature radius of the wavefront, and  $\zeta(z) = \tan^{-1}(z/z_0)$  is the Gouy phase. The LG mode is bounded between the two spherical mirrors of radii  $R_1$  and  $R_2$ , with the wavefront matching the mirror surfaces. The resonance frequencies of the cavity depend on the transverse mode numbers  $p$  and  $l$ ,

$$v_{q,p,l} = \left( q + (2p + l + 1)\frac{\Delta\zeta}{\pi} \right) v_F, \quad (\text{A.3})$$

where  $q$  is the longitudinal mode number of the cavity,  $v_F = c/2L$  is the cavity free spectral range, and  $\Delta\zeta = \zeta(z_{M2}) - \zeta(z_{M1})$  is the Gouy phase difference between the two cavity mirrors.

The transverse modes of a near-concentric cavity follow the equations above, as the paraxial approximation is still valid in our operating regime, up to the last stable resonance. The paraxial approximation only breaks down in very short critical distances (see Section 2.1.2), and may then require non-paraxial treatments [226–228]. The cavity mode radius of a near-concentric cavity  $w(z) = w_0\sqrt{1 + (z/z_0)^2}$  is rapidly diverging along the cavity axis, due to a short Rayleigh range  $z_0 = \pi w_0^2/\lambda$ .

**Interaction Hamiltonian of an atom-cavity system** An electric field operator with a complex mode amplitude profile  $U_j(\mathbf{r})$  can be expressed as

$$\hat{\mathbf{E}}_j(\mathbf{r}) = i\mathbf{e}_\lambda N_j \left[ U_j(\mathbf{r})\hat{a}_j - U_j^*(\mathbf{r})\hat{a}_j^\dagger \right], \quad (\text{A.4})$$

where  $\mathbf{e}_\lambda$  is the electric field polarization unit vector,  $N_j$  is a normalization coefficient, and  $\hat{a}_j$  and  $\hat{a}_j^\dagger$  are the destruction and creation mode operators [202]. The free field Hamiltonian of the electromagnetic mode inside a cavity with volume  $V$  has a similar structure to a harmonic oscillator,

$$\hat{H}_0 = \frac{\epsilon_0}{2} \int dV \left[ \hat{\mathbf{E}}_j(\mathbf{r})^2 + c^2 \hat{\mathbf{B}}_j(\mathbf{r})^2 \right] = \hbar\omega_j \left( \hat{a}_j^\dagger \hat{a}_j + \frac{1}{2} \right) \quad (\text{A.5})$$

with  $\hat{\mathbf{B}}_j(\mathbf{r})$  as the corresponding magnetic field operator. By imposing the normalization condition

$$\int dV |U_j(\mathbf{r})|^2 = 1, \quad (\text{A.6})$$

APPENDIX A. THEORY OF NEAR-CONCENTRIC CAVITY PARAXIAL MODES

we obtain the normalization coefficient  $N_j = (\hbar\omega_j/2\epsilon_0)^{1/2}$ .

The interaction Hamiltonian between an electromagnetic field and an atomic dipole, in the electric-dipole approximation, is given by

$$\hat{H}_I(\mathbf{r}) = \hat{\mathbf{E}}_j(\mathbf{r}) \cdot \hat{\mathbf{d}} \quad (\text{A.7})$$

where  $\hat{\mathbf{d}} = d_a (\hat{\pi}^\dagger + \hat{\pi}) \mathbf{e}_d$  is the atomic electric-dipole operator with  $d_a$  as the dipole moment,  $\hat{\pi}^\dagger = |e\rangle\langle g|$  and  $\hat{\pi} = |g\rangle\langle e|$  as the transition operators between ground and excited atomic states, and  $\mathbf{e}_d$  as the dipole unit vector. Assuming that the atomic dipole and electric field polarization vectors point to the same direction,  $\mathbf{e}_\lambda = \mathbf{e}_d$ , we obtain

$$\hat{H}_I(\mathbf{r}) = id_a \sqrt{\frac{\hbar\omega_j}{2\epsilon_0}} [U_j(\mathbf{r})\hat{a}_j - U_j^*(\mathbf{r})\hat{a}_j^\dagger] [\hat{\pi}^\dagger + \hat{\pi}] , \quad (\text{A.8})$$

with an explicit dependence of the atom position  $\mathbf{r}$  on the mode amplitude  $U_j(\mathbf{r})$ .

**Radial transverse modes for atom-cavity coupling** A class of LG modes suitable for atom-cavity coupling with stationary atoms is the radial transverse modes, which are LG modes with no angular momentum ( $l = 0$ ) and maximum field strengths on the cavity axis. The complex amplitude of radial transverse modes is given by

$$U_{p,0}(\rho, \phi, z) = A_{p,0} \frac{w_0}{w(z)} \mathcal{L}_p^0 \left( \frac{2\rho^2}{w^2(z)} \right) \exp \left( -\frac{\rho^2}{w^2(z)} \right) \exp(i\psi_{p,0}(\rho, \phi, z)) . \quad (\text{A.9})$$

The radial transverse modes of a near-concentric cavity have spatial dependencies on both the axial and radial direction. Here, we assume that the atom is located at the center of the cavity mode ( $\mathbf{r} = \mathbf{0}$ ), such that  $\rho = 0$  and  $z = 0$  [77]. The amplitude of the radial transverse mode at this center point is

$$U_{p,0}(\mathbf{r} = \mathbf{0}) = A_{p,0} , \quad (\text{A.10})$$

where we have evaluated  $w(0) = w_0$ ,  $\mathcal{L}_p^0(0) = 1$ , and  $\exp(i\psi_{p,0}(0, \phi, 0)) = 1$ .

The prefactor  $A_{p,0}$  can be determined from the normalization condition (Eq. A.6), and has a physical significance as follows. If we assume a theoretical cavity with a uniform distribution of mode amplitude  $U_{p,0} = A_{p,0}$ , the normalization condition yields

$$A_{p,0} = \frac{1}{\sqrt{V_{m,p}}} , \quad (\text{A.11})$$

APPENDIX A. THEORY OF NEAR-CONCENTRIC CAVITY PARAXIAL  
MODES

where  $V_{m,p}$  is the mode volume of such theoretical cavity.

Using Eq. A.8, we evaluate the interaction Hamiltonian of an atom placed in the centre of a radial transverse cavity mode,

$$\hat{H}_I(\mathbf{r} = \mathbf{0}) = i\hbar g_{ac} [\hat{a}_j - \hat{a}_j^\dagger] [\hat{\pi}^\dagger + \hat{\pi}] , \quad (\text{A.12})$$

with the atom-cavity coupling strength

$$g_{ac} = \sqrt{\frac{\omega_j d_a^2}{2\hbar\epsilon_0 V_{m,p}}} . \quad (\text{A.13})$$

It is interesting to note that the coupling constant  $g_{ac} \propto 1/\sqrt{V_{m,p}}$  only depends on the radial mode number  $p$  through the mode volume  $V_{m,p}$ . This is not necessarily true for other classes of transverse modes. For example, non-radial transverse modes ( $l \neq 0$ ) have zero mode amplitude at the centre, i.e.  $U_{p,l \neq 0}(\mathbf{r} = \mathbf{0}) = 0$ , which complicates the interpretation of such mode volumes.

**Mode volume calculation of radial transverse modes** In this part, we show that the mode volume of radial transverse modes  $V_{m,p}$  only depends on the beam waist  $w_0$  and cavity length  $L$ , and does not depend on the radial mode number  $p$ . Using the normalization condition (Eq. A.6),

$$\int dV |U_{p,0}(\rho, \phi, z)|^2 = \int dz \int \rho d\rho \int d\phi \frac{1}{V_{m,p}} \left[ \frac{w_0}{w(z)} \mathcal{L}_p^0 \left( \frac{2\rho^2}{w^2(z)} \right) \right]^2 \exp \left( -\frac{2\rho^2}{w^2(z)} \right) \quad (\text{A.14})$$

$$1 = \frac{1}{V_{m,p}} \frac{\pi w_0^2 L}{2} \int_0^\infty du e^{-u} \mathcal{L}_p^0(u)^2 , \quad (\text{A.15})$$

where we have used the substitution  $u = 2\rho^2/w^2(z)$ . The integration can be calculated using the orthonormal property of Laguerre polynomial [343],

$$\int_0^\infty dx e^{-x} \mathcal{L}_m^0(x) \mathcal{L}_n^0(x) = \delta_{m,n} . \quad (\text{A.16})$$

The mode volume of radial transverse modes is thus calculated to be

$$V_{m,p} = \frac{1}{2} \pi w_0^2 L , \quad (\text{A.17})$$

independent of the radial mode number  $p$ . At a particular cavity length  $L$ , the beam waist parameter  $w_0$  is evaluated from the cavity boundary conditions, and is

APPENDIX A. THEORY OF NEAR-CONCENTRIC CAVITY PARAXIAL  
MODES

also independent on the radial mode number  $p$ . Hence, the atom-cavity coupling constant  $g_{ac}$  is maintained over all the radial transverse modes,

$$g_{ac} = \sqrt{\frac{\omega_j d_a^2}{\pi \hbar \epsilon_0 w_0^2 L}} . \quad (\text{A.18})$$

As a completing remark, we note that the mode of a physical cavity forms a standing wave on the longitudinal direction. Hence, the complex term  $\exp(i\psi_{p,0})$  in Eq. A.9 should be replaced with  $\cos(\psi_{p,0} + \delta)$  with  $\delta$  determined by the boundary conditions and longitudinal mode number. Assuming the atom is located at the anti-node of such standing wave, the evaluation of the atom-cavity coupling is similar as above, but with the mode volume reduced to half,

$$V_{m,p}^{sw} = \frac{1}{4} \pi w_0^2 L . \quad (\text{A.19})$$

## Appendix B

# Geometrical Alignment Theory of Near-Concentric Cavity

This appendix discusses geometrical considerations in aligning near-concentric cavity. In real systems, the optical axes of the two cavity mirrors may not coincide, and hence the cavity axis is located somewhere else. We present a way to determine the cavity axis, following the method described in Ref. [344]. We deduce the effect of transverse misalignment on the near-concentric cavity, and estimate the alignment sensitivity in small critical distances. In addition, we show that the angular and transverse misalignment are equivalent, which suggest that a full misalignment correction is sufficiently performed either in the angular or transverse directions, and not necessarily both, for ideal cavity mirrors.

Without loss of generality, the misalignment scenarios are described in two dimensions, i.e. transverse misalignment only in one direction, to ease the geometrical discussions and drawings. Such scenarios can be easily extended to three dimensions. We also assume that the mirrors are ideally spherical, with the same radius of curvature over all the mirror surface. Our cavity mirrors are designed as such, but some imperfections arise due to optical coatings and other factors (see Appendix C).

**Determining the cavity axis geometrically** In Figure B.1, the two mirror axes do not coincide with each other. The cavity axis can be drawn as a line passing through both curvature centres of the mirrors. In this case, the cavity axis is normal to both mirror surfaces, which satisfy the boundary conditions to form the cavity modes. Nonetheless, the cavity axis and the cavity modes have to be located within both the apertures of the cavity mirrors.

APPENDIX B. GEOMETRICAL ALIGNMENT THEORY OF  
NEAR-CONCENTRIC CAVITY

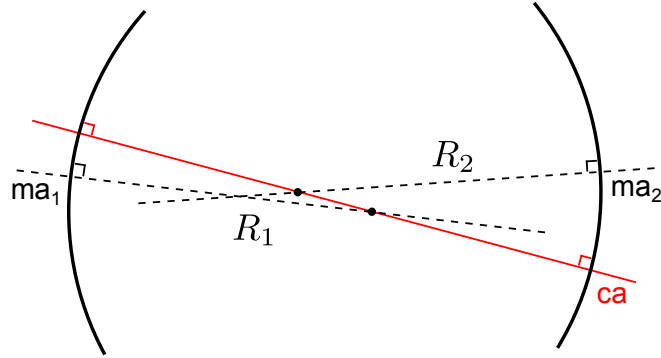


Figure B.1: Determining the cavity axis geometrically. In a cavity system where the mirror axes ( $ma_1$  and  $ma_2$ ) do not coincide, the cavity axis ( $ca$ ) is formed by passing through the two curvature centres of the cavity mirrors.

**Effect of the transverse misalignment** We use the geometrical method above to estimate the effect of the transverse misalignment in a near-concentric cavity. In Figure B.2, a small transverse misalignment  $\delta x$  of the second mirror causes the cavity axis to rotate by  $\delta\theta$ . The amount of rotation can be approximated as

$$\delta\theta = \frac{\delta x}{d}, \quad (\text{B.1})$$

which can get very large for a small critical distance  $d$ . The tolerable amount of cavity axis rotation depends on the setup, but is typically very small, particularly if the preceding and following optical elements are located far from the cavity with small apertures.

We can estimate how well our near-concentric cavity tolerates such cavity axis rotation, using the data provided in Section 3.3.2. At a critical distance of around  $1.7 \mu\text{m}$ , the cavity transmission after coupling through a single-mode fibre is halved by a transverse misalignment of around  $30 \text{ nm}$ . This corresponds to a transmission-halving rotation angle  $\delta\theta$  of around  $18 \text{ mrad}$ , which is quite large considering a fibre-coupling scenario. We attribute this to the anaclastic design of the lens-mirrors, which transforms radial wavefront normal to the mirror surface, to be parallel with the lens-mirror axis on the lens output. Hence, even with a rotated cavity axis, the collimated input and output modes are parallel with the mirror axes, but slightly displaced by around  $(R+t)\delta\theta = 0.18 \text{ mm}$ , where  $t$  is the thickness of the lens-mirror element.

APPENDIX B. GEOMETRICAL ALIGNMENT THEORY OF  
NEAR-CONCENTRIC CAVITY

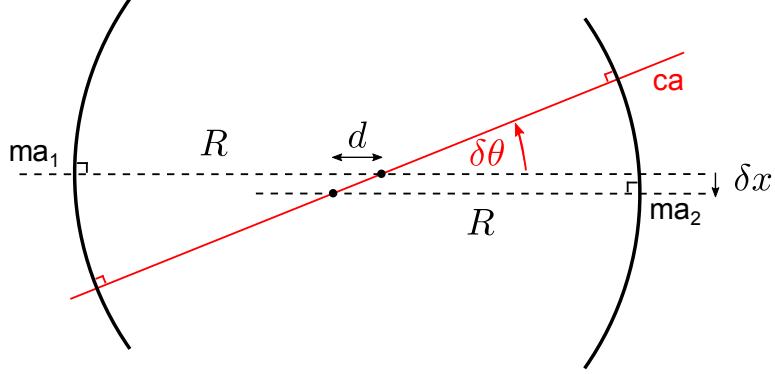


Figure B.2: Rotation of cavity axis due to transverse misalignment. In a near-concentric cavity with a critical distance  $d$ , a small transverse misalignment  $\delta x$  of the second mirror rotates the cavity axis by an angle  $\delta\theta$ .

With a slightly rotated cavity axis due to a small transverse misalignment, the coupling of an input beam to the fundamental near-concentric cavity mode can be re-maximised by simply displacing the input beam using the alignment mirrors. The cavity output mode is then displaced from the initial position in the opposite transverse direction, as observed with a camera. Hence, near-concentric cavity modes can in principle be formed at any spot on the cavity mirrors, with similar coupling efficiencies, as long as the cavity mode is located well within the mirror aperture.

**Equivalence of angular and transverse misalignment** Besides the transverse misalignments, tip and tilt rotational misalignments also occurs during the alignment and baking process. We show that they are equivalent – any transverse misalignment can be corrected by a rotational alignment, and vice versa. In Figure B.3, the transverse misalignment  $\delta x$  of the second mirror is corrected by a small tilt  $\delta\alpha$  on the mirror,

$$\delta\alpha = \frac{\delta x}{R}, \quad (\text{B.2})$$

which places the curvature centre of the mirror back on the first mirror axis. This puts the cavity axis back at the initial aligned location. Though, in this new configuration, the cavity axis is no longer parallel with the second mirror axis, but slightly tilted with a small angle  $\delta\alpha$ . Referring to the case described above, a small transverse misalignment of around 30 nm, which rotates the cavity axis by about 18 mrad, can be corrected with a small tilt angle  $\delta\alpha$  of around 5.4  $\mu\text{rad}$ .

APPENDIX B. GEOMETRICAL ALIGNMENT THEORY OF  
NEAR-CONCENTRIC CAVITY

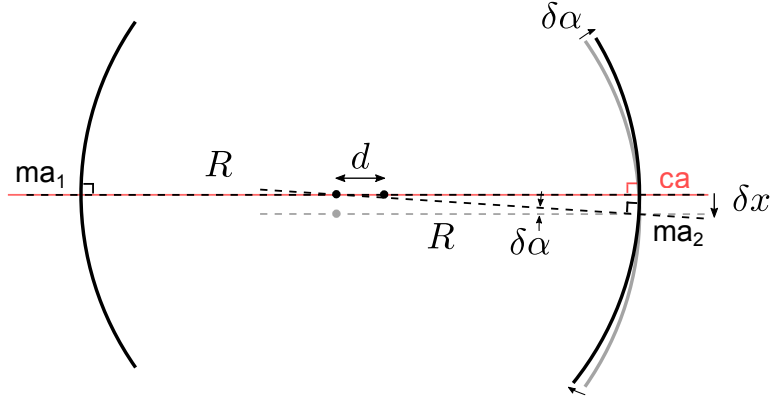


Figure B.3: Equivalence of angular and transverse misalignment. A small transverse misalignment  $\delta x$  can be corrected by rotating the mirror by a small angle  $\delta\alpha$ .

Therefore, any tip and tilt rotational misalignment accrued during the cavity alignment and baking processes can be corrected with the translation stages. In the near-concentric cavity mechanical design version 1 and 2 (see Section 2.2.2), rotational misalignment of around 1 mrad is equivalent to a transverse misalignment of around  $5.5 \mu\text{m}$ . The mechanical design version 3 (see Section 8.2.1) uses three thin piezo stacks to implement the tip and tilt rotation between the cavity mirrors, and a linear movement along the optical axis. Thus, any transverse misalignment accrued in this system can also be rectified with the rotational alignments.

## Appendix C

# Imperfections of the Cavity Mirror

This appendix discusses some possible sources of imperfections in the cavity mirrors. In particular, we examine how the cavity mirrors depart from an ideally spherical profile. We consider two main mechanisms that result in the mirror asphericity: (1) localised aberrations in the mirror surface and (2) variations of optical coating thickness. The mirror asphericity would thus cause the cavity to deviate from a cylindrical symmetry, resulting in an effective aperture size smaller than the design size.

**Localised aberrations in the mirror surface** There are a few possible causes of mirror surface aberrations. First, the spherical surface quality is specified by the manufacturer to exhibit irregularities of at most 0.3 fringes. Assuming that the characterisation is performed via interferogram with reference surfaces [345], this translates to a maximum surface height deviation of  $\sim 120$  nm (peak to valley) at some localised spots. While this aberration figure is sufficiently low for most applications, it can be relatively high for the near-concentric cavity modes.

Second, the mechanical stresses induced by the clamping process and temperature changes might cause some local aberrations in the mirror surface [346, 347]. The typical deformation figures are on the order of nm/kPa and nm/K for the clamping stresses and temperature changes, respectively.

**Variations in the optical coating thickness** To obtain a highly reflective cavity mirror, dielectric layers with alternating indices of refraction are deposited on the spherical surface. Although the coating materials and deposition techniques are closely-guarded trade secrets, we can point out a few properties of the optical

## APPENDIX C. IMPERFECTIONS OF THE CAVITY MIRROR

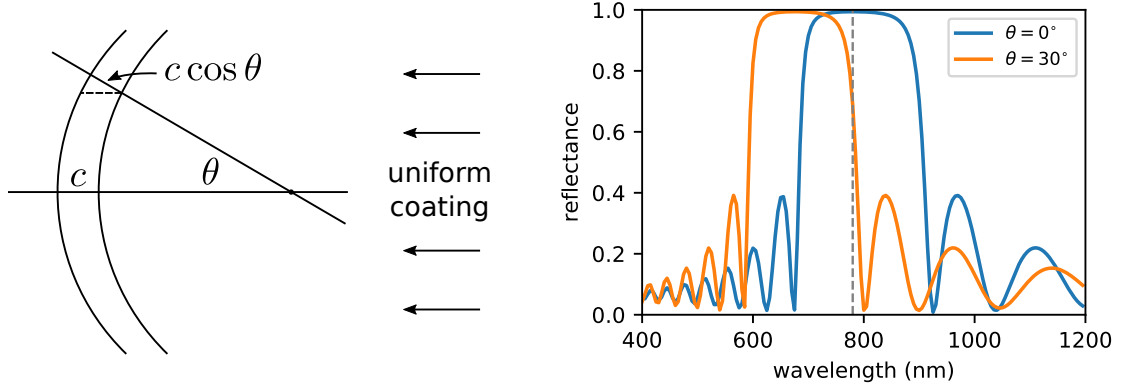


Figure C.1: The effect of uniform optical coating on the mirror reflectivity (left). With uniform coating thickness  $c$  and ray angle  $\theta$ , the thickness of the coating normal to the mirror surface is  $c \cos \theta$ . Thus, the reflection spectrum (right) for larger ray angles is shifted to lower wavelengths. The dashed line indicates 780 nm.

coating. First, the layers are deposited uniformly with the same thickness. Second, the main component of the optical coating is a periodic quarter-wave layers, which results in a high reflectance at the design wavelength [348].

On a spherical surface, the deposition of a uniform-thickness optical coating results in a variation of the coating thickness normal to the surface, which scales with  $\cos \theta$  of the ray angle (see Figure C.1). This shifts the operating range of the mirror to lower wavelengths, and with high enough ray angle, the mirror is no longer reflective at the design wavelength.

To estimate how the optical thickness variation modifies the mirror reflectivity, we construct a simple model based on thin-film interferences [348]. Quarter-wave layers with refractive indices of  $n_1 = 2.0$  and  $n_2 = 1.4$  are stacked alternately, with  $n_1$  forming the first and last layers. The input medium is air ( $n_i = 1$ ), and the output medium is the glass substrate ( $n_o = 1.77$ ), and the incident light wavelength is 780 nm. With 17 coating layers, this arrangement reproduces a similar behaviour as given in the mirror reflection spectra (see Figure C.1, right).

Figure C.2 (left) shows the mirror reflectivity  $\mathcal{R}$ , plotted in  $1 - \mathcal{R}$ , over different ray angles  $\theta$ . The expected cavity finesse formed with the two mirrors can be approximated by  $\mathcal{F} = \pi/(1 - \mathcal{R})$ . With 17 coating layers at 780 nm design wavelength, the mirror reflectivity and the cavity finesse are  $\mathcal{R} = 1 - 5.9 \times 10^{-3}$  and  $\mathcal{F} = 540$  at zero ray angle, respectively. The finesse decreases with larger ray angles,

## APPENDIX C. IMPERFECTIONS OF THE CAVITY MIRROR

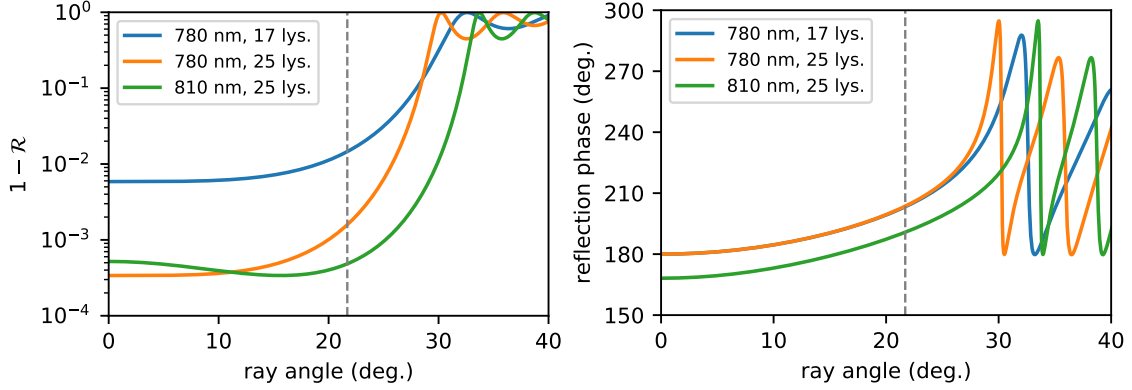


Figure C.2: The mirror reflectivity  $\mathcal{R}$  with 780 nm incident light, plotted in  $1 - \mathcal{R}$ , and the phase of the reflected beam as a function of the ray angle  $\theta$ . The dashed line indicates the nominal aperture angle of our cavity mirror. The expected cavity finesse can be estimated from the mirror reflectivity as  $\mathcal{F} = \pi/(1 - \mathcal{R})$ .

and halves at about 20.4 degrees. This finesse-halving angle is close to the nominal aperture angle of our cavity mirror at 21.7 degrees.

In higher finesse cavities, the finesse-halving angle decreases. With 25 coating layers, the initial finesse of  $\mathcal{F} = 9300$  halves at only about 17.9 degrees of ray angle. To increase the ray angle operational range, the design wavelength can be slightly increased. With 25 coating layers at 810 nm design wavelength, the finesse-halving angle is increased to around 25.3 degrees, with a lower initial finesse of  $\mathcal{F} = 6000$ .

Besides the variations in the mirror reflectivity and cavity finesse, the phase of the reflected light changes with the ray angles as well (see Figure C.2, right). Together, they change the mirror coating penetration depth at different ray angles, which contribute to the asphericity of the mirror surface.

**Cylindrical asymmetry** With perfectly spherical mirrors, the cylindrical symmetry of the near-concentric cavity would still hold even when the cavity axis is not aligned with the mirror axes (see Appendix B). This is because the curvature radii of the mirrors are the same at whichever point of the mirror. When the cavity does not have a cylindrical symmetry, the frequency spacing of the transverse modes would be different along the two transverse directions. With the cavity slightly misaligned, instead of a single  $LG_{01}$  peak, there are now two peaks with slightly different resonance frequencies. These peaks are most likely the Hermite-Gaussian modes  $HG_{01}$  and  $HG_{10}$ , the eigenmodes with a rectangular symmetry, although

## APPENDIX C. IMPERFECTIONS OF THE CAVITY MIRROR

they could well be a transition between the LG and HG modes [349]. The frequency difference between the  $HG_{01}$  and  $HG_{10}$  modes is larger with smaller critical distances, or with cavity axis further away from the centre of the mirrors.

**Limited aperture size** The effective aperture diameter of our near-concentric cavity is around 1.4 mm, which is much smaller than the nominal aperture diameter of 4.07 mm (see Section 7.2.1). It is likely that such aperture size limitation is due to the mirror asphericity. In some theoretical works, it has been shown that spherical mirrors are better suited to form highly-divergent cavity modes than parabolic mirrors [226]. It would be interesting to investigate how each component of the cavity mirror aberration [350] plays a role in limiting the cavity aperture size [229].

## Appendix D

# Miscellaneous Techniques in Noise Reduction

We have described two main techniques we use to reduce the mechanical noise of our near-concentric cavity (see Chapter 6). Here we discuss a few other techniques which also reduce the noise to some extent.

**Vacuum system damping** As the cavity setup is mounted inside a cuvette attached to the vacuum chamber, the mechanical noise of the vacuum chamber has a significant impact on the cavity noise. The vacuum chamber is mounted on a rigid optical table, which is supported by pneumatic vibration isolators. Nevertheless, we observe mechanical noise on the order of 1 nm in the cavity version 2 setups (see Section 8.2.1), which is most likely due to noise amplification by the resonant mechanical structures of the flexural translation stage and the cuvette mount.

The mechanical noise of the vacuum chamber can be reduced by damping the vacuum system. One of the most reliable method is to put some damping materials in-between the vacuum chamber and the optical table. Thus, the vacuum chamber is supported by the optical table not only at the mounting points, but across a larger area through the damping material. Furthermore, the mechanical vibration modes of the vacuum chamber have higher damping ratios.

We use mineral wool (Rockwool) as the damping material. We pack them in small compressible packets and place them sporadically beneath the vacuum chamber. We observe a noise reduction of around 10-30% with this method. Most importantly, we no longer have occurrences where the mechanical resonances of the vacuum chamber coincide with the mechanical resonances of the cavity setup, which in the past have

## APPENDIX D. MISCELLANEOUS TECHNIQUES IN NOISE REDUCTION

resulted in much higher noise figures.

The mechanical noise can also couple to the vacuum chamber through the electrical connections, in particular the ion pump and ion gauge cables, as they are quite rigid. Thus, we bend the ion pump cable by a  $\sim 90^\circ$  angle, to prevent transmission of the mechanical noise waves, and then also clamp the cable to the optical table. As the ion gauge is not necessary for continuous cavity operation, we remove the ion gauge cable before experiments.

**Electrical noise taming** The electrical noise is usually easy to identify as it often consists of sharp spikes in the frequency spectra with widths much less than 1 Hz. The most common electrical noise source is the mains electricity with 50 Hz fundamental frequency. Besides the fundamental frequencies, the noise spikes are typically also observed at their harmonic frequencies. The effect of the electrical noise on the mechanical noise depends on the actuator response, and can be fairly high if a few of the noise spikes are near the actuator resonances.

To reduce the electrical noise from mains electricity, we use dedicated low-noise power supplies to power the actuator drivers. The actuator response for the flexural translation stage can reach  $100 \mu\text{m}/\text{V}$  near the first mechanical resonance (see Figure 6.2), and consequently we require a power supply with noise lower than  $1 \mu\text{V}/\sqrt{\text{Hz}}$  near the resonance to achieve a noise level of less than  $0.1 \text{ nm}/\sqrt{\text{Hz}}$ .

Other common sources of electrical noise are from the USB cables and hubs connected to the computer, and unexpected ground loops particularly when sharing the grounding connection with other devices. It is beneficial to determine where the noise spikes each come from and to what extent they affect the total mechanical noise, before re-configuring the electrical circuits to tame the respective noise sources.

**Actuator shunting** In piezo-based actuators, the mechanical vibrations couple to the electrical vibrations. Thus, the mechanical noise can be damped via the electrical circuits, using passive components such as resistors, capacitors, and inductors [351]. The amount of damping provided depends on the “shunting” circuit and the electro-mechanical coupling factor.

With a resistor and capacitor in parallel with the actuator, we observed noise reduction across a wide frequency region (100 Hz to 2 kHz), which resulted in 5-10%

## APPENDIX D. MISCELLANEOUS TECHNIQUES IN NOISE REDUCTION

decrease in the total noise. This agrees with the simulation of the damping ratio, with an electro-mechanical coupling factor of around 0.5.

A higher damping performance can be achieved with a resonant RLC circuit, which could dissipate most of the energy near the resonance [352]. However, in the low frequency regime, the required inductance can be extremely high. For our actuators, we require inductance on the order of 1 H, which is not practical and might have to be synthesised artificially [353]. As it is not straightforward how to design a combined resonant circuit to operate in a larger frequency region, or how to design a driver which could handle the circuit impedance, we did not pursue this method, and opted for active noise cancellation strategy instead (see Section 6.1).